

University of Dundee

DOCTOR OF PHILOSOPHY

Microfluidic Methods for Investigating Cell Migration and Cell Mechanics

Belotti, Yuri

Award date:
2016

[Link to publication](#)

General rights

Copyright and moral rights for the publications made accessible in the public portal are retained by the authors and/or other copyright owners and it is a condition of accessing publications that users recognise and abide by the legal requirements associated with these rights.

- Users may download and print one copy of any publication from the public portal for the purpose of private study or research.
- You may not further distribute the material or use it for any profit-making activity or commercial gain
- You may freely distribute the URL identifying the publication in the public portal

Take down policy

If you believe that this document breaches copyright please contact us providing details, and we will remove access to the work immediately and investigate your claim.

DEPARTMENT OF CELL AND
DEVELOPMENTAL BIOLOGY

SCHOOL OF LIFE SCIENCES



**MICROFLUIDIC METHODS FOR
INVESTIGATING CELL MIGRATION AND
CELL MECHANICS**

A THESIS SUBMITTED FOR THE DEGREE OF DOCTOR OF
PHILOSOPHY IN CELL AND DEVELOPMENTAL BIOLOGY

Author: Yuri Belotti

Academic Year 2015-2016

DECLARATION

This thesis has been written solely by me and is a record of my research undertaken at the University of Dundee. It does not include material submitted in any previous application for a degree. All references cited have been consulted and any outcome resulting from collaborative work has been specifically stated in the text.

Date

06/07/2016

Signature

TABLE OF CONTENTS

List of Figures	i
Acronyms	xiii
Acknowledgements	xvii
Abstract	xx
1 Introduction	1
1.1 Basic Microfabrication Techniques	5
1.1.1 Rapid prototyping	5
1.1.2 Development of the mould: photolithography	6
1.1.3 Replica moulding	8
1.1.4 Bonding mechanisms	10
1.2 Investigating cell migration and cell mechanics	11
2 Chemotaxis in Confined Environments	13
2.1 Introduction and Background	13
2.1.1 Chemotaxis in <i>Dictyostelium discoideum</i>	14
2.1.2 Different modes of motion	20
2.1.2.1 Actin-based motility	21
2.1.2.2 Actin-independent motility: the blebbing mode	24
2.1.3 The role of cell adhesions	26
2.1.4 Microtubules in cell migration	29
2.1.5 Microfluidic technology for the study of cell migration	32
2.2 Aims and Objectives	35
2.3 Methods	36
2.3.1 Development of the migration chip	36
2.3.2 Cell preparation	38
2.3.3 Cell loading, microscopy and data analysis	39
2.3.4 Imaging	41
2.3.4.1 Confocal imaging	41
2.3.4.2 Total internal reflection fluorescence microscopy	43
2.3.5 Numerical simulation	46
2.3.6 Image and data analysis	47
2.4 Results	48
2.4.1 Development of the microfluidic chip	48
2.4.2 Characterisation of the microfluidic chip	48
2.4.3 Relationship between spatial confinement and cell speed	52
2.4.4 Actomyosin cytoskeleton in confined cells	56

2.4.4.1	Relationship between migratory modes and confinement	59
2.4.4.2	Dictyostelium cells move with constant speed in microchannels	66
2.4.4.3	The putative role of myosin VII in blebbing	71
2.4.5	Focal adhesions	73
2.4.5.1	Paxillin foci	73
2.4.5.2	Actin foci	75
2.4.5.3	FRY foci	79
2.4.6	The role of microtubules	82
2.4.6.1	Interaction between microtubules and actin foci	84
2.5	Discussion	86
3	Cell Migration in Bifurcating Microchannels	95
3.1	Introduction	95
3.2	Aims and Objectives	99
3.3	Methods	100
3.3.1	Development of the migration chip	100
3.3.1.1	Testing cellular response to hydraulic resistance	100
3.3.1.2	Decoupling hydraulic resistance from chemical gradient	101
3.3.2	Growth and development of <i>Dictyostelium</i> cells	102
3.3.3	Nocodazole treatment	103
3.3.4	Cell loading, microscopy and data analysis	103
3.3.5	Estimation of the difference in cAMP concentration at bifurcations	106
3.4	Results	108
3.4.1	Directional bias and the role of microtubules	108
3.4.2	The role of the actomyosin cytoskeleton	112
3.4.3	The case of dead-end channels	113
3.4.4	Decoupling hydraulic resistance from chemical gradient	117
3.5	Discussions	119
4	Cell Mechanics	123
4.1	Introduction and Background	123
4.1.1	Mechanical properties at the subcellular level	124
4.1.2	Mechanical properties of the cell	126
4.1.3	Measuring cellular mechanical properties	134
4.1.4	Applications in biomedical diagnostics	136
4.1.4.1	Early detection of prostate cancer	138
4.2	Aims and Objectives	140
4.3	Methods	141
4.3.1	Optical stretching	141
4.3.1.1	Theoretical explanation	142
4.3.1.2	Experimental set-up	146
4.3.1.3	Image analysis	150
4.3.1.4	Cell preparation	152
4.3.2	Hydrodynamic stretcher	152
4.3.2.1	Theoretical explanation	153
4.3.2.2	Device fabrication and experimental set-up	157

4.3.2.3	Numerical simulation	158
4.3.2.4	Cell culture protocol	159
4.3.2.5	Treatment with Latrunculin A	160
4.3.2.6	Image and data analysis	160
4.4	Results	161
4.4.1	Optical stretching of erythrocytes	161
4.4.2	Hydrodynamic stretching of human cell lines	162
4.4.2.1	Characterisation of the hydrodynamic stretcher	162
4.4.2.2	Hydrodynamic stretching of prostate and bladder cancer cells	166
4.4.2.3	Hydrodynamic stretching of healthy and cancerous prostate cells	167
4.5	Discussions	170
5	Conclusions	175
	Bibliography	207

LIST OF FIGURES

1.1	Thin film deposition of the photosensitive polymer by spin coating . . .	6
1.2	Photolithographic steps to obtain the mould.	7
1.3	Workflow of the photolithographic process.	8
1.4	Chemical structure of PDMS.	8
1.5	Development of a PDMS microfluidic chip by soft-lithography.	9
2.1	Life cycle of <i>Dictyostelium discoideum</i>	17
2.2	Schematic of the polarisation of a chemotactic cell	19
2.3	Schematic of the 'pseudopod-centred model'	21
2.4	Actin treadmilling at the leading edge of a migrating cell	22
2.5	Contractile action of myoII	23
2.6	Schematic of a blebbing cell	26
2.7	Schematic a focal adhesion	27
2.8	3D structure of the microfluidic device	37
2.9	Schematic of chemical gradient into the microfluidic device	38
2.10	Schematic of the confocal principle	42
2.11	Schematic of a laser scanning confocal microscope	42
2.12	Schematic of a TIRF microscope	44
2.13	Schematic of the evanescent field in a TIRF microscope	45
2.14	Phase of the micro-fabrication process	48
2.15	Time evolution of the cAMP gradient profile within a single microchannel	49
2.16	Testing the linearity of the chemical gradient	50
2.17	Influence of cells on the chemical gradient	51
2.18	Example of a cell migrating in a microchannel and its velocity profile .	52
2.19	Mean velocity of cells measured in microchannels with different cross-sectional area	53
2.20	Cells migrating in tapered channels	54
2.21	Representative kymograph of a cell migrating in a tapered channel . .	55
2.22	Displacement-time relationship for the uniformly decelerated motion .	55
2.23	Localisation of actin and myoII in channels with different cross section	57
2.24	Example of a myoII-null cell stuck at the entrance of a migration channel	58
2.25	Comparison between the mean velocity of WT myoII-null cells	58
2.26	F-actin dynamics during different phases of bleb formation	60
2.27	Kymographs of the leading edge of a blebbing cell	60
2.28	Percentage occurrence of the two migration modes as a function of the size of the microchannels	61
2.29	Comparison between the mean speed of cells that migrate by blebbing-mode by pseudopod-like mode	62
2.30	Kymographs of a blebbing cell	62

2.31	Sequential pictures of the distribution of VatM in a cell migrating in 2 μm by 5 μm channels	63
2.32	Sequential pictures of the distribution of VatM in a cell migrating in 2 μm by 2 μm channels	65
2.33	Kymograph of a blebbing cell	67
2.34	Kymograph of a cell migrating via pseudopodia	67
2.35	Blebbing cells migrating in a 5 μm wide, 2 μm high channel	68
2.36	Relationship between the mean velocity of the single cells and the protrusion rate	69
2.37	Schematic of the F-actin distribution within a confocal section of a cell migrating in a microchannel	70
2.38	Relationship between the extension of the actin polymerisation zone at the leading edge and the cell speed	70
2.39	Spatial distribution of myoVII in a cell that migrates via pseudopodia	72
2.40	Spatial distribution of myosin VII in a blebbing cell	72
2.41	Spatial distribution of PaxB foci in a confined cell	73
2.42	Spatial distribution of PaxB in confined cells	74
2.43	Comparison between the main speed of WT and paxB-null mutants	75
2.44	Confocal and TIRF images of actin foci	76
2.45	Kymograph of a LifeAct-labelled cell. Confocal image	77
2.46	Temporal distribution of the foci's duration and period	78
2.47	Relationship between the mean speed of migration and the mean number of foci	79
2.48	Relationship between the rate of actin foci activation and the rate contractile vacuole rate	80
2.49	Spatial distribution of FRY foci in a FRY-GFP knockin cell	81
2.50	Spatial distribution of FRY foci in a FRY-GFP knockin cell migrating in a indented channel	81
2.51	Effect of FRY foci on cell speed	82
2.52	Spatial distribution of actin (in red) a in FRY-null cell.	83
2.53	Microtubules dynamics in spatially confined cells	84
2.54	Direction of Nuclear-Centrosomal (NC) axis in Dictyostelium cells migrating in 3D environment	84
2.55	Colocalisation of actin foci and MTs, TIRF images	85
3.1	Schematics of the three types bifurcation.	101
3.2	Decoupling chemical and mechanical cues.	102
3.3	Schematics of the bifurcating channels.	104
3.4	Profiles of the cAMP gradient along the bifurcating channel and across each bifurcation.	105
3.5	Estimation of the difference in cAMP concentration at bifurcations.	106
3.6	Cell travelling through a symmetric bifurcating channel.	108
3.7	Cell travelling through an asymmetric bifurcating channel.	109
3.8	Results from the directional bias analysis.	110
3.9	Cells migrating in serial symmetric bifurcations.	111
3.10	Actin distribution in bifurcating channels.	112
3.11	Localisation of myoII in a cell migrating through bifurcating channel	113

3.12	Cells moving into alternating dead-end channels.	114
3.13	Cells protruding into symmetric dead-end channels.	115
3.14	Fluid displaced by a cell that invades dead-end channels	115
3.15	Interaction between cell and surrounding fluid at dead-end channels .	116
3.16	Cells migrating up the cAMPs gradient despite the higher hydraulic re- sistance.	117
3.17	Relationship between the cellular directional bias at each bifurcation and the difference in local cAMP	118
3.18	Putative explanation of the directional bias based on the hypothesis of <i>autologous chemotaxis</i>	122
4.1	Tangent vectors on a polymer	125
4.2	Qualitative responses of an uniaxial bar of different materials to a step- stress	127
4.3	Qualitative stress-strain diagrams for elastic and viscoelastic materials .	129
4.4	Empirical models of viscoelasticity	131
4.5	Laser beam acting on a dielectric particle	144
4.6	Dual-beam optical trap	144
4.7	Momentum exchange between an incident ray and a dielectric particle	145
4.8	Lensing effect of a spheric object on a laser beam	146
4.9	Mechanical deformation induced by the dual-beam optical trap	147
4.10	Schematics of the optical set-up of the opto-fluidic stretcher	148
4.11	Schematics of the opto-fluidic stretcher	149
4.12	Screenshot of the Virtual Instrument developed in LabVIEW to control the laser power	151
4.13	Schematic of the hydrodynamic stretching device	154
4.14	Lift forces acting on a suspended particle flowing in a microchannel . .	155
4.15	Optical stretching of erythrocytes	161
4.16	Design of the region downstream of the inertial focuser, meshed using Comsol	164
4.17	Velocity profile and stream lines evaluated in the absence and in the presence of a cell	164
4.18	Hydrodynamic forces acting on a cell	165
4.19	Example of a hydrodynamically stretched cell	167
4.20	Difference in mechanical properties between prostate and bladder can- cer cells before and after Latrunculin A treatment	168
4.21	Difference in mechanical properties between PNT2 and DU145 cells. .	169
4.22	Difference in deformability between PNT2 and DU145 cells at the posi- tion of maximum deformation and downstream of it.	170

LIST OF TABLES

2.1	Microfabrication steps to develop the first layer of the mould for the cell migration device	36
2.2	Microfabrication steps to develop the second layer of the mould for the cell migration device	37
2.3	List of the Dictyostelium strains that I used.	39
3.1	Results of the Fischer exact test among all the combinations of cAMP concentration for each bifurcation type	112
4.1	Techniques for measuring the mechanical properties of cells	135
4.2	Microfabrication steps to develop the hydrodynamic stretcher mould	158
4.3	Hydrodynamic parameters of the small and big bends that compose the inertial focuser	163
4.4	Hydrodynamic parameters of the main and side branches that join at the deformation region	163
4.5	Parameters used in the calculation of the drag and viscous forces	166

ACRONYMS

ACA Aggregation stage Adenylate Cyclase.

AFM Atomic Force Microscopy.

BFP Back Focal Plane.

CAD Computer-Aided Design.

cAMP 3',5'- cyclic Adenosine Monophosphate.

CV Contractile Vacuole.

DEV Development.

EM Extracellular Matrix.

EXP Exposure.

F-actin Actin filaments.

G-actin Actin monomers.

GFP Green Fluorescent Protein.

HB Hard Bake.

HS Hydrodynamic Stretcher.

IF Intermediate Filament.

MSD Mean Square Displacement.

MT Microtubule.

MTOC Microtubule Organising Centre.

myoII Myosin II.

NC Nuclear-Centrosomal.

OS Optical Stretcher.

PDE Phosphodiesterase.

PEB Post Exposure Bake.

PSA Prostate Specific Antigen.

RBC Red blood cell.

SB Soft Bake.

SGR Soft glassy rheology.

SibA Similar to Integrin Beta.

TFM Traction Force Microscopy.

TIRF total internal reflection.

WT Wild Type.

ACKNOWLEDGEMENTS

I would like to thank who helped in the work presented in this thesis, in particular my supervisor Dr David McGloin for always supporting me and my research, for giving me the possibility to explore new ideas and carry out a number of different projects and collaborations.

I am thankful to my second supervisor Professor Kees Weijer for all his valuable insights into the biological aspects of my PhD, and for inducing me to strengthen my critical approach to science.

I am also grateful to Professor Tim Newman, Professor Caroline Wilkinson, Professor Kate Storey, Professor Paul Crocker, Dr Alan Prescott, Mrs Marianne Reilly, Dr Eric Griffis and Dr Philip Murray, Dr Maria Ana Cataluna and Professor Douglas Steele for the scientific and personal support.

I would like to thank Mr Stuart Anthony and Dr Gary Callon for assisting me in the various phases of the microfabrication.

I want to thank all my collaborators: Dr Craig McDougall for introducing me to microfabrication; Ms Gail Singer for the tireless help and assistance with all the Dictyostelium-related work; Dr Greg Sobczyk for helping with cell culturing and for providing genetically modified cells; Dr Claudia Conte for giving me the Latrunculin; Mr Tianjun Huang for his work on the automatic cell tracking algorithm; Mr Scott Palmer for pro-

viding the prostate and bladder cells; Dr Michael Conneely for helping with COMSOL, high speed imaging and for our scientific conversations.

Further acknowledgements go to Dr Paul Prentice and Dr Paul Campbell for giving me the possibility to use their equipment; Professor Ghulam Nabi for providing bladder and prostate cells and supporting my research.

I thank the EPSRC for funding my PhD, Tenovus Scotland and SUPA for additional financial support.

A big thank you goes to Dr David McGloin's group for the shared time and for making the lab such a friendly place.

I want to thank my family, my friends and all the people who have always believed in me, in my capabilities, in my passions and who have contributed to help me becoming the person I aim to be, those who are still accompanying my journey and those that have sadly left this world and that will always be inside me and silently guide me.

Among all, the biggest acknowledgement goes to you, Serenella: my partner, best friend, greatest supporter and biggest love. Your attitude, positivity, strength, tireless presence and infinite love have always given me the motivation to not surrender and go further, reach my goals and become a better man, day after day, year after year.

ABSTRACT

In this thesis I explore how migratory properties of the model organism *Dictyostelium discoideum* are influenced by dimensionality and topology of the environment that surrounds the cell. Additionally, I sought to develop a microfluidic device able to measure mechanical properties of single cells with a sufficient throughput to account for the inherent heterogeneity of biological samples. Throughout this thesis I made use of microfabrication methods such as photo-lithography and soft-lithography, to develop ad hoc microstructured substrates. These tools enabled me to tackle different biological and biomedical questions related to cell migration and cell mechanics. Confining cells into channels with low dimensionality appeared to regulate the velocity of cellular locomotion, as well as the migration strategy adopted by the cell. Spatial confinement induced an altered arrangement of the acto-myosin cytoskeleton and microtubules. Moreover, the spatial constraint resulted in a simplified, mono-dimensional migration, characterised by constant average speed. Additionally, some cellular processes tended to occur in a periodic fashion, upon confinement. Interestingly, if *Dictyostelium* cells migrated through asymmetric bifurcating micro-channels, they appeared to be able to undergo a 'decision-making' process leading to a directional bias. Although the biophysical mechanism underlying this response is yet to be understood, the data shown in this thesis suggest that *Dictyostelium* cells respond to differences in local

concentrations of chemoattractants. The speed of a cell that crawls in a channel also depends on the cell's stiffness, that in turn represents a measure of the density and structure of its cytoskeleton. To date, only a few methods have been developed to investigate cell mechanics with sufficient throughput. This motivated my interest in developing a microfluidic-based device that, exploiting the recording capabilities of a modern high speed camera, enabled me to assess the cellular mechanical properties at a rate greater than 10,000 cells per second, without the need for cell labelling. In this thesis I presented an example of how this method can be employed to detect differences between healthy and cancerous prostate cells, as well as to differentiate between prostate and bladder cancer cells based on their mechanical response. In conclusion, the work presented in this thesis highlights the interdisciplinarity required to investigate complex biological and biomedical problems. Specifically, the use of quantitative approaches that span from microtechnology, live imaging, computer vision and computational modelling enabled me to investigate novel biological processes as well as to explore new diagnostic technologies that aim to promote the improvement of the future healthcare.

Life without enquiry is not worth living for a man.

Socrates

INTRODUCTION

On the first of March 1960, in the introductory lecture of the course 'The Molecular Control of Cellular Activity' at *The Institute of Science and Technology*, University of Michigan, the Austrian biologist Paul A. Weiss commented:

'Lest our necessary and highly successful preoccupation with cell fragments and fractions obscure the fact that the cell is not just an inert playground for a few almighty masterminding molecules, but is a system, a hierarchically ordered system, of mutually interdependent species of molecules, molecular groupings, and supramolecular entities; and that life, through cell life, depends on the order of their interactions (P. A. Weiss, 1961).'

During his lengthy career, Weiss came to understand that a cell cannot be understood as the summation of its constituents, but rather should be thought as a whole unit. In fact, all cellular components are subjected to non-linear interactions, which ultimately lead to global hierarchical organisation and order. With his work Weiss proposed an organicist view of the cell, where both *top-down* and *bottom-up* causation were integrated (Saetzler et al., 2011). In this way he encouraged scientists to go beyond

the *genetic determinism*¹ as it fails to explain the observed emergent phenomena that govern living organisms.

After more than 50 years, despite the advances in both fundamental science and technology, the gap persists between our knowledge of phenomena occurring at the single-molecule level and our insights into the cellular realm, where a myriad of molecules interplay and collectively give rise to complex, and yet efficient processes that make life possible.

In spite of their chaotic and extremely dynamic nature, biological systems are able to generate order from disorder, and avert the restrictions of the second law of thermodynamics through continuous energy dissipation (Huber et al., 2013). This observation was already pointed out in 1944 by Erwin Schrödinger in his book 'What is Life?' (Schrödinger, 1944).

One of the most valuable ways to explore the relationships between the molecular and the cellular levels is to study the cytoskeleton (Fletcher and Mullins, 2010). In fact, this cellular structure is involved in two important processes: the spatial organisation of the cellular contents, and the generation of forces that allow the cell to move and respond to external stimuli (Fletcher and Mullins, 2010). In addition, the self-assembly of cytoskeletal constituents, which is guided by biochemical and physical cues, explains the global organisation observed in cells (Huber et al., 2013).

In the next chapters I discuss the main properties of cytoskeletal polymers and how their dynamics and interactions are regulated by their accessory and motor proteins. Specifically, in Chapters 2 and 4 I describe the role of such polymers, and more impor-

¹Based on the idea that the organism is determined by a genetic program encoded into the DNA.

tantly the networks that they form in cell migration and cell mechanics respectively. The organisation of cytoskeletal polymeric networks is intimately related to the transmission of internal stresses to the surrounding cellular environment, as well as to the sensing of external stresses (Fletcher and Mullins, 2010). As a cell is an open system, a variety of external stimuli continuously act on it (Saetzler et al., 2011). Therefore, one cannot investigate the cell without taking into account the properties of the environment that surrounds it. It follows that the higher is the complexity of the micro-environment, the more difficult it will be to investigate the cell's behaviour. In light of these considerations, the importance of controlling the cell's 'boundary condition' emerges.

In the last two decades, advances in the field of microfluidics have allowed this specific issue to be addressed, offering unprecedented spatial and temporal control over a wide range of local environmental parameters, namely: biochemical gradients, temperature, charge, electric field, topology, mechanical properties and stresses (Velve-Casquillas et al., 2010). This technology has enabled scientists to perform experiments with more physiological conditions and study a variety of biological processes such as: chemotaxis (Li Jeon et al., 2002), stem cell differentiation (Chung et al., 2005), cellular response to virus infections (Walker, 2004), environmental effects on gene expression (Paliwal et al., 2007).

Another important aspect that accompanies the use of microfluidics in the life sciences is a growing interdisciplinary approach. Biologists are now working side by side with physicists, engineers, mathematicians and computational scientists, and combining sophisticated experimental analyses with mathematical modelling, are trying to unravel

natural phenomena. This rather recent 'cultural revolution' is probably the only way to address the complex and dynamic nature of living organisms, that was already clear at the time of Weiss. Moreover, such a holistic approach paves the way to more in-depth knowledge of diseases. This is enabling the development of better early-stage diagnostic tools and more effective, non-invasive treatments, and therefore contributing to the improvement of our lives.

Microfluidic methods are being developed to carry out various diagnostic tests in developing countries, where such tools might be the only solution to the lack of infrastructures and resources (Martinez et al., 2010; Chin et al., 2011). Cheap materials such as paper and wax are used to fabricate extremely simple and portable devices that can be coupled with mobile phones to provide reliable diagnostic outputs (Martinez et al., 2010).

Furthermore, physical properties that characterise the micro and nano scales offer the possibility to perform analyses otherwise impossible using conventional macroscopic methods (Sackmann et al., 2014). In Chapter 4 I give an example of how these 'microscopic effects' can be successfully exploited to discriminate different cell types, assess the effects of specific drugs on cells and detect the presence of cancer cell. Such a method allows conducting high throughput measurements at the single-cell level, without the need for cell labelling or pre-treatment.

In the following part of this introductory chapter I describe the main aspects of micro-fabrication, *i.e.* the technique used to develop the microfluidic devices that I employed in the whole experimental work discussed in this thesis.

1.1 Basic Microfabrication Techniques

The first microfluidic device was a gas chromatograph, developed by Terry et al. (1979) at Stanford University. This invention was made possible by technologies that were well established in the field of microelectronics, such as photolithography and silicon etching.

Advances in microfluidics were promoted by the rapid growth of molecular biology, especially the investigation of DNA and proteins in aqueous solutions (McDonald et al., 2000) but the biggest contribution to the wider spread of miniaturised fluidic devices was given by the discovery of new polymeric materials (Martynova et al., 1997; McCormick et al., 1997; Roberts et al., 1997). In fact, silicon-based technologies are expensive and time-consuming (development time in the order of weeks), while polymeric materials allow fabrication of inexpensive prototypes in less than two days, from the idea to the working device (Whitesides, 2006).

1.1.1 Rapid prototyping

The fabrication of a microfluidic device starts with a design, that is usually made via computer-aided design (CAD) software. High-resolution commercial systems are then used to print the design onto specific supports, which serve as photomasks for the next phase of the fabrication process. The material selected for the substrate depends on the size of the features on the design:

- For geometries bigger than 5-7 μm , inexpensive acetate substrates can be used.
- For smaller features, borosilicate glass or quartz substrates are required. They are coated with a thin film of chrome and patterned by an electron beam. Such

a technique allows one to achieve sub-micron resolution.

1.1.2 Development of the mould: photolithography

The geometric structures printed on the photomask are transferred through contact photolithography to a silicon wafer, previously coated with a thin layer of a particular photosensitive polymer. More specifically, a spin-coater is used for the deposition of the photopolymer. A spin-coater consists of a rotating chuck onto which a silicon wafer is fixed. An aliquot of the photopolymer is poured on the wafer and spread by centrifugal forces, as shown in Fig. 1.1. The thickness of the layer T is uniform and

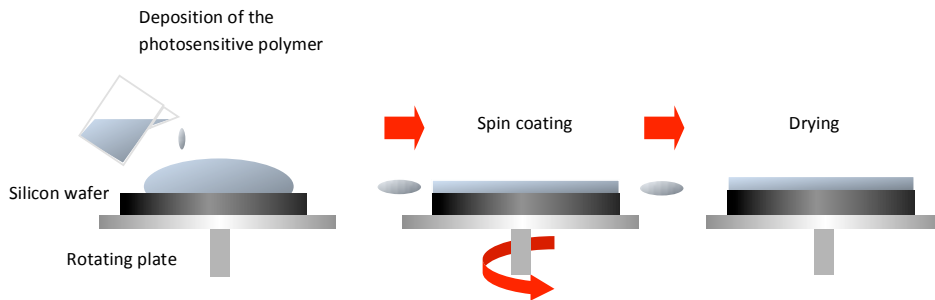


Figure 1.1: Thin film deposition of the photosensitive polymer by spin coating. The photopolymer is poured onto a silicon substrate that is rotated at high speed in order to spread the fluid by centrifugal force.

can be described by the following equation:

$$T = kC \left(\frac{\mu}{\omega^2} \right)^{1/3}, \quad (1.1)$$

where C is the concentration of polymer, k is a constant, ω is the angular velocity, and μ is the viscosity (Tabeling, 2010). Typically, a photopolymer with a specific viscosity is chosen to achieve a thickness that is within the particular range of interest, whereas changing the angular velocity allows for a fine tuning of the thickness. During the deposition the solvent starts evaporating, and the resist starts polymerising (Tabeling, 2010). To complete the reticulation a thermal treatment phase is required, commonly

1.1. BASIC MICROFABRICATION TECHNIQUES

referred to as *soft bake* (SB). The photopolymer-coated wafer is then placed in the *mask-aligner*, which allows transferring the geometrical features from the photomask to the photopolymer layer through exposure (EXP) to UV light. A photomask consists of an opaque surface which absorbs the incoming UV light, and patterned transparencies that allow light to illuminate the photopolymer underneath. Depending on the 'tone' of the photopolymer, UV light makes it more or less soluble in particular solvents after the exposure. The most commonly used photopolymer is SU-8, which is a 'negative tone' resist, meaning that after illumination it becomes cross-linked, and therefore more difficult to dissolve by the developer. Fig.1.2 describes the photolithographic process. Another heating phase is required to terminate the polymerisation of

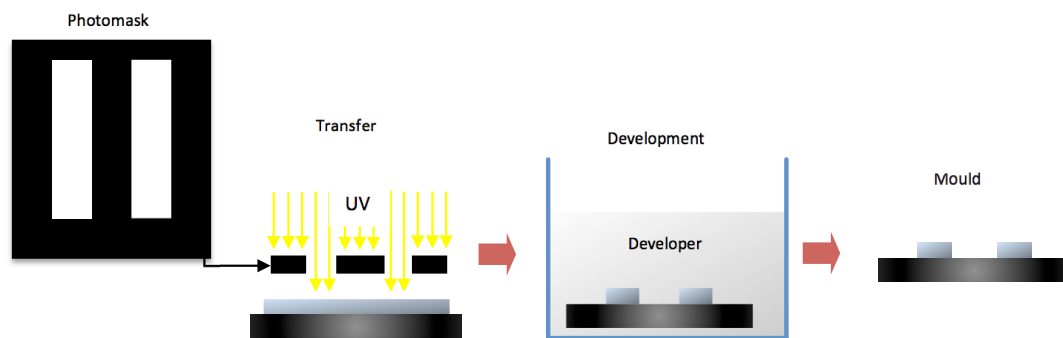


Figure 1.2: Photolithographic steps to obtain the mould.

the photopolymer, initiated during the exposure. This step is known as *post-exposure bake* (PEB). Once the patterns are completely visible in the resist, the next step, the *development* (DEV) phase, can be carried out. The wafer, coated with the fully polymerised resist, is submerged in a suitable solvent, known as *developer*, which dissolves all the unexposed areas, which are not cross-linked and therefore soluble in the solvent.

The last step of the photolithographic process is known as *hard bake* (HB), during

which the remaining SU-8 features are heated above the glass transition temperature of the photopolymer. This step is required for smoothing and hardening the photoresist and improving adhesion with the surface of the wafer. At this point, the mould is ready for the moulding phase, in which the final device is developed. The steps of the photolithographic process are summarised in Fig. 1.3.



Figure 1.3: Workflow of the photolithographic process.

1.1.3 Replica moulding

Once the mould is fabricated, the microfluidic device is developed via replica moulding. It consists in the generation of a 'bas-relief' of the mould on an elastomeric polymer. This phase is based on the material Polydimethylsiloxane (PDMS), which belongs to a family of polymers containing silicon oil. Its formula is $(-\text{Si}(\text{CH}_3)_2\text{O})-$ and its chemical structure is shown in Fig. 1.4. In the presence of a reticulating agent it

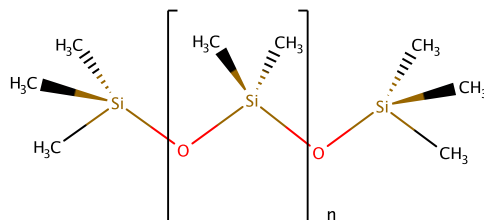


Figure 1.4: Chemical structure of PDMS.

forms an elastomer. Thermal treatment accelerates the reticulation (McDonald and Whitesides, 2002). PDMS is hydrophobic, non-toxic, permeable to gases and impermeable to water (Tabeling, 2010). These characteristics make PDMS a perfect candi-

1.1. BASIC MICROFABRICATION TECHNIQUES

date for handling biological samples, which require oxygen to survive (Taylor et al., 2003). Moreover, this polymer is transparent between 300nm and 2200nm and exhibits low autofluorescence, facilitating its coupling with imaging techniques (Piruska et al., 2005).

The moulding process begins by mixing PDMS pre-polymer with its reticulating agent, to a ratio that depends on the desired stiffness of the final chip. The mixture is then degassed using a desiccator connected to a vacuum pump, poured onto the mould and annealed at 65 – 70°C for two hours onto a hot-plate, or into an oven. During this period the mixture reticulates, solidifies and can be separated from the mould. Access holes are usually punched for tubing connections by the use of biopsy punchers. The phases of the replica moulding are summarised in Fig. 1.5. As PDMS is flexible, it can be easily de-moulded using a scalpel from the SU-8 master, leaving the master undamaged and ready for further replicas.

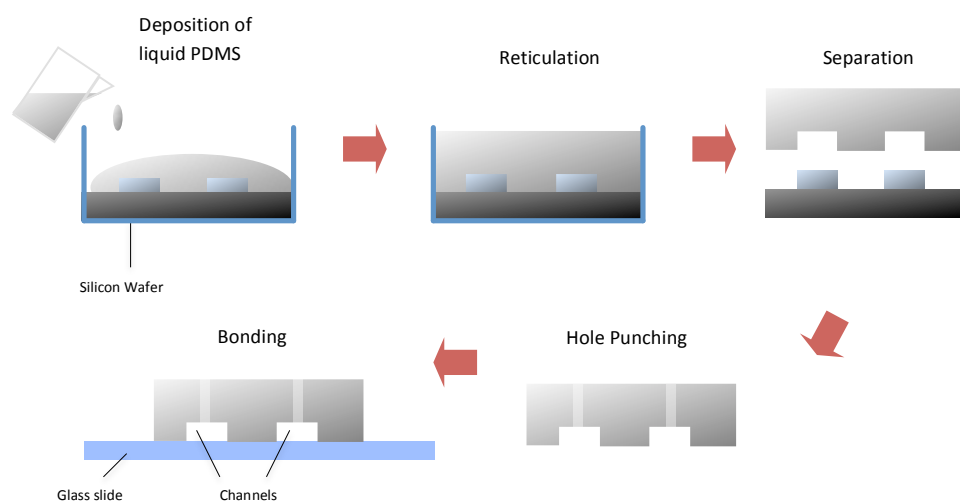


Figure 1.5: Development of a PDMS microfluidic chip by soft-lithography.

1.1.4 Bonding mechanisms

The final step required to develop a working device is to bind the patterned PDMS to a flat surface, so that microchannels can be formed, as depicted in the 'bonding' step, shown in Fig. 1.5. The easiest way of assembling a microfluidic chip is by bringing the patterned PDMS and a glass slide into contact. In this case weak Van der Waals forces bond the two materials reversibly. This sort of arrangement is sufficient to withstand low pressures (< 5 psi) in the channels (McDonald et al., 2000). It is suitable for flow-free devices or where small flow rates are generated by differences in hydrostatic pressure between the inlet and the outlet.

If high flow rates are required, other bonding alternatives become necessary. The most common option is to covalently functionalise PDMS through oxygen plasma treatment. Elastomeric PDMS consists of chains of silicon and oxygen atoms, as shown in Fig. 1.4 (Warrick et al., 1952). It is widely accepted that plasma oxidation of the surface introduces silanol groups (Si – OH), which replace methyl groups Si – CH₃. If a layer of glass is brought into contact with the oxidised PDMS surface, the silanol groups will bind to the OH groups on the surface of the glass with loss of H₂O. In this way strong Si – O – Si covalent bonds form between the two surfaces (Sofla and Martin, 2010; Koh et al., 2012). The two layers will be irreversibly bonded and capable of withstanding air pressures in the range 210 to 350 kPa (Koh et al., 2012). This technique enables the bonding of PDMS to a variety of different materials such as: glass, SiO₂, silicon, silicon nitride, polyethylene, polystyrene, quartz, and PDMS (Duffy et al., 1998). Another important consequence of the plasma oxidation is that it renders PDMS hydrophilic, due to the presence of silanol groups (Duffy et al., 1998).

This facilitates loading the microchannels with liquid solutions. This effect is transient and commonly stops in about 30 minutes (Duffy et al., 1998).

1.2 Investigating cell migration and cell mechanics

Throughout my PhD I developed various microfluidic devices with the aim of investigating different cellular processes and properties that have not been studied before.

In the work presented in Chapters 2 and 3, I fabricated two similar chips to investigate cell migration of the model organism *Dictyostelium discoideum* in the presence of a steady and linear chemical gradient. In addition, in Chapter 3, the linear gradient was combined with asymmetric bifurcating topologies, in order to test the ability of these cells to exhibit directional bias. In both cases, the devices were *flow-free*, meaning that no additional external components were required to generate flows inside the chip. The devices were loaded with solutions using hydrostatic pressure differences among different reservoirs within each chip and the chemical gradient was generated purely via diffusion.

For the experiments presented in Chapter 4 instead, a *flow-based* device was fabricated, with the aim of investigating cellular elasticity and the use of this physical property as an intrinsic biomarker. In this case, an external syringe pump was employed to generate high flow rates, which enabled the establishment of laminar flows and inertial effects capable of manipulating individual cells and impart stresses to them.

In each of the next three experimental chapters I provide the theoretical background of the topic of interest, list the aims of my research, describe the methods used, explain the experimental results obtained and discuss them in the context of existing literature.

CHEMOTAXIS IN CONFINED ENVIRONMENTS

2.1 Introduction and Background

Cell migration is a very important phenomenon playing a key role in several different biological processes, such as embryonic morphogenesis, immune responses and wound healing (Song et al., 2006). Various animal cells exhibit migratory capabilities, for instance macrophages and neutrophils crawl towards invaders and engulf them, osteoclast and osteoblast ensure the continuous remodelling of bones, fibroblast migrate to damaged sites of tissue helping to rebuild them (Alberts et al., 2007). Cell movement also takes place in some pathological processes namely osteoporosis, chronic inflammatory diseases and tumour metastasis (Ridley et al., 2003).

Deeper insights into the mechanisms underlying this phenomenon may lead to more effective medical treatments and could pave the way for new intervention approaches such as the creation of artificial tissues (Ridley et al., 2003). One of the most important

questions in understanding cell movement is how the cell interprets external cues and actuates the internal cytoskeletal machinery to achieve the motion (Petrie et al., 2009). A variety of biochemical and physical cues have been shown to trigger cellular responses. Chemical concentration gradients are one of the environmental signals which can enable the migration of certain cell types. This kind of response is known as *chemotaxis* and involves a directed migration as a consequence of directional sensing (Dormann and Weijer, 2006). During tissue repair, fibroblasts can move from softer substrates to stiffer ones, a process known as *durotaxis* (Lo et al., 2000). Dendritic cells can undergo *haptotaxis*, *i.e.* the ability to migrate towards increasing concentration of immobilized ligands (Schumann et al., 2010). In cell monolayers *plithotaxis* induces cells to migrate in order to minimise the stress among intercellular junctions (Tambe et al., 2011). Electrical fields have also been shown to trigger *galvanotaxis* in keratocytes (Allen et al., 2013). Moreover, cells could be sensitive to a combination of these stimuli, which makes it challenging to investigate the dependence of cellular responses.

2.1.1 Chemotaxis in *Dictyostelium discoideum*

Dictyostelium discoideum is a leading model for eukaryotic chemotaxis (Swaney et al., 2010; Cai and Devreotes, 2011). Research conducted on this organism contributed to generate data that anticipated results lately found in other organisms and enabled the establishment of experimental methods successively used in other systems. For instance, the discovery of cAMP as chemoattractant (Konijn and Meene, 1967) anticipated that of chemokines in mammals (Yoshimura et al., 1987). Other examples are: the role of G protein-coupled receptors in transducing chemical signal (Klein et al.,

2.1. INTRODUCTION AND BACKGROUND

1988); the investigation of *in vivo* dynamics of cytoskeletal components and intracellular vesicle trafficking, via GFP-tagged proteins both in phagocytosis and chemotaxis (Gerisch et al., 1995) that was more recently extended to macrophages (Bajno, 2000) and neutrophils (Servant et al., 1999). Eukaryotic cells such as Dictyostelium and neutrophils exhibit extraordinary sensitivity to environmental chemical gradients (Ma et al., 2004). The interactions between signalling, regulatory and cytoskeletal components involved in gradient sensing are conserved between *D. discoideum* and neutrophils (similarities and differences between the two organisms are reviewed in (Van Haastert and Devreotes, 2004), (Kay et al., 2008) and (Swaney et al., 2010)). For instance, the chemoattractant receptors are uniformly distributed along the cell membrane, both in Dictyostelium and in neutrophils (Van Haastert and Devreotes, 2004). These receptors signal through similar G proteins in both systems, and the distribution of actin and myosin filaments support cell polarity in the same fashion (Van Haastert and Devreotes, 2004; Kay et al., 2008).

Additionally, Dictyostelium discoideum's 34 Mb genome was completely sequenced in 2004 (Loomis, 2006) and is contained on six chromosomes. This genome is haploid¹ and this helps understanding the connection between a particular phenotype and the specific gene of interest (Weijer and Williams, 2009). Through homologous recombination it is possible to easily generate mutants in cytoskeletal components and in signalling components, as well as to tag them with Green Fluorescent Protein (GFP) to visualise their dynamics *in vivo*. In addition, Dictyostelium's genome often contains genes that encode for a single protein, unlike the case of mammalian cells where some

¹The nucleus of this organism contains a single set of chromosomes.

genes encode for multiple isoforms (King and Insall, 2009). Furthermore, several of its genes are homologous to human genes (Eichinger and Noegel, 2003; Song et al., 2006). Other important aspects that contributed to the popularity of *Dictyostelium* as a model organism are the ease of culture it in inexpensive media and its fast growth: the doubling time of these cells is 8-12 hours in axenic medium² (Ashworth and Watts, 1970), which is faster than mammalian cells, that typically range between 15 and 30 hours (Hauser and Wagner, 1997).

Chemotaxis plays a key role in the life cycle of this organism. *Dictyostelium* cells live in the soil as single cells, feed on bacteria and multiply through binary fission (Bukharova et al., 2005). Starvation enables a developmental cycle that leads up to 100,000 cells to form a multicellular structure known as a *slug*. The slug migrates towards a suitable environment where eventually gives rise to a fruiting body, which is up to 4 mm high and consists of a spore mass supported by a stalk (Weijer and Williams, 2009). The spores disperse and release amoebae, from which the life cycle restarts (Weijer and Williams, 2009) as summarised in Fig 2.1. More specifically, upon starvation some cells start to secrete the signal molecule 3'-5'-cyclic adenosine monophosphate (cAMP). This diffuses to neighbouring cells that detect the signal via highly specific cAMP transmembrane receptors. Binding of cAMP to the receptors activates two competing processes (Weijer, 1999):

- A quick excitation that induces the activation of aggregation stage adenylate cyclase (ACA), which catalyses the synthesis of intracellular cAMP. The cell secretes the intracellular cAMP, which in turn binds to the receptors of the same

²Axenic medium does not contain bacteria that are what *Dictyostelium* typically feed on in their natural environment.

2.1. INTRODUCTION AND BACKGROUND

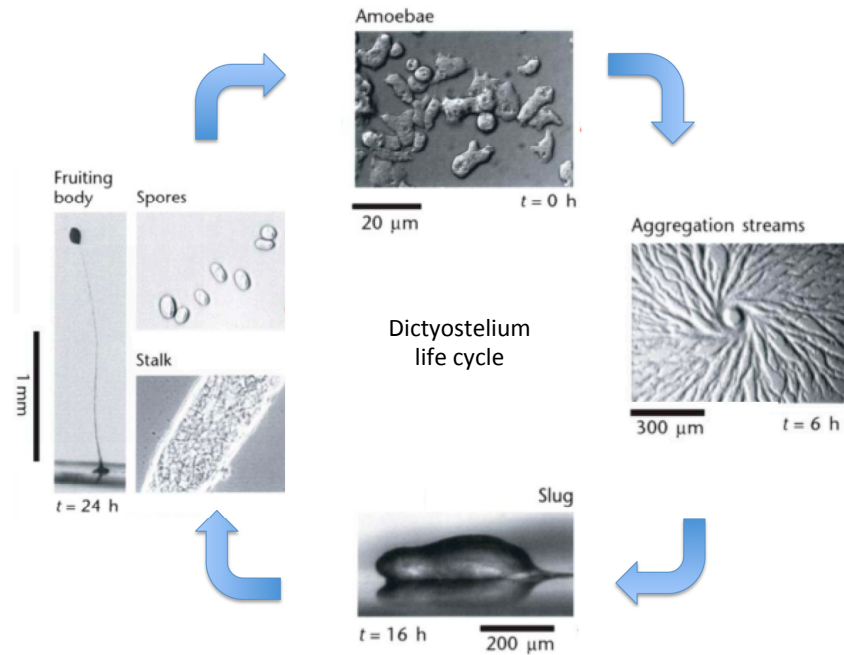


Figure 2.1: Life cycle of *Dictyostelium discoideum*. The cycle starts from vegetative amoebae (at the top), upon starvation cells start streaming and aggregate to form the slug that migrates towards the most suitable environment and eventually give rise to a fruiting body composed by spore cells supported by a stalk. Adapted from (Weijer and Williams, 2009).

cell. This induces an autocatalytic feedback that ultimately amplifies the cAMP levels initially detected by the cell.

- A slow adaptation that inhibits the activation of ACA and therefore terminates the positive feedback loop and the cAMP production.

The secreted cAMP also diffuses away from the cell and induces the surrounding cells to start synthesising cAMP (Weijer and Williams, 2009). This process iterates within a cell colony, generating cAMP waves that direct the chemotactic movement of the cells towards the centre of signal (Weijer, 1999; Dormann and Weijer, 2001). These waves are characterised by variation in concentration between 10^{-10} M and 10^{-6} M. This gives rise to small differences in receptor occupancy, up to 10% along the length of each cell (Tomchik and Devreotes, 1981).

Additionally, cells secrete cAMP phosphodiesterase (PDE) that degrades cAMP (Weijer

and Williams, 2009). Therefore, when the adaptation is started, the local concentration of the extracellular cAMP falls due to the presence of PDE. Such a decrease in cAMP levels initiates a re-sensitisation process that restores the synthesis of cAMP (Mahadeo and Parent, 2006). The described adaptation process is essential for the outward, unidirectional propagation of cAMP waves as a cell that releases the cAMP signal becomes refractory to it. The same process underlies the chemotactic response: in fact, cells migrate towards increasing concentrations of cAMP but they halt as the concentration stops increasing due to adaptation (Weijer, 2009).

The cAMP signal is detected by four specific G-protein-coupled receptors (GPCRs), known as cAR1-cAR4, which are situated on the cell's surface. The receptor cAR1 exhibits the highest affinity for cAMP and is expressed during early chemotactic aggregation. It has an extracellular ligand binding domain and an intracellular effector domain. The latter is involved in signal transduction cascades that result in a local, dynamic modification of the cytoskeleton, as well as the synthesis and secretion of additional cAMP for signal relay (Dormann and Weijer, 2006; Manahan et al., 2004). The final result of this signal transduction cascade is the polarisation of the cell and its motion towards an increasing concentration of chemoattractant molecules as depicted in Fig. 2.2.

The key aspects of the cell polarisation are:

- The polymerisation of actin filaments at the leading edge of the cell that are associated with the extension of pseudopodia (Van Haastert and Devreotes, 2004).
- The myosin II assembly at the trailing edge that is involved in the contraction of the uropod (Uchida, 2003).

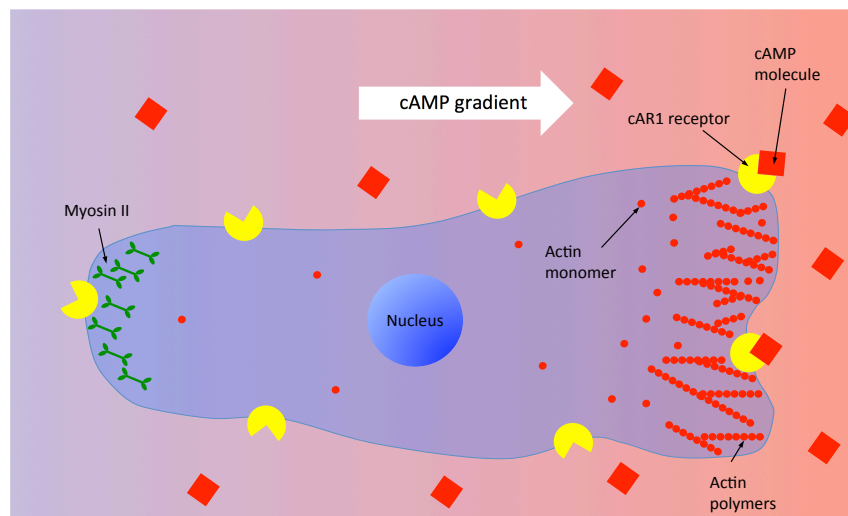


Figure 2.2: Schematic of the cellular polarisation occurring when a Dictyostelium cell is exposed to a cAMP gradient. Binding of cAMP to the cAR1 receptors activates a signal transduction cascade that results in the polymerisation of actin filaments at the leading edge (on the left) and myoII assembly at the uropod (trailing edge). Such a polarisation is required from the cell to be able to migrate up the chemical gradient.

The cell must translate small differences in receptor occupancy between its posterior and anterior regions into directed migration. However, it remains unclear how the cAR1/G-protein machinery is linked to the actin cytoskeleton. It has been suggested that actin polymerisation would self-organise in a wave-like manner in either stimulated and unstimulated cells (Gerisch et al., 2004; Weiner et al., 2007). Therefore the role of cAR1/G-protein signalling might be to coordinate these actin waves rather than causing the polymerisation of actin filaments in migrating cells.

Nevertheless, the general mechanism of how movement and signal sensing are coupled is still unclear (Andrew and Insall, 2007).

Most of the eukaryotic chemotaxis models are based on the concept of 'chemical compass', which would be orientated towards the chemoattractant and induce the generation of new pseudopods in the areas of the cell that are closest to the signal (King and Insall, 2009). In this way the actual direction of the cell would be independent

of the presumptive direction indicated by the 'compass' (Insall, 2013). More recent findings lead to a different model of chemotaxis that overlooks the existence of a 'compass': the cell would orient itself thanks to its pseudopods (Neilson et al., 2011). According to this model pseudopodia are produced by intrinsic self-generated cycles, at random directions and triggered by positive and negative feedback loops. The role of the chemoattractant would be to modulate the amount of positive feedback and hence the intrinsic cycles, rather than causing the actin polymerisation (Neilson et al., 2011). Such a model is supported by experimental analysis performed by Andrew and Insall (2007). The authors demonstrated that new pseudopods are commonly generated by bifurcations of existing ones, at a rate that seems to be constant (~ 2 per minute), internally regulated and independent of directional sensing. Moreover, the direction of movement would not be mediated by the generation of new pseudopods but by the maintenance of most accurate existing ones, as shown in Fig. 2.3. The receptor occupancy would modulate the positive feedbacks required for the stabilisation of the leading pseudopod (Neilson et al., 2011).

2.1.2 Different modes of motion

Cell motion can be described as a biphasic locomotory movement (Uchida, 2003): during the *extension* phase the cell protrudes its membrane at the leading edge (pseudopod) that subsequently adheres to the substratum, and exerts a pulling force to the remainder of the cell. Such a mechanical change is mainly driven by actin polymerisation. During the *retraction* phase, contractions mediated by myosin II lead the cell's posterior to detach from the substrate.

How the cell is able to regulate and synchronise all these steps is still not completely

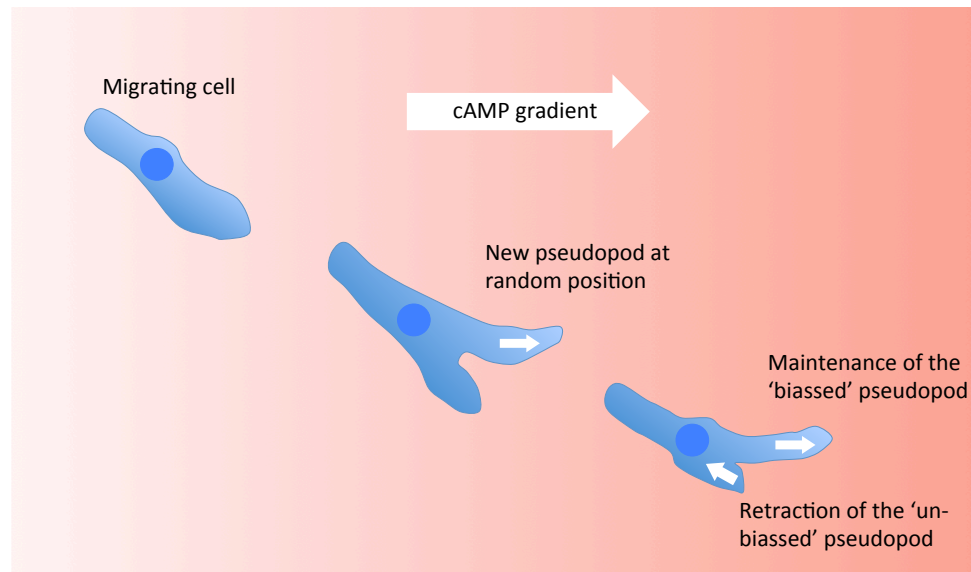


Figure 2.3: Schematic of the 'pseudopod-centred model'. Cell-autonomous processes dictate the position and the rate of the pseudopod formation. The role of the chemoattractant would be to bias the intrinsic cycles that triggers the generation of pseudopodia and their orientation, steering the cell after consecutive turns. Adapted from (Neilson et al., 2011).

understood.

2.1.2.1 Actin-based motility

The key concept of motility is that, to move from one position to another, the cell must be able to advance towards the direction of motion and withdraw in the opposite direction (Rafelski and Theriot, 2004). This principle holds also at the molecular level where the non-equilibrium process known as 'actin treadmilling' takes place.

Actin filaments (F-actin) are double helix polymers characterised by a structural polarity: a *barbed end* points towards the leading edge of the cell, and a *pointed end* directs towards the trailing edge. As sketched in Fig. 2.4 ADP-actin monomers (in red), disassemble from the filaments' pointed end, undergo ADP to ATP nucleotide exchange aided by the actin binding protein *profilin* (Selden et al., 1999) and diffuse to the cell front, where they self-assemble at the barbed end of the filament. According with the 'Brownian Ratchet Model' each ATP-actin monomer (in yellow) intercalates between

the actin filament and the plasma membrane only when the gap width is bigger than the size of the monomer. Therefore, the probability of monomer insertion is governed by thermal fluctuations of the membrane and depends on the local monomer concentration (Peskin et al., 1993). Such a polymerisation would generate the mechanical force required for the membrane protrusion (Peskin et al., 1993). This cycle is reg-

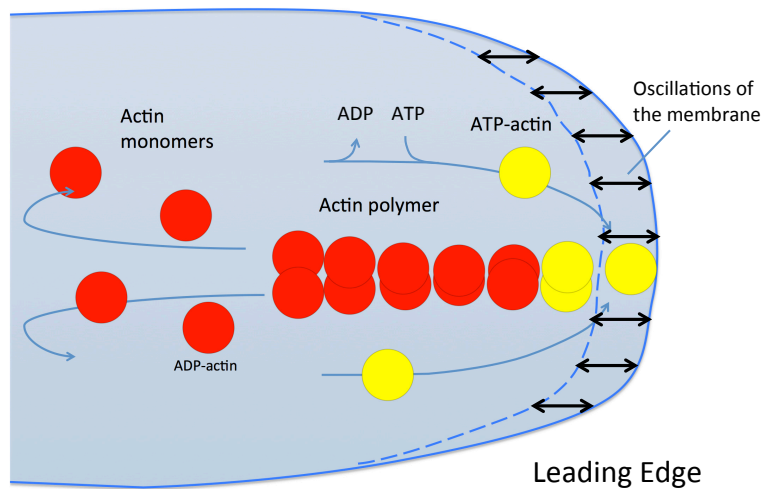


Figure 2.4: Actin treadmilling at the leading edge of a migrating cell. According to the 'Brownian Ratchet Model' ATP-actin monomers intercalate in the gap between the actin filaments and the plasma membrane when, occasionally, the brownian oscillations of the membrane are big enough to allow the insertion of the monomer. ADP-actin monomers disassemble from the pointed end. Following the ADP to ATP nucleotide exchange, ATP-actin monomers polymerise at the barbed end of the filaments. Adapted from (Ladoux and Nicolas, 2012)

ulated by the interactions among actin and its accessory proteins. For instance, the assembly of the actin cortex, *i.e.* the 200 nm thick mesh that supports the plasma membrane, is enabled by the Arp2/3 complex. This complex is capable of nucleating filaments branching from existing ones. It also exhibits a preferential association near the ATP-actin (Ichetovkin et al., 2002) and therefore increases the number of barbed ends available at the cell front (Amann and Pollard, 2001). The availability of barbed ends is also controlled by other accessory proteins involved in severing actin

2.1. INTRODUCTION AND BACKGROUND

filaments, such as ADF/cofilin (Ichetovkin et al., 2002), gelsolin (Pollard et al., 2000; Falet et al., 2002) and by capping proteins that prevent filament annealing (Cooper, 1973). ADF/cofilin is also important in controlling the F-actin depolymerization rate and the recycling of actin monomers (G-actin) (Carlier et al., 2012).

Moreover, in many cell types non-muscle myosin II (myoII) localises at the uropod, where is known to play a key role in generating contractions of the actin cytoskeleton (Conrad et al., 1993; Eddy et al., 2000; Uchida, 2003). MyoII is one of the thirteen members of the myosin gene family (Kollmar, 2006). It is composed by two heavy chains and two couples of light chains. Each heavy chains contains a globular *head domain*, where actin and ATP binding sites are present, an α -helical *neck region* that contains the light chains and a *tail domain* (Kollmar, 2006). The head domain is a

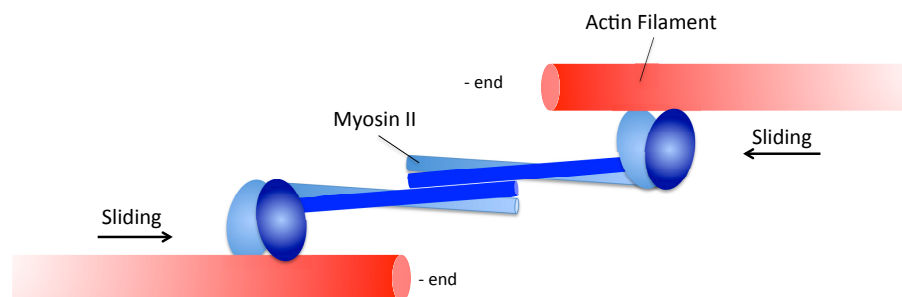


Figure 2.5: Schematic of myoII-mediated contractions of actin filaments. The globular heads of myoII bind actin, forming a contractile assembly where myoII generates contractions by sliding the actin filaments relative to one another. Adapted from (Cooper, 2000).

specialized ATPase that is responsible to hydrolyse ATP and generate motion along the actin filament. MyoII and actin filaments arrange in contractile assemblies, where myoII generates contractions by sliding the actin filaments relative to one another (Cooper, 2000), as shown in Fig. 2.5. MyoII-mediated contractions, that in cells are mainly localised at the cell's rear, appear to be responsible of large-scale disassembly of the actin meshwork and this would provide intrinsic coordination of the treadmilling

of the entire motile cells (Wilson et al., 2010).

2.1.2.2 Actin-independent motility: the blebbing mode

Blebs are actin-independent, spherical protrusions that have been long considered a hallmark of apoptosis (Coleman et al., 2001). Over the last few years, researchers started to realise that these structures are also present at the leading edge of migrating cells and implicated in cell motility (Langridge and Kay, 2006; Charras et al., 2008; Paluch and Raz, 2013). Two extreme cases are the zebrafish primordial germ cells (PGCs) that migrate exclusively using blebs (Blaser et al., 2006), and fish keratocytes that adopt pure actin-driven locomotion (Svitkina et al., 1997). Another interesting case is represented by the ability of metastatic cancer cells to switch between the two protrusive modes. This facilitates their adaptation to the environment (Friedl, 2004). Other cells present pseudopods and blebs simultaneously (Diz-Muñoz et al., 2010). The formation of a bleb can be divided in three phases as shown in Fig. 2.6:

1. **Initiation**, caused by either a rupture of the actin cortex or a local detachment between the cortex and the plasma membrane. In fact, blebs can be synthetically induced by breaking the connection between the cortex and the membrane via micropipette aspiration (Rentsch and Keller, 2000), by local delivery of an actin depolymerising drug (Paluch et al., 2005) or by local destruction of the actin cortex via laser ablation (Sedzinski et al., 2011).
2. **Growth**, associated with the increase in intracellular pressure building up against the unsupported plasma membrane. It is believed that the hydrostatic pressure is generated in the cytoplasm as a consequence of the myoII-mediated contractions at the uropod (Charras et al., 2005; Yoshida and Soldati, 2006; Lämmer-

2.1. INTRODUCTION AND BACKGROUND

mann and Sixt, 2009). It has been shown that the synthetic enhancement of the contractility in cells that normally do not exhibit blebbing, resulted in bleb generation (Goudarzi et al., 2012). Interestingly, in a recent work by Beckham et al. (2014) myoII-independent bleb formation has been observed as a consequence of Arp2/3 inhibition in human breast epithelial cells. Although this result might be associated with cell type-specific levels of myoII contractility, the authors suggested that the reduced membrane-cortex attachment, induced by the Arp2/3 inhibition, would be sufficient to generate bleb-like protrusions.

3. **Retraction**, caused by the polymerisation of new actin cortex at the plasma membrane of the bleb and the recruitment of myoII to the same region. MyoII-induced contractility stops the growth of the protrusion and restores the initial shape of the leading edge (Charras et al., 2006).

Blebs have been observed in cells migrating on 2D substrates (Maugis et al., 2010) but it appears that this type of protrusive motion is prevalent in 3D environments (Charras and Paluch, 2008). It has been recently shown that they form in Dictyostelium cells migrating under agarose of increasing stiffness and that they appear to be enabled by PI3-kinase (Zatulovskiy et al., 2014). Moreover, it has been proposed that localised water uptake might also induce bleb formation (Loitto et al., 2009) but experimental evidence is still lacking. More generally, many questions remain open:

1. What sort of mechanisms account for the limited elasticity of the cell membrane?

The cell membrane is capable of stretching about 2 – 3% of its surface before lysing (Mohandas and Evans, 1994), therefore membrane reservoirs must be present in proximity of the forming bleb.

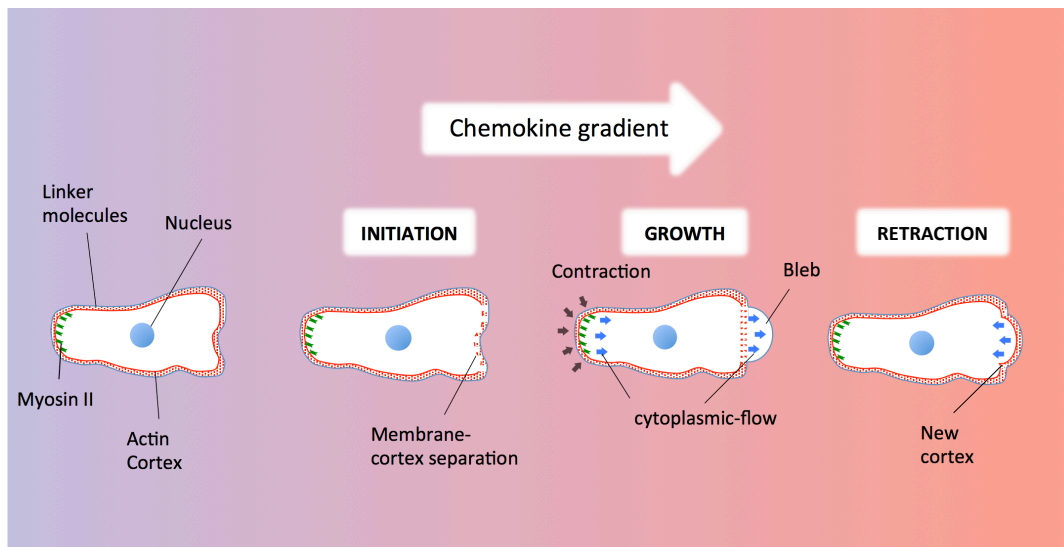


Figure 2.6: Schematic of a blebbing cell (Adapted from (Paluch and Raz, 2013)). A bleb is characterised by three phases: *initiation*, caused by either a rupture of the actin cortex or a local decrease in the attachment between the cortex and the cell membrane. *Growth*, caused by the intracellular pressure against the unsupported plasma membrane. Such a hydrostatic pressure is generated by myoII - mediated contractions at the uropod. *Retraction*, induced by the combined effect of the polymerisation of new actin cortex at the plasma membrane of the bleb and the recruitment of myoII to the same region that stops the growth of the protrusion and restores the initial shape of the leading edge.

2. How can migrating cells produce blebs in the direction of the motion?
3. What are the molecular pathways that link the activation of the chemoattractant receptor to the establishment of directional blebbing?
4. Are blebs indispensable for cell motility or they are a by-product of cellular contractility?
5. What is the relationship between spatial confinement and migration mode?

2.1.3 The role of cell adhesions

During their movement cells require to gain traction from the environment in which they migrate (Bukharova et al., 2005). Therefore, cells need to create physical contacts with the surrounding material such as: substrate, extracellular matrix (EM) or other

2.1. INTRODUCTION AND BACKGROUND

cells. Furthermore, these contacts have to be coordinated to enable a directed motion (Gardel et al., 2010).

In higher organisms the links with the EM are mediated by *integrins* (Hynes, 2002), which in turn interact with extracellular matrix molecules, namely *fibronectin*, *laminin* and *vitronectin*. Upon binding to these extracellular molecules, intracellular focal adhesion complexes cluster and bridge the integrins to the actin cytoskeleton as shown in Fig. 2.7. *Paxillin* is a key regulatory component as it acts as 'molecular clutch' between the integrins and the actin cytoskeleton (Smilenov et al., 1999; Ananthakrishnan and Ehrlicher, 2007).

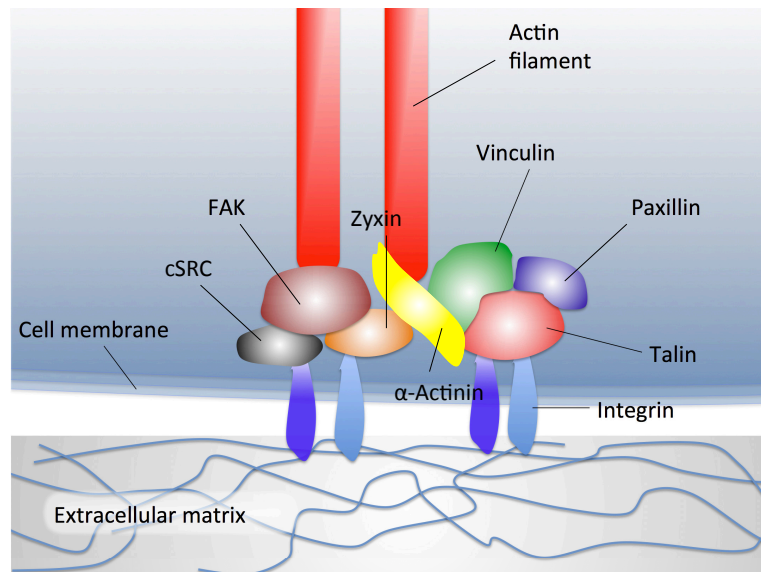


Figure 2.7: Schematic a focal adhesion. The image shows how integrins and F-actin are linked through a number of signaling complexes (adapted from (Huttenlocher and Horwitz, 2011)).

In *Dictyostelium* the SibA (Similar to Integrin Beta) protein was found (Cornillon et al., 2006). It is a type I transmembrane protein, and its extracellular, transmembrane and cytosolic domains are similar to those of integrin β . SibA inactivation affects adhesion to phagocytic particles, to the substrate and to other cells but it does not impact the actin cytoskeleton, the multicellular development or migration (Cornillon et al., 2006).

Dictyostelium cells also have a paxillin homologue, PaxB, which appears to have a role in cell-substrate adhesion (Bukharova et al., 2005). On the other hand, PaxB null cells are able to migrate normally on a variety of substrates during the early developmental stages (Bukharova et al., 2005).

Although the exact mechanism of cell-substrate adhesion remains elusive in Dictyostelium, traction force microscopy (TFM) experiments facilitated measurement of the small forces that adherent cells exert upon the substrate in a very accurate way (Uchida and Yumura, 2004; Iwadate and Yumura, 2008; Buenemann et al., 2010). This technique consists of an optically transparent, elastic substrate of known stiffness in which fluorescent microbeads are embedded. The cell, migrating on the substrate, displaces these beads. Knowing the mechanical properties of the substrate allows to link the translational displacement of the beads with the forces exerted by the cell. These studies revealed the following important properties:

1. Dictyostelium cells are able to crawl on glass substrates through non-specific interfacial forces (Ladam et al., 2005).
2. The total forces at the front and back halves of the cell are in the order of 90 pN (Buenemann et al., 2010).
3. Contractile forces tend to be focussed in micron-size F-actin rich discrete spots (Uchida and Yumura, 2004; Iwadate and Yumura, 2008). These actin foci have a lifetime of ~ 20 s in wild-type (WT) (Uchida and Yumura, 2004).
4. Cell motion is characterised by contraction and retraction cycles (Buenemann et al., 2010). The first phase starts with the pseudopod attachment and it is followed by an increase in local stress. During the second phase the rear detaches

2.1. INTRODUCTION AND BACKGROUND

and is passively dragged forward. The duration of a cycle is about 1 - 2 min for wild-type (WT) cells and about 4 min in cells lacking myoII. At each cycle the cell displaces about 15 μm .

On the other hand, the mechanisms behind the actin foci adhesion are poorly understood as well as how these structures are spatio-temporally regulated.

2.1.4 Microtubules in cell migration

A microtubule (MT) is a polymer that results from the assembly of α/β -*tubulin* dimers, which bind laterally to form a hollow cylinder. Microtubule polymerisation is a polarised process that in most cells begins at the *microtubules organising centre* (MTOC) and continues radially towards the cell periphery, where the MTs' plus ends are localised. The main MTOC is represented by the centrosome that, in interphase cells, is positioned approximately at the cell's centre of mass.

MTs have a very dynamic nature. Their plus ends are involved in a process known as *dynamic instability*, that consists in stochastic growth and shrinkage phases. Their functions (reviewed by Etienne-Manneville (2010)) are controlled by:

- Microtubule-associated motors: *kinesins* and *dyneins* that actively transport their cargos (proteins, transport vesicles, mRNA) from and to the cell periphery, respectively.
- Microtubule-associated proteins (MAPs) through which MTs interact with other cytoskeletal components.

MTs have been shown to play a significant role in cell migration due to their numerous interactions, physical and mechanical properties and signalling properties (Rodriguez

et al., 2003). An extreme case is represented by astrocytes³, where MTs are directly involved in cell protrusions (Etienne-Manneville, 2013). Interestingly, in these cells actin depolymerisation induces protrusive events whilst depolymerisation of MTs inhibits them (Etienne-Manneville, 2013).

In higher eukaryotic organisms, centrosome and nucleus are structurally linked (Bornens, 2008). The positioning of the nucleus is mediated by the activity of the cytoplasmic *dynein-dynactin* complex, this feature is conserved in different species (Reinsch and Gönczy, 1998; Koonce et al., 1999). The nucleus-centrosome linkers are cell-type dependent: in animal cells, for instance, the *SUN-KASH* complex and the nuclear membrane protein *emerin* have been found to be involved, while in *Dictyostelium*, *kinesins* have been found to be associated with this process (Tikhonenko et al., 2009). In general, as a consequence of such a link, the nucleus-centrosome complex moves towards the direction of movement at each protrusive displacement of the cell.

Moreover, in many cell types a correlation has been found between the position of the centrosome with respect to the nucleus and the direction of cell movement (Ueda et al., 1997; Li and Gundersen, 2008). The *nuclear-centrosomal* (NC) *axis* has been found to align with front-back morphological polarity (Schliwa et al., 1998), meaning that typically the centrosome is located between the leading edge and the nucleus (Schliwa et al., 1998). This configuration, known as *anterior orientation*, biases MTs towards the cell's front and would enable the correct transport of organelles to the anterior region (Vinogradova et al., 2009). This positioning is also important in stabilising the direction of movement (Ueda et al., 1997). More specifically, it has been shown that

³Astrocytes are star-shaped glial cells in the brain and spinal cord.

2.1. INTRODUCTION AND BACKGROUND

centrosome repositioning occurs after a few seconds (~ 12 s) from the extension of a pseudopod (Ueda et al., 1997). Furthermore, the lack of reorientation within ~ 30 s leads to the pseudopod's retraction (Ueda et al., 1997).

The link between the orientation and the polarised events within the cell body requires better understanding. In fact, some cell types are able migrate directionally despite having a reversed NC axis (Luxton and Gundersen, 2011). Deeper insights into this process could help understanding and facing the several diseases that appear to be related to NC axis disruption (Zhang et al., 2007; Gros-Louis et al., 2007). The topology of the environment surrounding the cell is another factor that can influence the NC axis orientation: for instance, fibroblasts undergo posterior NC axis re-orientation when migrating in 3D environments (Schütze et al., 1991), and BSC1 cells switch their NC axis orientation as a consequence of the width of micropatterned fibronectin strips they migrate on (Pouthas et al., 2008).

MTs have also been shown to be important in the regulation of cell adhesion: they contribute in the formation of nascent adhesions but also in their maturation and disassembly (Waterman-Storer et al., 1999; Ren et al., 1999). MTs would elongate alongside actin cables toward focal adhesions, but it is not clear how MTs find and interact with them. It is recently been suggested that cytoskeletal crosslinkers, such as *spectraplakins*, which bridge MTs and actin filaments, might be involved in this process (Suozzi et al., 2012). Kaverina and co-workers demonstrated that MTs plus end targets cortical actin foci in migrating fibroblasts (Kaverina et al., 1998). The same behaviour was reported in *C. elegans* embryos by Goode et al. (2000).

2.1.5 Microfluidic technology for the study of cell migration

Historically, various conventional assays have been used for cell migration experiments: e.g. the Boyden chamber (Boyden, 1962), micropipette based assay (Gerisch and Keller, 1981), Zigmond chamber (Zigmond, 1977) and Dunn chamber (Zicha et al., 1991). They were based on free diffusion and commonly did not allow neither for a control of chemical gradients nor for a real-time analysis at the single-cell level. Moreover, they often require large amounts of reagents and cell samples (Li and Lin, 2011) and the generated gradient is commonly neither linear nor stable in time and space (Li Jeon et al., 2002).

To face these limitations, microfluidic devices, which consist of channels with micrometer dimensions have been recently developed (Kim et al., 2010). These devices are designed to control precisely and flexibly the chemical concentration gradients with reduced requirements for reagents and cells (Li and Lin, 2011). In particular, this new type of devices allows for a more efficient and quantitative evaluations of cell migration in spatio-temporally varying chemoattractant signals that better mimic *in vivo* situations (Dertinger et al., 2001; Irimia et al., 2007; Ahmed et al., 2010; Kim et al., 2010; Skoge et al., 2010).

Most of the knowledge on the mechanisms governing cell migration arose from *in vitro* investigations on planar surfaces, but recent studies showed that this classical picture of cell locomotion (described earlier in this chapter) is inadequate to recapitulate the properties of cell migration within tissues (Wirtz et al., 2011). In their physiological environment, cells typically navigate through complex 3D matrices or channel-like paths (Alexander et al., 2008; Friedl and Alexander, 2011). Cells encounter constrict-

2.1. INTRODUCTION AND BACKGROUND

tions that range from 3 μm to above 30 μm in width (Pollard and Borisy, 2003). The adoption of microfluidics allowed scientists to simulate the physical confinement *in vitro*, enabling the possibility to investigate whether the cellular mechanisms governing confined migration diverge from the non-confined case. In addition, microfabricated devices help to determine how the mechanical and biochemical properties of the microenvironment affect these mechanisms.

During *in vivo* cell migration, a number of physical parameters from the micro-environment, in which cells move, interact simultaneously on the migrating cell: mechanical properties, geometries, adhesion, degree of confinement (Lämmermann et al., 2008; Rolli et al., 2010). Recent experiments have shown striking different migration behaviours of cells confined in constrained microenvironment: motility characteristics, such as the velocity, cell adhesions and locomotory strategy can be very different in environment with different dimensionality (Doyle et al., 2009; Rolli et al., 2010; Balzer et al., 2012; Pathak and Kumar, 2012). For instance, Lämmermann and colleagues studied the motility of leukocyte cells in microchannels (3D confinement) and showed that cells were able to migrate in a adhesion-independent fashion. The motion would be caused only by the action of the actin-network expansion inducing protrusive flowing of the leading edge supported by the contraction of the trailing edge (Lämmermann et al., 2008). These findings led Hawkins and Voituriez to create a novel model of the cell motion in confined geometries (Hawkins and Voituriez, 2010) where the cell was treated as a polymerising viscoelastic gel confined in a small channel. The authors showed that polymerisation alone would be sufficient to support spontaneous motion and no adhesions with the channel walls would be required. Also, myosin-mediated

2.1. INTRODUCTION AND BACKGROUND

contractility would not be necessary for inducing motion but its action would only contribute to slightly increase the velocity of the movement generated by actin polymerisation.

2.2 Aims and Objectives

In the work presented in this chapter I aimed to develop a microfluidic assay that allowed for controlling individual important parameters of the cell migration: mechanical properties, geometries, degree of confinement, shape of the chemoattractant gradients. Such an assay was designed to confine cells in environments with only one degree of freedom to simplifying the complexity of the actual three-dimensional motion of migrating cells. In this way I sought to provide qualitative and, more importantly, quantitative observations of Dictyostelium wild-type (WT) cells as well as Dictyostelium cells carrying genetic modifications and labelling of the cytoskeletal components of interest. More specifically, I focussed on the following aspects:

1. To understand the relationship between the spatial confinement and the cell velocity.
2. To investigate the response of the actomyosin cytoskeleton to confined environments and how this relates with the different migration modes.
3. To explore different types of focal adhesions and their role in confined migration.
4. To elucidate the role of microtubules in cells migrating through microchannels.

2.3 Methods

2.3.1 Development of the migration chip

The migration device was developed using the microfabrication process described in the previous chapter. The negative resist SU-8 (Microchem) was used for the photolithographic step. Specifically, two layers with different thicknesses were sequentially spun onto the silicon wafer (IDB technologies ltd): I used SU-8 2002 for the first, 2 μm thick layer and the more viscous SU-8 2050 for the second, 80 μm thick layer. For the first layer I followed the microfabrication steps listed in Table 2.1. After the HB step the second layer was spun over the first layer. The protocol to realise the second layer is described in Table 2.2.

Step	Description
COAT	1800 rpm for 40 s
SB	1 minute at 95°C
EXP	30 s
PEB	1 minutes at 95°C
DEV	1 minutes
HB	15 minutes at 150°C

Table 2.1: Microfabrication steps to develop the mould for the cell migration chip. The photopolymer SU8-2002 was used to coat the first 2 μm thick layer.

After the HB of the second layer, the mould was placed into a plastic Petri dish and submerged with polydimethylsiloxane (PDMS) (Sylgard 184 Silicone Elastomer Kit, Dow Corning Corp.) cured at 80°C and de-moulded using a scalpel. Ports were punched through the inlets and outlets using a 8 mm biopsy puncher (Harris Uni-Core). The patterned PDMS slab was then bonded to a standard microscope cover glass (VWR, Micro Cover Glasses, Round, No. 1) by bringing the PDMS and the glass slide into con-

2.3. METHODS

Step	Description
COAT	2000 rpm for 60 s
SB	5 minute at 65°C, 10 minutes at 95°C
EXP	90 s
PEB	5 minute at 65°C, 10 minutes at 95°C
DEV	10 minutes
HB	30 minutes at 150°C

Table 2.2: Microfabrication steps to develop the mould for the cell migration device. The to coat the second 80 μm thick layer I used SU8-2050.

tact and exploiting Van der Waals forces that generate at the interface. The structure of the device is similar to that proposed in other studies on neuronal cultures (Taylor et al., 2003) and tumour cell invasiveness and migration (Rolli et al., 2010). It is characterised by the presence of two main loading channels, each of which connects two cylindrical reservoirs that act as infinite source and as sink, respectively. The 'loading channels' are bridged by a number of 'migration channels' having a cross-sectional area that is much smaller than that of the loading channels. The 3D schematics of the device can be seen in Fig. 2.8. The two main channels are filled with a solution

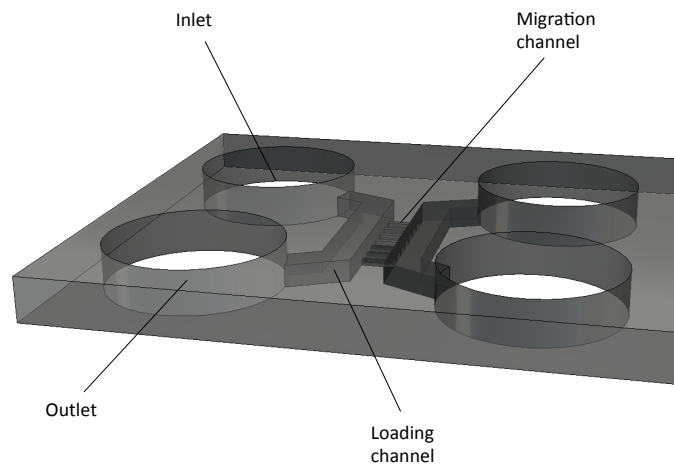


Figure 2.8: 3D structure of the microfluidic device. The two symmetric arms are arranged in 'ladder-like' structure. Each side comprises an inlet, an outlet and a loading channel. A set of cross-channels (or migration channels) bridges the two arms.

containing cells and chemoattractant, respectively. A linear gradient forms within the small bridging micro-channels as shown in Fig. 2.9.

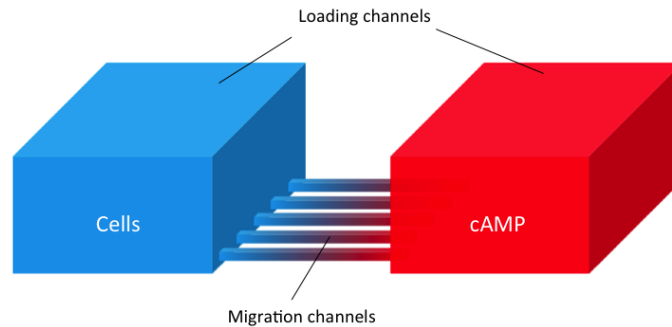


Figure 2.9: Schematic of chemical gradient into the microfluidic device. In blue the cell solution, in red the solution containing cAMP. The color gradient into the migration channels represents the chemical gradient that establishes within them.

2.3.2 Cell preparation

The wild-type (WT) cells used in this thesis belong to the Ax2⁴ strain, one of the most widely used *Dictyostelium discoideum* strain. The inactivation of genes, as well as the fluorescent labelling of specific proteins was achieved through homologous recombination.

Cells were grown in shaking cultures in HL5 medium using glass flasks, at room temperature (about 22°C). Certomat R moving platform at 155 rpm was used.

Myosin II knockout cells were cultured in axenic HL5 medium using plastic Petri dishes (90 mm). Shaking cultures are generally not suitable for these cells as they require to be adherent to a substrate to undergo cell division.

When the cell concentration in the cultures reached 4×10^6 cells/mL they were harvested by centrifugation (1800 rpm for 2 minutes), washed twice and resuspended in

⁴Ax stands for *axenic* as these cells can be grown using axenic conditions, *i.e.* in the absence of bacteria.

Strains	Description
Ax2 + LifeAct	F-actin is labelled with LifeAct.
Ax2 + myoII-GFP + LifeAct	myoII is labelled with GFP, actin is labelled with LifeAct.
Ax2, myoII-null + GFP-ABD ⁵	myoII heavy chain gene has been inactivated. F-actin is labelled with GFP.
Ax2 + VatM-GFP + LifeAct	VatM is labelled with GFP and actin with LifeAct.
Ax2 + 2471-GFP + LifeAct	The protein 2471 that targets microtubules is labelled with GFP, F-actin is labelled with LifeAct.
Ax2 + PaxB-GFP + LifeAct	Paxillin B is labelled with GFP, F-actin with LifeAct

Table 2.3: List of the Dictyostelium strains that I used.

KK2 buffer at the concentration of 1×10^7 cells/mL. Cells are then subjected to pulsation of cAMP for 4.5 hours (45 doses of 0.02 mL are delivered, time interval 360 s) using a 505Di pump (Watson-Marlow Pumps Limited, Falmouth, UK). As explained by Iranfar et al. (2003) cAMP pulses induce the synthesis of cAMP receptors, G proteins, ACA and cAMP phosphodiesterase, resulting in increased excitability during aggregation and a faster convergence to a chemotactically competent stage that resembles their natural development on a solid substrate.

2.3.3 Cell loading, microscopy and data analysis

After starvation, cells were washed twice and suspended in KK2 at a final concentration of 1×10^7 cells/mL. An aliquot of 200 μ L was loaded inside one of the two inlets of the microfluidic device using a pipette. The other inlet was filled with 200 μ L of cAMP 1 μ M. After loading the system with the cell and chemoattractant solutions, it becomes subjected to a transient flow directed from the source to the sink reser-

⁵GFP-ABD is a fusion protein formed by the green fluorescent protein (GFP) of *Aequorea victoria* and the highly conserved actin-binding domain (ABD) from the amino terminus of the actin cross-linking protein ABP-120 (Pang et al., 1998).

voirs. The flow lasts until the hydrostatic pressure at these two ends of the loading channels is equal. During this phase the concentration of chemicals within the main channels remains constant. This enables the establishment of a linear spatial gradient of chemoattractant inside the bridging channels mainly by diffusion, as previously shown by Abhyankar and co-workers (Abhyankar et al., 2006). When the device is hydrostatically balanced, the gradient is completely formed and the system reaches a pseudo steady state characterised by two identical fluxes: chemical flux entering the microchannels and the chemical flux leaving the microchannels. The gradient remains stable as long as the two fluxes equal ($dc/dt = 0$ when $dc/dx_{in} = dc/dx_{out}$) (Abhyankar et al., 2006). The symmetry guaranteed by the microfluidic device allows for a very good equilibration of the system. Cells sediment and adhere to the substrate during the hydrostatic balancing of the system, when they are still subjected to the flow. Once the equilibration is achieved, the cells that are close to the entrance of the migration microchannels start sensing the gradient and move towards it, undergoing drastic modification of their shape. As a cell migrates up the gradient, it starts secreting intracellular cAMP at a concentration comparable to that imposed by the system (1 μ M) (Tomchik and Devreotes, 1981). Moreover, Dictyostelium cells express and secrete phosphodiesterase (PDE), which degrades cAMP into 5'-adenosine monophosphate (Bagorda et al., 2009; Weijer and Williams, 2009). This means that after some time the cells stop sensing the original cAMP gradient. The local concentration around the single cell is the result of the two previously mentioned competing effects and cells that migrate close to each other could interact reciprocally. To account for this I focused my analyses on the first cells that moved in the migration channel. At the end

2.3. METHODS

of each experiments the glass cover slip was separated from the PDMS chip and discarded whereas the patterned PDMS device was rinsed with ethanol 70% and stored for following experiments. Additionally, in order to maintain the chemical gradient steady, the four reservoirs were covered using small slabs of PDMS. In this way evaporation of the liquid phase was prevented, and therefore the concentration of cAMP was kept constant over time.

2.3.4 Imaging

2.3.4.1 Confocal imaging

In a conventional wide-field fluorescence microscope, the entire specimen is excited simultaneously, and the fluorescence emitted by it forms an image that is detected by the microscope's photodetector. The light comes from the excited volume and therefore contains a large unfocussed background component. A confocal microscope instead makes use of two pinholes positioned in two optically conjugate planes (in front of the light source and before the light detector as shown in Fig. 2.10) to reject out-of-focus signal (represented by the point B in Fig. 2.10).

In Minsky's invention (Minsky, 1988) the optics were kept stationary and the specimen positioned using a translation stage.

In modern systems the light source is a laser (in blue in Fig. 2.11) that is reflected by a dichroic mirror towards a couple of motor-driven mirrors, through which the illumination can be steered to scan the specimen. The fluorescent light emitted by the sample (in green) travels along the same optical path, up to the dichroic mirror, where it is transmitted towards the detector as shown in Fig. 2.11.

⁶A dichroic mirror reflects light below a certain wavelength and transmits light above it.

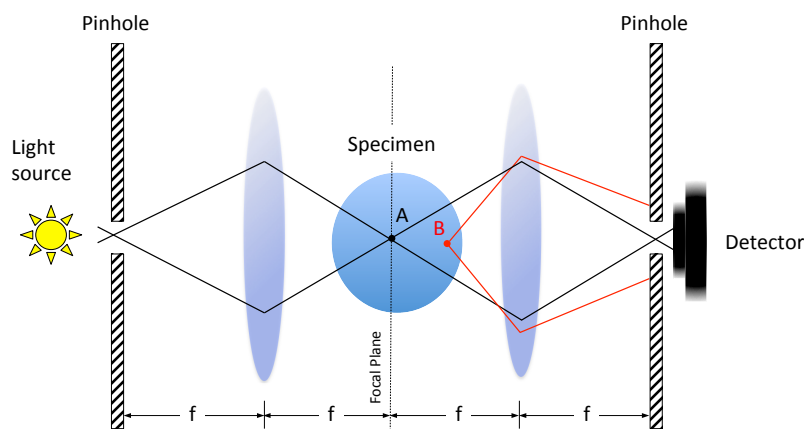


Figure 2.10: Schematic of the confocal principle as it was conceived in 1957 by Marvin Minsky (adapted from (Minsky, 1988)). Light coming from the focal plane (point A) travels through the pinhole and reaches the detector. On the other hand, the fluorescence emitted by out-of-focus regions is not confocal with the pinhole and therefore becomes rejected.

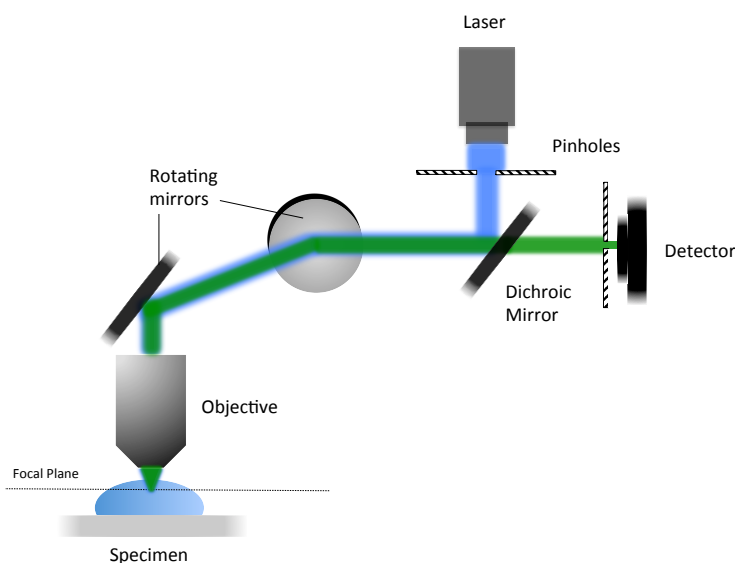


Figure 2.11: Schematic of a laser scanning confocal microscope. The laser light (in blue) passes through a pinhole, is reflected by a dichroic mirror⁶ and by a couple of rotating mirrors that steer the excitation light over the sample to scan it pixel-by-pixel. The light emitted by the specimen (in green) follows the reverse optical path, is transmitted through the dichroic mirror and reaches the detector, after passing through a second pinhole that rejects the out-of-focus light coming from the specimen. Adapted from (Prasad et al., 2007).

Each point of the thin planar region of the specimen at the focal plane is excited at a different time, therefore to visualise the entire field of view, the detector must be connected to a computer where the image is built, one pixel at a time. This process

2.3. METHODS

is known as optical sectioning and allows one to obtain high resolution and sharp 2D images. Moreover, it allows for z-stacking each section to reconstruct 3D images of the sample. The light transmitted through the specimen can be collected too, as well as the epifluorescence signal. The different channels can be merged using image processing software and by doing so the precise localisation of labelled proteins can be observed within a single cell or in tissues. Furthermore, multi-labelled samples can be simultaneously monitored, both in fixed and living specimens.

In this thesis time-lapse fluorescence images were taken using a Leica SP2 AOBS confocal microscope equipped with a 100 \times , 1.4 N.A. plan-apochromat objective lens.

2.3.4.2 Total internal reflection fluorescence microscopy

A total internal reflection microscope (TIRF) microscope exploits an evanescent field to illuminate a very thin section the specimen proximal to the interface between the sample and the glass cover slip. The evanescent wave forms at the interface between the two media, where the incident light is totally internally reflected. The field penetrates into the sample for about 100 nm and decays exponentially. TIRF microscopes allow to selectively visualise the ventral plasma membrane of living cells sitting onto a cover slip and to investigate events that occur in this region of the cell with high resolution. These type of microscopes also enable the observation of the fluorescence of single-molecules. In the through-the-objective TIRF configuration that is most widely used for cellular microscopy, the laser beam is focussed at the back focal plane (BFP) of the microscope objective, away from the centre of the aperture as depicted in Fig. 2.12. In this way the light exiting the objective, travels through the immersion oil and the glass cover slip without being affected, as they have the same refractive indices.

At the interface between the cover slip and the aqueous sample, the direction of the incident light changes.

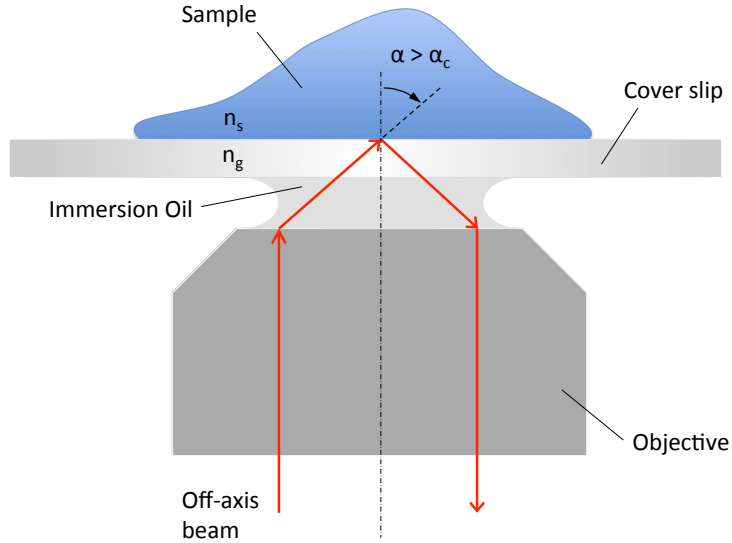


Figure 2.12: Schematic of a through-the-objective TIRF configuration. The laser beam is focussed at the BFP of the microscope objective, away from the centre of the aperture so that the light exiting the objective can travel through the immersion oil and the glass cover slip without being affected. At the interface between the cover slip and the aqueous sample, the beam is totally internally reflected (adapted from (Mattheyses et al., 2010)).

After having defined the *critical angle* as:

$$\alpha_c = \sin^{-1} \left(\frac{n_s}{n_g} \right), \quad (2.1)$$

using Snell's law, where n_s and n_g are the indexes of refraction of the sample and the glass cover slip, respectively, we can identify two cases (Mattheyses et al., 2010):

1. If $\alpha < \alpha_c$, most of the beam is refracted and goes through the sample (epifluorescence).
2. If the angle of incidence of the excitation light on the interface, $\alpha > \alpha_c$, the beam is totally internally reflected and does not propagate into the sample. In this case $n_s < n_g$.

2.3. METHODS

In this second case the excitation beam reflected at the glass-sample interface travels back through the cover slip. Some of the light leaks through the interface, creating a standing wave known as evanescent field as shown in Fig. 2.13. Such a wave is used as excitation field in TIRF microscopy. The intensity, I , of the evanescent field follows an exponential decay as it penetrates the sample:

$$I(x) = I(0) e^{-\frac{x}{d}}, \quad (2.2)$$

where $I(0)$ is the intensity of the evanescent field at the glass-sample interface, x is the distance along the normal to the interface and d is the penetration depth of the evanescent field (Axelrod et al., 2002), defined as

$$d = \frac{\lambda_0}{4\pi\sqrt{n_g^2 \sin^2(\alpha) - n_s^2}}, \quad (2.3)$$

where λ_0 is the excitation wavelength in vacuum.

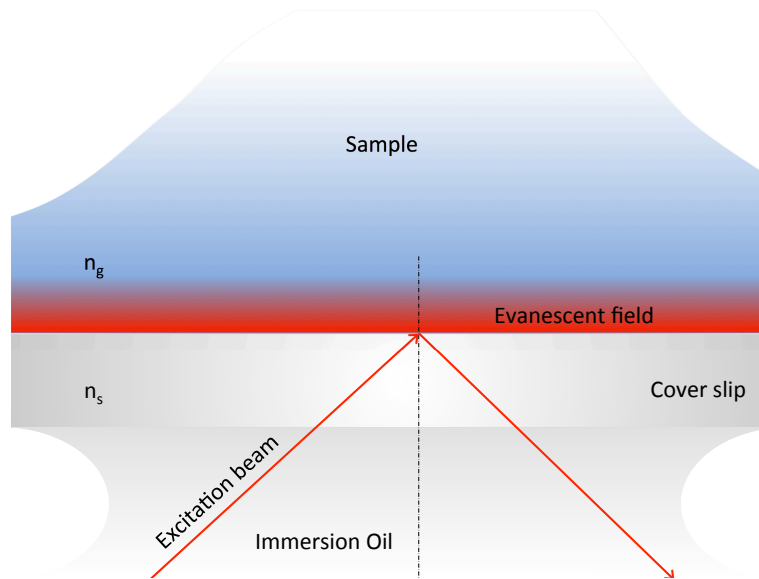


Figure 2.13: Schematic of a through-the-objective TIRF configuration. Close-up of the evanescent field forming at the interface between the glass cover slip and the sample.

For the work described in this chapter I used a Nikon Total Internal Reflection Fluores-

cence imaging system equipped with a Plan-Apochromat 60x NA 1.45, oil immersion objective lens and automatic focussing system for time lapse imaging.

2.3.5 Numerical simulation

After loading the system with cell and chemoattractant solutions, a transient flow directed from the source to the sink reservoirs establishes. The flow lasts until the hydrostatic pressure at all the opposite reservoirs is equal. During this phase the concentration of chemicals within the main channels remains ideally constant, this enables the establishment of a linear spatial gradient of chemoattractant inside the bridging channels mainly driven by diffusion. To compute the time-scale of the gradient formation I modelled the diffusion of cAMP through a single migration channel using the software Comsol Multiphysics 5.1 (Comsol, Inc.). The purely diffusive transport is described by Fick's second law

$$\frac{\partial c}{\partial t} = D \nabla^2 c. \quad (2.4)$$

where c is the cAMP concentration and D is the diffusion coefficient. As the cross-section of a migration channel is much smaller than that of the loading channels, the problem can be reduced to a 1D diffusion. Therefore equation 2.4 can be simplified to

$$\frac{\partial c}{\partial t} = D \frac{\partial^2 c}{\partial x^2}. \quad (2.5)$$

I calculated the time-dependent solution of the 1D diffusion equation for a single migration channel using the module '*Transport of Diluted Species*'. *Constant-concentration* boundary conditions were imposed at the two ends of the channel, the values at these positions were set to be $c = 1 \mu\text{M}$ and $c = 0 \mu\text{M}$, respectively, as in the actual experiments. The boundary conditions were set as '*no-flux*' at the edges of the channel.

2.3. METHODS

The initial conditions were 0 μM throughout the channel. The mesh size was set as 'Extremely fine', which corresponded to spatial steps in the range of $\sim 1 \mu\text{m}$. The value of the cAMP diffusion coefficient, D , in water is $4.44 \times 10^{-6} \text{ cm}^2/\text{s}$ (Dworkin and Keller, 1977).

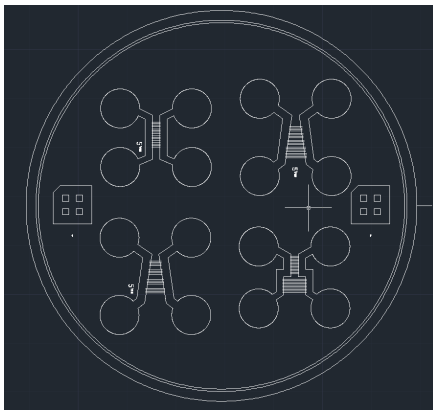
2.3.6 Image and data analysis

Images were analysed using the ImageJ software (<http://rsbweb.nih.gov/ij/>). An important plugin that I used is the kymograph analysis. A kymograph is a time-space plot that allows for the representation of a dynamic process in a single image. More specifically, by selecting a straight or segmented linear region of interest from a the first picture of an image sequence, the kymograph is constructed by juxtaposing the intensity content along the selected line from each time frame. Therefore, in one image the information coming from the chosen line can be followed over time. As a convention all the kymograph in the next chapters, unless stated otherwise, have on the x-axis the coordinate of the line, and time on an inverted y-axis (pointing downwards). In the case of the cells migrating in microchannels I was able, by selecting a line parallel to the axis of the channel, to measure the relationship between the displacement of the cell and time. For most of the cells such relationship appeared to be linear, therefore the mean migration speed has been calculated by measuring the slope of the regression line that fitted the trailing edge of the cell in the kymographs. The mean and standard deviation of the averaged migration speeds have been calculated for each cell sample using Microsoft Excel. Moreover, one-way Anova tests with 95% confidence level have been performed using StatPlus (AnalystSoft) to investigate quantitative relationships among different groups.

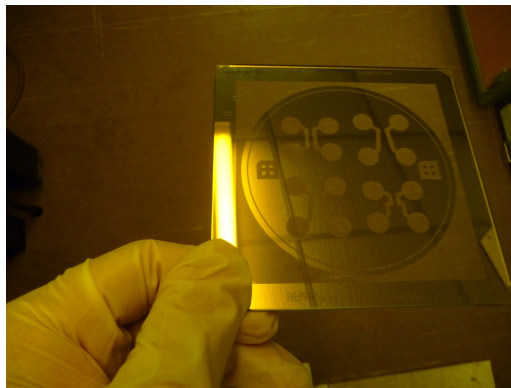
2.4 Results

2.4.1 Development of the microfluidic chip

The flow-free device has been fabricated by following the microfabrication processes described above. The results of each single phase is summarise in the Fig. 2.14.



(a) CAD Design of the mask



(b) Mask



(c) Mould



(d) PDMS chip

Figure 2.14: Results of the individual phase of the micro-fabrication. (a) CAD design of different geometries. (b) Photomask made by Compugraphics International Ltd based on the designs in (a). (c) Mould obtained via photolithography. (d) Chip reversibly bonded onto a microscope cover glass.

2.4.2 Characterisation of the microfluidic chip

Equation 2.5 was solved numerically for a 1.5 mm long channel using Comsol. The output of the simulation can be viewed in Fig. 2.15. The calculation predicts that a

2.4. RESULTS

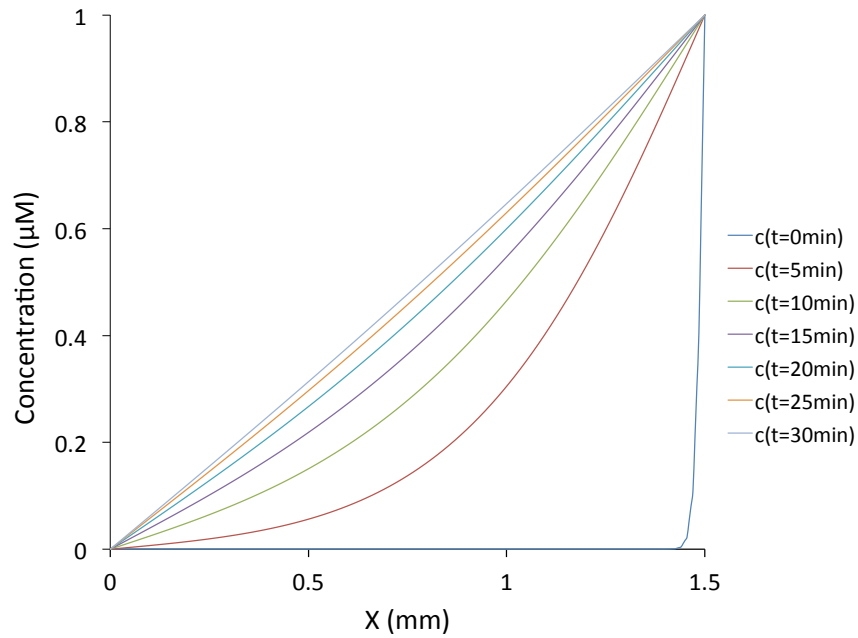


Figure 2.15: Time evolution of the cAMP gradient profile within a single 1.5 mm long microchannel. A concentration of cAMP 1 μM is imposed on the right hand side which is connected to the cAMP loading big channel (as in Fig.2.9), whereas the concentration on the left hand side is 0 μM . The graph shows the concentration profile every 5 minutes. The equilibrium is reached after about 25 minutes when the profile of the concentration is almost linear. The value of the diffusion coefficient (D) used is $4.44 \times 10^{-6} \text{cm}^2/\text{s}$ (Dworkin and Keller, 1977).

linear spatial gradient establishes after about 25 minutes from the hydrostatic equilibration of the system.

Experiments using the fluorescence dye FITC Dextran (Dextran FD-70, Sigma-Aldrich) to mimic the chemical gradient confirmed that, at the equilibrium, a linear gradient establishes across the migration channels, as shown in Fig. 2.16. It is important to note that the fluorescent dye Dextran FD-70 (70kDa) has a diffusion coefficient $D=39 \mu\text{m}^2/\text{s}$ in phosphate buffer (Lang et al., 1986). Therefore, it would require about an order of magnitude longer to reach the equilibrium, compared to cAMP, that is characterised by $D = 444 \mu\text{m}^2/\text{s}$, (Dworkin and Keller, 1977).

Furthermore, loading 1 μm silica beads (Sigma-Aldrich) in the system I verified that no flow was present at the hydrostatic equilibrium. Beads were only moving by Brownian

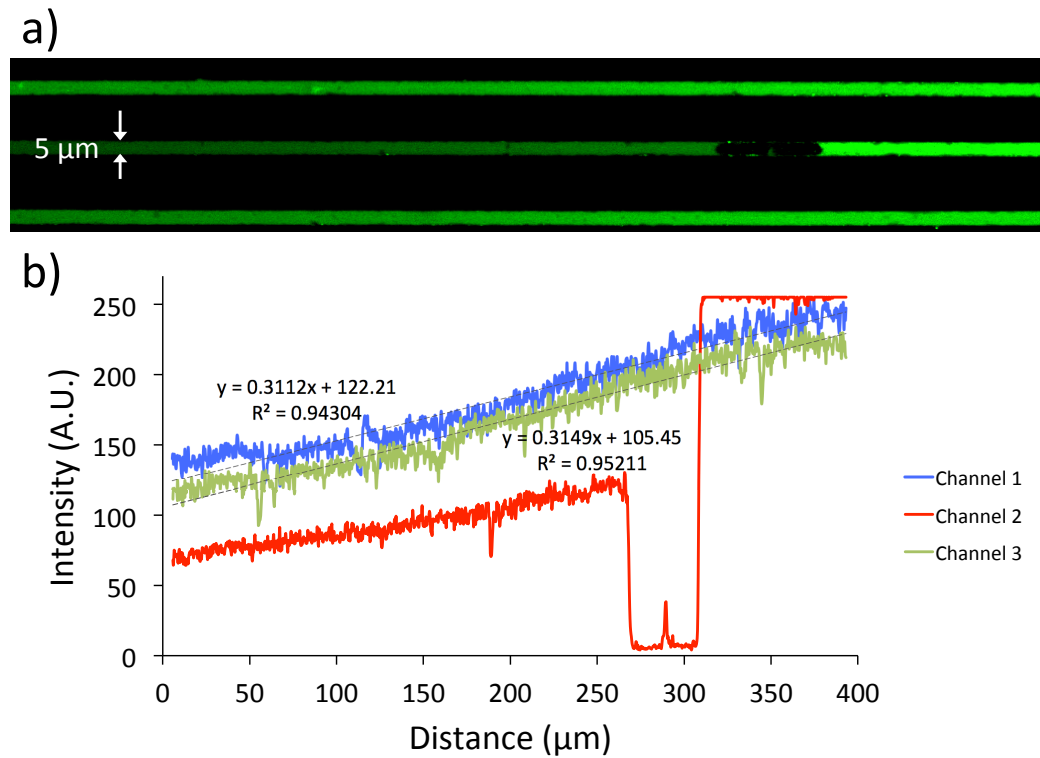


Figure 2.16: Testing the linearity of the chemical gradient. (a) The fluorescent dye Dextran is loaded in the right-hand side reservoir to mimic the spatial distribution of cAMP. (b) The intensity profile of the fluorescence signal is measured for the three channels. In the absence of cells the profile is linear. The presence of a cell in the second channel leads to an increase in the signal at the front of the cell. In this case the Dextran leaks around the cell and a linear gradient can be observed also at the back of the cell.

motion. Furthermore, when cells move along the channels two different cases could be observed, as shown in Fig. 2.17:

- Some cells completely plugged the channel, hence no gradient was found behind them.
- Some cells did not plug the channel and therefore the dye leaked around the cell and a fluorescence signal could be measured at the back of the cell.

It is important to note that, as discussed in the 'Methods' section, the local concentration in the proximity of a single cell migrating into a microchannel is the net result of

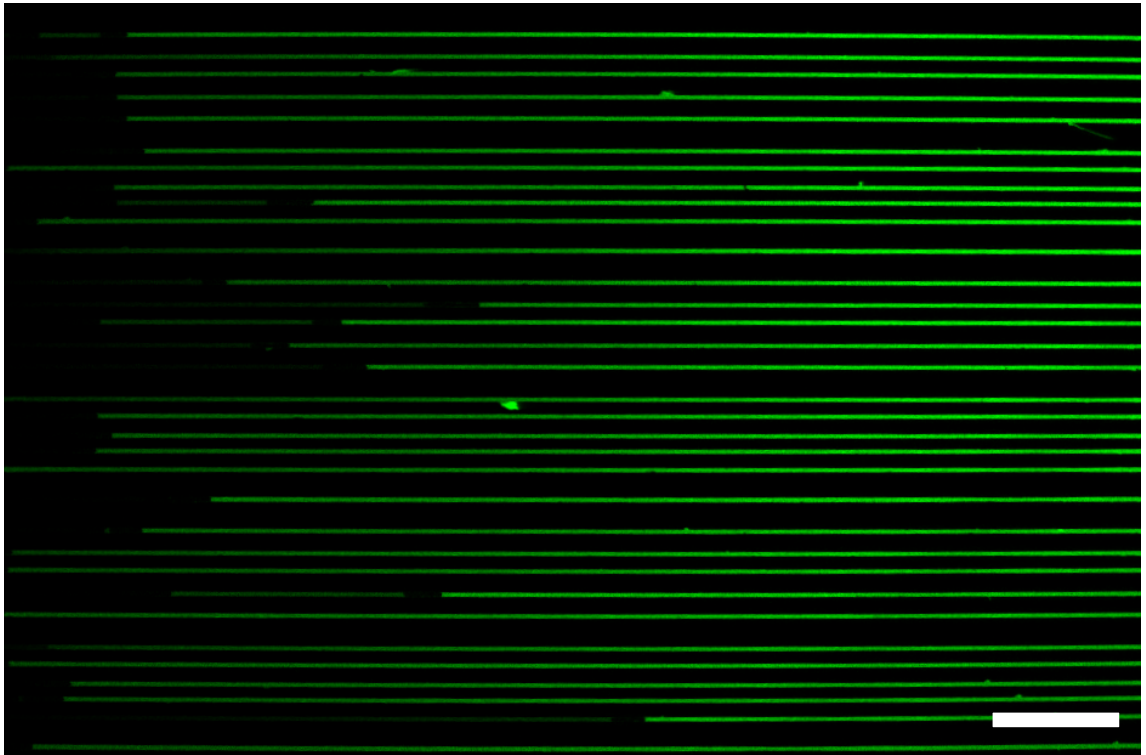


Figure 2.17: Influence of cells on the chemical gradient. The fluorescent dye Dextran is loaded in the right-hand side reservoir to mimic the spatial distribution of cAMP. Some cells completely plug the channels, hence no gradient is found at behind them. In other cases the Dextran leaks around the cell and a fluorescence signal is visible at the back of the cell. Scale bar is 100 μm .

the following three contributions:

- The concentration of the cAMP imposed by the microfluidic system.
- The concentration of the cAMP secreted by the cell.
- The concentration of PDE secreted by the cell.

In the next sections I show and discuss the results obtained by combining the developed microfluidic device with live imaging and image analysis techniques. In all the images showing migrating cells, by convention, the concentration of cAMP is increasing as one moves to the right hand side.

2.4.3 Relationship between spatial confinement and cell speed

To assess how the spatial confinement affects the migration velocity I developed a microfluidic device with migration channels of different widths: 2, 5 and 8 μm , whereas the height was constant and equal to 2 μm . The velocity of the cells was estimated exploiting the fact that cells tended to exhibit a constant average velocity. Specifically, I extracted a kymograph from each migrating cell, at the location of the axis of the channels. The mean velocity was then calculated using the following formula:

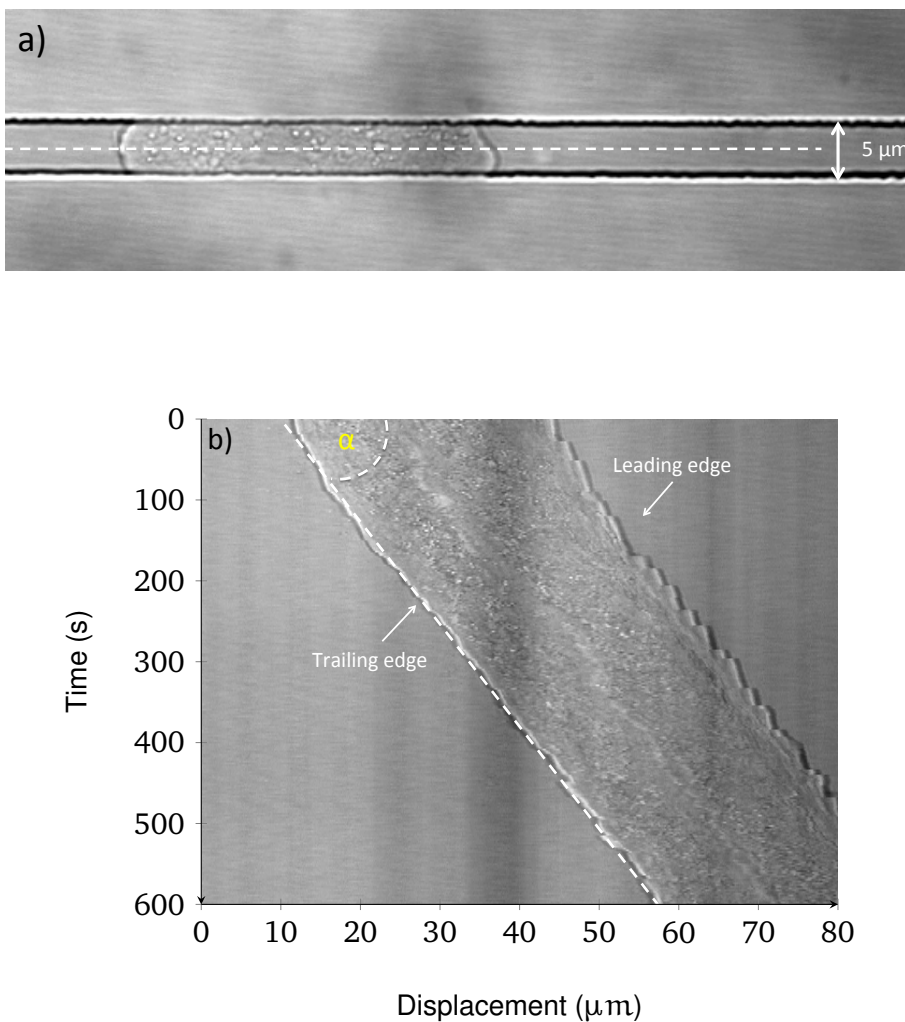


Figure 2.18: Example of a cell migrating in a microchannel and its velocity profile. (a) Cell migrating in a 2 μm high, 5 μm wide channel. (b) Kymograph of the cell in (a) taken along the axis of the channel. The velocity of the channel is calculated by measuring the angle α and the Eq. 2.6.

2.4. RESULTS

$$\langle v \rangle = \frac{1}{\tan(\alpha)} \cdot \frac{\text{pixel size}}{\text{time step}} \cdot 60, \quad (2.6)$$

where α is the angle indicated in Fig. 2.18, expressed in radians. The velocity calculated using Eq.2.6 gives the cell speed in $\mu\text{m}/\text{min}$. The results of the quantitative analysis presented in Fig. 2.19 show that cells that migrate in 2 μm wide channels are significantly slower ($5.3 \pm 3.5 \mu\text{m}/\text{min}$) than those that migrate in 5 and 8 μm wide channels ($13.8 \pm 5.8 \mu\text{m}/\text{min}$ and $12.3 \pm 4.9 \mu\text{m}/\text{min}$, respectively).

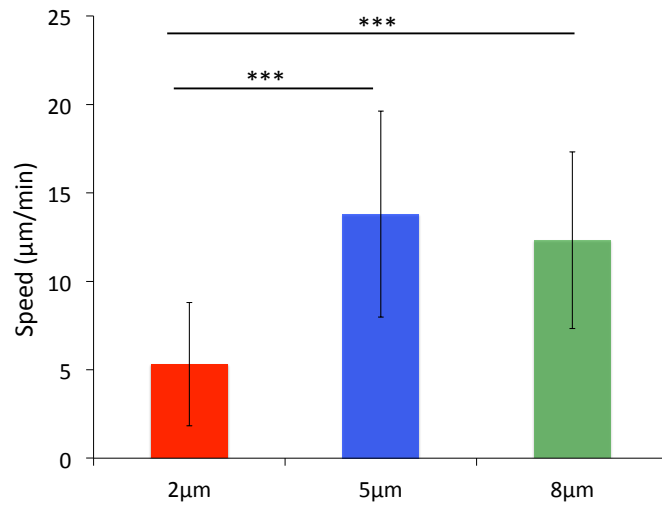


Figure 2.19: Mean velocity of cells measured in microchannels with different cross-sectional area. The channels are 2 μm high, whereas the width is 2 μm ($n = 48$, collected in 14 independent experiments), 5 μm ($n = 56$, collected in 11 independent experiments) and 8 μm ($n = 56$, collected in 9 independent experiments, respectively). Error bars represent the SD, $P < 0.0001$.

Dictyostelium cells have been reported to move on a flat surface at an average speed of $11.7 \pm 1.4 \mu\text{m}/\text{min}$ towards the tip of a micropipette that releases cAMP (McCann et al., 2010). Despite the absence of spatial constraint this speed is comparable with that of cells confined in 5 and 8 μm wide channels as shown in Fig. 2.19. Notably, when moving in 2 μm wide channels, cells exhibited a slower phenotype. To further investigate this behaviour I developed a variant of the chip that allowed me to expose each individual cell to a progressively decreasing width between 5 and 2 μm across

the 250 μm long channels, as shown in Fig. 2.20. Most of the cells analysed ($> 90\%$)

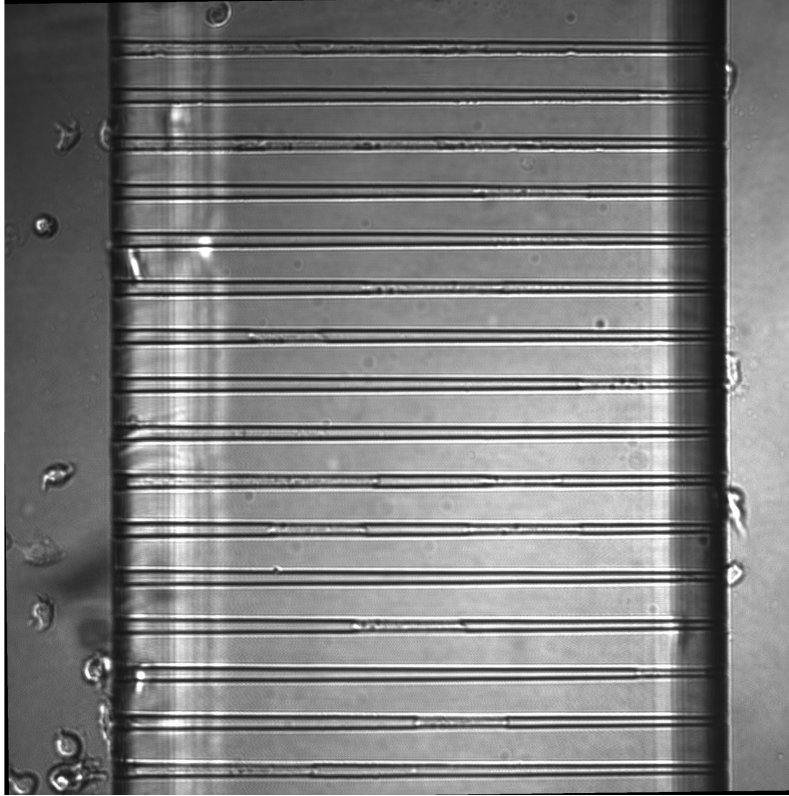


Figure 2.20: Cells migrating in tapered channels. The width decreases from 5 μm (left) to 2 μm (right). The length of the channels is 250 μm .

showed a velocity profile similar to that shown in Fig. 2.21. Interestingly, this trend can be modelled with a uniformly decelerated motion equation:

$$y(t) = v_0 t - \frac{1}{2} a t^2, \quad (2.7)$$

where $y(t)$ is the displacement of the cell, v_0 is the initial velocity of the cell and $-a$ is the deceleration. The theoretical relation between displacement and time is shown in Fig. 2.22. Using ImageJ I manually tracked the velocity profile from the kymograph of 25 cells. For each cell I saved the coordinates of the trailing edge and fitted the Eq.2.7 to the coordinate data. All the profiles could be described as uniformly decelerated motion ($R^2 > 0.98$). The extrapolated mean values of v_0 and a are $17.5 \pm 1.5 \mu\text{m}/\text{min}$ ($M \pm SD$) and $0.78 \pm 0.15 \mu\text{m}/\text{min}^2$ ($M \pm SD$), respectively. The relationship between

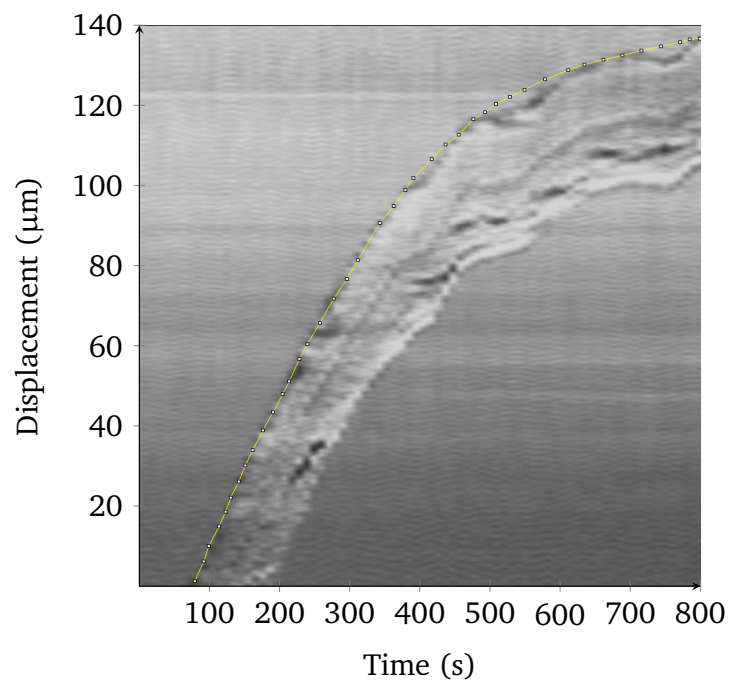


Figure 2.21: Representative kymograph from the axis of the channel of a WT cell migrating in a tapered channel. The picture shows that the speed decreases constantly over time as a consequence of the linear decrease in channel width.

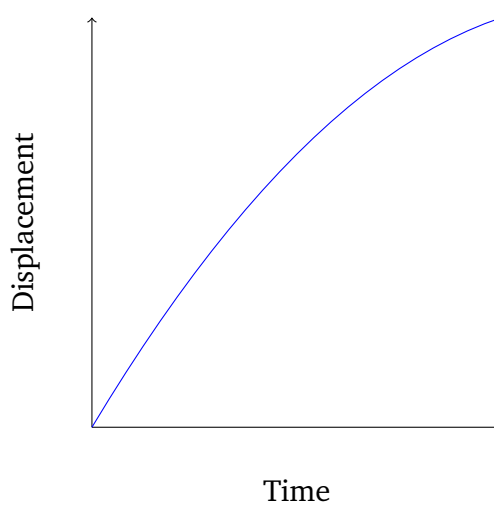


Figure 2.22: Displacement-time relationship for the uniformly decelerated motion. The graph does not reflect experimental data and was generated for illustrative purposes.

the cell velocity and the width of the channel can be described by:

$$v(x, t) = \sqrt{v_0 t - 2a(W_{\max} - W(x))}, \quad (2.8)$$

where W_{\max} is the maximum width, that is 5 μm and $W(x)$ is the width of the channel at a given x . The value of $W(x)$ and x are related by the following linear relationship:

$$W(x) = W_{\min} + (W_{\max} - W_{\min})(1 - x/L), \quad (2.9)$$

where W_{\min} is the width at the narrowest end of the tapered channel and L is the length of it.

2.4.4 Actomyosin cytoskeleton in confined cells

To investigate how the actomyosin cytoskeleton responds to the spatial confinement I qualitatively analysed the localisation of myosin II (myoII) and actin by using cells where the two proteins were labelled with GFP and LifeAct, respectively. In addition, I quantitatively tested the behaviour of WT and myoII knockout (myoII-null) cells. The localisation of actin and myoII for a cell in a 5 μm wide channel is shown in Fig. 2.23. As expected, the myoII (in green) localises at the uropod of the cell, while the actin is abundant at the cell front. This type of localisation is similar to the case in which cells migrate in 2D or on a substrate. Interestingly, when the width of the channels is reduced to about 2 μm by 2 μm , actin shows an increased localisation at the uropod, and myoII at the pseudopod, as shown in Fig. 2.23. Moreover, actin appears increasingly localised at the plasma membrane in areas where the cell is in contact with the walls of the channel. This peculiar distribution of actin and myoII might be required to counteract the mechanical stress associated with the spatial confinement. Furthermore, the actin tread-milling would lead to the transport of such an enhanced

2.4. RESULTS

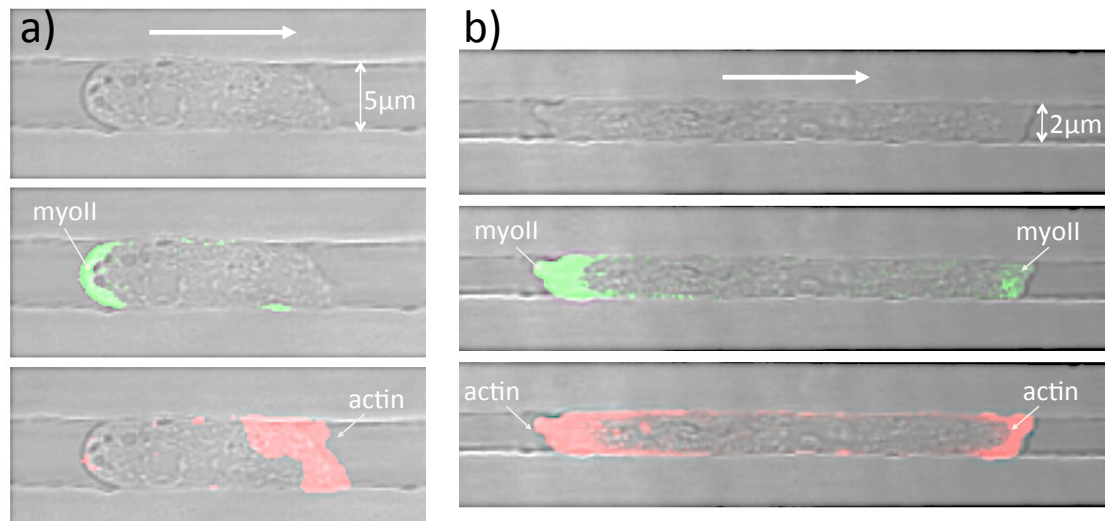


Figure 2.23: Localisation of actin and myoII in channels with different cross section. (a) The first picture at the top shows the transmitted light image, while the second and the third show the overlapping between the green and red channels, with the transmitted light image. In the second picture the localisation of myoII at the back of the cell can be observed. The third image shows the localisation of actin at the leading edge. (b) In this case the cell migrates in a 2 μm high, 5 μm wide channel. MyoII appears to be present at the uropod as in (a) but also at the cell front and actin is also present at the uropod. The cell is migrating to the right (as indicated by the big white arrow at the top), where the concentration of cAMP is higher.

peripheral mesh-work resulting in the observed increased posterior actin localisation.

The role of myoII in confined migration was investigated using mutants, where myoII was knocked out (myoII-null). These cells were not able to migrate in 2 μm high microchannels (regardless of the width): although their leading edges were able to extend in the direction of the gradient, their uropods appeared rounded and unable to squeeze into the channel as shown in Fig. 2.24. It was then necessary to develop a modified version of the migration device where the height of the migration channels was 3.5 μm. For the same reason only 5 μm wide channels were considered. The new chip was used to test the difference in speed between WT and mutant cells. The inhibition of myoII resulted in slower migration ($3.9 \pm 2 \mu\text{m}/\text{min}$) compared with the WT ($13.8 \pm 5.8 \mu\text{m}/\text{min}$) as shown in Fig. 2.25.

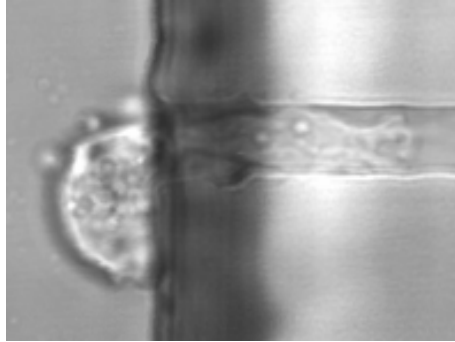


Figure 2.24: Representative myoII-null cell stuck at the entrance of a 2 μm high, 5 μm wide channel. On the right-end side the leading edge of the cell elongates towards higher concentration of cAMP. On the left, the uropod is blocked outside the migration channel.

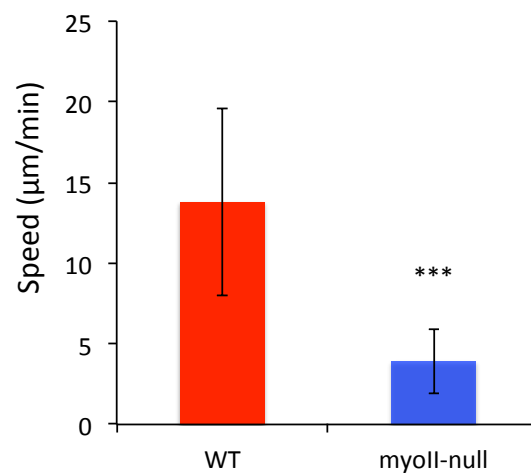


Figure 2.25: Comparison between mean velocities of WT cells ($n = 56$, collected in 11 independent experiments) moving in 5 μm wide, 2 μm high channels and myoII-null cells ($n = 30$, collected in 11 independent experiments) confined in 5 μm wide, 3.5 μm high channels, error bars represent SD, $P < 0.0001$.

2.4.4.1 Relationship between migratory modes and confinement

Cells that migrated in microchannels showed two different ways of motion:

- In the first case the protrusions were irregular in shape and appeared enriched in F-actin. This corresponds to the pseudopod-based migration mode.
- In the second case the protrusions were much faster, almost spherical in shape and devoid of actin at the early stage of their formation. This second phenotype has been described in the literature as blebbing mode.

In all the experiments I noticed that each migration mode tends to be persistent: as one cell starts migrating into a channel with a specific mode, it tends to maintain it. A detailed example of the actin dynamics during bleb generation is depicted in Fig. 2.26. The pictures show the temporal evolution (time-step = 3 s) of a single bleb forming at the leading edge of a cell migrating into a 2 μm channel.

The kymograph taken from the axis of the channel of the blebbing cell in Fig. 2.26 is shown in Fig. 2.27. The pictures show two consecutive blebbing events captured using the confocal and the transmitted images, respectively. The occurrence of a bleb corresponds to the horizontal segments, indicating that the time-scale of the bleb formation is below the acquisition time (3 s). Indeed, velocities of about 10 to 20 $\mu\text{m}/\text{s}$ have been measured during the expansion phases (Maugis et al., 2010). Interestingly, the constant localisation of F-actin at the leading edge is interrupted by the formation of the blebs. It can be noticed that cells alternate sudden displacements, and constant velocity motion, in a relatively periodic way. The conditions that lead to the formation of pseudopods rather than blebs are still not clear, but I observed for the first time that *Dictyostelium* cells exhibit an increasing tendency to protrude blebs when the size of

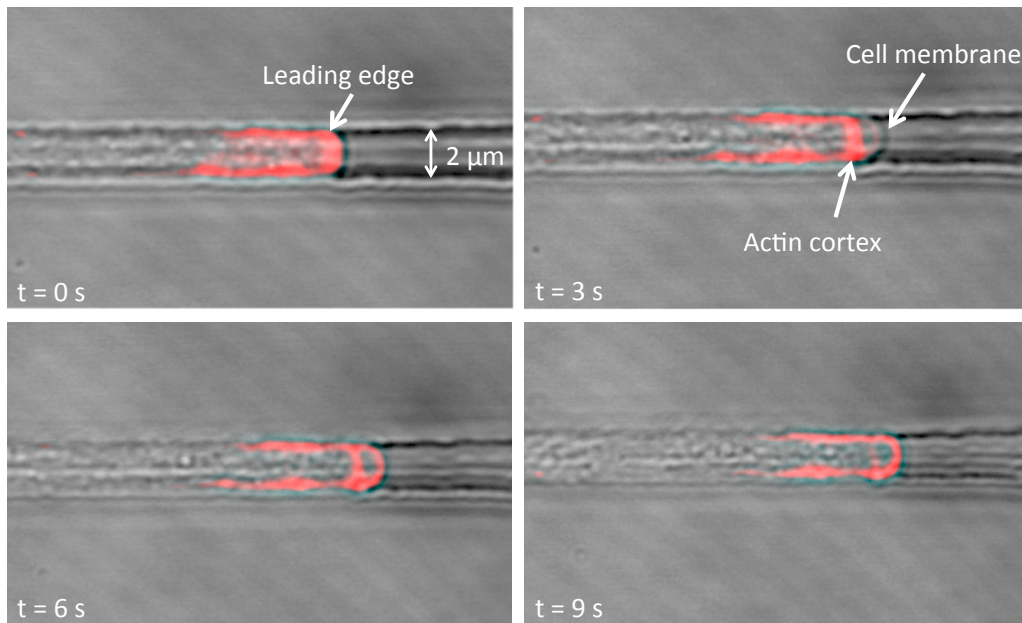


Figure 2.26: F-actin dynamics during different phases of bleb formation. Consecutive time-lapse images of a cell moving in $2\ \mu\text{m}$ wide, $2\ \mu\text{m}$ high channel in which F-actin is labelled with LifeAct. Bright field and confocal images are merged. At $t = 0\ \text{s}$ F-actin can be observed at the leading edge; at $t = 3\ \text{s}$ the membrane expands quickly without being supported by the actin cortex; at $t = 6\ \text{s}$ cortical actin starts to translocate inside the bleb; at $t = 9\ \text{s}$ the cortex at the leading edge is restored to the normal conditions.

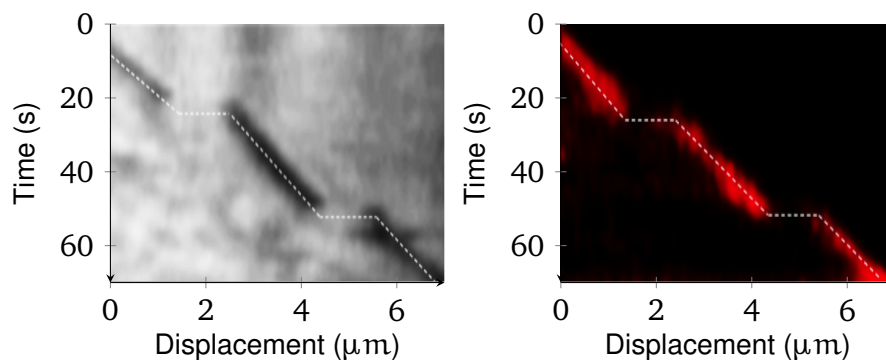


Figure 2.27: Kymographs from the middle line of the migration channel of the blebbing cell in Fig. 2.26. The pictures show only a small portion of the leading edge of the cell. The position of the membrane is outlined by the broken line in both the bright field and the confocal images. The horizontal segments correspond to the bleb generation during which the membrane is detached from the cell cortex and extended impulsively forward without being supported by actin.

2.4. RESULTS

the channel decreases, as shown in Fig. 2.28. The histogram shows that 16 out of 35 cells migrating in 2 μm wide channel moved via blebbing motion, while only 3 out of the 36 cells in 5 μm wide channel adopted such a mode.

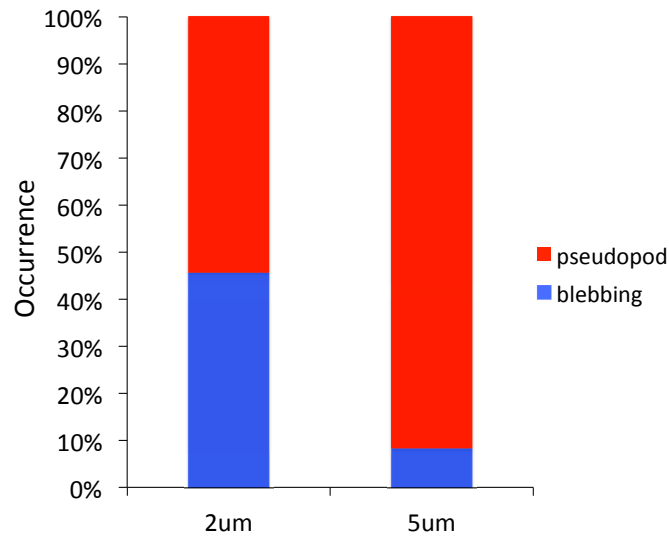


Figure 2.28: Percentage occurrence of the two migration modes as a function of the size of the microchannels. Running seven independent experiments, about half of the 35 cells migrating in 2 μm by 2 μm channels moved by pseudopod-based motion, whereas less than 10% of the 36 cells in the 5 μm by 2 μm channels moved by blebbing motion.

On average, blebbing cells exhibit lower migration speed ($4.6 \pm 2.7 \mu\text{m}/\text{min}$) than cells moving by pseudopods ($9.3 \pm 4 \mu\text{m}/\text{min}$) as shown in Fig. 2.29. During bleb formation it appears that the entire cell body is quickly shifted forward. Fig. 2.30 shows a kymograph from the centreline of a blebbing cell moving in a 2 μm wide channel. It is clear that the movement starts at the uropod and then the rest of the body is pushed towards the direction of migration. It is important to note that a minority of cells exhibited a mixed phenotype where pseudopodia and blebs coexisted. In these cells the localisation of actin at the leading edge appeared at an intermediate level between the two modes. This suggests that the a diminished presence of actin at the cell front might be the main cause of the bleb formation.

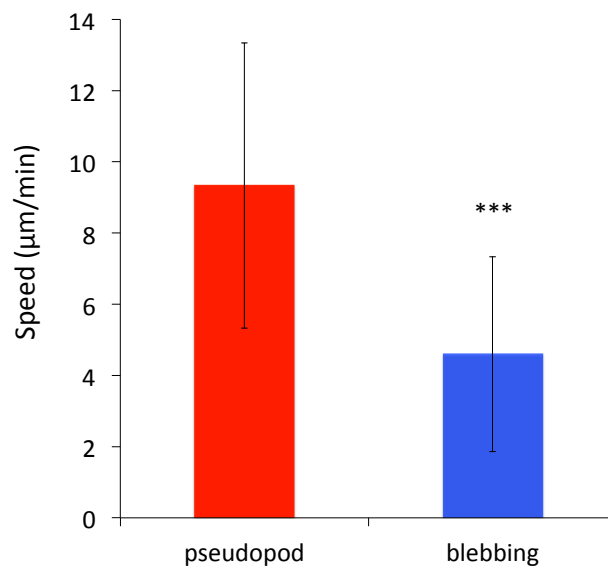


Figure 2.29: Mean speed of cells that migrate by 'blebbing mode' (n = 17, collected in 13 independent experiments) and 'pseudopod-like mode' (n = 14, collected in 13 independent experiments). Error bars indicate the SD, P = 0.0005.

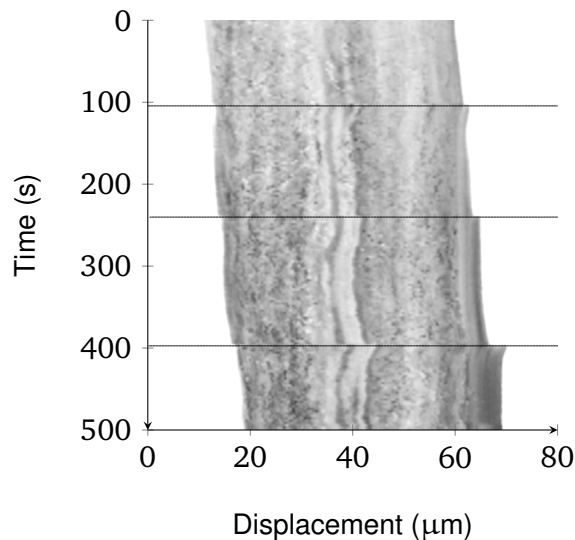


Figure 2.30: Kymographs from the middle line of a blebbing cell. Horizontal lines delineate the bleb protrusions. It is evident that the movement starts at the uropod and it is then transferred to the rest of the cell body. The nucleus, the clear stripe in the middle of the cell is shifted forward too.

The putative role of VatM in blebbing

It has been reported that the plasma membrane can only be stretched by 2–3% before rupturing (Mohandas and Evans, 1994), therefore sudden protrusions like blebs impli-

2.4. RESULTS

cate the presence of particular mechanisms which would serve as membrane reservoir, such as in exocytosis (Traynor and Kay, 2007).

In *Dictyostelium*, the protein VatM has been found to localise at the membranes of two systems: the contractile vacuole system (Fok et al., 1993) and the endo-lysosomal system (Adessi et al., 1995). VatM is a transmembrane subunit of V-ATPase, a vacuolar-type H^+ -ATPase, which is a highly conserved enzyme that transports protons across intracellular and plasma membranes, thanks to the energy extracted from ATP hydrolysis.

Contractile vacuoles (CVs) are organelles involved in osmoregulatory functions (Heuser et al., 1993): they periodically expand into a spherical shape, filling with water, and then contract, discharging the water from the cell body. These cycles help the cell to control its water content, and hence its volume and the internal pressure (Gabriel et al., 1999; Tani, 2002). In wild-type cells the cycles are in the order of ≈ 80 s (Fountain et al., 2007). Proton pumps are required on the vacuole's membrane to induce water influxes from the cytosol. Endosomes are involved in sorting material that is

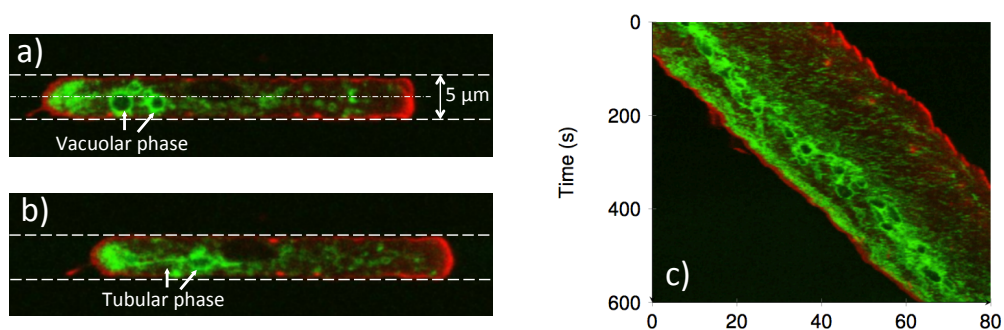


Figure 2.31: Sequential pictures of the distribution of VatM in a cell migrating in a $2 \mu\text{m}$ by $5 \mu\text{m}$ channel. The cell expresses both F-actin and VatM-GFP. The circular structures represent the contractile vacuoles (CVs), whereas the green small particles represent the endolysosomal vesicles. The cell is confined in $5 \mu\text{m}$ by $2 \mu\text{m}$ channels. (a) Vacuolar phase, during which the CVs appear circular. (b) Tubular phase, during which the CVs collapse into a rod-like shape releasing the liquid content outside the cellular body. (c) Kymograph taken from the middle line of the channel (dashed line in (a)).

internalised at the plasma membrane from the external microenvironment. Some endosomes fuse with lysosomes where their content is degraded. Other endosomes fuse with the cell membrane instead, releasing their cargos into the extracellular medium (Gruenberg and van der Goot, 2006).

Endosomes and CVs are physically distinct but the fact that mutations have been discovered that affect both systems would suggest that membrane trafficking might exist between them (Clarke et al., 2002). Looking at *Dictyostelium* cells expressing VatM-GFP allowed me to follow the dynamics of contractile vacuole complexes and endosomes over time. Specifically, I was able to observe the localisation of proton pumps in CVs during the reversible transition between their vacuolar to tubular configuration in which they take up and expel liquids as shown in Fig 2.31.

It is important to observe that during the tubular phase, CVs appeared parallel to the direction of migration and they created a sort of network that connected other contractile vacuole systems. Moreover, they were always localised in the region between the nucleus and the uropod as shown Fig. 2.31 and Fig. 2.32. In addition, in many cells, I noticed that the CVs' phases tended to be periodic as shown in the kymograph in Fig. 2.31(c) where, on the left-hand side, the vertical distance between consecutive CVs appears relatively regular.

By following the VatM dynamic it was possible to detect the trafficking of small vesicles: some of them were directed towards the back of the migrating cell but a large amount of them translocated towards the leading edge and eventually went into the blebs. Presumably such vesicles fuse with the cell membrane releasing their content outside. The kymographs in Fig. 2.32 show the translocation of VatM towards the leading edge

2.4. RESULTS

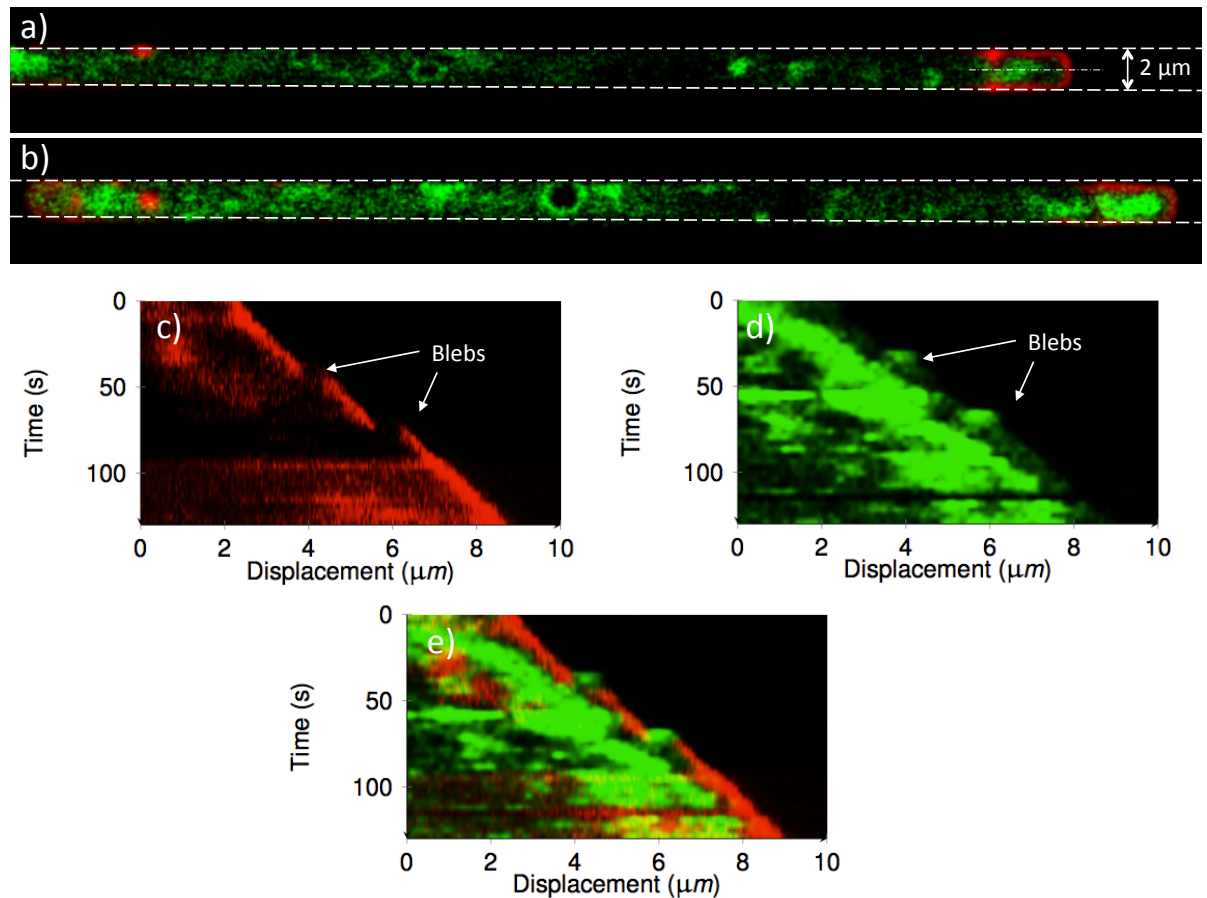


Figure 2.32: Sequential pictures of the distribution of VatM in a cell migrating in 2 μm by 2 μm channels. The cell expresses both F-actin and VatM-GFP. The circular structures represent the contractile vacuoles, whereas the small green spots represent the endolysosomal vesicles. In (b) some vesicles move towards the leading edge (right-hand side). (c) Kymograph of the leading edge taken from the red channel, along the dashed line at the front of the cell in (a). In the early phases blebs are devoid of actin. (d) Same kymograph shown in (c) but from the green channel. The two green spots at the right-hand side represent the translocation of VatM into the blebs at the early stages of their formation. (e) Red and green channels merged: the kymograph shows how VatM and F-actin appear mutually exclusive into the blebs.

(right-hand side) with a velocity that is higher than the migration speed of the cell.

In addition, in Fig. 2.32(d) it can be observed that the two blebs are enriched in VatM during the early stages of their generation. This suggests that such a little and dynamic vesicles in the vicinity of the leading edge could presumably act as membrane reservoirs required for the sudden protrusion of the membrane.

2.4.4.2 Dictyostelium cells move with constant speed in microchannels

Dictyostelium cells showed the interesting tendency to move with relatively constant average velocity once confined in microchannel. This property could be the consequence of two different contributions:

1. Periodic protrusions at the leading edge.
2. Constant polymerisation rate of F-actin at the leading edge.

Periodic protrusions

As mentioned in the previous section, one interesting quantitative observation was that the occurrence of the blebbing tended to be periodic. A more striking example is shown in Fig. 2.33. The picture shows a centre-line kymograph of a LifeAct labelled cell migrating in 2 μm high, 2 μm wide channel. A very persistent bleb formation can be noticed at the leading edge. A similar observation has been made in a recent work by Maugis et al. (2010) where cells of the human parasite *Entamoeba histolytica* (Eh) were aspirated in micropipettes. In non-confined situations these cells form blebs without any periodicity but when they were forced into the micropipettes the blebs start to be generated periodically. The authors suggested that myosin-driven cortical contractions would generate an instability of the intracellular pressure that, in the case of a constant geometry and shape of the environment, would induce a periodic formation of blebs.

The tendency to generate periodic protrusions under spatial confinement is valid also for the pseudopod-based motion, but less pronounced than in the blebbing case, as shown in Fig. 2.34. The picture shows that the length, the position and the dynamic of pseudopodia is more variable than in the case of blebs. By measuring the vertical

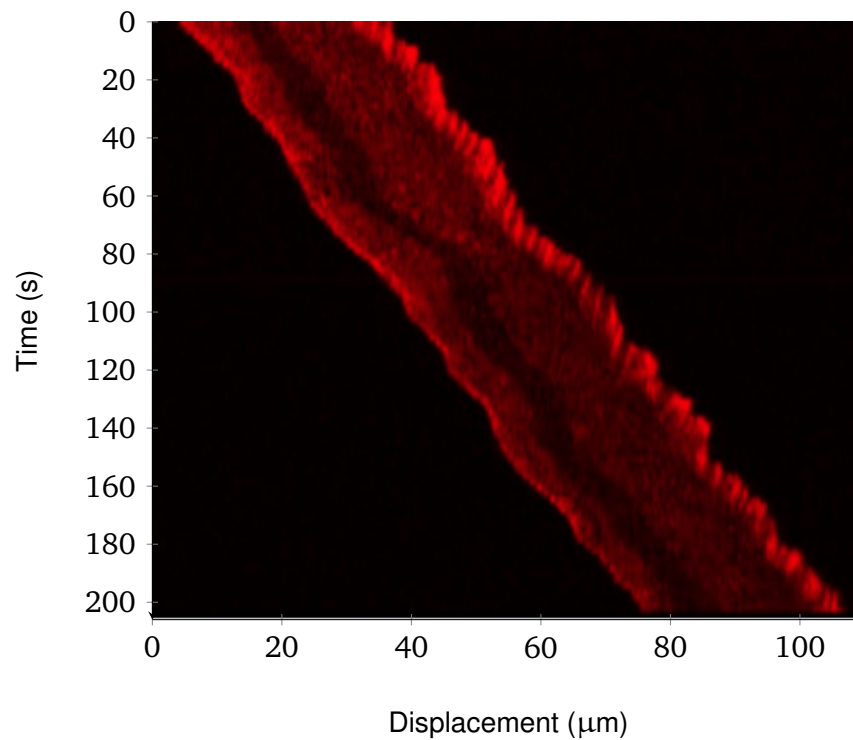


Figure 2.33: Kymograph of a blebbing cell. The kymograph is taken from the centre-line of a cell migrating into a 2 μm wide channel. A periodic blebbing pattern is noticeable at the leading edge (right-hand side).

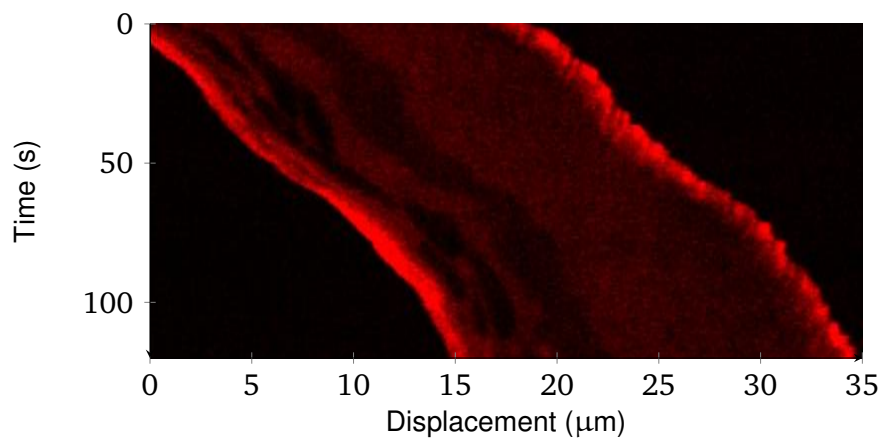


Figure 2.34: Kymograph of a cell migrating via pseudopodia. The kymograph is taken from the centre-line of a cell migrating into a 5 μm wide channel. A periodic pattern of protrusions is notable at the leading edge.

distance between two consecutive protrusion events in the kymographs, I was able to extract the value of the mean protrusion rate for each cell. Cells that migrate into channels wider than $2\ \mu\text{m}$ are able to generate multiple blebs in different locations of the leading edge as shown in Fig. 2.35. As a kymograph shows the temporal evolu-

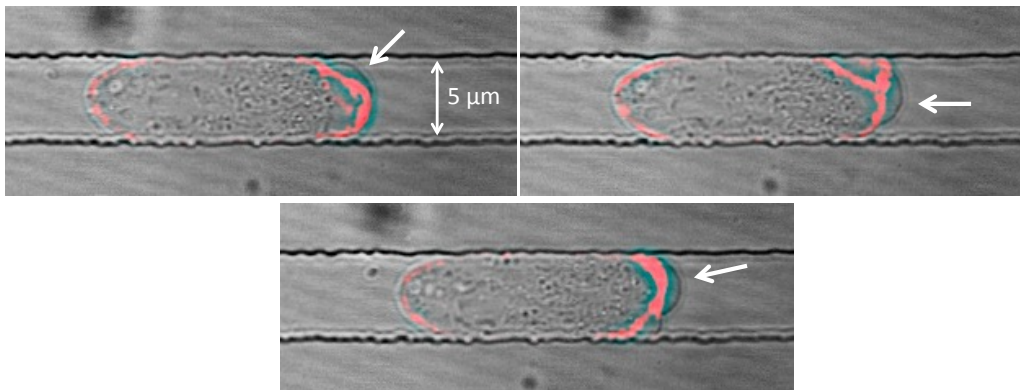


Figure 2.35: Blebbing cells migrating in a $5\ \mu\text{m}$ wide, $3.5\ \mu\text{m}$ high channel. The pictures show the same cell at different time frames. In each frame a bleb forms at a different position of the leading edge, as indicated by the white arrow.

tion of only a lateral section of the migration channel, it was impossible to account for the presence of multiple protrusions generated at different locations using this tool. Therefore, I decided to refine the analysis and to take into account only the cells confined in $2\ \mu\text{m}$ high, $2\ \mu\text{m}$ wide channels, where I could observe all the blebbing events. On the other hand, the analysis of the cell migration in such a confined environment was more challenging as cells are more constrained, and therefore the throughput was limited compared to the case of bigger channels. The relationship between the cell speed and the protrusion rate for 31 cells migrating in $2\ \mu\text{m}$ by $2\ \mu\text{m}$ channels appears to be linear, as shown in Fig. 2.36. Interestingly, this graph highlights for the first time the role of the protrusion rate in defining the mean speed of a cell. In fact, it can be observed that, on average, blebbing cells tended to move more slowly due to

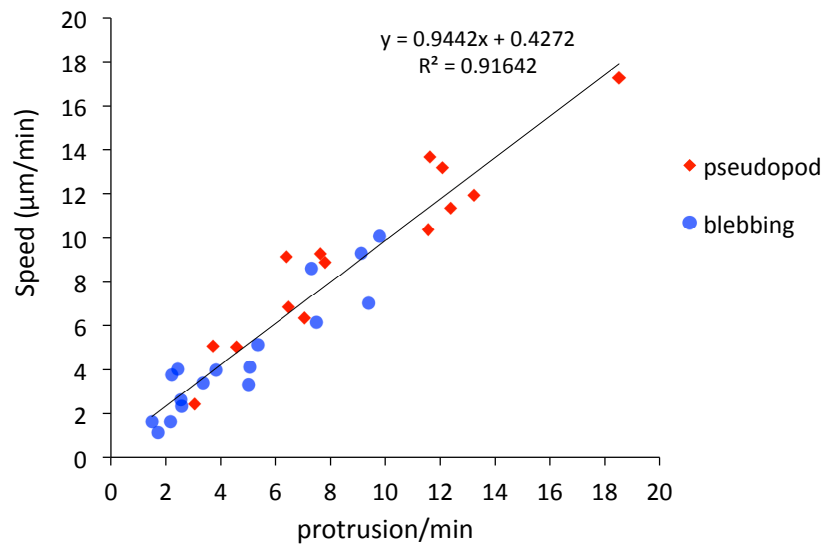


Figure 2.36: Relationship between the mean velocity of the single cells and the protrusion rate for 31 cells confined in 2 μm high, 2 μm wide channels, observed in 13 independent experiments. The cells are the same as in Fig. 2.29. The plot shows that on average blebbing cells tend to move slower than the pseudopod-driven cells, due to a lower protrusion rate.

a lower protrusion rate.

Constant actin polymerisation at the leading edge

An important aspect emerged from this study: actin is always present at the leading edge during the migration but the extension of the area in which the polymerisation takes place varies from cell to cell, and it appeared to decrease as the channel size decreased. This behaviour is not only present in pseudopod-based moving cells but also in blebbing cells, where I observed a consistent, constant speed displacement of the cell, between consecutive blebs, during which the actin is constantly localised at the leading edge. This would suggest that the actin is polymerised with constant rate, which is interrupted by the sudden formation of a bleb. This phenomenon is described in Fig. 2.27: as blebs are formed, F-actin polymerisation undergoes an interruption at the cell front.

Moreover the size of the polymerisation area at the leading edge appeared to have

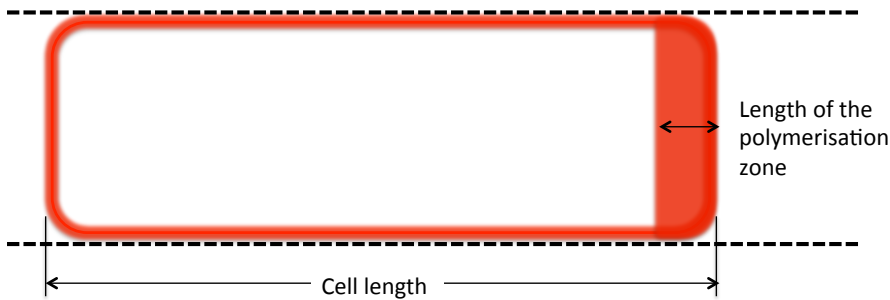


Figure 2.37: Schematic of the F-actin distribution within a confocal section of a cell migrating in a microchannel. Dashed lines represent the walls of the channel. In red the F-actin.

an impact on the cell speed. A linear relationship between the cell speed and the length of the actin-enriched front is shown in Fig. 2.38 for 31 cells. More specifically, I considered only the length of this area, as the width is fixed by the width of the channel ($2\ \mu\text{m}$) as in Fig. 2.37. Furthermore, it appeared that blebbing cells tended

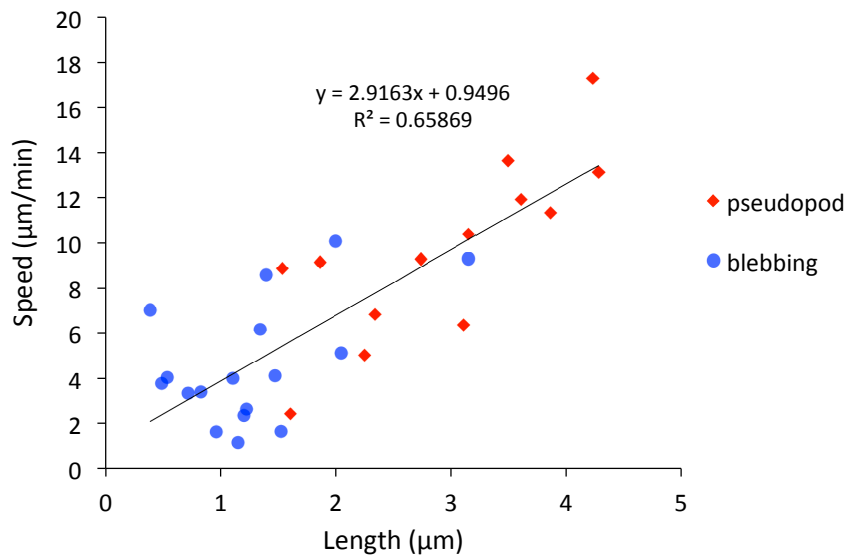


Figure 2.38: Relationship between the extension of the actin polymerisation zone at the leading edge and the cell speed for 31 cells confined in $2\ \mu\text{m}$ high, $2\ \mu\text{m}$ wide channels, observed in 13 independent experiments. The cells are the same as in Fig. 2.29 and Fig. 2.36. On the x axis the length of the polymerisation area.

to have a smaller actin-enriched leading edge.

2.4.4.3 The putative role of myosin VII in blebbing

Myosin VII (myoVII) is a member of the myosin superfamily⁷. Mutations of this protein have been associated to sensory disorders in many organism (Hasson, 1999). In *Dictyostelium*, myoVII localises at the tip of the filopodia⁸ where is thought to be required for their extension and for phagocytosis (Tuxworth et al., 2001). Moreover myoVII-null cells have been observed to show reduced adhesion to the substrate, to particles and to other cells (Tuxworth et al., 2001). The molecular mechanism of this unconventional myosin remains unclear. It could be involved in anchoring membrane proteins to recruit them at the site of the adhesion (Tuxworth et al., 2001). Another theory describes it as a molecular sensor able to measure the strength of the adhesion (Maniak, 2001). Once in 3D environment, I observed that the localisation of myoVII at the filopodial tip of *Dictyostelium* cells is preserved as shown in Fig. 2.39. Interestingly, looking at blebbing cells I noticed a strong localisation of myoVII inside the forming blebs, as shown in Fig. 2.40. This would suggest a possible role of such a protein in the early stages of the bleb generation, where it might be involved in promoting adhesion of the protruding membrane to the substrate as required for the cell to move forward.

⁷A protein superfamily is a group of proteins having similarities such as areas of structural homology and are believed to descend from the same ancestral gene (Miller-Keane, 2003).

⁸Filopodia are thin plasma-membrane protrusions, supported by bundles of aligned actin filaments. They are responsible of probing the cellular microenvironment (Mattila and Lappalainen, 2008).

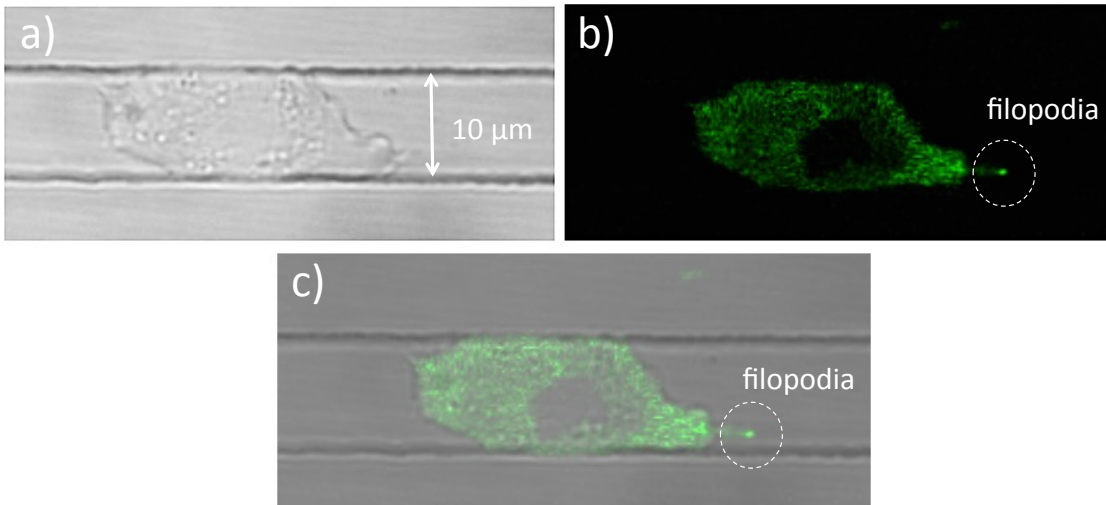


Figure 2.39: Spatial distribution of myoVII (GFP labelled) in a cell that migrates via pseudopodia in a $10\ \mu\text{m}$ wide, $2\ \mu\text{m}$ high channel. Images are recorded using a confocal microscope. (a) Transmitted light image. (b) Green channel image. (c) Overlapping between the transmitted light and the green channel. The myoVII localises at the leading edge and especially at the tip of the filopodia as it is visible on the right-hand side of the cell.

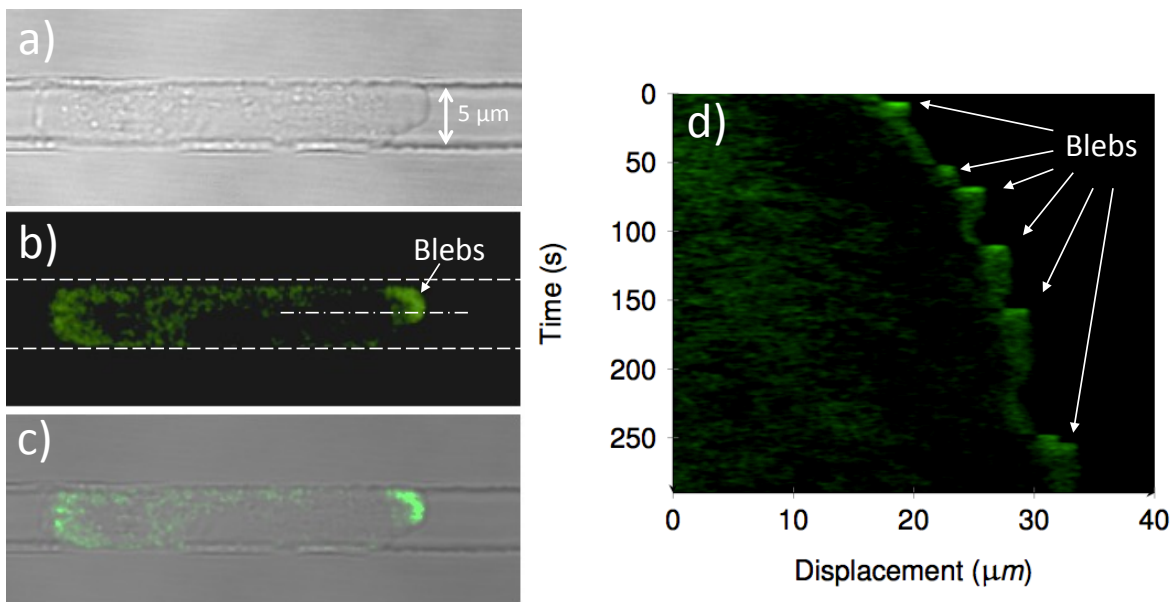


Figure 2.40: Spatial distribution of myoVII in a cell that migrates via blebbing motion in a $5\ \mu\text{m}$ wide, $2\ \mu\text{m}$ high micro-channel. (a) Image from the transmitted light channel of the confocal microscope. (b) Image from the green channel. (c) Overlapping between the transmitted light channel and the green channel. Strong localisation of myoVII can be observed inside blebs, visible on the right-hand side of the cell. (d) Kymograph taken from the dashed line at the leading edge of the cell in (b), myoVII quickly translocates into the blebs as they form.

2.4.5 Focal adhesions

2.4.5.1 Paxillin foci

Paxillin is an adapter protein in focal adhesion sites. Its role has been reported to be important in linking the actin cytoskeleton to cell-substrate adhesion receptors (Giannone et al., 2004; Webb et al., 2004). These structures adhere to the substrate at the leading edge of a migrating cell, maintain their position over time, and are eventually released at the trailing edge. The adhesive function of a *Dictyostelium discoideum* paxillin homologue, PaxB, was first investigated few years ago by Bukharova et al. (2005). Looking at a PaxB-GFP knockin strain I was able to investigate how this protein localises in spatially confined cells. Specifically, the use of a TIRF microscope enabled the observation of small PaxB foci at the ventral region of the cell as shown in Fig. 2.41. Such a spatial distribution resembled that described by Bukharova *et al.* in cells migrating on 2D substrates. The kymographic visualisation of such a focal con-

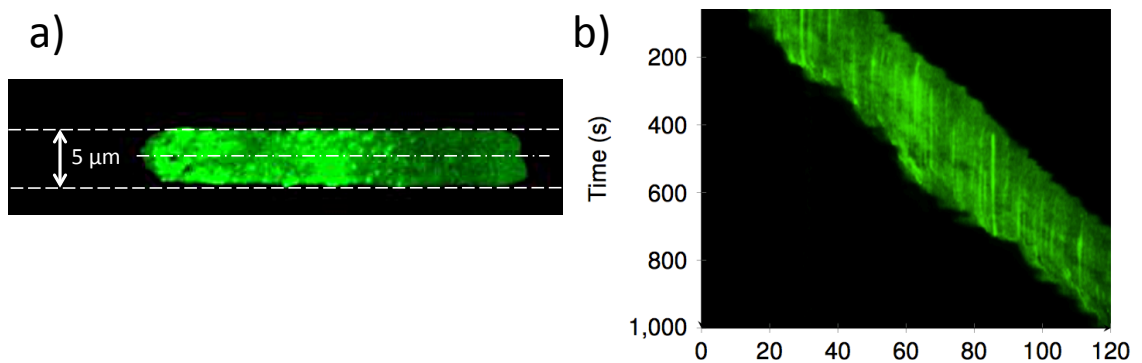


Figure 2.41: Spatial distribution of paxillin foci in a confined cell. The image has been acquired using a TIRF microscope. (a) The cell migrates in a 5 μm wide, 3 μm high channel. The green spots represent PaxB foci. (b) Kymograph from the middle line of the microchannel in (a). The vertical stripes indicate the behaviour of paxillin focal adhesions: they form at the front region, stay stationary during the migration and they are released at the trailing edge.

tacts appeared as vertical stripes, as shown in Fig. 2.41(b). This indicates that they adhere statically at the leading edge and remain active as long as the ventral surface

of the cell is in contact with the substrate. Interestingly, using a confocal microscope, the spatio-temporal distribution of paxillin in the bulk of the cell revealed a difference between pseudopod-like and blebbing modes, as shown in Fig. 2.42. In the first case

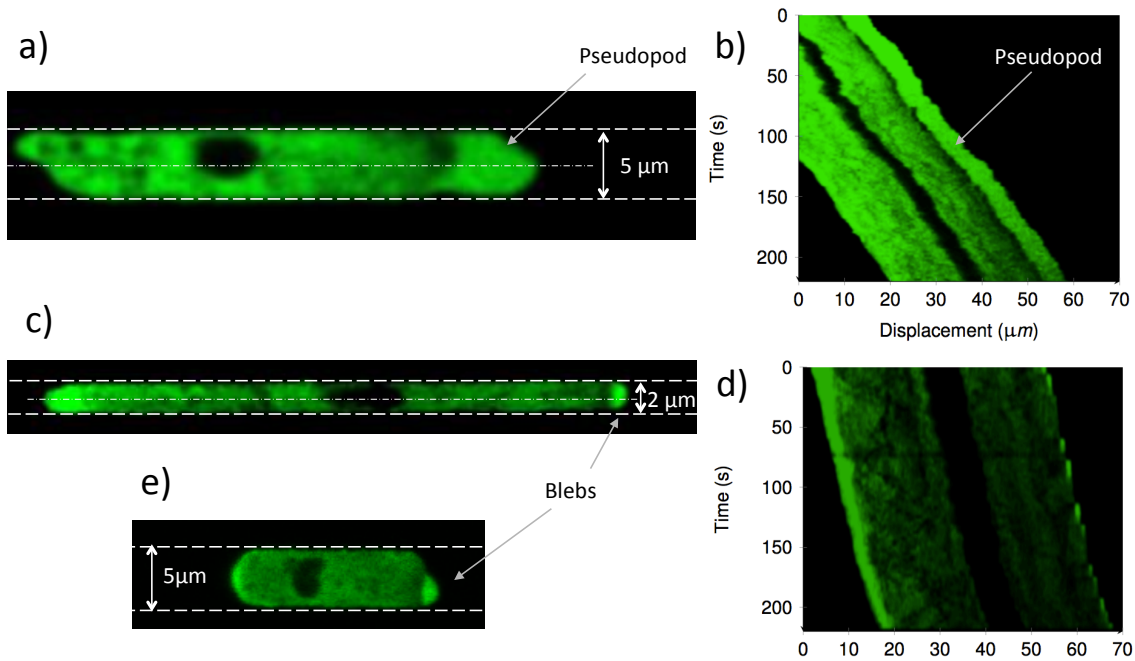


Figure 2.42: Spatial distribution of PaxB in confined cell. The images have been acquired using a confocal microscope. (a) The cell migrates in a 5 μm wide, 2 μm high channel via pseudopodia. PaxB does not enter the the nucleus and is abundant at the leading edge. Interestingly, a small region about 5 μm away from the cell front is almost devoid of PaxB. (b) Kymograph taken from the middle line of the microchannel in (a). (c) A blebbing cell that migrates in a 2 μm by 2 μm channel. PaxB localises at the uropod and into the blebs. (d) Kymograph taken from the middle line of the microchannel in (c), PaxB translocates into the blebs as they form (green spots on the right). (e) PaxB translocates into blebs also in cells migrating in wider channels.

the PaxB was present in the whole cell, apart from the nucleus, and appeared abundant within an area at the front that extended few microns from the leading edge. In addition, a small region about 5 μm away from the cell front devoid of PaxB was present. In the second case paxillin did not constantly localise at the leading edge but instead translocated quickly into the blebs. Furthermore it was also abundant at the uropod.

2.4. RESULTS

To further investigate the role of paxillin in 3D migration, I performed chemotaxis experiments with PaxB knockout mutants (PaxB-null). The deletion of this gene did not lead to any significant change in the cell speed when cell types were confined in 5 μm by 2 μm channels, as shown in Fig. 2.43. Therefore, although the knockout

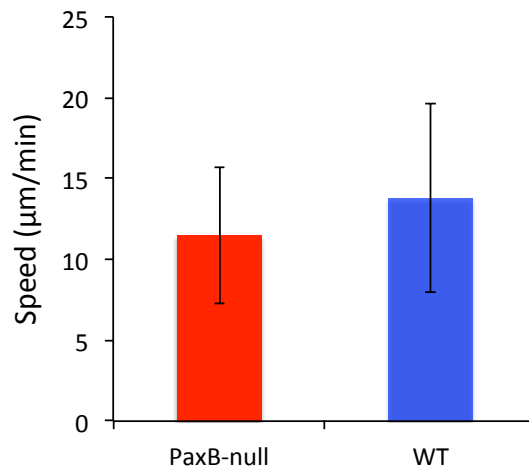


Figure 2.43: Comparison between the main speed of WT ($n = 72$) cells and the PaxB-null mutants ($n = 29$) migrating in 5 μm wide channels. $P = 0.058$.

of PaxB has been reported to induce considerably decreased adhesiveness to various substrates (Bukharova et al., 2005), it has no effect on the cell migration under spatial confinement.

2.4.5.2 Actin foci

Dot-like structures enriched in actin have been observed in Dictyostelium cells (Yumura and Kitanishi-Yumura, 1990). These structures, known as *actin foci*, are believed to be involved in cell adhesions: it has been suggested that they are small areas where F-actin exerts pushing forces to the substrate to generate movement (Uchida and Yumura, 2004; Skoge et al., 2010; Iwadate and Yumura, 2008). Actin foci tend to remain fixed on the substrate as the cells migrate. Combining interference reflection microscopy (IRM) and confocal fluorescence microscopy Uchida and Yumura (2004)

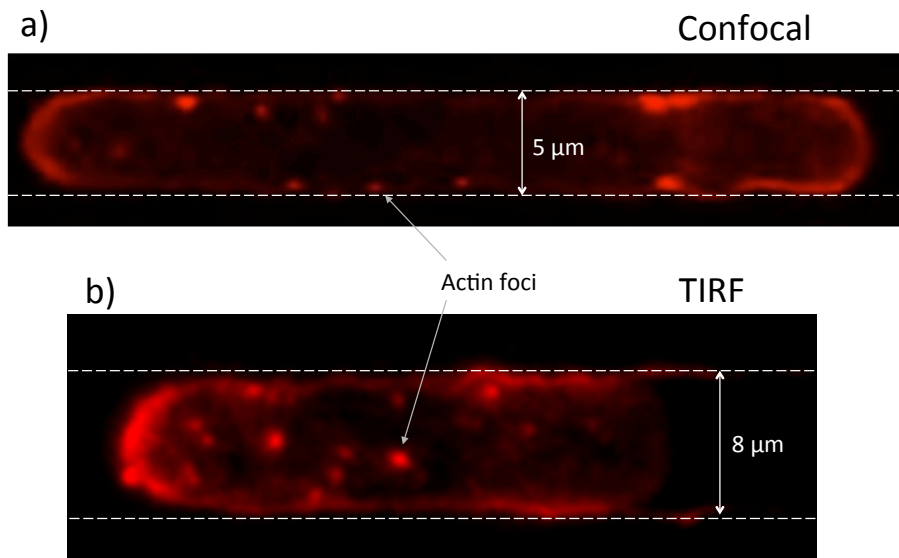


Figure 2.44: Confocal and TIRF images of actin foci. (a) Confocal image of a Dictyostelium cell migrating in a 5 μm by 2 μm channel. (b) TIRF image of a Dictyostelium cell migrating in a 8 μm by 2 μm channel. In this case only the foci in the ventral region are imaged. The cells are F-actin labelled (LifeAct). The red spots represent the actin foci.

showed that the ventral cell membrane is closest to the substratum at the location of an actin focus. Moreover, their averaged duration has been quantified: their lifetime tends to be ~ 20 s (Uchida and Yumura, 2004; Skoge et al., 2010).

A complete picture of how these structures function and their role in cell migration is still missing. It appears that their abundance, in fact, would result in a decreased cell speed (Uchida and Yumura, 2004).

The use of F-actin labelling allowed me to look at the spatial distribution of actin foci in cells under confinement, as shown in Fig. 2.44. By looking at a kymograph of LifeAct labelled cells (in Fig. 2.45), one could observe that actin foci form at the leading edge, maintain the same positions over time and get released at the trailing edge. Interestingly, looking at their vertical alignment, it could be noticed that their occurrence tends to be periodic, as shown in Fig. 2.45. In this case the image sequence was taken using a confocal microscope. The kymograph was reconstructed from a line

2.4. RESULTS

in the proximity of the microchannel's wall. The vertical broken lines in the kymograph correspond to the activation and inactivation of actin foci.

The spatial confinement enabled me to investigate also the temporal behaviour of multiple foci at the same time using the kymograph analysis tool, as they tend to be aligned along the channel's walls in confocal image sequences. To quantify the tem-

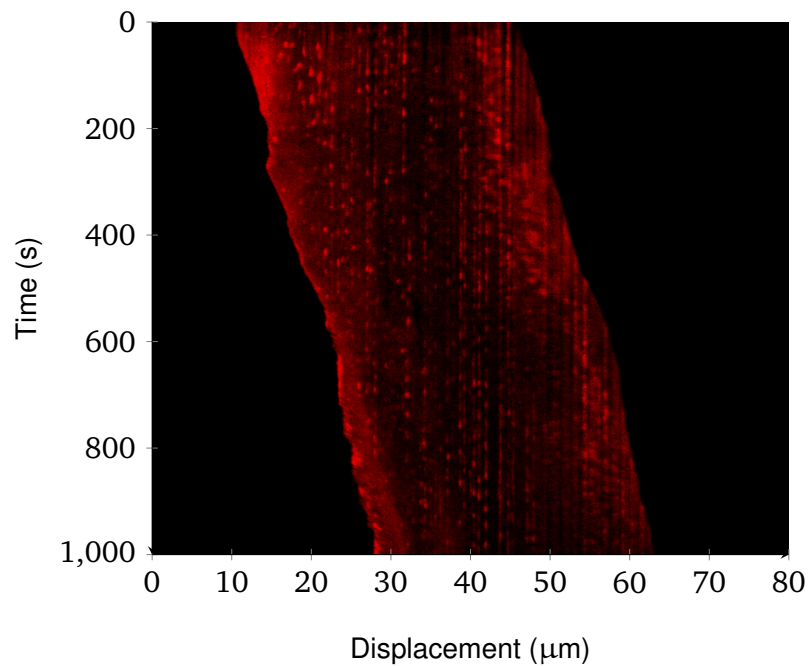


Figure 2.45: Kymograph of a LifeAct-labelled cell. Vertical broken lines indicate the periodic activation of actin foci forming in stationary positions throughout the migration. The kymograph is taken for a section of the cell close to the PDMS wall.

poral evolution of such a structures, from each image sequence I generated a couple of kymographs (one for each wall) from which I extracted the following quantitative information:

- The slope of the trailing edge, that corresponds to the speed of the cell.
- The vertical size of each actin focus, that represents the duration of it.
- The vertical distance between consecutive actin spots, that corresponds to the period of their activation.

I then computed the mean period and the mean duration of the actin foci for different cells. Interestingly, the values of both quantities were always within a certain range. Therefore, I grouped the data from different cells into two separate datasets representing the mean period and the mean duration. The two distributions are shown in Fig. 2.46(a) and Fig. 2.46(b), respectively. The distributions could both be fitted

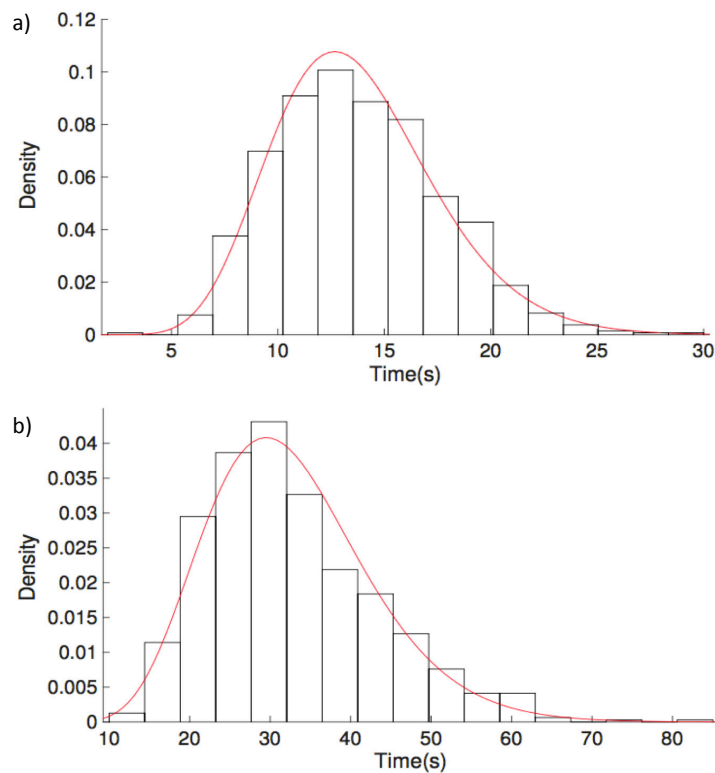


Figure 2.46: (a) Temporal distribution of the foci's duration for 808 foci extrapolated from each wall of 11 distinct migrating cells. (b) Temporal distribution of the foci's period calculated on 717 counts extrapolated from each wall of 11 distinct migrating cells.

using a lognormal distribution. The extrapolated averaged foci duration was about 13.8 ± 4.1 s ($M \pm SD$), whereas their mean period was 32.7 ± 10.7 s ($M \pm SD$).

Another interesting observation came from the relationship between the mean cell speed and the number of foci. In fact, it appeared that cells tended to have a consistent number of foci over time. By plotting the mean migration speed against the

2.4. RESULTS

mean number of foci for 12 cells, it became evident that the two quantities were inversely proportional, as shown in Fig. 2.47. Intriguingly, plotting the mean rate of

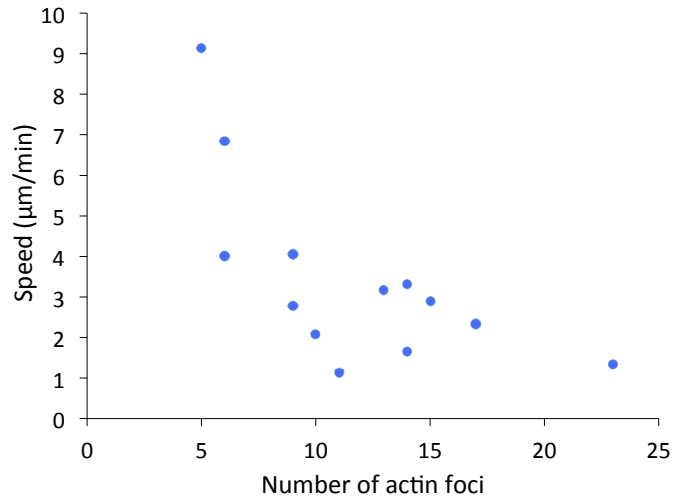


Figure 2.47: Relationship between the mean speed of migration and the mean number of foci for 12 cells analysed in 6 independent experiments.

foci activation (that is the inverse of the mean foci period) against the mean rate of the contractile vacuoles cycles, a linear relationship emerged between the two quantities, as shown in Fig. 2.48. The reason behind this correlation is unknown and would require further investigation. It might suggest the existence of some sort of internal clock regulating different processes inside each individual cell.

2.4.5.3 FRY foci

The Furry (FRY) gene is an evolutionary conserved gene that can be found in many organisms, ranging from yeast to humans (Nagai and Mizuno, 2014). In *Drosophila* the FRY gene is essential for tiling and branching control of sensory neuron dendrites (Emoto et al., 2004) and maintaining the integrity of these cellular extensions during morphogenesis (Cong et al., 2001). Mammalian FRY is a microtubule-binding protein

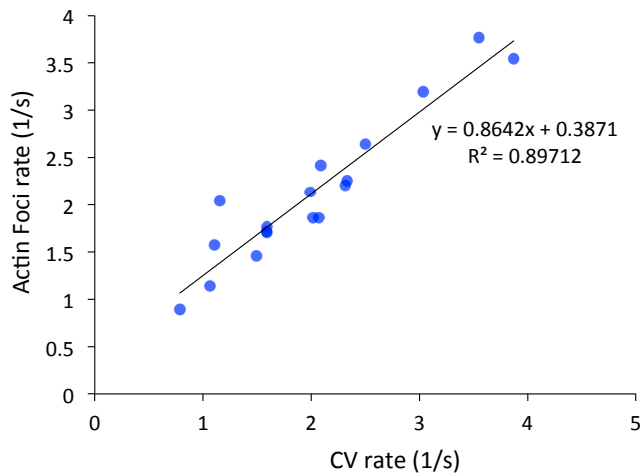


Figure 2.48: Relationship between the rate of actin foci activation and the rate of the contractile vacuole cycles for 18 cells analysed in 13 independent experiments.

and it has recently been shown to be involved in microtubule organisation and stability during mitosis and chromosome alignment (Chiba et al., 2009).

Its function in *Dictyostelium discoideum* is still unknown. In this section I show a few qualitative results that allude to the potential role of this protein in cell migration. By labelling the FRY protein with GFP and observing transfected cells at the TIRF microscope I have been able to observe the localisation of the protein: it is concentrated in spot-like structures and small clusters at the periphery of the ventral surface of the cells, as shown in Fig. 2.49. I hypothesised that FRY foci have a role in forming adhesive sites onto the substrate and at the walls of the channels, similarly to actin foci. To test whether the topology of the environment affected the position of such foci I developed an *ad hoc* microfluidic device where the migration channels had symmetric indentations, as shown in Fig. 2.51. Indeed, the position of the FRY foci was, to some extent, biased by the indentations at the microchannel's walls. The spatio-temporal behaviour of these structures was similar to the paxillin counterpart, with the only

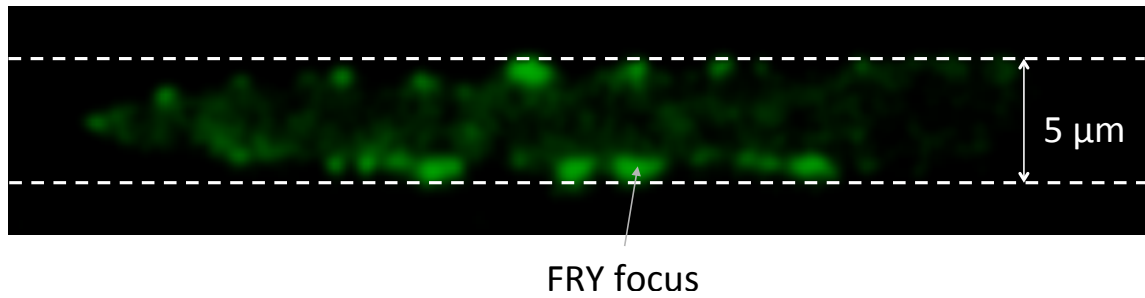


Figure 2.49: Spatial distribution of FRY foci in a FRY-GFP knockin cell migrating in a straight 5 μm wide, 2 μm high channel imaged with a TIRF microscope. FRY foci are spot-like structures at the periphery of the ventral surface of the cell.

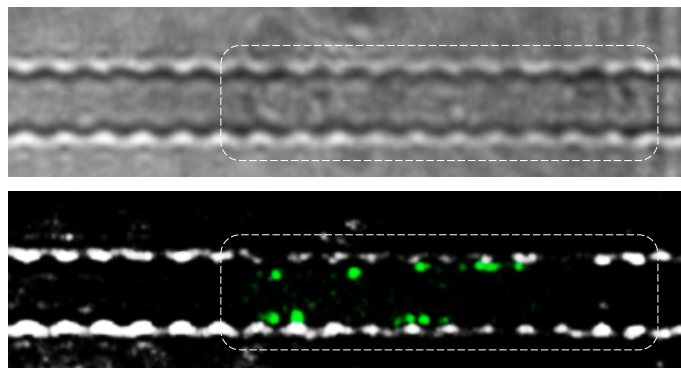


Figure 2.50: Spatial distribution of FRY foci in a FRY-GFP knockin cell migrating in a straight 5 μm wide, 3 μm high indented channel, imaged with a TIRF microscope.

exception that they localise in the proximity of the walls of the channels but not in the ventral region. In addition, the same type of negative correlation between the number of foci and the cell speed (discussed for the case of actin foci) was observed, as shown in Fig. 2.50. The kymograph shows that the cell is completely static when a few FRY foci are active. Successively, the cell appeared to detach from the foci and started moving up the cAMP gradient, whereas the foci maintain their position onto the substrate (green vertical stripes in Fig. 2.51(c)). This qualitative result was observed frequently in my experiments and it would suggest the role of the FRY protein in controlling the 'adhesiveness' of the cell to the substrate, and presumably in the generation and

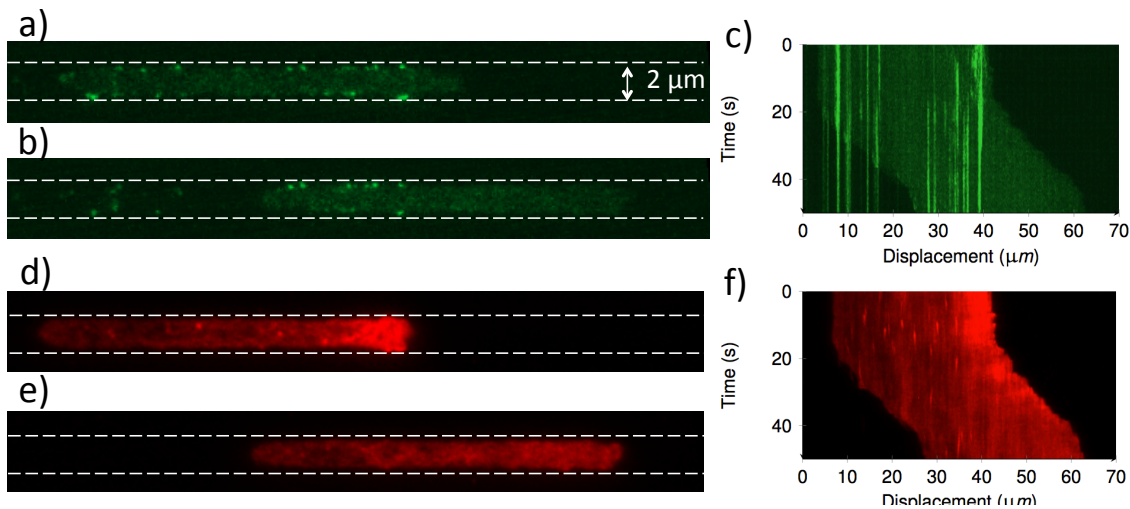


Figure 2.51: Effect of FRY foci on cell speed. (a) Spatial distribution of FRY foci in a cell migrating in a straight 5 μm wide, 3 μm high channel, imaged with a TIRF microscope. (b) The same cell is imaged about 20 s later: the cell appears to detach from the foci and starts migrating up the gradient, while the foci are left behind. (c) Kymograph of the cell taken as maximum intensity projection of all the lateral section of the micro-channel to have all the foci of the cell in the same picture. The vertical stripes indicate that FRY foci form at the front region and stay stationary over time. (c-f) The same cell is also labelled with LifeAct and therefore actin foci are visible. Also in this case the cell do not exhibit foci when migrates, while few of them are active when it is static.

transfer of the forces required to regulate the cell locomotion. To further investigate the adhesive role of this protein I analysed the phenotype of the knocked-out mutant. Interestingly, cells exhibited single or multiple tails enriched in actin as shown in Fig. 2.52. This would suggest a role of FRY in maintaining the integrity of the cytoskeleton at the rear of the cell.

2.4.6 The role of microtubules

Microtubules (MTs) are known to have an important role in the development and maintenance of cell polarity (Etienne-Manneville, 2013). This process is mediated by the interplay among microtubules, actin cytoskeleton, signaling molecules (PI3Ks, PTEN, Rac, Rho, and Cdc42 (Etienne-Manneville, 2013)), and focal adhesions (Waterman-Storer and Salmon, 1999; Rodriguez et al., 2003; Etienne-Manneville, 2013). On the

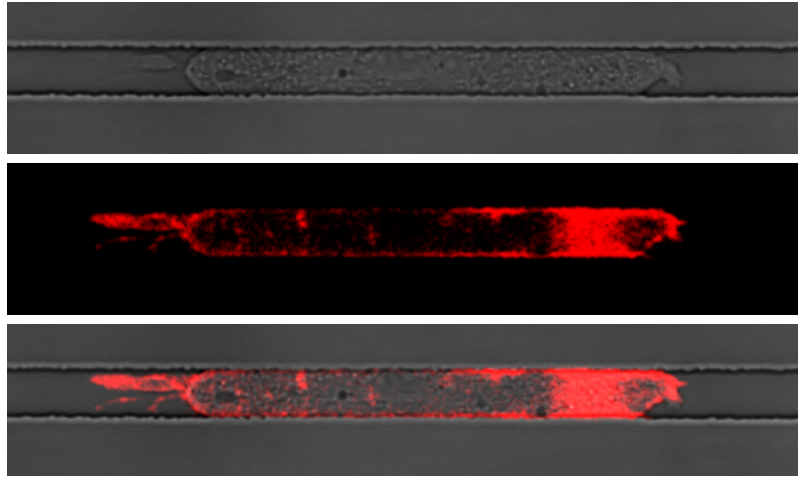


Figure 2.52: Spatial distribution of actin (in red) a in FRY-null cell migrating in a straight 5 μm wide, 2 μm high channel imaged with a confocal microscope. The third image is the composite of bright field and red channel. The pictures show anomalous protrusive and adhesive structures at the uropod.

other hand, due to the inherent complexity of the control circuit that governs cell polarisation, scientists still miss a full mechanistic picture of this process. To investigate how the behaviour of MTs is affected by the spatial confinement I used a *Dictyostelium* strain in which the protein 2471 that targets microtubules was labelled with GFP (see Table 2.3). MTs are very dynamic and long structures spanning the entire cellular body. Once the cell is confined into a microchannel, usually few main bigger MTs depart from the MTOC towards both ends. They tend to be aligned along the direction of motion, as shown in Fig. 2.53. As the cross section of the channel decreases, the number of MTs appears diminished as depicted in Fig. 2.53(b). MTs are all connected to the MTOC that corresponds, in most of the cases, to the centre of mass of the cell. The MTOC is always linked to the nucleus, as shown in the two examples in Fig. 2.53 where two cells are confined in a 5 μm by 2 μm and in a 2 μm by 2 μm channels, respectively. Moreover by looking at 27 different cells I observed that 74% of them exhibited anterior orientation of the Nuclear-Centrosomal (NC) axis (as shown in Fig.

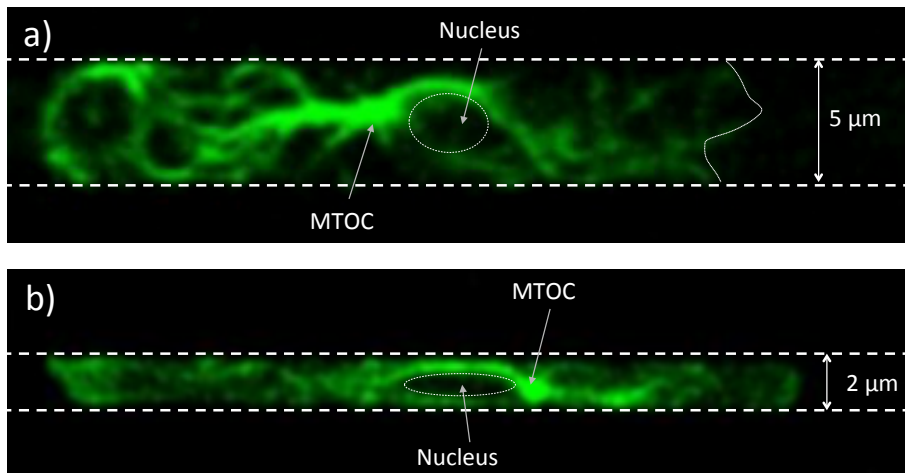


Figure 2.53: Microtubules dynamics in spatially confined cells. (a) MT dynamics in a cell confined in a $5\ \mu\text{m}$ by $2\ \mu\text{m}$ channel. In this case NC axis is in the posterior arrangement (the centrosome is between the nucleus and the uropod), most of the MT are localised at the back of the cell. (b) MT dynamics in a cell confined in a $2\ \mu\text{m}$ by $2\ \mu\text{m}$ channel. The NC axis is anterior and the number of MT is noticeably smaller than in (a).

2.54), meaning that the centrosome was localised between the leading edge and the nucleus.

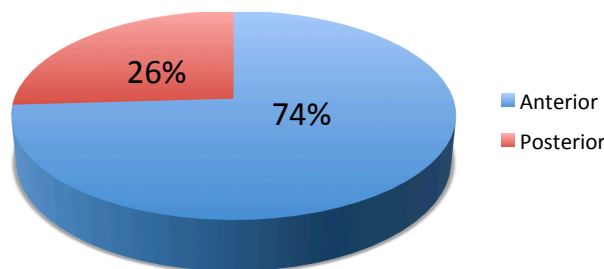


Figure 2.54: Nuclear-Centrosomal (NC) axis in *Dictyostelium* cells migrating in 3D environment. $N = 27$. In the 74% of the cases the orientation cell show an anterior orientation, meaning that the centrosome localises between the nucleus and the leading edge.

2.4.6.1 Interaction between microtubules and actin foci

While performing TIRF imaging using cell with both MTs and actin labelled I observed that, in many cases, actin foci were forming in the vicinity of MTs. This qualitative observation can be seen in the representative example shown in Fig. 2.55. Here the LifeAct has been re-coloured in magenta for clarity. It is important to note that, in this

2.4. RESULTS

case, the visible MTs are close to the cell membrane in the ventral region. Interestingly, most of the actin foci appeared positioned between the MTs and the glass cover slip. This observation would generalise the interaction between these two structures. In fact, the link would not be only at the growing end of the MTs, as explained in the introduction of this chapter, but also along their length.

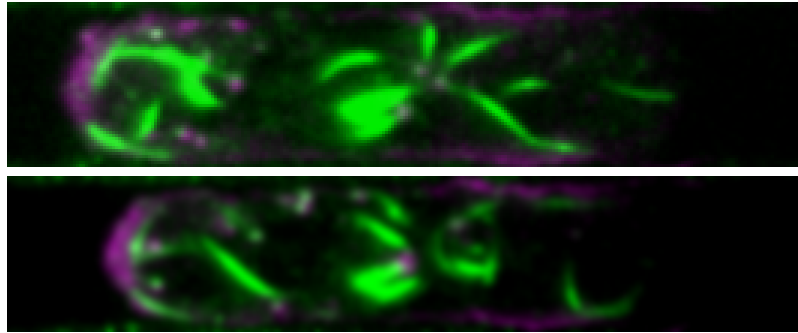


Figure 2.55: Colocalisation of actin foci and MTs. Sequential TIRF pictures of a cell migrating cell confined in 8 μm by 2 μm channels. The microtubules (green) and actin (magenta) have been labelled with GFP and LifeAct, respectively. The two figures show the overlap between the two TIRF channels. The red channel has been converted into magenta for clarity.

2.5 Discussion

In this chapter I showed how cell velocity depends on spatial confinement. More specifically, I found that speed tends to decrease by decreasing the cross section of the migration channels. The motivation behind the choice of the size of the migration channels was associated with the aim of confining *Dictyostelium* cells in environments with only one spatial degree of freedom in order to simplifying the complex three-dimensional motion of migrating cells. To do this I decided to set the height of the channel to 2 μm that is in the range of the average diameter of the nucleus in *Dictyostelium discoideum*, that is known to be 2-3 μm (Rachel et al., 2010; Stevense et al., 2011). A range of widths was then tested. It turned out that a width greater than 8 μm was not sufficient to laterally confine cells. Notably, the data shown in Fig. 2.19 suggest that, on average, the cell speed is significantly different only in the case of 2 μm wide channels. This was further investigated using tapered channels that enabled me to study the effect of a progressively decreasing width (from 5 to 2 μm) on each individual cells rather than comparing averaged information from different cells migrating in channels with different cross section. The fact that each cell tended to decelerate across a tapered channel, together with the results shown in Fig. 2.19 suggest that the nucleus might play an important role in limiting the cell speed as the channel cross section approaches the size of the nucleus. This result is quite unexpected for soft objects like cells that crawl actively into a channel, as they should adapt to surrounding environment. One explanation could be that the nucleus, that is the stiffest cellular organelle (Guilak et al., 2000; Hu et al., 2005; Dahl et al., 2008),

2.5. DISCUSSION

behaves as a load that slides against the walls of the channel, the substrate and the ceiling, generating a friction force. In addition, cells are able to maintain their nucleus in the proximity of the centre of mass thanks to microtubules-related centring mechanisms (Etienne-Manneville, 2013). The net result is that instead of observing the nucleus displaced towards the uropod as a consequence of the friction, the entire cell decelerates uniformly as it moves along the progressively narrower channel.

The inhibition of myoII resulted in a defective cell contractility. This induced a slower migration of these mutants with respect to WT cells, consistently with previous studies on Dictyostelium cells moving in 2D under-agar assays (Jay et al., 1995; Uchida, 2003). A complete failure in migration was observed by using microchannels with 2 μm high ceiling. In fact, myoII-null cells tended to stop their *taxis* at the entrance of the microchannels. Again, this observation could be ascribed to the rigidity of the nucleus and suggests that myoII might be involved in mediating nuclear deformations. The existence of two different migration modes was demonstrated in Dictyostelium cells migrating in a 3D environment: an actin-independent blebbing motion, and an actin-based pseudopod motion. I did not observe any blebbing motion in the case of myoII-null cells, confirming the importance of myoII in the generation of blebs, already shown in previous studies conducted in 2D environments (Langridge and Kay, 2006; Traynor and Kay, 2007). Although the cause of the occurrence of these migration modes is not fully understood, I showed that the blebbing motion appears to be associated with a higher degree of confinement. The reason behind this could be that, in confined environments, an increased amount of F-actin is required in the vicinity of the walls of the channel to resist the mechanical constriction. This could

also explain why I observed an altered distribution of F-actin in cells confined in wider channels compared to that exhibited in narrower ones. Similar results have been reported for cancer cells of higher organisms: cells that undergo a transition into an amoeboid mode of migration in 3D collagen matrix show reduced accumulation of F-actin at the cell front (Friedl and Wolf, 2003). Moreover, such reduced abundance of F-actin at the leading edge could trigger the formation of blebs. One of the functions of the F-actin at the leading edge might be to counteract the hydrostatic pressure generated by the myoII-induced contraction of the cortex at the uropod. Therefore, if the amount of actin at front is lower than a certain level, this might lead to an increased probability to generate a bleb. This would explain why the two modes appeared to be mutually exclusive. This idea is supported by the observation by Langridge and Kay (2006), according to which mutants with a partially inactivated Arp2/3 complex exhibit a large increase in blebbing. In the same article the authors suggested that bleb formation is not enhanced by actin, but is actually inhibited by it. Another possible scenario could see blebs and pseudopodia as strongly correlated entities, which interplay continuously in open space or in 2D (Tyson et al., 2014) and the spatial constriction would 'select' the most efficient mode for each cell, depending on the relative amount of F-actin present at the leading edge. In addition, I found that cells that exhibit a bigger polymerisation zone at the leading edge tend to migrate faster (Fig. 2.38). As the polymerisation area decreases, the cell velocity diminishes proportionally and, at the same time, the probability that the cells adopt a blebbing motion increases (Fig. 2.36). Taken together these two results help explaining the causes of the slower migration exhibited by blebbing cells, that I have observed for the first time in *Dictyostelium* mi-

2.5. DISCUSSION

grating in microchannels (shown in Fig. 2.29). Interestingly, the correlation between the cell speed and the size of the polymerisation zone is consistent with the results of a previous study on lamellipodial fragments from fish epithelial keratocytes (Ofer et al., 2011). These simplified models are very interesting systems as they lack a cell body, microtubules, nucleus and most organelles but retain migratory capacity. The authors found that faster migration correlated with larger front-to-rear length of the lamellipodial fragment. These systems tend to migrate without changing their shape, speed and direction for many minutes (Ofer et al., 2011) and therefore are, in many ways, comparable with *Dictyostelium* cells migrating under spatial confinement.

I found that multiple proteins translocate into blebs at the early stage of their growth: myoVII, VatM and PaxB. The latter exhibited a longer lifetime into the bleb. This could presumably suggest a distinct role of these proteins at different stages of the bleb generation, which requires further investigations. Potential interactions among these proteins could also take place. Another possibility is that these proteins were, to some extent, present in a diffusible form and they would be passively pushed into the bleb by the intracellular flow responsible for the initiation stage of the bleb generation. Looking at cells expressing VatM-GFP, I noticed that small vesicles moved towards the leading edge and quickly translocated into the blebs. This could presumably be a consequence of the fusion of these vesicles to the plasma membrane at the leading edge, accounting for the membrane source required by such impulsive protrusions.

I investigated the role of PaxB, as well as actin foci and FRY foci as adhesion proteins. I characterised their spatio-temporal distribution, enlightened their differences and analogies. Using TIRF and confocal microscopy I was able to show that actin and

PaxB foci tend to form at the interface with the glass substrate but also in the proximity of the walls of the micro-channels. PaxB foci are stationary structures, whereas the actin foci have the tendency to activate in a periodic way with a period of ~ 30 s. Moreover, a negative correlation between the cell average speed and the number of actin foci. This result is consistent with the relationship between instantaneous velocity and instantaneous number of foci reported few years ago by Uchida and Yumura (2004). Similar results have also been recently shown for Dictyostelium cells migrating in microchannels in the absence of a chemoattractant (Nagel et al., 2014). Intriguingly, I observed a similar periodicity in contractile vacuoles and I found that a linear relationship exists between the rate at which actin foci activates and the rate at which CVs cycle. FRY foci behave similarly to PaxB foci, with the only difference being that FRY foci are not present in the ventral region of the cell but only at the edge, in the proximity of the walls of the channel in which they migrate. Also, the number of FRY foci appeared to negatively correlate with cells' average speed similarly to the case of actin foci. This suggests that FRY might mediate cell-substrate adhesions. Furthermore, confocal images of PaxB-GFP labelled cells showed an interesting dynamics and localisation of this protein depending on the migration mode: it localised at the leading edge of cells moving by pseudopodia and at the uropod of blebbing cells. In addition, I found that cell speed was not altered by deletion of PaxB and therefore this protein might be dispensable in the case of migration in 3D environments.

Finally, the role of microtubules was assessed. They appeared to decrease in number when the cross section of the microchannel was decreased. The centrosome showed the tendency to localise between the nucleus and the leading edge of the cell as it has

2.5. DISCUSSION

been shown in 2D migration (Sameshima et al., 1988). Looking at the dynamics of MTs with a TIRF microscope, I observed a close proximity of ventral MTs to actin foci. This would suggest a interaction between the two structures.

Interestingly, the velocity of confined cells was essentially constant over time, in most instances. This characteristic seems to be associated with two properties: cellular protrusions tend to occur periodically, and actin continuously polymerise at the leading edge. The latter is also true in the case of blebbing cells, where the polymerisation is only interrupted by the formation of blebs. On the other hand, a big variability in the cells' mean velocity was observed. This cell-to-cell variability can be explained as the result of multiple characteristics of an individual cell: its protrusion rate, the amount of actin at its leading edge, the mean number of actin and FRY foci.

A pivotal cellular mechanism to maintain cell functions is volume regulation (Lang, 2007; Hoffmann et al., 2009). In fact, cells can maintain their volume constant over time thanks to rapid ion exchange through transport systems and channels across the cell membrane (Lang, F; Busch, G L; Völkl, 1998). Therefore, assuming volume constancy, a cell that moved from a given microchannel to another of smaller cross section would experience an increase in its surface area. The portion of cell membrane in contact with the substrate, the walls and the ceiling of the channel would increase too. As a consequence, the number of focal adhesion the cell forms would tend to increase. Hence, considering that the average speed of a cell tends to be negatively correlated to the number of focal adhesion (as shown for both shown actin and FRY foci), the reduction in channel dimensionality would contribute to the observed decrease in cell speed.

Dictyostelium cells have been reported to exhibit sensitivity to thermal gradients (*Thermotaxis*) only at the level of cellular aggregates and not at the single cell level (Bonner et al., 1989; Flegel et al., 2011). Moreover, this collective behaviour has been explained as a consequence of the response of individual cells to local changes in chemical gradients across the slugs. Specifically, the amount of ammonia (NH₃) produced by the cells that compose the slug is proportional to temperature (Bonner et al., 1989). Therefore, temperature gradients within the slug induce local differences in NH₃ production. Ammonia was reported to affect the cAMP signalling (Schindler and Sussman, 1979) by inhibiting the cAMP-induced cAMP release. In fact, NH₃ inhibits the transitory activation of adenylate cyclase and therefore blocks the intracellular cAMP accumulation (Williams et al., 1984; Davies et al., 1993). In light of these considerations thermal effects were neglected in the present study.

It is noteworthy that in the presented data, some cells were omitted from the analysis, as they behaved very differently from the average. For instance, some cells migrated particularly slowly, this could be associated with singular environmental conditions or local phenomena. In fact, cells could be locally exposed to residues of the ethanol used for cleaning the system before each measurement. It has also been shown that PDMS absorbs small molecules, and this could alter its local composition (Toepke and Beebe, 2006). Un-crosslinked PDMS and other species leaching from it could potentially be toxic (Lee et al., 2004). All these aspects might lead to alteration of the physiological state of cells, or even to their death. In some instances I observed a sudden disruption of the cell membrane, the nature of this phenomenon is still unknown although it seems diminished by pre-treating the microchannels with bovine

2.5. DISCUSSION

serum albumin (BSA). Reversal of the migration direction has also been observed. This phenomenon could be likely due to competing cAMP signals occurring in the case of multiple cells in a channel.

It is important to note that in this chapter the term '*periodic*' has been used in the sense of '*repetitive pattern*', as in the previous literature of cell motility (Dormann and Weijer, 2001; Giannone et al., 2004; Vicker and Grutsch, 2008; Maugis et al., 2010). In fact, biological phenomena are characterised by numerous complex interactions among networks (e.g. metabolic pathways, gene regulation networks, signal transduction networks, etc.). Therefore, biological temporal data typically contain multiple harmonics with different periods (Tominaga, 2010). Hence, the rigorous mathematical notion of '*periodicity*' fails describing these phenomena. The concept of '*bioperiodicity*' (or '*near periodicity*') has been introduced instead, where the constrictive notion of periodic functions has been replaced by the concept of '*repetitive patterns*' (SMETS and Bartholomay, 1971).

CELL MIGRATION IN BIFURCATING MICROCHANNELS

3.1 Introduction

As discussed in the previous chapter, directional migration is commonly described as a *random walk* biased by the presence of an external cue, that in the case of chemotaxis is a chemical signal. Although this is valid for cell migration on a substrate or in 2D, I demonstrated that cells that migrate in confined environments do not exhibit randomness in their locomotion speed, which, instead, tends to be constant over time. Moreover, it has also been shown that some cell types can effectively navigate through complex environments *in vivo* (Mathias et al., 2009) as well as maze-like microfluidic networks (Scherber et al., 2012). Human neutrophils enclosed in asymmetric bifurcating channels have been shown to 'choose' the shorter path in over 90% of the cases (Ambravaneswaran et al., 2010). These observations were explained in the context of chemotaxis, where a shorter path would simply corresponds to a steeper chemical gra-

dient. Thus, the directional decision-making would be a consequence of asymmetric chemical gradients within the microenvironment.

More recently, Prentice-Mott et al. (2013) showed that neutrophil-like HL60 cells could also be able to interpret differences in hydraulic resistance, and the authors defined such a novel type of cellular response as '*barotaxis*'. Here I summarise the main findings reported in the article:

1. The cross section of the microchannels was small enough that cells were able to occupy the entire cross section and push the liquid as they migrated.
2. Cells did not show directional bias when exposed to symmetric bifurcating microchannel.
3. When cells encountered asymmetric bifurcations, where one arm was four times longer than the other, cells exhibited a strong bias towards the shorter path (about 75% of the time). Furthermore, this behaviour was independent of the presence of a chemoattractant gradient across the channel. In addition, the extension of two pseudopods, and the competition between them appeared to be essential to bias the directional choice.
4. By keeping the length of the two arms constant and reducing the width of one arm, a four-fold increase in its hydraulic resistance was achieved. About 75% of cells migrated towards the arm with lower resistance.
5. When the ratio between the hydraulic resistance of the two arms was eight, about 80% of the cells migrated into the branch with lower-resistance and the percentage grew to 90% when the ratio was 32.
6. Cells exhibited actin localisation of at the leading edges of both bifurcating pseu-

3.1. INTRODUCTION

dopodia but no correlation was found between the chemical polarisation and the direction chosen by the cells.

7. If loaded into channels where one arm of the bifurcation was a dead-end channel, cells still extended two pseudopodia, but the pseudopod along the dead-end arm protruded for a short distance and 98% of the cells migrated towards the open arm.
8. To test the competition between the chemical and the mechanical cues a photoactivatable chemokine was locally activated into the dead-end arm of asymmetric bifurcations: 70% of the cells migrated into the open arm despite exhibiting strong chemical polarisation toward the dead-end side. The other 30% entered the dead-end channels.

Taken together these observations suggested that cells confined in bifurcating microchannels were able to recognise the path of lower hydraulic resistance and that this response could override the chemical one.

The hydraulic, or hydrodynamic resistance, is defined by the Hagen-Poiseuille law, as the proportionality factor ratio between the pressure drop ΔP and the flow rate Q (Bruus, 2008):

$$\Delta P = R_h Q . \quad (3.1)$$

This formula can be considered the hydrodynamic analogous to Ohm's law, $\Delta V = R I$, which relates the current I through a wire to the voltage drop ΔV along the wire (Bruus, 2008). The hydraulic pressure originates from the fact that, under strong confinement, migrating cells seal the channel and therefore they are able to displace the column of fluid downstream of them. According to Prentice-Mott et al. (2013) the

'decisional' process consists of two phases :

- Generation of two pseudopods, one in each arm of the bifurcation.
- Retraction of the 'losing' pseudopod.

The directional choice appears to be biased by the speed at which the leading edge is protruded inside the two arms of the bifurcation (Prentice-Mott et al., 2013). Specifically, lower hydraulic resistance results in faster protrusions.

Although a mechanistic description of this phenomenon is still absent it has been proposed that microtubules might play a role in the decision-making, functioning as mechanical sensors (Ambravaneswaran et al., 2010). In this model the dynamically unstable MTs would help balancing the mechanical load at the leading edge of the bifurcating pseudopodia. In vitro experiments have shown that MTs dynamic instability can be biased by an applied load (Putnam et al., 2001). In a bundle of MTs, the failure of a small group of them would induce the entire bundle to depolymerise due to the redistribution of the load on a diminished number of MTs (Putnam et al., 2001). On the other hand, the effect of MTs in the directional bias has not been directly tested, for instance, by inhibiting or stabilising MTs.

3.2 Aims and Objectives

In the work presented in this chapter I aimed:

1. To test whether the 'barotactic' response were present also in the ancient eukaryote *Dictyostelium discoideum*. Additionally I sought to investigate the possible presence of a 'directional memory' that could bias successive choices.
2. To explore the role of microtubules (MTs) and actomyosin cytoskeleton in the decisional process.
3. To decouple the effect of the chemical gradient from that of the hydraulic resistance.

3.3 Methods

3.3.1 Development of the migration chip

3.3.1.1 Testing cellular response to hydraulic resistance

The migration device was developed using the microfabrication process described in the first chapter. It has the same structure as the chip used in the previous chapter with the only difference that the migration channels harbour multiple bifurcations of the following types:

1. Symmetric bifurcation.
2. Asymmetric bifurcation where one arm has three times higher hydraulic resistance than the other.
3. Asymmetric bifurcation where one arm has eight times higher hydraulic resistance than the other.

The different bifurcation types are similar to those presented by Prentice-Mott et al. (2013), and are shown in Fig. 3.1. These structures have been designed following the definition of hydraulic resistance for a channel with rectangular cross section:

$$R_h = \frac{12\mu L}{wh^3 \left(1 - 0.63 \frac{h}{w}\right)}, \quad (3.2)$$

where w is the width of the channel, L is its length, h is its height and μ is the fluid dynamic viscosity (Bruus, 2008). The height of the migration channels is $3 \mu\text{m}$. The width of the straight region is $4 \mu\text{m}$, whereas the width and the length of the bifurcating arms depends on the hydraulic resistance of the specific path as shown in Fig. 3.1.

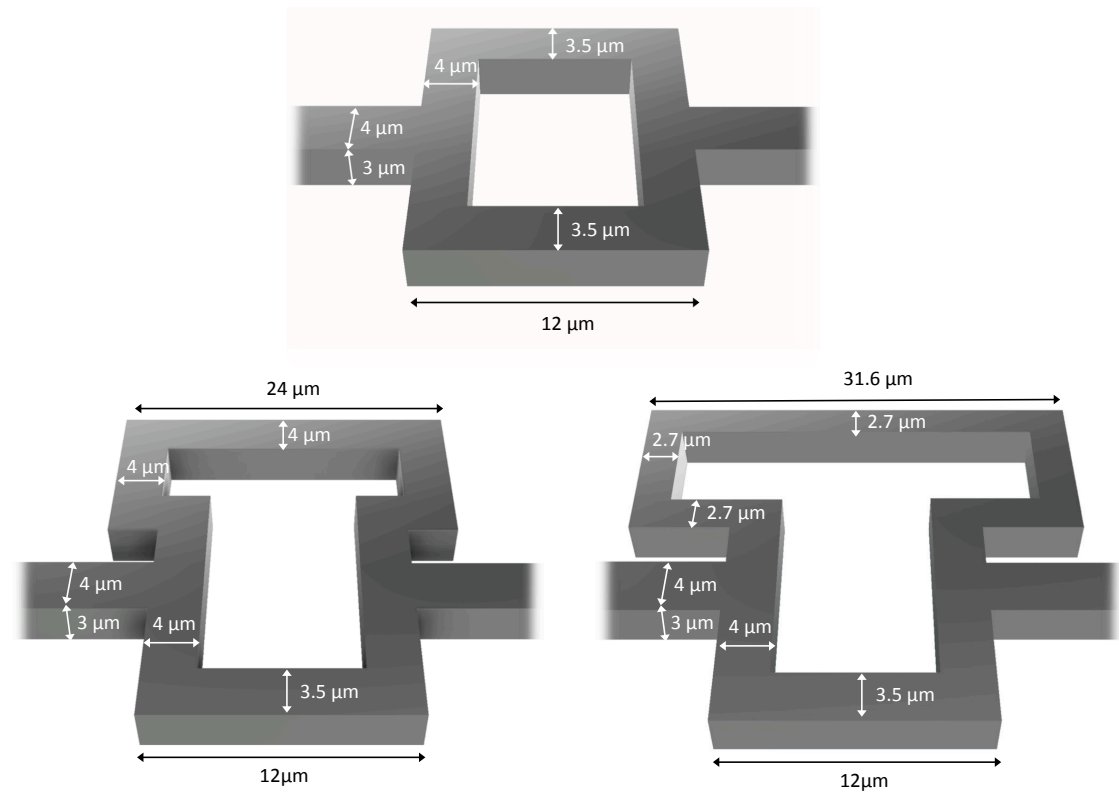


Figure 3.1: Schematics of the three types bifurcation used in the experiments. (a) The two arms have the same hydraulic resistance. (b) The longer arm has a hydraulic resistance about three times higher than that of the other arm. (c) The longer arm has a hydraulic resistance about eight times higher than that of the other arm.

3.3.1.2 Decoupling hydraulic resistance from chemical gradient

To further investigate the role of the hydraulic resistance in the cellular 'decisional process' I designed a novel type of migration channel able to decouple the effect of the chemical gradient from that of the hydraulic resistance. Such of topology, shown in Fig. 3.2, is characterised by a single asymmetric bifurcation from where:

- A narrow channel connects the bifurcation with the right-hand loading channel.
- A wider and longer channel that connects the bifurcation directly to the cell loading channel.

The two arms were designed so that the narrower channel had hundred times higher

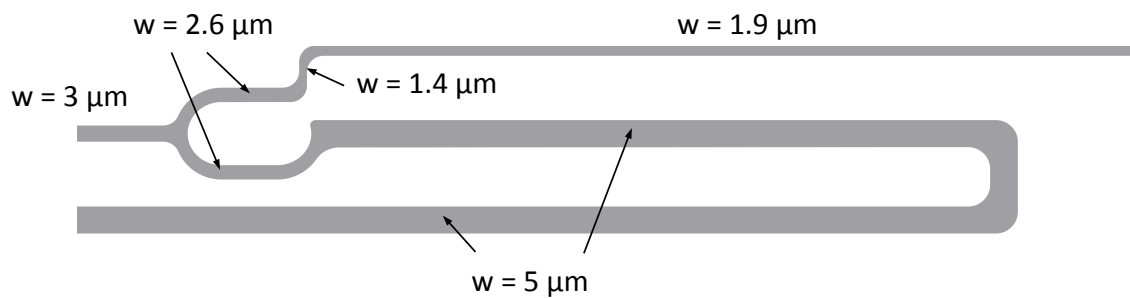


Figure 3.2: Decoupling chemical and mechanical cues. a) Novel topology characterised by a single asymmetric bifurcation. The narrower arm joins the cAMP loading channel (on the right hand side, not visible), whereas the wider and longer channel goes back into the cell loading channel. Cells can therefore either migrate up the chemical gradient or towards the wider channel, where the hydraulic resistance is hundred times lower compared to the narrower arm.

hydraulic resistance than the wider and longer channel. In addition, at the bifurcation, a cell would experience a positive gradient towards the narrow channel, that is connected to the cAMP source, and a negative chemical gradient towards the wider channel. In this way a cell can therefore either migrate up the chemical gradient or towards the wider channel, where the hydraulic resistance is hundred times lower compared to the narrower arm.

3.3.2 Growth and development of *Dictyostelium* cells

Dictyostelium discoideum wild-type cells (Strain Ax2) were grown in shaken cultures in HL-5 medium using glass flasks, at room temperature (22°C). Certomat R moving platform at 155 rpm was used. When their concentration reached 4×10^6 cells/mL they were harvested by centrifugation (1800rpm for 2 minutes) and resuspended in KK2 buffer twice to the concentration of 1×10^7 cells/mL. Cells are consequently starved by pulsation of cAMP for 4.5 hours (45 doses of 0.02 mL are delivered, time interval 360 s) using a 505Di pump (Watson-Marlow Pumps Limited). Once starved cells were harvested by centrifugation (1800 rpm for 2 minutes) and resuspended in

KK2 buffer twice to the concentration of 2×10^7 cells/mL. The actin cytoskeleton and myosin-II were observed using the LifeAct peptide fused with RFP (Riedl et al., 2010) and GFP-tagged myosin-II.

3.3.3 Nocodazole treatment

To test the effect of MTs on barotaxis, Nocodazole was added to the cell solution to a final concentration of 5 μ M for 30 minutes (Ueda and Ogihara, 1994) prior to be loaded into the microfluidic chip.

3.3.4 Cell loading, microscopy and data analysis

Each migration channel is composed by a symmetric bifurcation followed by a set of two identical bifurcations of the second or third type as shown in Fig. 3.3. The motivation of this arrangement was to test whether cells possessed a 'directional memory'. The two ends of the migration channels are connected to bigger loading channels as in Fig. 2.8. Cells and chemoattractant were introduced into the microfluidic device as in Chapter 2. To investigate the competition between the chemotactic and barotactic responses I imposed a linear gradient of cAMP along the migration channel by introducing solutions of cAMP with different concentrations in the loading channel:

1. Conventional cAMP 1 μ M.
2. Conventional cAMP 100 μ M.
3. Non degradable homologue cAMPs 100 μ M.

The choice of the concentration 100 μ M was associated with the fact that a minimum cAMP concentration of 10 μ M is required to saturate the CAR1 receptors at the leading edge of the cell (Brzostowski and Kimmel, 2006; Bagorda et al., 2009). The introduc-

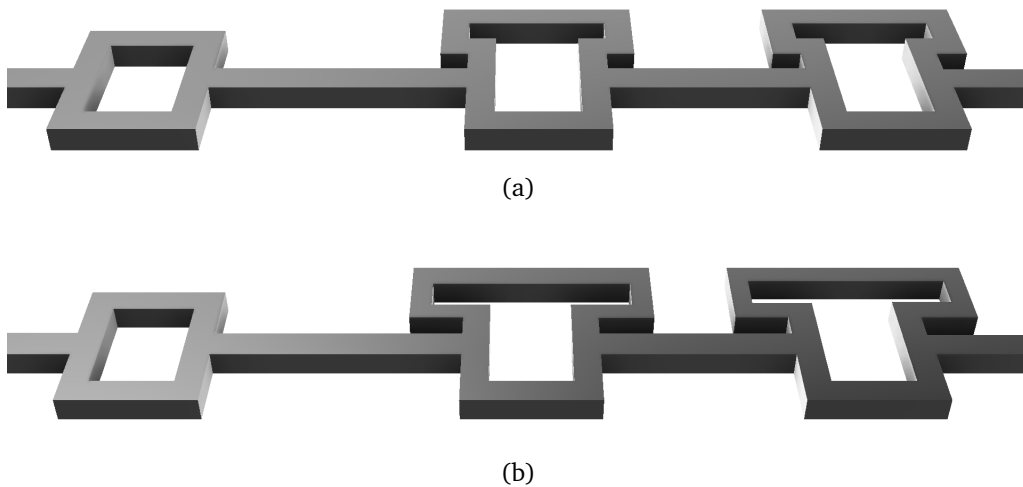


Figure 3.3: Schematics of the bifurcating channels. They are designed so that cells can travel from the left to the right. In both cases at the first bifurcation (on the left) the two arms are symmetric, whereas at the following bifurcations one arm has a higher hydraulic resistance than the other. (a) The longer arms have about three times higher hydraulic resistance than that of the other arm. (b) The longer arms has a hydraulic resistance about eight times higher than that of the other arm. The two ends of these channels are connected to the bigger loading channels (not visible).

tion of a $100 \mu\text{M}$ chemoattractant solution into the loading channel guaranteed that at all the bifurcations the concentration was always above $10 \mu\text{M}$ as shown in Fig. 3.4. The picture describes the distribution of cAMP (and cAMPs) along the migration channel estimated by solving the 2D diffusion equation for the actual geometry using Comsol for a concentration of $100 \mu\text{M}$. The concentration at the first bifurcation is about $19 \mu\text{M}$ and therefore higher than the saturation concentration. At the following bifurcations, the chemical concentration between the two arms differs, due to the asymmetric paths. On the other hand, the concentration is always higher than the saturation concentration and hence the cells that reach the bifurcation should not be able to detect the difference in cAMP concentration between the two arms. Therefore the 'directional decision' should be made purely on the difference in local hydraulic pressure. Conversely, using a concentration of $1 \mu\text{M}$ would open the possibility that

3.3. METHODS

cells sensed the arm with higher concentration of chemoattractant and made a choice based on the chemical cue. Even at high concentrations it is still possible that cells are able to degrade cAMP at a rate that is comparable with the time scale of the decision-making process. Therefore the use of cAMPs would account for the cell degradation. The cell motion was recorded at room temperature on a Leica SP2 AOBs confocal

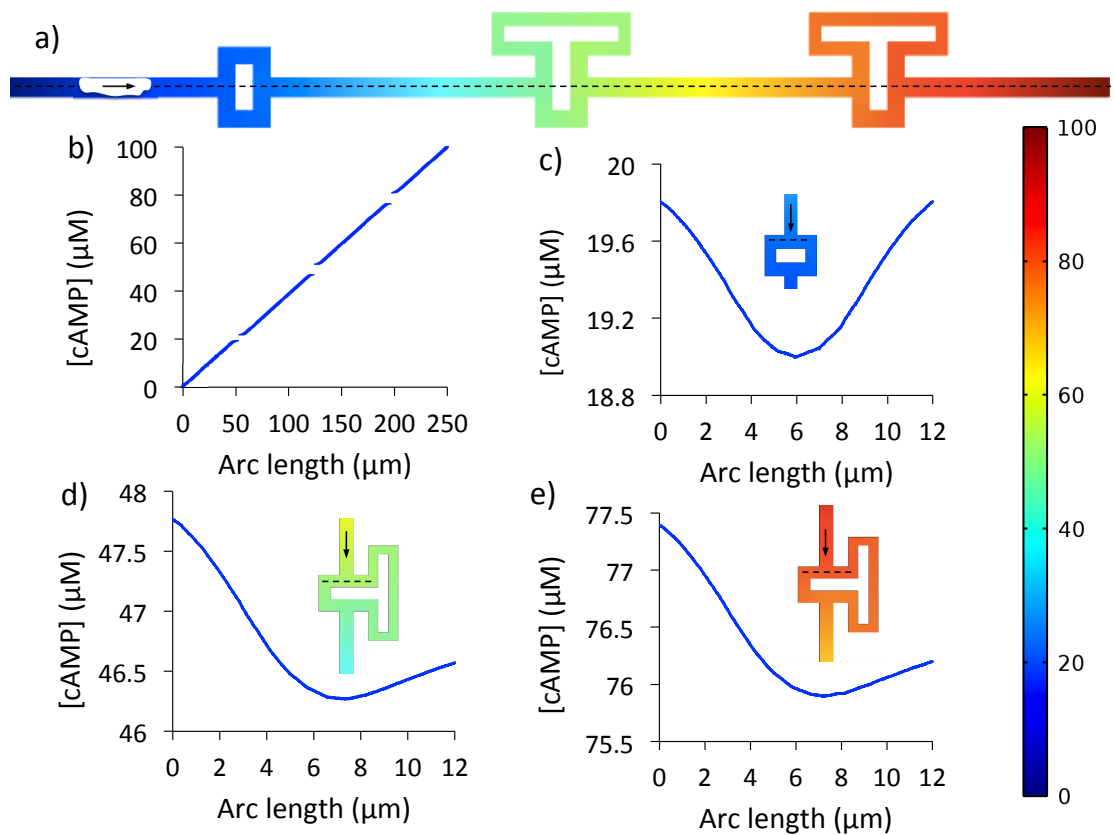


Figure 3.4: Profiles of the cAMP gradient along the bifurcating channel and across each bifurcation in the case of a concentration of $100 \mu\text{M}$ imposed at the loading channel. (a) Output of the steady-state solution of the diffusion equation computed using Comsol for the actual geometry. A concentration of cAMP $100 \mu\text{M}$ was imposed at the right-hand reservoir and $0 \mu\text{M}$ at the left-hand one. The arrow indicates the direction of the cell migration. (b) Concentration profile along the axis of the channel depicted in (a) (broken line). The discontinuities of the curve are associated with to the presence of the bifurcations. (c) Concentration profile across the first bifurcation (dashed line in the inset). (d) Concentration profile across the second bifurcation (dashed line in the inset), the cAMP concentration is higher within the shorter channel. (e) Concentration profile across the third bifurcation (dashed line in the inset), the cAMP concentration is higher within the shorter channel.

microscope equipped with a 100 \times , 1.4 N.A. plan apochromat objective lens.

The results were arranged in two-rows by three-columns contingency tables and the statistical significance was tested using the Freeman-Halton test, an extension of the Fisher exact probability test. Differences were considered significant at 95% confidence level.

3.3.5 Estimation of the difference in cAMP concentration at bifurcations

Comsol was used to simulate the cAMP distribution across the three different channels shown in Fig. 3.5 based on the assumption of pure diffusion as in Section 4.3.2.3. In this case the simulation was carried out in 2D and for the actual geometries directly imported from the CAD files. A concentration of cAMP 1 μM was imposed at the right-hand reservoir and 0 μM at the left-hand one. The local concentration difference did

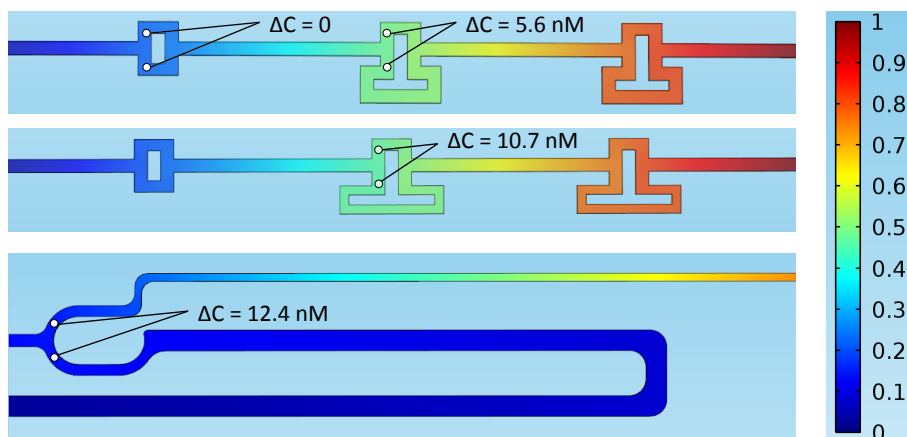


Figure 3.5: Estimation of the difference in cAMP concentration at the four types of bifurcations. Comsol was used to simulate the cAMP distribution across the different channels. Pure diffusion was assumed and a concentration of 1 μM was set at the right end, that in the real chip is connected to the right-hand side loading channel.

3.3. METHODS

not depend on the position of the bifurcation along the migration channel, but only on its geometry. Moreover, the local difference was proportional to the concentration set at the right-hand end of the channel. For instance if the cAMP concentration at the right-and side reservoir were $10 \mu\text{m}$, then the estimated local differences would be 10 times higher.

3.4 Results

3.4.1 Directional bias and the role of microtubules

When a Dictyostelium cell encountered a bifurcation along a straight microchannel, it protruded one pseudopod in each arm. One of the two leading edges became 'dominant' whereas the other retracted, allowing the cell to continue migrating towards the 'chosen' direction, as observed in neutrophils (Prentice-Mott et al., 2013). Representative examples of cells migrating through a bifurcation are reported in Fig. 3.6 and Fig. 3.7, for a symmetric and an asymmetric case, respectively. Interestingly, cells

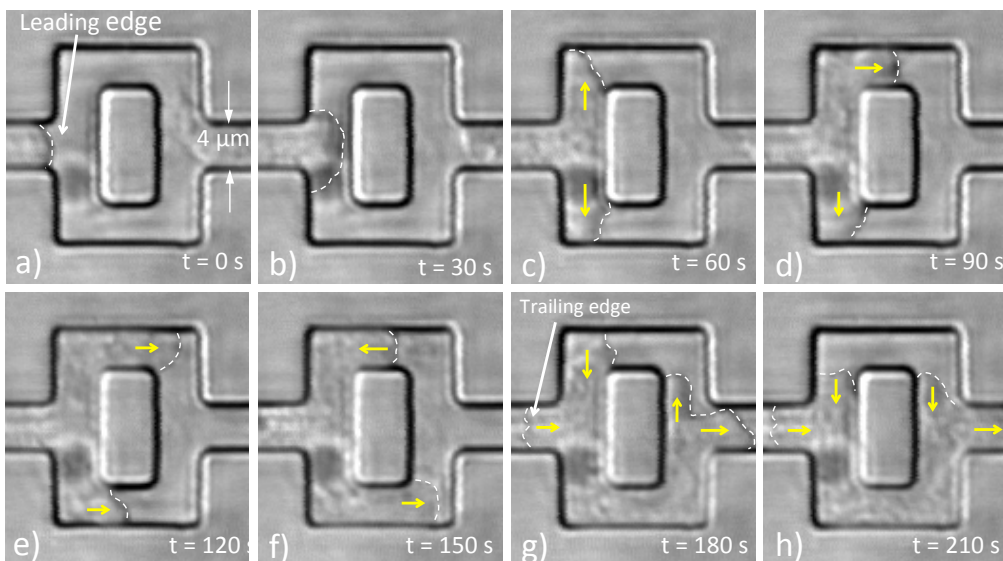


Figure 3.6: Image sequence of a Dictyostelium cell travelling through a symmetric bifurcating channel in the case of a cAMPs concentration of $100 \mu\text{M}$. The cell generates two almost symmetric pseudopods one in each arm of the bifurcation (b-c). A competition between the two pseudopod follows (d-f). (g) The 'winning' pseudopod splits again where the two paths rejoin with the main channel. (h) The secondary pseudopods retract and the cell moves towards the exit of the bifurcation.

generated two leading edges not only at the bifurcation but also at the second junction, where the two bifurcating channels reconnect with the main channel, as shown in Fig. 3.7.

3.4. RESULTS

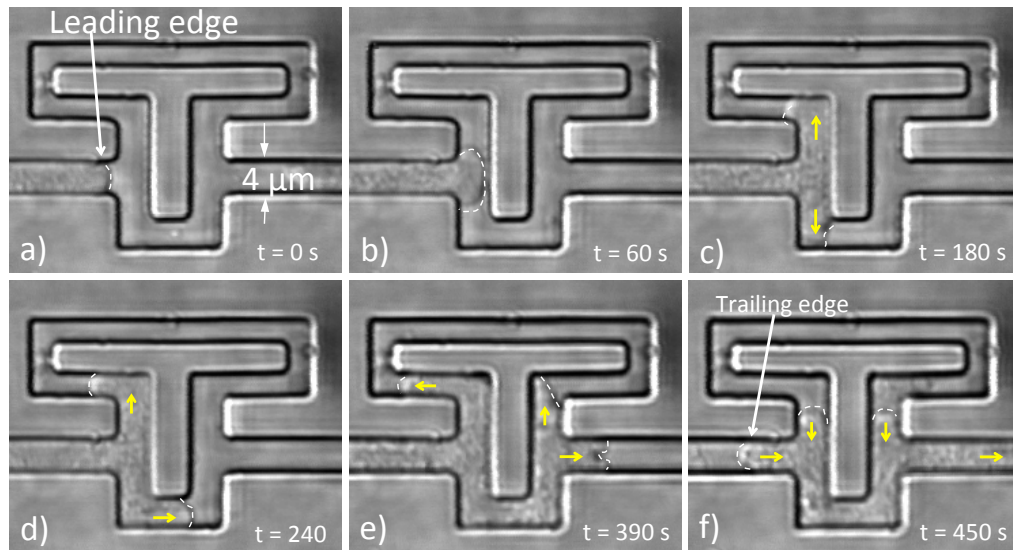


Figure 3.7: Image sequence of a *Dictyostelium* cell travelling through an asymmetric bifurcating channel in the case of $100 \mu\text{M}$ cAMPs. The cell generates two almost symmetric pseudopods, one in each arm of the bifurcation (b-c). The competition between the two pseudopods follows (d). (e) The 'winning' pseudopod splits again where the two paths rejoin with the main channel (e). (f) The secondary pseudopods retract and the cell moves towards the exit of the bifurcation.

The response of *Dictyostelium discoideum* to different hydraulic resistance ratios and chemoattractant concentrations was tested and summarised in Fig. 3.8.

Data were summarised in 3×2 contingency tables and the Freeman-Halton test was performed for each of the four cases in Fig. 3.8. The analyses resulted in p-values always smaller than 0.05. Hence, the null hypothesis could be rejected and I could conclude that cells in three different bifurcation types did not have the same decision-making trends, but a directional bias existed towards the path with lower R_h . Additionally, successive decisions did not appear to be biased by the previous ones. In the case of symmetric bifurcations, after splitting symmetrically, cells showed an almost completely stochastic decision (as shown in Fig. 3.9). Conversely, in the case of asymmetric bifurcations the directional choice appeared to be biased by local 'differential sensing'. In addition, no correlated behaviour was observed between consecutive

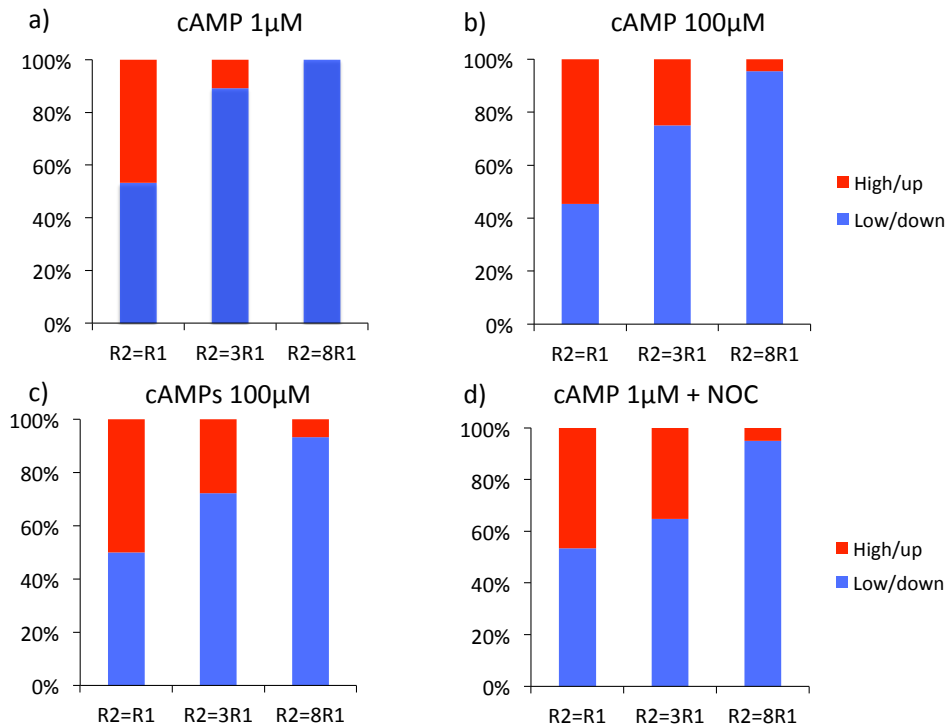


Figure 3.8: Results from the directional bias analysis performed in different conditions. R2 and R1 represent the hydraulic resistance of the *upper* and *lower*¹ arms at each bifurcation. In red (blue) the cells that chose the arm with higher (lower) resistance. In the case of the symmetric bifurcation red (blue) corresponds with upper (lower) arm. (a) Conventional cAMP at the concentration of 1 μ M was used. Cells are close to the 50/50 ratio at the symmetric bifurcation (N=30), about 27% of the cells went into the arm with three times higher R_h (N=34) and none of the cells went into the arm with eight times higher R_h (N=12). P-value=0.00002. (b) Conventional cAMP 100 μ M was used. Nearly half of the cells took one direction of the symmetric bifurcation and the other half the opposite one (N=64), ~ 25% of the cells went into the arm with three times higher R_h (N=28) and less than 5% went into the arm with eight times higher R_h (N=43). P-value= 4×10^{-8} . (c) Non-degradable cAMPs at the concentration of 100 μ M was used. Cells are exactly split at 50 : 50 at the symmetric bifurcation (N=40), ~ 27% of the cells went into the arm with three times higher R_h (N=18) and less than 7% went into the arm with eight times higher R_h (N=30). P-value=0.00026. (d) Conventional cAMP at the concentration of 1 μ M is loaded into the migration channel. Cells are treated with Nocodazole 5 μ M. The decision appeared unbiased at the symmetric bifurcation (N=30), ~ 35% of the cells went into the arm with three times higher R_h (N=34) and less than 5% went into the arm with eight times higher R_h (N=20). P-value=0.0047. Freeman-Halton test, extension of the Fisher exact test was performed.

cells within the first couple of hours of experiment, after which Dictyostelium cells are known to start forming aggregates (that ultimately will form the slug) as discussed in the previous chapter. Even in this case if cells were at sufficient distance, they did

3.4. RESULTS

not tend to make correlated decisions. To account for potential cell-to-cell interactions in this chapter I only considered cells that were at a distance bigger than $10\ \mu\text{m}$, that turned out to be sufficient to observe every cell splitting at each bifurcation, rather than following the preceding cell. Furthermore, I sought to test whether there were

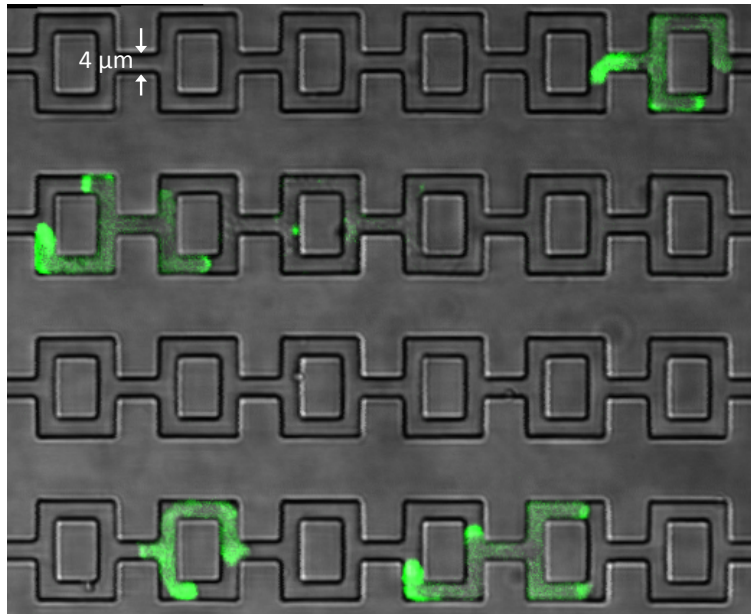


Figure 3.9: Cells migrating in serial symmetric bifurcations. At each bifurcation every cell generates two symmetric pseudopodia, one in each arm. A stochastic symmetry-breaking process occurs and eventually the cell 'chooses' the direction to follow and retracts the 'losing' pseudopod. Cells are MyoII-GFP labelled.

any difference in cell behaviour due to the concentration of cAMP, the use of cAMPs and the treatment with Nocodazole, for each bifurcation type. The Fisher exact test was applied pair-wise to all the combinations of chemoattractant that I investigated and the results are summarised in Table 3.1. No statistically significant differences appeared among the analysed cases and this would suggest that neither the concentration of cAMP nor the Nocodazole treatment affect the directional bias.

¹*Upper* and *lower* refer to the position of the bifurcating arms with respect to each other. In the case of asymmetric bifurcations 'up' coincides with higher R_H .

	p-values		
	$R_2 = R_1$	$R_2 = 3R_1$	$R_2 = 8R_1$
1 μM cAMP vs 100 μM cAMP	0.5736	0.1844	1
1 μM cAMP vs 100 μM cAMPs	1	0.1348	1
1 μM cAMP vs 1 μM cAMP + Noc	1	0.1165	1
100 μM cAMP vs 100 μM cAMPs	0.6894	1	1
100 μM cAMP vs 1 μM cAMP + Noc	0.5120	0.4201	1
100 μM cAMPs vs 1 μM cAMP +Noc	0.8133	0.7580	1

Table 3.1: Results of the Fischer exact test among all the combinations of cAMP concentration for each bifurcation type.

3.4.2 The role of the actomyosin cytoskeleton

The protrusions at the leading edge appeared to be driven by actin polymerisation in all the cases, as shown in Fig. 3.10. No blebbing mode was observed, at least in the performed experiments. The growth of the 'losing' pseudopod seemed to be arrested as a consequence of a strong localisation of myoII at its leading edge, also involved in the retraction of such a pseudopod, as shown in Fig. 3.11.

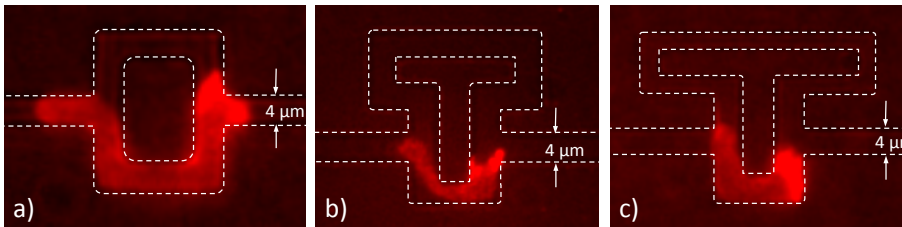


Figure 3.10: Representative examples of the actin distribution in cells migrating through the three bifurcation types. (a) Symmetric bifurcation. (b) Asymmetric bifurcation with hydraulic resistance ratio between the two arm equal to three. (c) Asymmetric bifurcation with hydraulic resistance ratio between the two arm equal to eight. cAMP 100 μM was added into the loading channel.

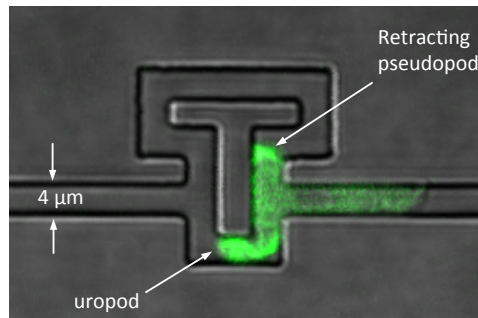


Figure 3.11: Localisation of myoII in a cell migrating through bifurcating channel. MyoII localises at the uropod but also at the retracting leading edges. cAMPs 100 μ M was loaded into the loading channel.

3.4.3 The case of dead-end channels

As mentioned in the previous section and shown in Fig. 3.6, some cells appeared to be able to split at the second junction and to protrude back into the arm with higher hydraulic resistance for a small extent. To further investigate this phenomenon I fabricated a migration device harbouring asymmetric and symmetric dead-end microchannels and I performed various experiments using different cAMP concentrations. Interestingly, cells appeared to be able to penetrate dead-end channels, as shown in Fig. 3.12. As in the case of finite hydraulic resistance, cells are able to generate actin-driven pseudopods in each arm of the bifurcations, regardless of the infinite resistance of the blind arms. This behaviour was not influenced by the concentration of cAMP used and was still observable in the presence of non degradable cAMPs 100 μ M as shown in Fig. 3.13. MyoII localised at the uropod and at the retracting leading edge. Such localisation was not affected by the concentration of cAMP (or cAMPs) used. Importantly, the fact that cells were able to migrate into dead-end channels would argue against the hypothesis of barotaxis. To further investigate this aspect I added a fluorescent dye FITC Dextran (Sigma-Aldrich) into the loading channel at the right-

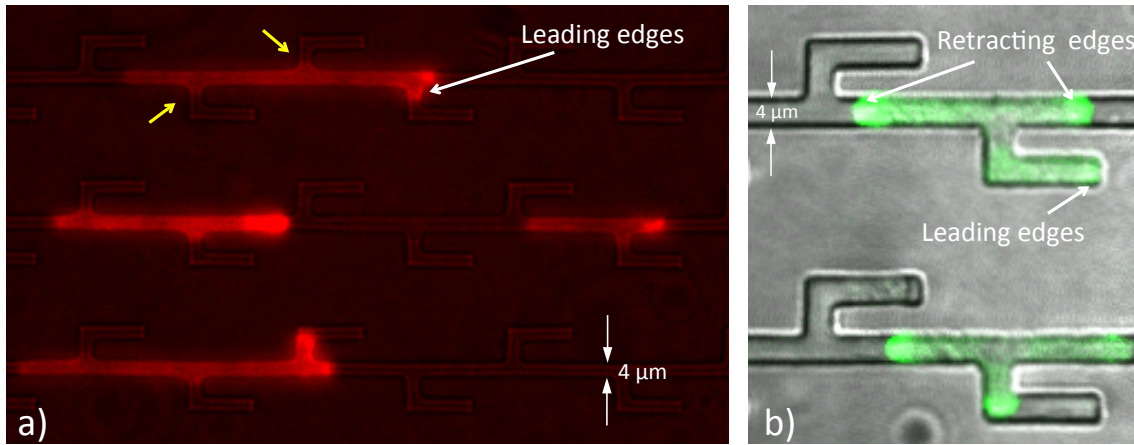


Figure 3.12: Behaviour of cells in microchannels with alternating dead-end bifurcations. (a) Example of four cells that protrude one pseudopod in each arm of each bifurcation, regardless of the presence of blind arms. This happens only at the leading edge of the cell, whereas when other regions of the cell body that are in proximity of a bifurcation they are passively pushed into the dead ends for a very small extent. This characteristic seemed to be consistent for all the cells under investigation. In fact, it can be observed that the actin polymerisation occurs only at the leading edge and not elsewhere, indicating no active protrusions away from the cell front. Cells were labelled with LifeAct. (b) A further example of two cells that protrude extensively into the blind channels. Cells express myoII-GFP. MyoII localises at the uropod but also at the retracting leading edges. The channels are 3 μm high.

hand side of the chip, where cAMPs 100 μM was present. The idea was to test whether cells were able to uptake the fluid at the invading leading edge or whether the fluid was displaced around it.

In none of the cases analysed the dye was found inside the cells. Many cells were able to partially or fully penetrate the dead-end channels as in Fig. 3.14, whereas other cells did not exhibit invasion, as in the case reported in Fig. 3.15.

In the cases of total or partial penetration, the pseudopods appeared smaller than the cross section of the channel and therefore the fluid downstream of them could be displaced around the cell. Conversely, in the cases of no invasion, the leading edges seemed to seal the channel and stopped at the entrance and could not invade the dead-end branches. In these cases the fluorescence signal exhibited a drop in intensity, as

3.4. RESULTS

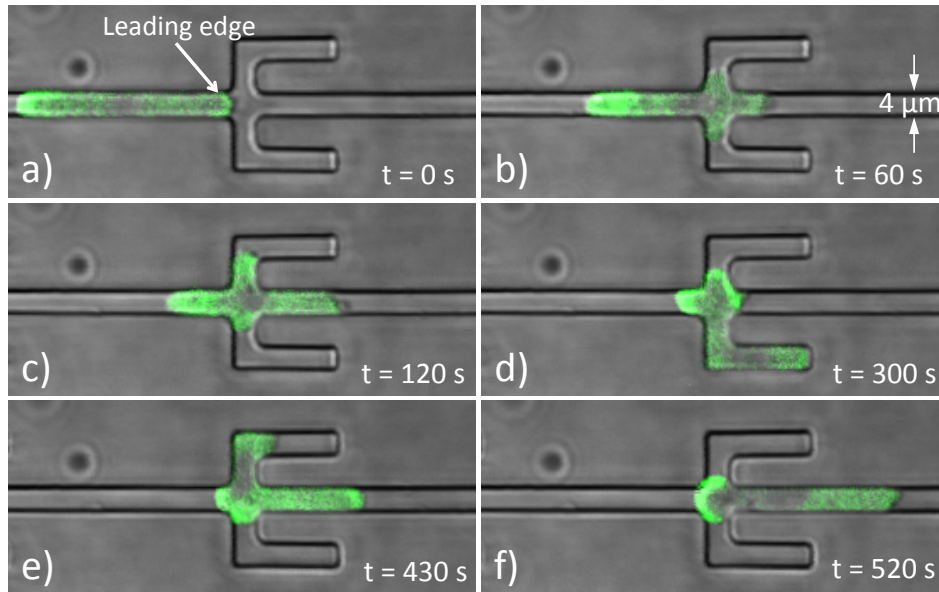


Figure 3.13: Cell protruding into symmetric dead-end channels. The cell is able to protrude into the blind channels and even to reach the end of them. Cells were expressing myoII-GFP. MyoII localises at the uropod but also at the retracting leading edges. The channels are 3 μm high.

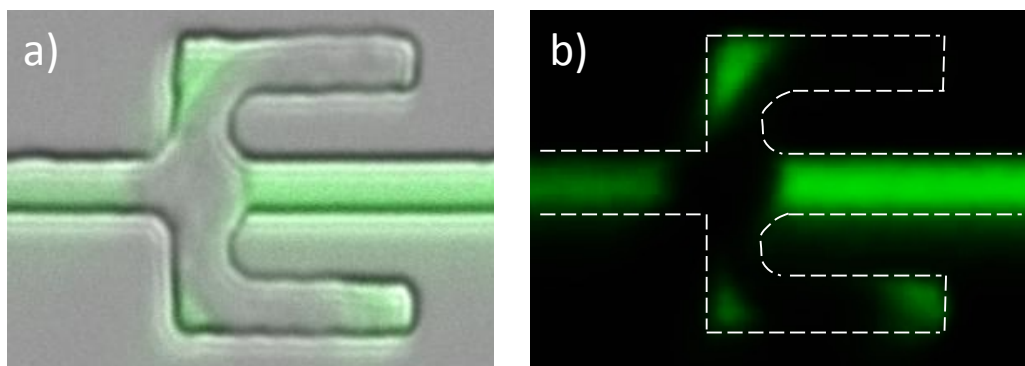


Figure 3.14: Fluid displaced by a cell that invades dead-end channels. The two pictures show that the leading edges does not fill the cross section of the channel and hence the surrounding fluid is able to flow past them.

shown in Fig. 3.15(c), presumably associated with photobleaching of the Dextran, as reported by Mahmoudian et al. (2011).

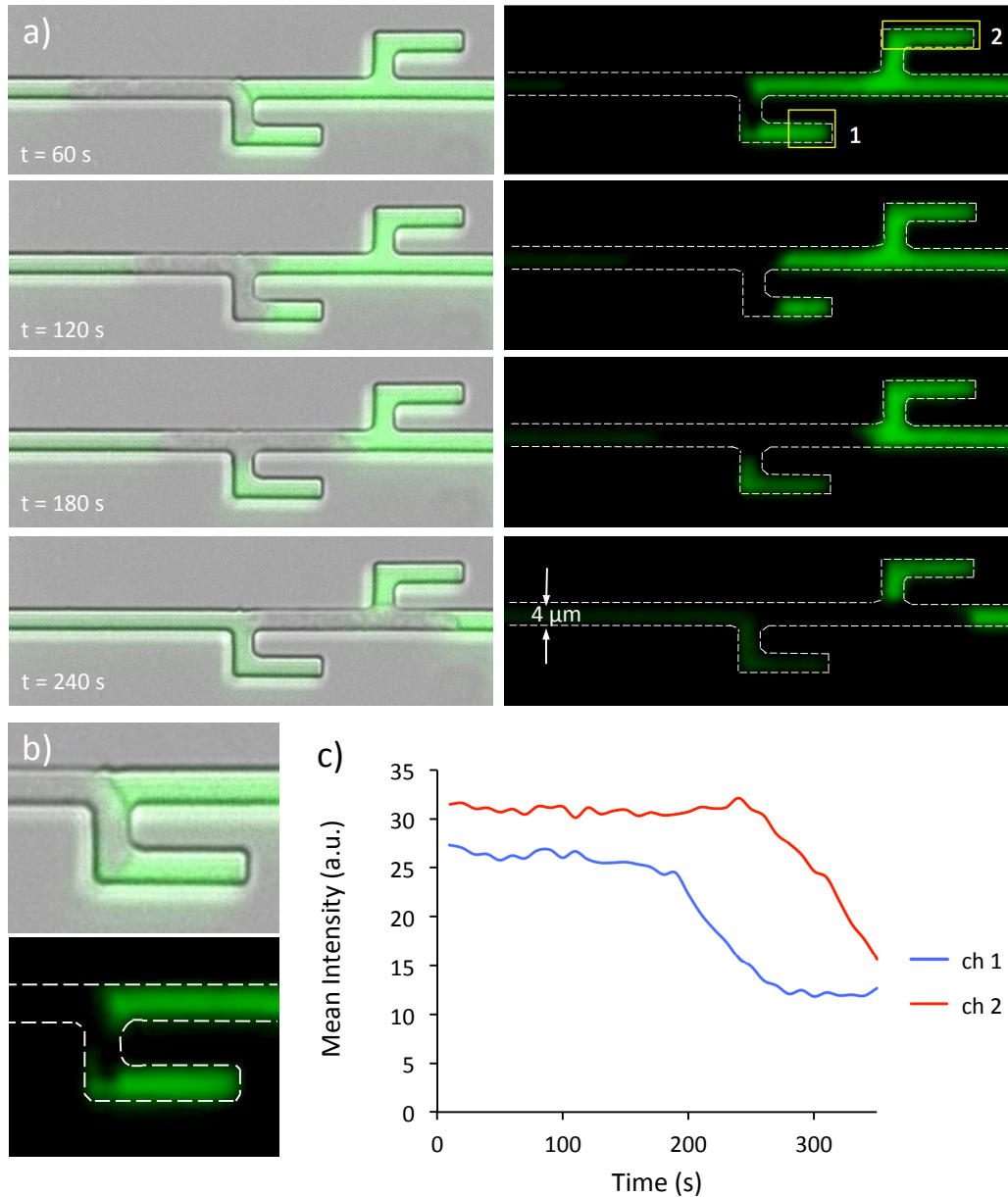


Figure 3.15: Interaction between cell and surrounding fluid at dead-end channels. FITC Dextran is added to the right-hand side loading channel to investigate whether the fluid was displaced or internalised by the cell upon invasion of a dead-end channel. (a) Image sequence showing a cell that encounters two consecutive dead-end channels. The cell partially protrudes into the first but not into the second channel. (b) A close-up of the first branching dead-end channel reveals that the leading edge is thinner than the cross section of the channel, and the liquid is displaced around it. (c) The mean intensity of the fluorescence at the position '1' and '2' drops over time after the cell seals the entrance of the dead-end channels.

3.4.4 Decoupling hydraulic resistance from chemical gradient

Using the novel topology described in Section 3.3.1.2 I could test whether cells direction was dictated by the chemical or mechanical cues. Interestingly, 96 out of 96 cells, analysed over seven independent experiments, migrated up the chemical gradient, in spite of the hundred times higher resistance of the narrow path. In this case non degradable cAMPs $1 \mu\text{M}$ was loaded in the chemoattractant channel to not saturate the CAR1 receptors.

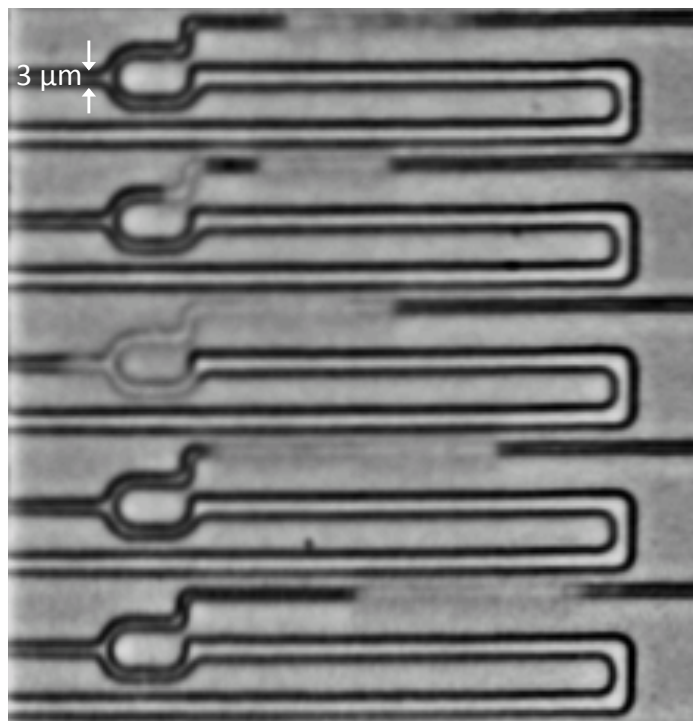


Figure 3.16: Cells migrating up the cAMPs gradient despite the hundred times higher hydraulic resistance of the channel.

In light of this observation the results presented in Fig. 3.8 can be interpreted as a consequence of the difference in the local chemical concentration between the two bifurcating arms, rather than the hydraulic resistance ratio. This was supported by data shown in Fig. 3.17 where a linear relationship emerged by plotting the percentage

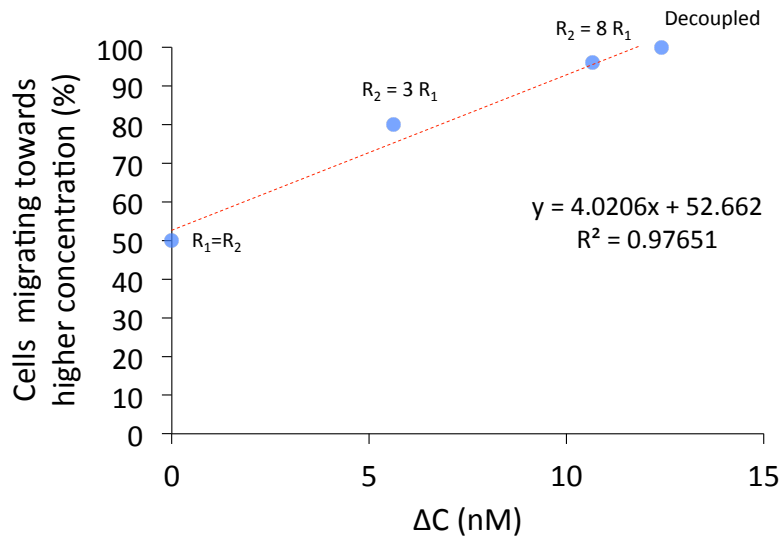


Figure 3.17: Relationship between the cellular directional bias at each bifurcation and the difference in local cAMP estimated at a distance of $3 \mu\text{m}$ away from the centre of the bifurcation in each bifurcating arms as shown in Fig. 3.5. Comsol was used to simulate the distribution of cAMPs across the four types of migration channels as described in Fig. 3.5.

of cells that migrated towards the higher concentration at each bifurcation against the estimated local difference in cAMPs. In this case, the percentages of the directional bias for each type of bifurcation were grouped together as no correlation was found with the type or concentration of cAMP (cAMPs). Therefore, 143 cells were considered at the symmetric bifurcation, 95 cells at the bifurcation with three times resistance ratio, 75 cells at the bifurcation with eight times resistance ratio and 96 cells for the case of the 'decoupling' geometry.

3.5 Discussions

In this chapter I showed that *Dictyostelium discoideum* cells migrating in asymmetric bifurcating channels exhibited biased directional 'choices'. In the first instance it seemed that such a behaviour could be accrued to the hydraulic resistance that cells find while migrating into the microfluidic channels, similarly to the more evolved human neutrophils (Prentice-Mott et al., 2013). More specifically, asymmetric bifurcations, cells seemed to be biased towards the arm of lowest hydraulic resistance and that this tendency appeared to correlate with increasing ratios of hydraulic resistance between the bifurcating arms. Exposing cells to physiological or saturating levels of cAMP, as well as to the non degradable homologue cAMPs did not influence the directional bias. In addition, each cell made a choice at each bifurcation along the migration channel that was independent of the previous ones. This would exclude the existence of any directional memory, in agreement to what was reported for neutrophils (Ambravaneswaran et al., 2010). This result is in line with a recent model of chemotaxis according to which pseudopodia are produced by intrinsic self-generated cycles, at random directions and triggered by positive and negative feedback loops (Neilson et al., 2011).

Furthermore, I tested the role of MTs in the decisional process. The results showed that, upon MTs inhibition by Nocodazole treatment, cells neither altered their directional bias at asymmetric bifurcations nor were impaired to undergo symmetry breaking at the symmetric bifurcations, at least using Nocodazole at the concentration of 5 μ M.

Interestingly a controversial observation emerged from this first analysis: many cells could move inside dead-end channels, despite their infinite hydraulic resistance. This could be explained assuming that the fluid inside the blind channels, ahead of the leading edge of the cell, were displaced either around or through the cell. It has been postulated that the physical confinement might modify cellular hydraulics as a consequence of altered cellular parameters, namely: membrane permeability, adhesion, contractility and cytoskeletal structure (Stroka et al., 2014a). In addition, it has been shown that the protrusion of the leading edge is associated with local solute and water uptake, thanks to the combined action of Na^+/H^+ or $\text{Cl}^-/\text{HCO}_3^-$ exchangers at the cell front (Schwab, 2001). A recent work demonstrated that tumour cells confined in microchannels display a polarised distribution of ion pumps (Na^+/H^+) and aquaporins in the cell membrane, that ultimately create a net influx of water at the leading edge and a net outflow at the uropod (Stroka et al., 2014b). Such an anterior-posterior flow would induce a forward movement of the cell and would represent an alternative to the actin-driven motion that has been named the 'Osmotic Engine Model' (Stroka et al., 2014b). I then tested whether such a fluid exchange was present in my experiments. I loaded a fluorescent dye into the migration channels and performed chemotaxis assays using cAMPs at the concentration of 100 μM . No dye was found to flow into the cells, suggesting that no fluid uptake occurred, at least within the time-scale of the invasion of the blind branches. Moreover, it appeared that many cells could indeed protrude into these channels but only if the cross section of their leading edge was smaller than that of the channel. In this case no fluid column would be pushed, but a very thin and fast flux would flow past the leading edge and displace around

3.5. DISCUSSIONS

the cell as it advances into the dead-end branch. Another evidence of this observation was that the fluorescent dye was subjected to photobleaching when confined into the blind channel by a sealing leading edge (Fig. 3.15). In this case the cell, by completely occluding the entrance of the branch, would 'trap' the dye into the dead-end channel and prevent it from being replenished, and hence photobleaching would induce the observed drop in fluorescence intensity.

In summary, the fact that cells can dynamically modify their shape and defy the infinite hydraulic resistance of a dead-end branch would argue against the *barotactic* hypothesis proposed by Prentice-Mott et al. (2013), at least in *Dictyostelium discoideum*.

To further investigate the cause of the directional bias, I sought to decouple the two contributions: the chemical gradient and the hydraulic resistance. The novel topology described in Section 3.3.1.2, allowed me to show that the totality of cells analysed (n=96) exhibited a directional bias towards the chemical gradient, rather than moving into the arm of least resistance. This observation could not be achieved without being able to dissect the chemical and the mechanical contributions. In fact, the bifurcating arms of least hydraulic resistance are also characterised by a slightly higher cAMP concentration. Interestingly, the results shown in Fig. 3.8 appeared to be independent of the concentration of cAMP (or cAMPs) used. Furthermore, the concentration difference between any bifurcating channel is proportional to the concentration set at the right-hand loading channel. Therefore one would expect that the percentage of cells migrating towards the higher concentration arm of a bifurcation changed widely, depending on the concentration set at the right-hand loading channel. Conversely, the fact that the use of a wide range of cAMP concentrations did not influence the direc-

tional bias suggests that cells might be sensitive to some other types of chemical cue. An intriguing hypothesis would be that cells might undergo *autologous chemotaxis*, as previously observed in cancer cells and neutrophils (Shields et al., 2007; Swartz and Lund, 2012). Autologous chemotaxis relies on the release of chemokines at the leading edge of a cell that, diffusing away establish a chemical gradient. Cells would then be able to sense this gradient. In the case of asymmetric bifurcating arms the geometric features of each arm would dictate the asymmetry in local concentration of the chemokine. Hence, within this framework the cell would sense differences in the secreted chemokine concentration, and polarise to fulfil directional choices, as described in Fig. 3.18.

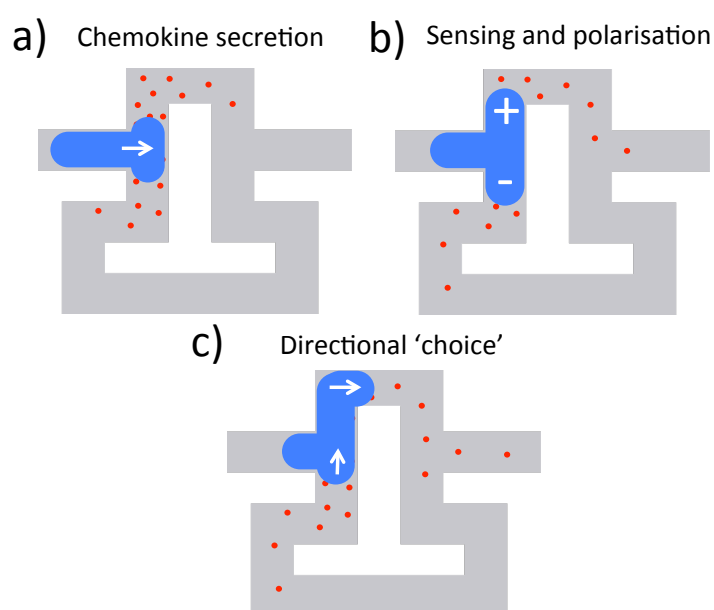


Figure 3.18: Putative explanation of the directional bias based on the hypothesis of *autologous chemotaxis*. (a) Specific chemokines would be secreted at the leading edge of the cell, that diffusing away from it would establish a chemical gradient along the advancing leading edges. (b) The cell would sense such gradient. The geometric characteristics of an asymmetric bifurcation would impose an asymmetric local concentration of the chemokines. Hence, the two leading edges would become polarised. (c) Myosin II would localised at the 'losing' leading edge to retract it, whereas actin would push the 'winning' leading edge forward.

CELL MECHANICS

4.1 Introduction and Background

Until recently, the biomedical investigation of cellular structure and functions, as well as the interactions between the cell and its extracellular environment was carried out within the framework of biochemistry (Christopher R. Jacobs, Hayden Huang, 2012). Physiological and pathological processes were considered to be only associated with specific biochemical signalling events (Christopher R. Jacobs, Hayden Huang, 2012). Over the last two decades, advances in micro and nano-technology opened up the possibility to investigate another important characteristic of a cell: its mechanical properties. Cells are not only capable of continuously generating forces, as explained in the previous chapters, but also to detect mechanical stimuli and respond to them by actively reorganising their cytoskeleton (Fletcher and Mullins, 2010).

A growing body of evidence indicates the existence of a link between genetic information and mechanical properties of the cell. Forces and mechanical signals, in fact, turned out to regulate a wide range of cellular processes (Discher et al., 2005; Vogel and Sheetz, 2006) not only at the single cell level (*e.g.* motility) but also at the

multicellular level (e.g. development), where interactions among cells occur via mechanical cues, as well as biochemical ones (Hoffman and Crocker, 2009). Interestingly, mechanical stimuli can also be converted into biochemical responses through a process known as mechanotransduction (Janmey and McCulloch, 2007).

Although the field of cell mechanics is still in its infancy, it has already enabled numerous insights into the mechanisms by which cells can sense intracellular, as well as extracellular forces and fulfil active responses (Moeendarbary and Harris, 2014).

4.1.1 Mechanical properties at the subcellular level

The mechanical properties of a cell can mainly be ascribed to its cytoskeleton (Fletcher and Mullins, 2010). The cytoskeleton is a very dynamic assembly of various types of polymers that support the cellular body. Its dynamic nature confers the cell the ability to adaptively change shape in response to the continuous interactions with the surrounding environment. Intriguingly, its dynamics are characterised by a certain degree of order and hierarchical organisation that results from permanent energy dissipation (Huber et al., 2013).

At the molecular level single polymers are subjected to thermal fluctuations and are usually characterised by a mechanical parameter known as *persistence length* l_p . The magnitude of l_p is a measure of the polymer's resistance to the entropic effect associated with thermal agitation, and is a property of a specific polymer type (Huber et al., 2013; Moeendarbary and Harris, 2014). More specifically, the correlation between tangent vectors along the polymer decreases exponentially (Phillips et al., 2010):

$$\langle \mathbf{t}(0) \cdot \mathbf{t}(s) \rangle \propto e^{-s/l_p}, \quad (4.1)$$

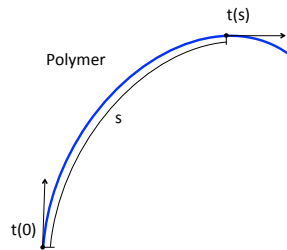


Figure 4.1: Tangent vectors on a polymer. $t(0)$ is the unit vector tangent to the polymer at a reference position $s=0$ and $t(s)$ is tangent to the polymer at the arclength s . Adapted from (Phillips et al., 2010).

where $t(0)$ is the unit vector tangent to the polymer at a reference position $s = 0$, $t(s)$ is the unit vector tangent to the polymer at the arclength s and l_p is the decay constant. The key components of the cytoskeleton are:

- Microtubules (MTs), that are the stiffest and longest cytoskeletal polymers, their persistence length is in the range 1 to 8 mm (Janson and Dogterom, 2004). MTs can withstand high-pressures, and generate pushing and pulling forces in range of several piconewtons (Dogterom et al., 2005).
- Actin filaments, are semiflexible fibres with a persistence length in the range 10 to 20 μm (Isambert and Maggs, 1996). They represent the most dynamic cytoskeletal structure and play a pivotal role in shape adaptation, as explained in the previous chapters.

These two types of polymers constantly interplay, giving the cell the capability to respond to various stimuli and conditions, within time-scales of seconds, that is much shorter than that of gene expression (Huber et al., 2013).

Another class of polymers, known as intermediate filaments (IFs), exhibits interaction with F-actin and MTs. Although their role in cellular processes is still not completely understood, IFs have been shown to provide lateral reinforcement to MTs, contribut-

ing to increase their resistance to applied forces (Brangwynne, 2006). Moreover, IFs entangled with actin networks, yield an increased stiffness, suggesting their role in maintaining cellular mechanical integrity (Esue et al., 2006).

The order of the cytoskeletal architecture is given by the presence of numerous accessory proteins that control the nucleation, polymerisation cross-linking, depolymerisation and severing of actin filaments, MTs and IFs. Such a complex regulation is made possible by a number of local and global feedback-loops and signaling-cascades (Huber et al., 2013).

4.1.2 Mechanical properties of the cell

The overall mechanical properties of a cell can indeed be explained as an emergent consequence of the complex interactions among the constituents of the cytoskeleton. Therefore cell mechanics need to be investigated at the network level rather than at the single filament level (Huber et al., 2013).

The cell comprises both solid and liquid structures, represented by the cytoskeleton and the cytosol, respectively and therefore exhibits the mechanical properties of the two phases. This kind of response is typical of viscoelastic materials (Huber et al., 2013; Moeendarbary and Harris, 2014). An elastic solid, for instance, is able to deform when subjected to a mechanical stress, and its original shape is restored once the stress stops. Additionally during the deformation phase, it stores elastic energy. Conversely, in the presence of a load, fluids flow, and they are unable to store elastic energy (Moeendarbary and Harris, 2014). A viscoelastic material exhibits both viscous and elastic responses to an external load: it simultaneously stores and dissipates elastic energy. If a constant load, or *step-stress*, is applied to an uniaxial bar at time t_0

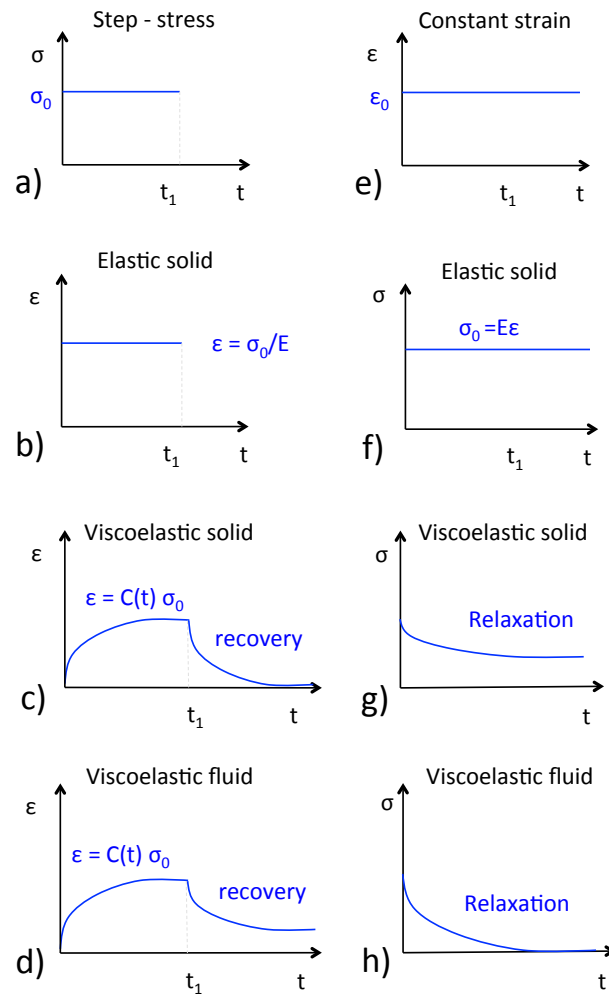


Figure 4.2: Qualitative responses of an uniaxial bar of different materials to a step-stress and constant strain. Adapted from (Joints, 2012).

and removed at time t_1 , the strain profile will depend on the material of the bar, as summarised in Fig. 4.2 (Joints, 2012). The mechanical response to the external load is:

- Constant in the case of a solid, $\epsilon = \sigma/E$, where E is the Young's modulus. At time t_1 the material instantly restores its initial shape.
- A non-decreasing function of time $C(t)$, known as the *creep compliance* in the case of a viscoelastic material. At time t_1 the material starts to gradually recover. Specifically, for a viscoelastic solid the recovery will eventually be complete (Fig.

4.2(c)), whereas for the viscoelastic fluid a residual deformation remains in the material (4.2(d)).

Furthermore, if a uniaxial bar is subjected to a stress relaxation test, that consists of applying an instantaneous constant strain ϵ_0 , its response depends on the type of material:

- An elastic solid develops a stress $\sigma_0 = E\epsilon_0$ that remains constant as long as the strain is maintained.
- A viscoelastic material responds with a progressively decreasing stress. In the case of a viscoelastic fluid the stress eventually tends to zero, while in a viscoelastic solid, a residual stress remains in the material.

Moreover the stress-strain diagram differs between the two cases as shown in Fig. 4.3:

- For an elastic material the relationship between the stress and strain is linear, $\sigma = E\epsilon$, where the proportionality constant E is known as Young modulus. In addition, the loading and the unloading paths coincide and therefore there is no energy loss (Joints, 2012).
- For a viscoelastic material the strain depends on the magnitude of the stress and its time derivative. A hysteresis loop exists and the area enclosed between the the loading and unloading paths represents the energy dissipated as heat (Joints, 2012).

Although most studies on cell mechanics indicate that cells can be described as soft materials, more recent works proposed an interesting analogy to soft glassy materials for both adherent and suspended cells (Trepats et al., 2007; Maloney and Van Vliet, 2014). Soft glassy rheology (SGR) links macroscopic mechanical properties to local

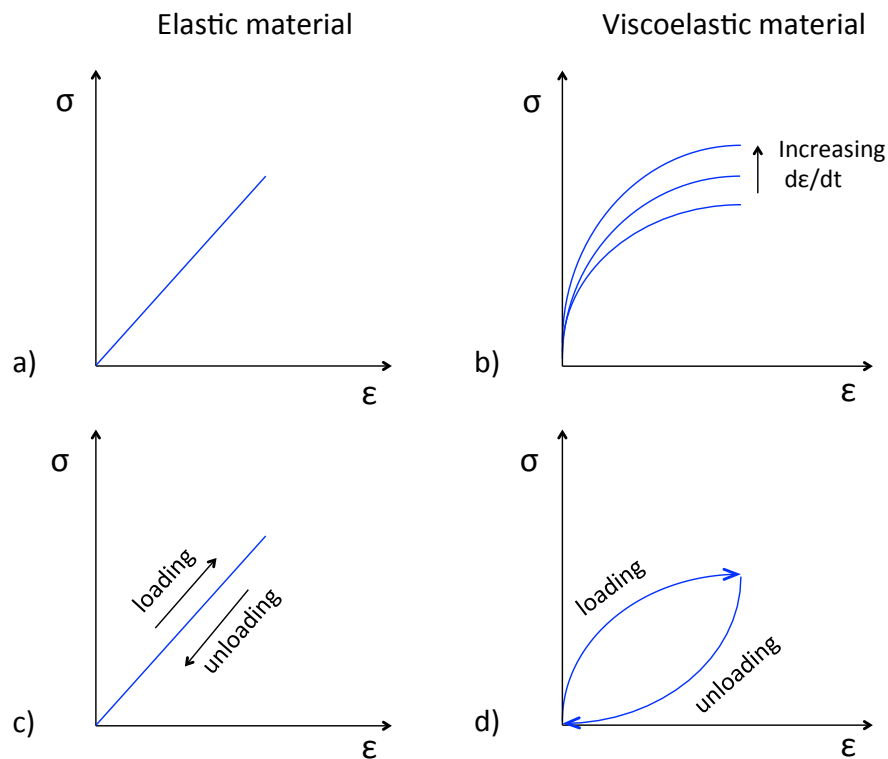


Figure 4.3: Qualitative stress-strain diagrams for elastic and viscoelastic materials. (a) Stress and strain are linearly proportional for an elastic material. (b) In a viscoelastic material the strain depends on the magnitude of the stress and also on the rate at which the stress is applied or removed. (c) For an elastic material the loading and the unloading paths overlap, resulting in no energy loss. (d) For a viscoelastic material a *hysteresis* loop exists and the area enclosed between the the loading and unloading paths represents the energy dissipated as heat. Adapted from (Joints, 2012).

rearrangements of the cytoskeletal architecture (Treat et al., 2007). Upon stretching cells have been shown to fluidise and then slowly re-solidify (Treat et al., 2007). This phase transition is associated with the interactions among the numerous particles that populate the intracellular environment. Their energy landscape is characterised by multiple energy barriers that are too high to be overcome by thermal energy. Therefore, the system becomes trapped in several metastable micro-configurations, and any structural rearrangement is thermally forbidden and only achievable via non-thermal, ATP-driven changes or external forces (Treat et al., 2007).

Another relevant property that emerged from recent studies is that the elastic modulus of living cells is orders of magnitude larger than that measured in *in vitro* F-actin gels (Gardel et al., 2006). This suggests that the cellular elastic properties could not be explained exclusively as a result of the interactions within the actin networks but it would arise from myosin-driven tension and pre-stress (Gardel et al., 2006). These findings are predicted by the *tensegrity model*, where geometrical rearrangement of actin stress fibres and MTs are modelled as pre-stressed networks of cables and struts (Ingber et al., 1981). Recent experimental works demonstrated that myosin-driven contractility also induces pressure gradients inside cells, which can be accounted for by considering the cell as a sponge-like material filled with fluid (Moeendarbary et al., 2013). According to this *biphasic theory*, also known as *poroelasticity*, cytoplasm consists of a porous elastic solid meshwork, represented by cytoskeleton, organelles and macromolecules, bathed in cytosol. Within this framework, the cellular viscoelasticity would depend on the time-scale of the redistribution of the liquid phase after the application of an external load (Moeendarbary et al., 2013). Therefore, the mechanical response could be described by knowing the drained elastic modulus of the meshwork E , its pore size ξ and the viscosity of the cytosol μ , which contribute to the definition of the poroelastic diffusion coefficient $D_p = E\xi^2\mu$ (Moeendarbary et al., 2013).

Although a unified theory that comprehends all of the complex cellular mechanical properties is still missing, empirical simplified linear viscoelastic models are commonly adopted to evaluate mechanical responses in cells under a variety of biochemical and physical conditions. Two simple models have been adopted to describe viscoelastic materials: the *Kelvin-Voight model* and the *Maxwell model*. These models comprise

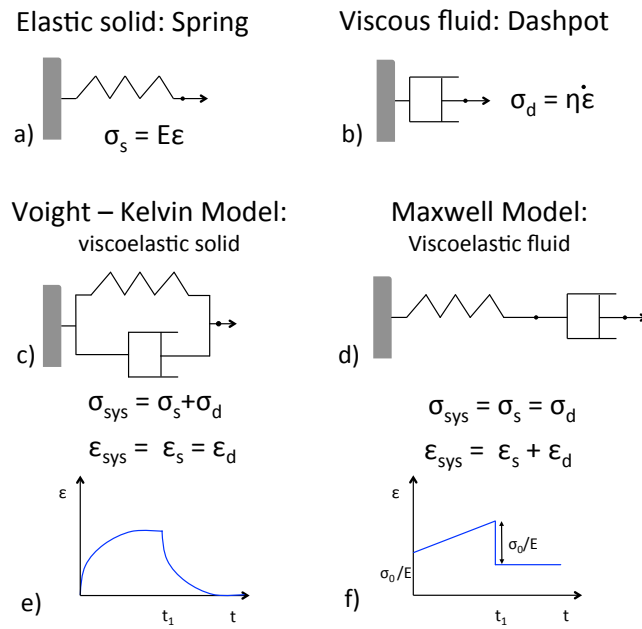


Figure 4.4: Empirical models of viscoelasticity. (a) Stress and strain are linearly proportional for an elastic material. (b) In a viscoelastic material the strain depends on the magnitude of the stress and also to the rate at which the stress is applied or removed. (c) For an elastic material the loading and the unloading paths overlap, resulting in no energy loss. (d) For a viscoelastic material a hysteresis loop exists and the area enclosed between the the loading and unloading paths represents the energy dissipated as heat. For Adapted from (Joints, 2012).

two structural elements, *springs* and *dashpots*, arranged in different ways as depicted in Fig. 4.4. Springs represent the elastic solid response, whereas dashpots mimic the behaviour of viscous fluids. A constant stress σ induces a constant strain ϵ in a spring and a constant strain rate $\dot{\epsilon}$ in a dashpot (Joints, 2012). The Voight-Kelvin model, illustrated in Fig. 4.4(c), is the simplest model used to describe a viscoelastic solid and consists of a spring and a dashpot in parallel. If an external stress σ_{sys} is applied to the system, the two components deform by the same amount, due to the parallel arrangement, hence the two strains are equal $\epsilon_s = \epsilon_d = \epsilon$. On the other hand, the stress is shared by the spring and the dashpot so that

$$\sigma_{sys} = \sigma_s + \sigma_d = E\epsilon + \eta\dot{\epsilon} , \quad (4.2)$$

where σ_s and σ_d are the stresses produced in the spring and in the dashpot, respectively. If a constant stress $\sigma_{sys} = \sigma_0$ is applied Eq. 4.2 becomes a first order differential equation whose solution is

$$\epsilon(t) = \frac{\sigma_0}{E} (1 - e^{-(E/\eta)t}) , \quad (4.3)$$

where E/η is the rate of relaxation (Stachurski, 2009). If at time $t = t_1$ the stress is removed ($\sigma_{sys} = 0$), the recovery of the material follows the equation

$$\epsilon(t > t_1) = \frac{\sigma_0}{E} e^{-(E/\eta)t} (e^{-(E/\eta)t_1} - 1) . \quad (4.4)$$

Therefore, if the time at which the stress is applied is $t_0 = 0$ the strain

$$\epsilon(t) = \begin{cases} \frac{\sigma_0}{E} (1 - e^{-(E/\eta)t}) , & 0 < t < t_1 \\ \frac{\sigma_0}{E} e^{-(E/\eta)t} (e^{-(E/\eta)t_1} - 1) , & t > t_1 \end{cases} \quad (4.5)$$

models the behaviour depicted in Fig. 4.2(c) (Stachurski, 2009).

The simplest viscoelastic fluid consists of a spring and a dashpot in series and it is known as Maxwell model (Joints, 2012). In this case the stress is applied equally to the two components, therefore $\sigma_{sys} = \sigma_d = \sigma_s = \sigma$ and the total strain is given by

$$\epsilon_{sys} = \epsilon_s + \epsilon_d , \quad (4.6)$$

that leads to the following differential equation:

$$\dot{\epsilon} = \frac{\sigma}{\eta} + \frac{1}{E} \frac{d\sigma}{dt} . \quad (4.7)$$

If a constant stress $\sigma = \sigma_0$ is applied, hence $\dot{\sigma} = 0$ between 0 and t , therefore the integration of Eq. 4.7:

$$\int_{\epsilon(0)}^{\epsilon(t)} d\epsilon = \frac{1}{E} \int_{\sigma(0)}^{\sigma(t)} d\sigma + \frac{\sigma}{\eta} \int_0^t dt , \quad (4.8)$$

leads to

$$\epsilon(t) - \epsilon(0) = \frac{\sigma_0}{\eta} t. \quad (4.9)$$

It can be assumed that the initial strain of the system corresponds to that of the spring, as its response is much faster than that of the dashpot. Therefore, $\epsilon(0) = \sigma_0/E$ and the Eq. 4.9 can be written as

$$\epsilon(t) = \frac{\sigma_0}{\eta} t + \frac{\sigma_0}{E} = \sigma_0 \left(\frac{1}{\eta} t + \frac{1}{E} \right). \quad (4.10)$$

The relaxation behaviour of the system can be modelled by applying a constant strain $\epsilon = \epsilon_0$ to it. In this case $\dot{\epsilon} = 0$ between 0 and t and the Eq. 4.7 becomes

$$\frac{d\sigma}{\sigma} = -\frac{E}{\eta} dt, \quad (4.11)$$

its integration gives

$$\int_{\sigma(0)}^{\sigma(t)} \frac{d\sigma}{\sigma} = -\frac{E}{\eta} \int_0^t dt \Rightarrow \ln \sigma(t) - \ln \sigma(0) = -\frac{E}{\eta} t, \quad (4.12)$$

but if a constant strain is applied the dashpot does not deform, therefore the initial stress of the system corresponds to that of the string $\sigma(0) = E\epsilon_0$ and therefore

$$\sigma(t) = E\epsilon_0 e^{-(E/\eta)t}. \quad (4.13)$$

This model is able to describe the permanent residual strain and the stress relaxation that characterise a viscoelastic response (Fig. 4.2(g-h)) but, on the other hand, it fails to predict the exponential-like creep and the anelastic recovery typical of a viscoelastic fluid (shown in Fig. 4.2(d)). In fact, the predicted creep increases linearly with time $c(t) = t/\eta + 1/E$ and as the load is removed, the system behaves as a spring and an instantaneous elastic response restores the strain to the initial value σ_0/E as illustrated in Fig. 4.4(f).

It is important to note that none of these models alone are sufficient to accurately model the actual fluid-like viscoelasticity of a cell. This can be fulfilled by adding multiple springs and dashpots either in series and in parallel. On the other hand the derivation of the constitutive relations would be complex and beyond the scope of this thesis.

4.1.3 Measuring cellular mechanical properties

Many techniques have been developed to provide cellular or sub-cellular spatial resolution and force sensitivity in the range pico to micro Newton. These techniques, reviewed in (Guck et al., 2010; Huber et al., 2013; Moeendarbary and Harris, 2014) and summarised in Table 4.1, allowed researchers to assess the mechanical response of different cell types, in a variety of environmental and experimental conditions. They can be grouped under different categories based on:

1. *The dimension of the probed area*: the external load can be applied either locally or to the whole cell, resulting in local or global rheological properties.
2. *The temporal profile of the stress*: the stress can be applied to a cell (or a fraction of it) as a step-function or in an oscillatory fashion, hence stress-strain relationship or time dependent mechanical properties can be assessed, respectively.
3. *Adhesive state of the cells*: they can be analysed when adherent to a substrate or in suspension. This is an important aspect to take into account, as it has been demonstrated that cells are capable of adapting their stiffness to that of their environment (Zemel et al., 2010).

In general, 'local techniques', such as *particle tracking microrheology*, *magnetic bead rheology*, *atomic force microscopy* and *optical tweezers* have a high spatial resolution

4.1. INTRODUCTION AND BACKGROUND

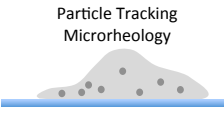
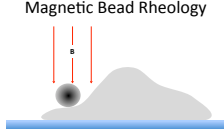
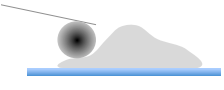
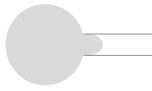
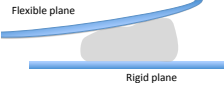
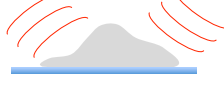
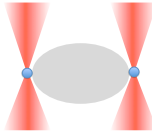
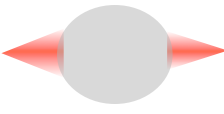
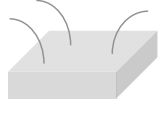
Techniques	Description
 <p>Particle Tracking Microrheology</p>	<p>Adherent cells are injected with particles. The MSD of the particles is tracked over time. Their motion can be driven by thermal oscillations or induced by magnetic or optical forces. Cells embedded in a 3D matrix can also be measured. The force field can be static or oscillatory, allowing time-dependent rheology over a wide spectrum of frequencies (Cicuta and Donald, 2007).</p>
 <p>Magnetic Bead Rheology</p>	<p>Adherent cells are indented using magnetic beads in a magnetic field. In this way, a torque is induced that results in the rotation and displacement of the beads. The cellular mechanical properties can also be studied in case the cell internalises the bead by phagocytosis (Bausch et al., 1999; Fabry et al., 2001).</p>
 <p>Atomic Force Microscope</p>	<p>Adherent cells are indented by a rigid probe connected to a cantilever. Depending on the shape and size of the probe the measurement can be local or global. Creep and stress-relaxation experiments can be performed. Time-dependent cellular mechanical properties can be measured by applying an oscillatory load (Müller and Dufrière, 2008).</p>
 <p>Micropipette Aspiration</p>	<p>Suction pressures are exerted on a cell using a pipette smaller than the diameter of the cell. Assessing the volume of the cell's portion that moves into the pipette and knowing the suction pressure, the cellular mechanical properties can be calculated. Depending on the size of the pipette the measurement can be either local or global (Hochmuth, 2000).</p>
 <p>Microplate Manipulation</p>	<p>Adherent cells are placed between two glass microplates. The rigid plate is moved towards the flexible one, inducing a deformation of the cell. Moreover, the flexible plane is calibrated, hence from its deflection the global mechanical properties of the cell can be extracted (Caille et al., 2002).</p>
 <p>Acoustic Microscopy</p>	<p>Adherent cells are exposed to acoustic waves that propagate through the cell volume, revealing variations in thickness, density and stiffness associated with the various cellular structures (Kundu et al., 1991).</p>
 <p>Optical Tweezers</p>	<p>Small beads are trapped by a focussed laser beam. The position of each bead can be controlled and the forces acting on it measured as elastic displacements from the centre of the optical trap. The bead is pushed against the cell and the local mechanical properties can be investigated in either step-like or oscillatory fashion (Laurent et al., 2002).</p>
 <p>Optical Stretcher</p>	<p>Suspended cells are globally deformed by a couple of counter-propagating, divergent, identical laser beams. The mechanical deformation is achieved without mechanical contact, by increasing the laser power in a step-stress fashion and the induced strain is measured. The potential throughput of this technique is ~ 100 cells/h. Oscillatory stress can also be generated (Guck et al., 2002, 2005; Lincoln et al., 2007a,b).</p>
 <p>Microfluidic Methods</p>	<p>Global mechanical deformation of suspended cells can be obtained, for instance, by forcing them through microchannels that are smaller than their diameter or via hydrodynamic interaction (extensional or pinched flow). The throughput of these techniques ranges between $\sim 10,000$ cells/h and $10,000$ cells/s (Lange et al., 2015; Dudani et al., 2013; Gossett et al., 2012).</p>

Table 4.1: Techniques for measuring the mechanical properties of cells.

and allow for very accurate measurements of subcellular structures. On the other hand, the interpretation of the data can be difficult due to the cellular heterogeneity and cell-probe interactions, that in turn depend on the size and shape of the probe. Moreover these approaches are restricted to adherent cells.

The earliest 'global techniques', such as *micropipette aspiration* and *microplate manipulation* allow for very accurate measurements but their throughput is very low. In addition they require a mechanical contact with the cell, which could induce active mechanical responses. Optical methods circumvent this problem as the application of the external stress is contact-free. The *optical tweezers* can generate forces in the range 0.1 to 200 pN that are usually not sufficient to globally deform a cell. Moreover, the application of a high power, focussed laser beam can potentially damage the cell. Therefore this technique is mainly employed to perform local measurements. The *optical stretcher* enables the accurate application of step-like or oscillatory loads, in a serial way, to large samples of suspended cells and measure their mechanical response with a throughput in the range of 100 cell/h. The highest throughput can be achieved with microfluidic methods, which allow one to probe extremely large cell populations with or without mechanical contact.

4.1.4 Applications in biomedical diagnostics

A growing body of evidence suggests that cellular response to an applied load can provide valuable information on the organisation of the cytoskeleton. In addition, disease-related alterations of this organisation are closely linked to changes in the mechanical properties of the cell (Cross et al., 2007) . The assessment of cell deformability provides a label-free biomarker for probing cellular characteristics namely: cell-cycle

4.1. INTRODUCTION AND BACKGROUND

stage (Théry and Bornens, 2008), differentiation state of stem cells (Pajeroski et al., 2007), metastatic state of cancer cells (Guck et al., 2005; Cross et al., 2007). From a clinical prospective, biopsy samples and biological fluids could be analysed and this would allow for an additional guidance for treatment decisions, enabling a personalised medicine approach (Gossett et al., 2012). Moreover, effects of specific drugs targeting the cytoskeletal integrity can be tested.

To account for the inherent heterogeneity of biological samples, diagnostic techniques need to provide high throughput characterisation of individual cells. A disease might involve a small sub-populations of cells, therefore the capability of detecting rare cellular anomalies is a key requirement. All the techniques listed in Table 4.1 allow for single-cell analysis but only a few enable high throughput measurements. Among all, microfluidic methods, and especially their combination with high-speed imaging and computer-aided automatic tracking, are proving to be a practical solution to the discussed biomedical requirements. Small volumes of cell solutions can be handled through a variety of micro-patterned topologies that induce observable strains on each cell. In this way, several thousands of cells can be analysed in few seconds and their global mechanical properties extrapolated and statistically analysed (Gossett et al., 2012; Dudani et al., 2013; Otto et al., 2015). On the other hand, these techniques are still lacking the spatial and temporal sensitivity needed to investigate the cell at the local level, where other techniques, like AFM and micropipette aspiration, excel. Moreover, microfluidic methods do not allow for a trivial way of applying oscillatory stresses, important to investigate time-dependent rheological properties.

4.1.4.1 Early detection of prostate cancer

Prostate cancer is the second most common type of cancer in the world and the fifth highest cause of cancer-related deaths in men (Siegel et al., 2015). Early prostate cancer is usually asymptomatic, about 50% of men over 50 may have cancer cells in their prostate, and the percentage grows to over 80% at the age 80 (Hricak and Scardino, 2009).

Blood tests are commonly used to check the level of the prostate specific antigen (PSA). On the other hand, these tests are non-specific for prostate cancer (Faria et al., 2008) and for instance, an enlarged or inflamed prostate can cause elevations in PSA levels. Values above the standard level of 4.1 ng/ml are considered as indicative of the need for a biopsy (Morote et al., 1997).

Currently, the aggressiveness this tumour is assessed by using the Gleason scoring system that evaluate the morphological architecture of histologic samples (Humphrey, 2004). The arrangement of the cells within the prostatic tissue sections are visually inspected and a score is assigned based on their pattern. However, this method is characterised by a higher degree of subjectivity, as well as intraobserver and interobserver variability (Allsbrook et al., 2001; Humphrey, 2004). Moreover, because of the heterogeneous and multifocal nature of this disease the likelihood of missing the lesion during the biopsy is high. Therefore, early-stage diagnosis is not effective and this makes treatments extremely invasive. Thus, new methods would be required to improve the existing clinical setting.

Although the common diagnostic techniques are mainly based on the measurement of biochemical markers, intrinsic biophysical properties might be used to assess the

4.1. INTRODUCTION AND BACKGROUND

presence and the state of the disease. For instance, it has been shown that measuring the cellular elasticity not only allows to discriminate between cancer and healthy cells, but also to determine their metastatic potential: more aggressive cells are, in fact, softer than less aggressive ones (Guck et al., 2005; Faria et al., 2008). In recent years a few techniques have emerged with the aim of looking at cellular mechanical properties (Guck et al., 2005; Cross et al., 2007; Pajerowski et al., 2007), but their translation into clinical practice has been limited mainly due to their low throughput.

4.2 Aims and Objectives

In the work described in this chapter I aimed to develop an experimental set-up that would allowed me to accurately and robustly analyse the global mechanical properties of different cell types. At first, I focussed on the development of a *microfluidic optical stretcher* (Lautenschlaeger and Guck, 2009) that enabled me to characterise the viscoelastic mechanical response of red blood cells (RBCs). The emergence of new microfluidic techniques and the acquisition of a high-speed camera by my group gave me the opportunity to explore a different approach to investigate single-cell deformability. The *hydrodynamic stretcher* (Dudani et al., 2013) allows for a throughput that is orders of magnitude higher than that achievable with the optical stretcher and overcomes some of the limitations associated with it. Therefore, I decided to focus on the development of a hydrodynamic stretcher by which I sought:

1. To test whether the technique was capable of detecting the effect of Latrunculin A, that is known to prevent actin filaments from polymerising and globally soften the cytoskeleton.
2. To test the capability of differentiating cells from different tissues, namely prostate and bladder, based on their deformability.
3. To investigate the possibility to discriminate samples of healthy and cancerous prostate cell based on the cellular deformability.

4.3 Methods

4.3.1 Optical stretching

An *Optical Stretcher* consists of two counter-propagating, divergent and identical laser beams (Guck and Ananthakrishnan, 2000; Guck et al., 2001). Each laser beam imposes an optical force to a dielectric object that is placed along the axis of the propagation. In the case of two identical counter-propagating beams, the optical forces balance each other in the centre of mass of the particle, that in turn becomes stably trapped. These forces arise from the momentum exchange between the photons that impinge on the particle and its surface. Therefore, even if the total force acting on the centre of the particle is zero, the surface forces are not. If the particle is deformable, e.g. a cell, such surface forces are able to induce a mechanical deformation of the object along the axis of the beam that depends on the intensity of the incident beams (Guck and Ananthakrishnan, 2000). It is well known that structural changes of the cytoskeleton cause changes in the mechanical response of the cell. For instance, normal, cancerous and metastatic breast epithelial cells have been classified by comparing their optical deformability (Guck et al., 2005). The advantages of this technique are that it does not require mechanical contacts and that the sample can be non-adherent to any substrate, moreover the global mechanical properties of the object can be assessed (Wottawah et al., 2005; Guck et al., 2005; Huber et al., 2013).

4.3.1.1 Theoretical explanation

When dealing with biological samples the choice of the laser wavelength is important. In the near-infrared (NIR) region of the spectrum proteins and chromophores in most eukaryotic cells manifest minimum absorption, and therefore optically-induced damages can be limited (Guck and Ananthkrishnan, 2000; Lincoln et al., 2007b). As the wavelength of the laser λ is in the range of $1 \mu\text{m}$ and the diameter d of an eukaryotic cell is in the order of tens of microns, hence $d \gg \lambda$. This limit is known as *Mie regime*, where a laser beam can be treated as a bundle of rays that propagate in straight lines, in a uniform and non-dispersive medium, and described using geometric optics (Guck et al., 2002; Bhushan, 2010). In such a regime, the interaction between the light and a dielectric object can be explained by momentum transfer. The momentum \mathbf{p} carried by a photon is

$$\mathbf{p}_{\text{photon}} = n \frac{E}{c_0} \mathbf{e}, \quad (4.14)$$

where $E = h\nu$ is the energy of a photon, ν its frequency and h the Planck's constant, c_0 the speed of light in vacuum and n the refractive index and \mathbf{e} the unit vector along the direction of propagation.

When the laser beam, composed by N photons, hits the interface between the particle and the surrounding medium with an angle θ , the ray is refracted according to the Snell's law:

$$n_m \sin(\theta) = n_p \sin(r), \quad (4.15)$$

where n_m and n_p are the refractive indexes of the surrounding medium and the particle, respectively and r the angle of the refracted ray. As the total momentum must

4.3. METHODS

be conserved at the interface, a momentum exchange between the photons and the particle occurs. The momentum acquired by the particle is

$$\mathbf{p}_{\text{res}} = Nn \frac{E}{c_0} \mathbf{e}_{\text{res}}, \quad (4.16)$$

where \mathbf{e}_{res} is the unit vector in the direction of the resulting momentum. The resulting force, acting on the particle's centre of mass, can be calculated using Newton's second law:

$$\mathbf{F}_{\text{res}} = \frac{d\mathbf{p}_{\text{res}}}{dt} = n \frac{N}{c_0} \frac{dE}{dt} \mathbf{e}_{\text{res}} = Nn \frac{P}{c_0} \mathbf{e}_{\text{res}}, \quad (4.17)$$

where P is the power of the beam. The resulting force can be decomposed into the two components depicted in Fig. 4.5:

- *Scattering force*, $\mathbf{F}_{\text{scatt}}$, that tends to push the particle in the direction of the beam.
- *Gradient force*, \mathbf{F}_{grad} , that draws the particle into regions of higher intensity.

Therefore,

$$\mathbf{F}_{\text{res}} = \mathbf{F}_{\text{grad}} + \mathbf{F}_{\text{scatt}}, \quad (4.18)$$

where:

$$\begin{aligned} \mathbf{F}_{\text{grad}} = & \frac{n_m}{c_0} \int_0^{\pi/2} d\theta \int_0^{2\pi} I(\theta, \phi, \rho) \rho^2 \sin^2(\theta) \sin(\phi) \times \\ & \times \left\{ R(\theta) \sin(2\theta) - \frac{T(\theta)^2 [\sin(2\theta) - 2r] + R(\theta) \sin(2\theta)}{1 + R(\theta)^2 + 2R(\theta) \cos(2r)} \right\} d\phi, \end{aligned} \quad (4.19)$$

$$\begin{aligned} \mathbf{F}_{\text{scatt}} = & \frac{n_m}{c_0} \int_0^{\pi/2} d\theta \int_0^{2\pi} I(\theta, \phi, \rho) \rho^2 \sin(\theta) \cos(\phi) \times \\ & \times \left\{ 1 + R(\theta) \cos(2\theta) - \frac{T(\theta)^2 [\cos(2\theta) - 2r] + R(\theta) \cos(2\theta)}{1 + R(\theta)^2 + 2R(\theta) \cos(2r)} \right\} d\phi, \end{aligned} \quad (4.20)$$

where n_m is the refractive index of the surrounding medium, $T(\theta)$ and $R(\theta)$ are the

Fresnel coefficients. In the case of a dual-beam optical trap, where two counter-

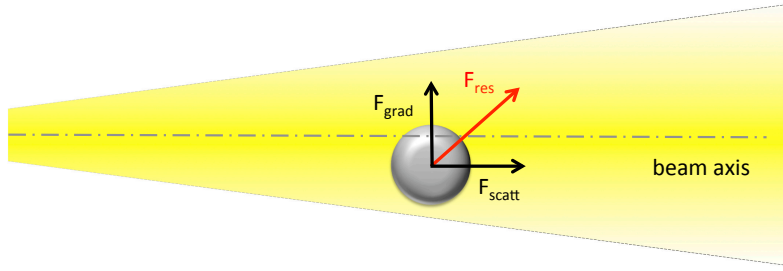


Figure 4.5: Laser beam interacting with a dielectric particle. Two forces act on the particle's centre of mass: the *scattering force*, $\mathbf{F}_{\text{scatt}}$, that pushes the particle in the direction of the beam and the *gradient force*, \mathbf{F}_{grad} , that pulls the particle towards the axis of the beam. The resulting force is indicated by the red arrow.

propagating laser beams are incident upon the particle, the scattering forces balance each other in the middle of the trap whereas the gradient forces add up to provide a stable trap at the beam axis, as shown in Fig. 4.6. Once the particle falls into the

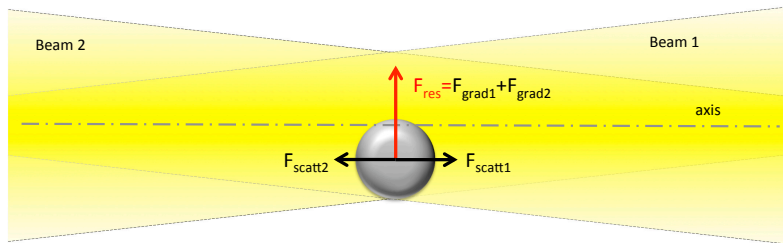


Figure 4.6: Dual-beam optical trap. The scattering forces associated with each beam balance each other in the middle of the trap, whereas the gradient forces add up to provide a stable trap at the beam's axis.

optical trap the resulting force acting on its centre of mass is zero. On the other hand, the surface forces, arising at each surface element of the interface due to momentum exchange between every single ray and the particle, cannot be neglected (Guck et al., 2002). The net change in momentum for each ray is:

$$\Delta \mathbf{p} = \mathbf{p}_i - \mathbf{p}_{\text{refr}} - \mathbf{p}_{\text{refl}}, \quad (4.21)$$

4.3. METHODS

where $\mathbf{p}_i = n_m E/c$, $\mathbf{p}_{\text{refr}} = n_p(1 - R)E/c$ and $\mathbf{p}_{\text{refl}} = n_p R E/c$ are the momentum of the incident, refracted and reflected rays, respectively. The amount of light that is refracted into the cell and reflected back depends on the angle of incidence. On the other hand, the rays that travel through the cell gain momentum due to its higher refractive index compared to the outer medium. This effect dominates the change in momentum associated with the reflected light, as cells are almost transparent (Guck et al., 2002). This leads to a net outward force (Guck et al., 2001, 2002). Therefore, the fraction of reflected light, R , at normal incidence ($\theta = 0^\circ$) equals:

$$R = \left(\frac{n_{\text{cell}} - n_m}{n_{\text{cell}} + n_m} \right)^2. \quad (4.22)$$

For a $n_{\text{cell}} = 1.380$ and $n_m = 1.335$, R is in the order of $\approx 0.03\%$ and therefore \mathbf{p}_{refl} can be neglected.

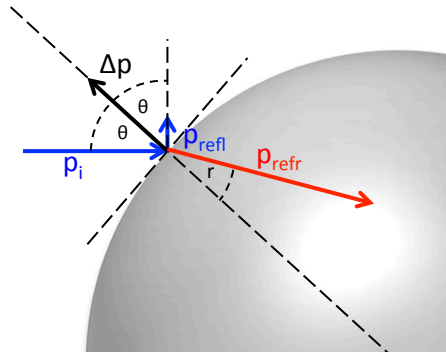


Figure 4.7: Momentum exchange between an incident ray and a dielectric particle. As $n_p > n_m$ for each ray hitting the particle, the resulting momentum (and therefore the resulting force) is perpendicular to the surface and points towards the surrounding medium. It can be noticed that the contribution of the loss in momentum due to the reflected light can be neglected. Adapted from Guck et al. (2002).

The resulting surface forces are perpendicular to the interface and point towards the surrounding medium, as a result of the increased momentum due to the higher refractive index inside the cell, as shown in Fig. 4.7.

The spherical particle induces a lensing effect on the incoming rays: when a ray travels through the particle, it leaves the particle at a point that is closer to the axis of the beam, as shown in Fig. 4.8. This leads to a decreased component of the forces in the direction perpendicular to the beam axis at the exiting side. Overall, the particle tends to be pushed by the radiation pressure in the direction of the beam. In the dual-

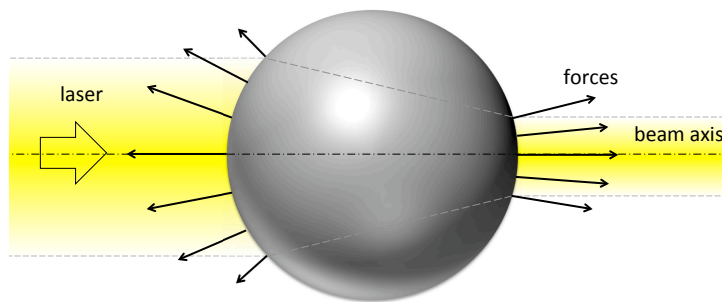


Figure 4.8: Lensing effect of a spheric object on a laser beam. The black arrows represent the surface forces that arise from the momentum exchange of individual rays at the interface. At the right-hand side, where the rays exit the particle, the surface forces have a smaller component perpendicular to the direction of the propagation. The net force on the sphere pushes the particle in the direction of the laser. Adapted from Guck et al. (2002).

beam configuration the particle is firmly trapped and the net force acting on it is zero. Conversely, if the particle is elastic the surface forces tend to push the interface at the exiting side in the direction of the beam. Each laser beam induces such an effect onto the opposite edges of the deformable object, leading to a overall elongation along the axis of the beams, as shown in Fig. 4.9. The optical stress is propostional to the intensity of the incident beams.

4.3.1.2 Experimental set-up

In this section I describe the optical stretcher that I developed. The set-up was implemented in its opto-fluidic version, similarly to that presented by Lincoln et al. (2007a) where two optical fibres are held perpendicularly to a glass capillary by the use of a

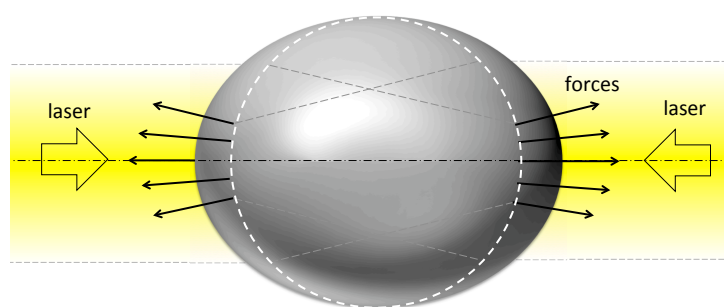


Figure 4.9: Mechanical deformation induced by the dual-beam optical trap to an elastic particle. The net force acting on the particle is zero but the surface deforms according to the force profile that is proportional to the intensity of the beams. Adapted from Guck et al. (2002).

SU-8 structure. In my setup such a structure was replaced with a PDMS holder. The laser source was a 10 W, single mode, IR, cw, yttrium fibre laser (YLR-10-1070-LP, IPG Photonics). The laser beam travels through an optical isolator (IO-3-1064-HP, Free-Space Isolator, Thorlabs) and a beam splitter, where it splits in two halves. Each half is then coupled into a single mode optical fibre (1060XP, Thorlabs) thanks to a couple of steering mirrors, and a fibre collimator (FC/APC fixed focus collimation packages, Thorlabs). The latter was mounted on a mirror mount to facilitate the coupling of the beam with the 6 μm core of the fibre.

The two optical fibres have a FC/APC connectorised end and a pigtailed one. The former was connected to the fibre collimator, while the latter is stripped, cleaved using a fibre cleaver (precision fibre optic cleaver, Fitel) and placed in the proximity of a square cross-section glass capillary (Virtrocells, 0.05 square ID, VitroCom) as depicted in Fig. 4.11. Each end of the capillary was connected to a TFE tubing (0.8 mm ID, 1.58 mm OD, Supelco) through a custom made PDMS connector, whereas the other end of the tubings connected to an open syringe.

Cell solutions were loaded into one of the two syringes and the flow controlled hydrostatically by varying the relative height of the two syringes. The diameter of the fibres'

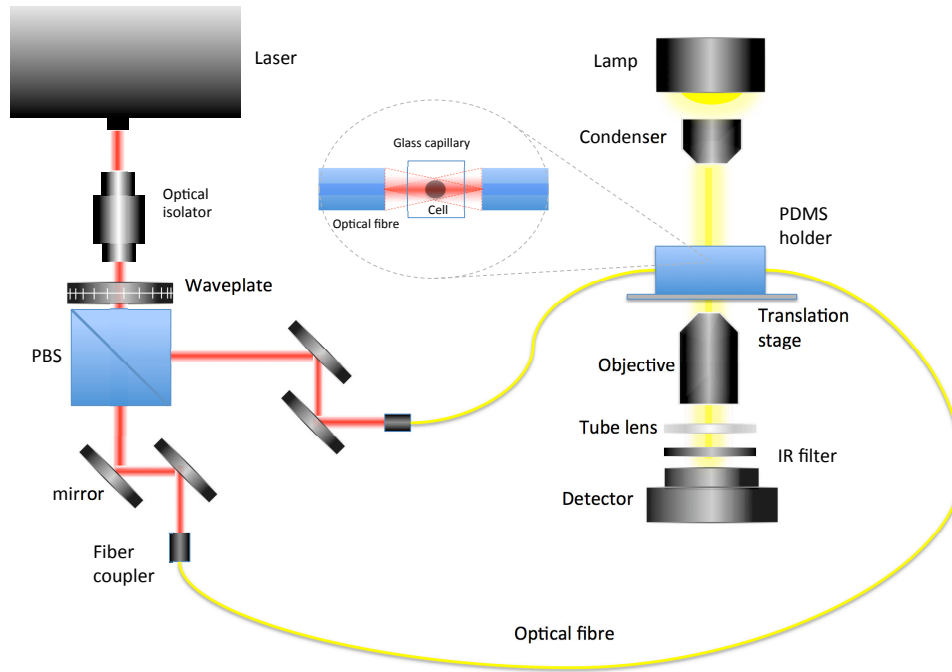


Figure 4.10: Schematics of the optical set-up of the opto-fluidic stretcher.

cladding was $125\ \mu\text{m}$, while the capillary was $160\ \mu\text{m}$ wide and its walls were $40\ \mu\text{m}$ as shown in the inset in Fig. 4.11.

In this configuration the beam axis was approximately $22.5\ \mu\text{m}$ above the internal floor of the capillary, and therefore accounted for the rapid sinking of the cell and enabled the possibility to optically manipulate them.

The beam waist depends on the distance between the fibres and the capillary z_{f-c} and the distance between the cell and the internal wall of the capillary z_m (Lincoln et al., 2007b):

$$w = w(z_{f-c}, z_m) = w_0 \sqrt{1 + \frac{B_T^2}{z_0^2}}, \quad (4.23)$$

where:

$$B_T = \left(\frac{z_m}{n_m} + \frac{z_{\text{glass}}}{n_{\text{glass}}} + \frac{z_{f-c}}{n_{\text{air}}} \right) n_{\text{air}}, \quad (4.24)$$

4.3. METHODS

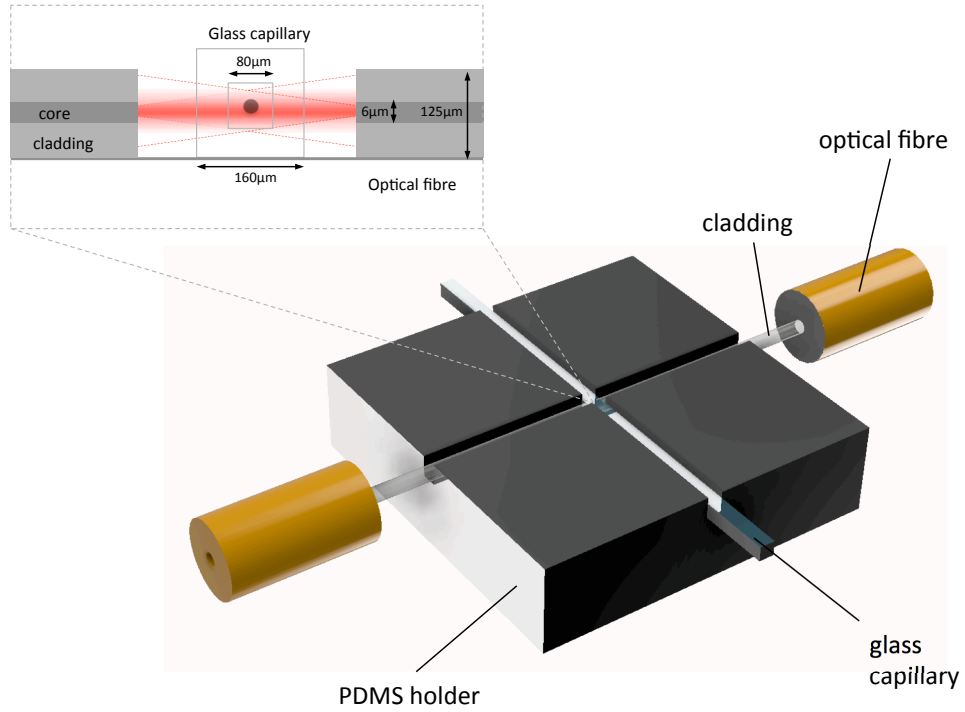


Figure 4.11: Schematics of the opto-fluidic stretcher. A PDMS support holds the bare end of two optical fibres and glass capillary. The fibres are aligned perpendicularly to the glass capillary. The inset shows the vertical arrangement of the bare ends of the optical fibres and the glass capillary.

$$z_0 = \frac{n_{\text{air}} \pi w_0^2}{\lambda}, \quad (4.25)$$

where $n_{\text{air}} = 1$, $n_{\text{glass}} = 1.474$, $n_{\text{m}} = 1.335$, $z_{\text{glass}} = 40 \mu\text{m}$ is the thickness of the capillary's wall. The imaging apparatus comprised:

- A LED lamp in *critical illumination* arrangement where the light was focussed onto the sample through a 10x condenser.
- A translational stage (M-562 Series, Newport) that allowed for a precise positioning of the sample in three dimensions.
- A long working distance 100x objective (Plan APO, SL, Mitutoyo).
- A Firewire CCD camera (EC1280, Prosilica Inc) operating at 20 frames/sec.

To impart a step-stress optical force onto cells, a control over the laser power was

necessary. Therefore, I developed a sub-VI (Virtual Instrument) in LabVIEW (Laboratory Virtual Instrument Engineering Workbench) to control the laser source through a GPIB cable. This subVI was then integrated into a existent VI, previously developed to control a CCD camera, so that imaging and stretching could be performed simultaneously using the same graphical interface. A snapshot of the entire graphical interface is shown in Fig. 4.12: the buttons and the options for the image acquisition are visible on the left hand side, the rectangular region shows the image acquired through the CCD camera (in this case the glass capillary) and the commands for the laser control are shown in the inset. The program was set to send a rectangular signal to the laser: the minimum current corresponds to the minimum power sufficient to trap cells, whereas the maximum current corresponds to the stretching power. Minimum and maximum current, as well as the trapping and stretching time can be independently controlled by changing the numbers in the proper fields. A switch button activates the stretching signal.

4.3.1.3 Image analysis

To analyse the cellular deformation within image sequences I used the 'Active Contours' plug-in of the open source software ICY (Dufour et al., 2011). This plug-in allows to extract the outline of an object and to track it over time. First of all it requires an initial region of interest (ROI) that identifies the object, in this case a circle is drawn around the cell. The edge of the object is then used as the initial position to segment the successive frame. The search for the contours is automatically iterated for the entire sequence. This plug-in relies on the definition of an energy functional that is minimised as a result of the optimal positioning of a polygonal contours closest to

4.3. METHODS

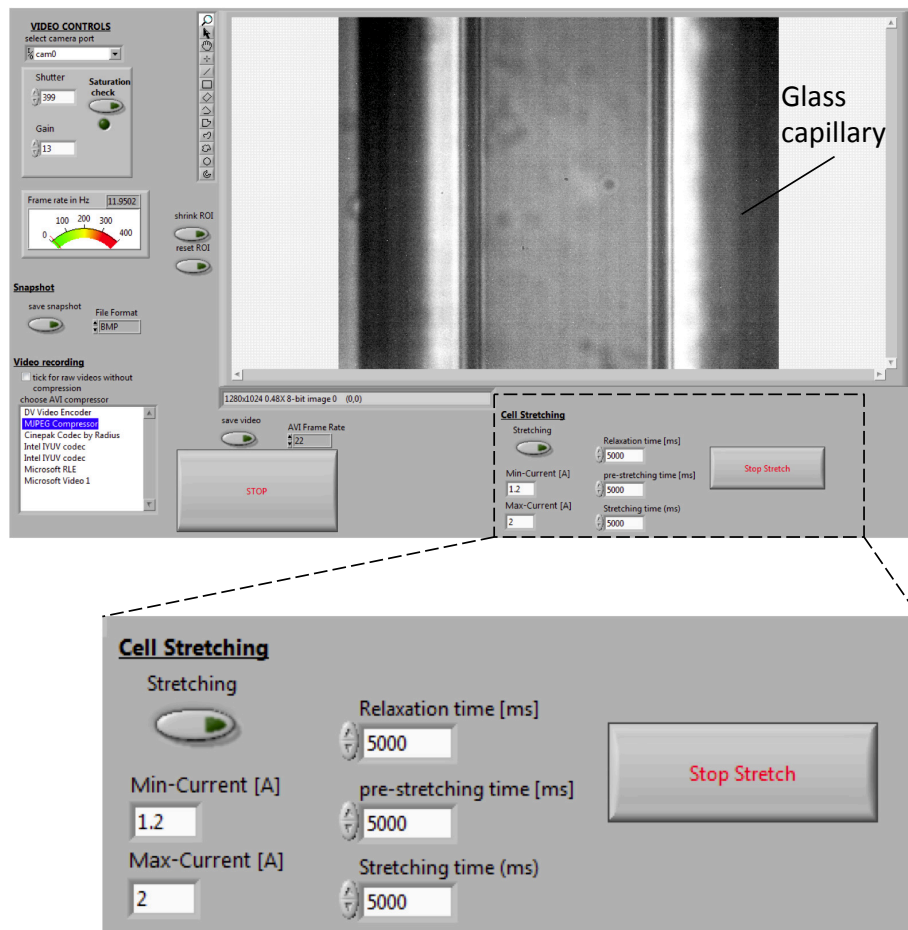


Figure 4.12: Screenshot of the graphical interface of the LabVIEW VI to control the laser power: the buttons and the options for the image acquisition are visible on the left hand side, the rectangular region shows the image acquired through the CCD camera. The inset shows the commands for the laser control that allows one to send a rectangular signal to the laser: the minimum current corresponds to the trapping power, while the maximum current corresponds to the stretching power. The duration of the stretching can also be controlled. The switch button enables the stretching signal.

the boundary of the object of interest. The contour evolution depends on the choice of the appropriate parameters of the plug-in. Once the edge of the cell is correctly tracked over time informations of the fitting ROIs can be exported in a spreadsheet file and quantitatively analysed.

4.3.1.4 Cell preparation

To test the optofluidic stretcher I made use of Red Blood Cells (RBCs) extracted from sheep (Innovative Research Inc.). This cell type has been extensively exploited as a model system for this sort of experiment due to their structural properties: they lack internal organelles, they have a homogeneous hemoglobin internal composition and they are very soft (Guck et al., 2001). Moreover, their elastic properties have been well characterised (Zeman et al., 1990; Discher et al., 1994). Under physiological conditions in isotonic serum-containing media, healthy erythrocytes assume a biconcave discoid shape, but upon osmotic swelling they become spherical. This makes it easier to quantitatively analyse their deformation (Sraj et al., 2012). To achieve cell swelling, 5 μL of concentrated erythrocytes were mixed with 5 mL of a hypotonic solution of PBS buffer (Sigma-Aldrich, Gillingham, UK) and de-ionized water (1:1).

4.3.2 Hydrodynamic stretcher

The first microfluidic studies of cellular mechanics were carried out by flowing cells through narrow constrictions and measuring the cell transit time, whose magnitude was used as an indirect readout of the cellular stiffness (Abkarian et al., 2006; Rosenbluth et al., 2008). On the other hand, the width of the constrictions is fixed and hence one cannot account for the size heterogeneity of the samples. Additionally, as cells squeeze through the narrow channel, their adhesiveness and size influence their transit time.

In solving these limitations, a few recent studies have emerged where cellular mechanical phenotyping was performed using hydrodynamic forces, previously employed in many lab-on-a-chip devices for particle or cell trapping (Hur et al., 2011), sorting (Di

4.3. METHODS

Carlo, 2009), focussing (Di Carlo et al., 2007), and rotation (Shelby and Chiu, 2004). Using this method, Dudani et al. (2013) demonstrated the capability of assessing the cellular 'deformability' with a maximum throughput of about 115,000 cells/s. This technique consists of a dual counter-propagating fluxes that apply a pinching flow perpendicularly to the cells that flow along the main channel. The cells were deformed due to the hydrodynamic stress generated by the lateral pinching fluxes.

4.3.2.1 Theoretical explanation

The microfluidic chip that I developed is based on that proposed by Dudani et al. (2013) and its schematic is shown in Fig. 4.13. The cell solution is introduced into the system through the inlet (Fig. 4.13). The asymmetric wavy structure highlighted by the first rectangle in Fig. 4.13 acts as an inertial focuser. It is composed by alternating bends with different radii of curvature and widths. As explained by Di Carlo et al. (2007) such a geometry has two main important implications:

1. Suspended cells flowing through it become focussed down to a single stream, centred in the middle of the straight channel downstream of the inertial focuser.
2. Cells tend to be evenly spaced along the stream. Such a particle ordering is the result of the proper ratio between the secondary Dean flow and inertial lift that, in turn, depend on channel's dimensions, aspect ratio, radius of curvature, particle diameter, and flow rate.

To explain how a suspended spherical object become focussed downstream of the inertial focuser, two dimensionless numbers need to be defined (Di Carlo et al., 2007):

$$R_c = \rho \frac{v_{\max} D_h}{\mu}, \quad (4.26)$$

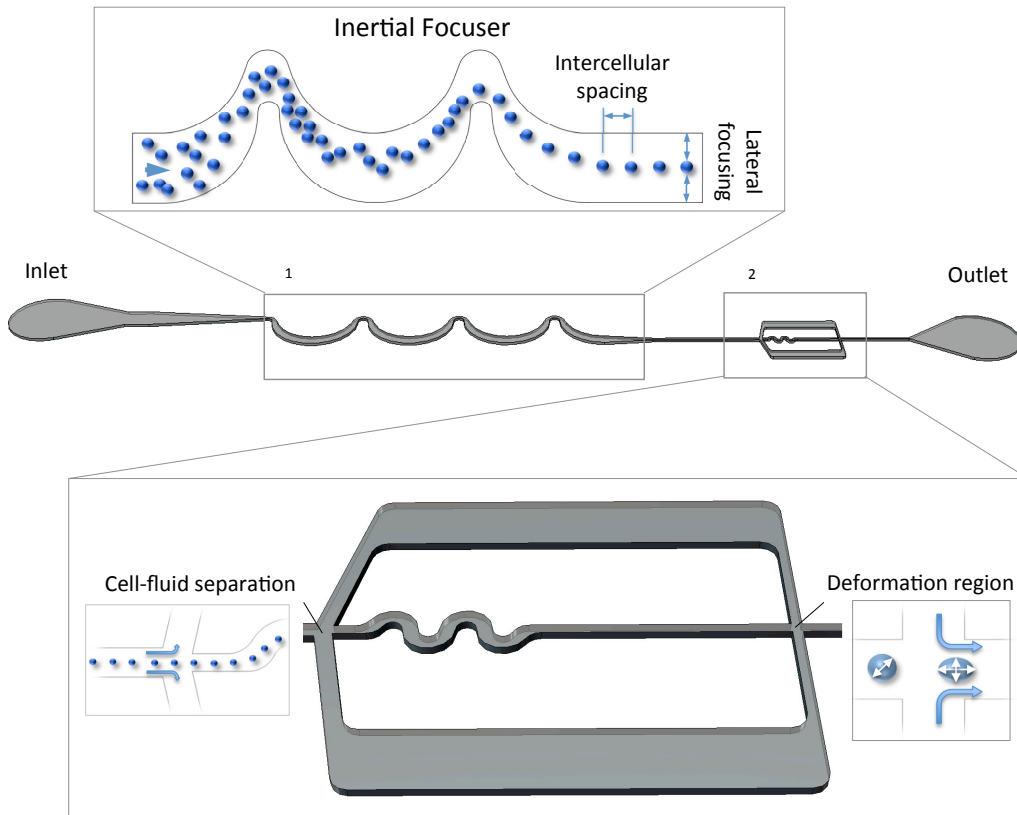


Figure 4.13: Schematic of the hydrodynamic stretching device. Cell solutions are loaded through the inlet, flow through the inertial focuser (rectangle 1) where cells become focused down to the centreline of the channel. In addition, cells become evenly spaced along the direction of the flow. At the first junction (the 'cell-fluid separation' region within the rectangle 2) the ordered streak of cells tends to travel straight into the second inertial focuser, whereas the peripheral fluid, devoid of cells, is split in each lateral arms of the junction. The three fluxes regather at the 'deformation region' where the streams coming from the two symmetric branches establish a pinching flow.

that is the *channel Reynolds number* and the *particle Reynolds number*,

$$R_p = R_e \left(\frac{a}{w} \right)^2 = \rho a^2 \frac{v_{\max}}{D_h \mu}, \quad (4.27)$$

where a is the diameter of the particle (in this case a cell), v_{\max} is the maximum velocity of the fluid, $D_h = 2wh/(w + h)$ is the *hydraulic diameter*, w and h are the width and the height of the channel, μ and ρ are the dynamic viscosity and the density of the fluid, respectively. Typically, a particle flowing in microchannels is characterised by $R_p \ll 1$. In this regime the main force acting on the particle is the viscous drag

4.3. METHODS

(Di Carlo et al., 2007) and particles do not migrate across streamlines. If R_p increases the *lift forces* become dominant: the 'wall effect' tends to lift the particles away from the channel's walls, while the shear-gradient tends to push the particle towards them. The lift forces in a parabolic flow between two infinite plates, for $R_p < 1$ can be

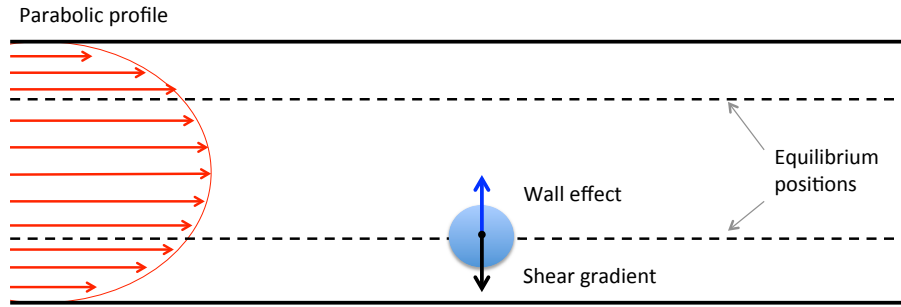


Figure 4.14: Lift forces acting on a suspended particle flowing in a microchannel: the 'wall effect' lifts the particle away from the walls and the shear gradient pushes the particle towards the walls. The combined effect of these two forces lead induce the particles to flow along the equilibrium position.

represented by

$$F_z = \frac{\rho v_{\max}^2 a^4}{D_h^2} f_c(R_c, \chi_c), \quad (4.28)$$

where: f_c is a function of R_c and of the position χ_c of the particle within the cross-section of the channel (Asmolov, 1999). This force tends to move the particle towards the equilibrium position, where $f_c = 0$. Additionally, if the channel is curved the particle is also subjected to the Dean flow. This secondary flow originates from the velocity difference between the stream at the centre and at the peripheral regions of the channel. In fact, at the central region, the fluid experiences a bigger tendency to flow towards the external side of the curve, due to its parabolic profile. To conserve mass, the peripheral liquid flows inwards giving rise to a couple of vortices, which rotate in opposite direction, below and above the mid-line, and perpendicularly to the

primary flow (Di Carlo, 2009). The magnitude of this secondary flow is given by the Dean number,

$$D_e = R_e \sqrt{\frac{D_h}{2R}}, \quad (4.29)$$

where R is the radius of curvature of the channel and $R_e = 2/3R_c$ is the Reynolds number $R_e = \rho v_{\text{mean}} D_h / \mu$ (Ito, 1987). The force associated with the Dean flow is proportional to

$$F_D \propto \frac{\rho v_{\text{max}}^2 a D_h^2}{R}, \quad (4.30)$$

as shown by Squires and Quake (2005). The interplay between lift and Dean forces determines the equilibrium positions of a particle in a curved channel (Di Carlo et al., 2007). It can be demonstrated experimentally that asymmetric consecutive bends lead to a single equilibrium position in the middle of the channel and therefore the particles become aligned along a focussed streak downstream of the inertial focuser (Di Carlo et al., 2007). On the other hand, the causes of the longitudinal regular spacing is still not fully understood but may be due to particle-particle interactions within and across the cross section of the microchannel (Russom et al., 2009).

At the first junction in Fig. 4.13, the ordered cell train tends to flow straight on, and any deviation from the centreline is adjusted by the second inertial focuser. The peripheral fluid, devoid of cells, leaves the main channel at the 'cell-fluid separation' region and flows into the two symmetric side arms. At the second junction the main flow, containing an ordered and centred streak of cells becomes pinched by the two fluxes coming from the side branches. In the 'deformation region' cells undergo a shape change from sphere-like to ellipse-like due to the contribution of two main forces: the first is the

4.3. METHODS

drag force, best described by the equation:

$$F_D = \frac{1}{2} \rho C_d A v_{av}^2, \quad (4.31)$$

where ρ is the density of the fluid, C_d the drag coefficient, A the cross section of the cell and v_{av} the average velocity of the fluid in the side arms (Gossett et al., 2012).

For $1 < Re < 800$, that is referred to as the *transition regime*, C_d can be expressed as (Clift et al., 2005):

$$C_d = \frac{24}{Re} (1 + 0.15 Re^{0.687}). \quad (4.32)$$

The drag force is exerted onto the cells by the side fluxes, perpendicularly to the direction of the main stream. In this case The second contribution is the *viscous force* (Gossett et al., 2012), that arises from the difference in fluid speed across the pinched flow region, due to the sum of the three fluxes that rejoin:

$$F_V = \mu \frac{\Delta v}{\Delta y} S, \quad (4.33)$$

where μ is the dynamic viscosity of the fluid, Δv is the difference in fluid speed between two points, A and B , respectively upstream and downstream of the cell at the pinched flow region. Δy corresponds to the distance between A and B along the axis of the flow.

4.3.2.2 Device fabrication and experimental set-up

The mould of the microfluidic chip was developed using the photolithographic techniques illustrated in Chapter 1. To obtain 30 μm high microchannels I used the photopolymer SU8-2050 (Microchem) and I followed the protocol in Table 4.2.

Soft lithography was adopted to cast the patterned devices using polydimethylsiloxane

Step	Description
COAT	5000 rpm for 60 sec
SB	3 minutes at 65°C, 6 minutes at 95°C
EXP	60s
PEB	6 minutes at 95°C
DEV	5 minutes
HB	30 minutes at 150°C

Table 4.2: Microfabrication steps to develop the mould for the hydrodynamic stretcher.

(PDMS) (Sylgard 184 Silicone Elastomer Kit). Ports were punched through the inlets and outlets regions using 1 mm biopsy punches (Harris Uni-Core, Sigma-Aldrich). Patterned PDMS was bonded to standard microscope glass slides (VWR) using a glow discharge system (Agar Scientific). Cell solutions were loaded into the devices using a syringe pump (Harvard Apparatus) through 1/16 inches teflon tubing. Microfluidic chips were held onto a Nikon Eclipse TE2000-U equipped with a high-speed camera (FASTCAM SA-X2, Photron). Cellular deformation was imaged at the resolution of 256x80 pixels, frame rate of 300,000 fps, using a 20x objective (Nikon CFI TU Plan Epi ELWD 20x, NA=0.40, WD=19.0 mm). The illumination used was the built-in halogen lamp of the microscope, operating at the maximum intensity, the exposure time of the camera was set at 0.29 μ s allowing for minimal motion blur.

4.3.2.3 Numerical simulation

The stationary solution of the incompressible Navier-Stokes equation for a Newtonian fluid:

$$\frac{\partial \mathbf{v}}{\partial t} + (\mathbf{v} \cdot \nabla) \mathbf{v} - \nabla \cdot (\mu \nabla \mathbf{v} + \nabla \mathbf{v}^T) + \nabla p = \mathbf{F}; \quad \nabla \cdot \mathbf{v} = 0, \quad (4.34)$$

4.3. METHODS

was calculated using Comsol Multiphysics 5.1 for the actual 2D geometry that characterises the device. Specifically, I exploited the axial symmetry of the flow along the vertical axis to simplify the problem from 3D to 2D. In the Eq. 4.34 \mathbf{v} is the velocity of the flow, p is the pressure, μ is the dynamic viscosity and \mathbf{F} the total external force. 'No-slip' boundary conditions were applied at the channels' walls, 'laminar inflow' of 800 $\mu\text{L}/\text{min}$ was set at the inlet and a pressure of 1 atm at the outlet. The physical properties of water at room temperature were used, namely $\rho = 1000 \text{ Kg}/\text{m}^3$ and $\mu = 0.001 \text{ Pa} \cdot \text{s}$.

4.3.2.4 Cell culture protocol

Prostate cancer cell line DU145, the bladder cancer cell line 5637 and the healthy prostate cell line PNT2 were purchased from LGC Standards (Teddington). The first two cell lines were cultured in Corning T-75 flasks (VWR) using Dulbecco's Modified Eagle Medium (DMEM), whereas for the latter cell line RPMI medium was used. In both cases 10% Fetal Bovine Serum and 1% Penicillin-Streptomycin were added (all Sigma-Aldrich). Flasks of cells were maintained in CO_2 controlled 37°C incubator until 70% confluent. Samples were prepared for analysis once 70% confluent by removing supernatant media, washing each flask with 5 mL Trypsin-EDTA (Sigma-Aldrich) and incubating with 3 mL Trypsin-EDTA until cells had detached. Trypsin was neutralised using 7 mL pre-warmed complete DMEM. After trypsinisation, cells were spun at 1500 rpm for 5 minutes to form a pellet. Pellets were gently resuspended in 2 mL pre-warmed complete DMEM and samples were placed on ice until required for analysis.

4.3.2.5 Treatment with Latrunculin A

Latrunculin A (Sigma-Aldrich) dissolved in dimethyl sulfoxide (DMSO) to a concentration of 100 μM and diluted in Dulbecco's Modified Eagle Medium/DMEM containing 10% Fetal Bovine Serum and 1% Penicillin-Streptomycin to the concentration of 10 μM . Latrunculin A was added to the cell samples to the final concentration of 1 μM and kept on ice for 1 hour before the experiment.

4.3.2.6 Image and data analysis

Cellular deformation was evaluated manually using ImageJ, by measuring the diameter of the sphere-like cells about 20 μm upstream of the second junction and the deformability (aspect ratio) at the end of the 'deformation region', where the stress is maximum and cells are deformed into an elliptical shape. I used Microsoft Excel, Stat-Plus (AnalystSoft) and SPSS (IBM, version 20) to conduct the statistical analysis. Data were first tested for normality and then non-parametric Wilcoxon rank sum tests were performed to assess differences in deformability between samples of different cell populations. A 95% confidence level was used. The function *dscatter.m* was downloaded from MATLAB file exchange and used in Matlab R2014b (MathWorks) to generate the density scatterplots.

4.4 Results

4.4.1 Optical stretching of erythrocytes

Preliminary measurements were collected using erythrocytes extracted from sheep.

In Fig. 4.15(a) the effect of the optical trapping and stretching can be observed. By

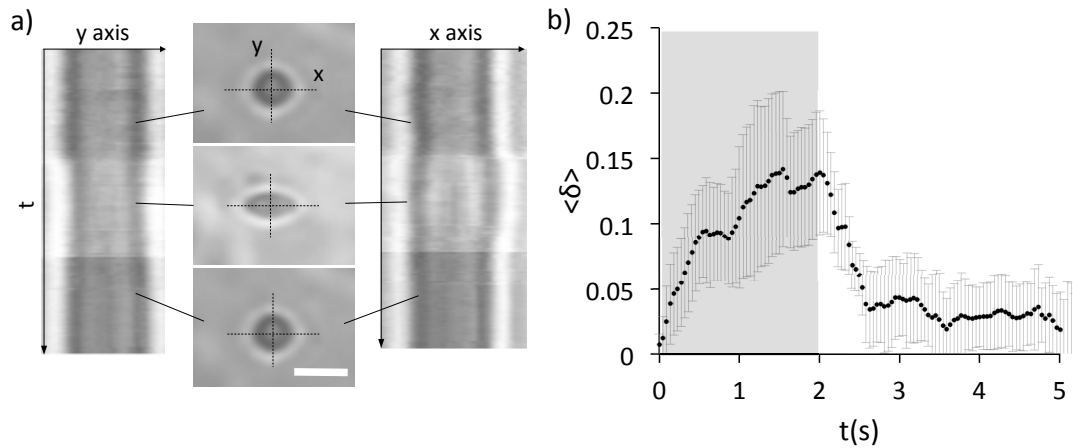


Figure 4.15: Optical stretching of erythrocytes. (a) Three sequential pictures of an erythrocyte optically trapped and stretched. The cell is trapped using a power of 184 mW/fiber and then stretched increasing the laser power to 495 mW/fiber for 2 s. After the deformation the power is restored to the trapping power of 184 mW/fiber. The two kymographs show the temporal evolution of along the two axes of the cell. The brighter regions, in the kymographs and in the figure of the stretched cell, correspond to the increase in the laser power. Scale bar 10 μm . (b) The plot shows the time-dependent strain averaged over three cells. The shaded area corresponds to the time frames in which the power of the laser was increased to the stretching value. The error bars represent the standard error.

increasing the power from 184 mW/fibre to 495 mW/fibre cells elongate along the axis of the beams as shown in Fig. 4.15(a), where the three snapshots in the middle represent a cell, before, during and after the optical stretching. The two kymographs show the deformation of the cells over time along the two axes x and y.

The optical deformation was calculated in terms of relative axial extension, or strain:

$$\delta(t) = \frac{r(t) - r_0}{r_0}, \quad (4.35)$$

where $r(t)$ is the length of the cell along the beam axis at time t after the application of the optical force and r_0 is the initial radius of the cell. Fig. 4.15(b) shows how the strain, averaged over three different cells, varies over time. The profile of the graph is expected for a viscoelastic fluid as explained in section 4.1.2 and in agreement with the literature (Lincoln et al., 2007b). To assess the order of magnitude of the optical force acting on the centre of mass of the cells I performed 'shooting experiments': a cell was trapped in the middle of the capillary using two identical beams, by blocking one of them the cell was pushed by the opposite beam with a certain speed, v . The force acting on the cell can be thought to be equal to the Stokes' drag $F_d = 6\pi\mu r v$ (only valid for $Re \ll 1$ (Batchelor, 2000)), where μ is the dynamic viscosity of the medium (0.00255 $\text{Pa}\cdot\text{s}$ for PBS (Sok Won et al., 2011)), r is the radius of the cell. For a cell of $r = 4 \mu\text{m}$ the estimated force was $\approx 1.89 \text{ pN}$ using a power of 184 mW/fibre.

4.4.2 Hydrodynamic stretching of human cell lines

4.4.2.1 Characterisation of the hydrodynamic stretcher

The cell solution was loaded into the device with a flow rate Q_{in} and cells became focussed to the centre of the channel thanks to the role of the three asymmetric curving channels that compose the inertial focuser. All the parameters involved in the inertial focuser are listed in Table 4.3. Using Comsol I simulated the velocity profile within the region downstream of the inertial focuser shown in Fig. 4.16. The estimated mean speed v_{mean} is 2.84 m/s for both the main and side branches, resulting in a Reynolds number $Re = 113.6$ as indicated in Table 4.4. The velocity profile and the stream lines were evaluated in the presence of a spherical cell at the junction upstream of the pinching flow and in the presence of stretched cell at the pinched flow region as

4.4. RESULTS

Parameter	Small bend	Big bend	Unit	Description
W	98	419	μm	Width
H	30	30	μm	Height
R	168	1330	μm	Radius of curvature
D_h	45.94	55.99	μm	Hydraulic diameter
μ	0.001	0.001	Pa s	Dynamic viscosity
ρ	1000	1000	Kg/m ³	Density
Q_{in}	1.33x10 ⁻⁸	1.33x10 ⁻⁸	m ³ /s	Flow rate
A	2.94x10 ⁻⁹	1.26x10 ⁻⁸	m ²	Cross section
v_{mean}	4.54	1.06	m/s	Mean flow speed
R_e	208.33	59.39		Reynolds number
D_e	77.03	8.62		Dean number

Table 4.3: Hydrodynamic parameters of the small and big bends that compose the inertial focuser.

Parameter	Side branches	Main channel	Unit	Description
W	60	60	μm	Width
H	30	30	μm	Height
D_h	40	40	μm	Hydraulic diameter
v_{mean}	2.84	2.84	m/s	Flow speed
R_e	113.6	113.6		Reynolds number

Table 4.4: Hydrodynamic parameters of the main and side branches that join at the deformation region.

shown in Fig. 4.17. It is important to note that the purpose of this simulation was to assess how the flow profile is affected by the presence of the cell. Therefore, the steady-state solution of the 2D problem was estimated for all the cases, where the cell was treated as a fixed, impenetrable domain, whose aspect ratio resembled real values exhibited in the experiments. 'No-slip' boundary conditions were applied to the cell's edges. Such a simulation highlights that the reconstruction of the force profile

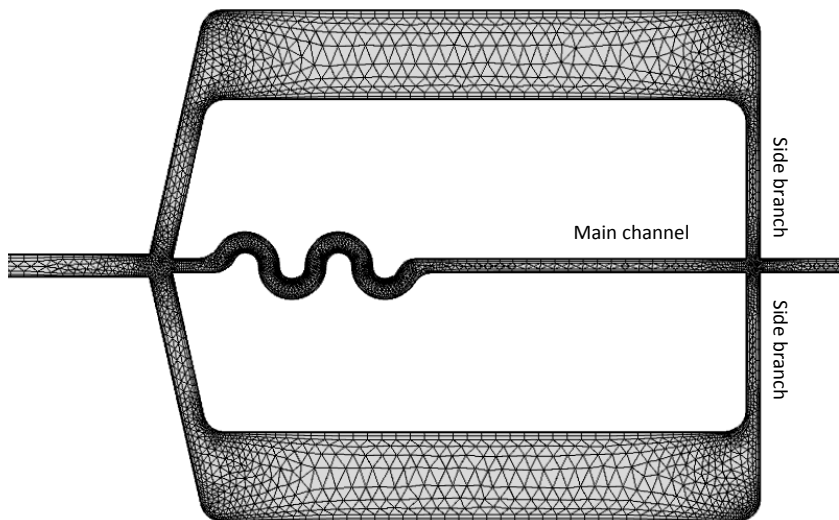


Figure 4.16: Design of the region downstream of the inertial focuser, meshed using Comsol.

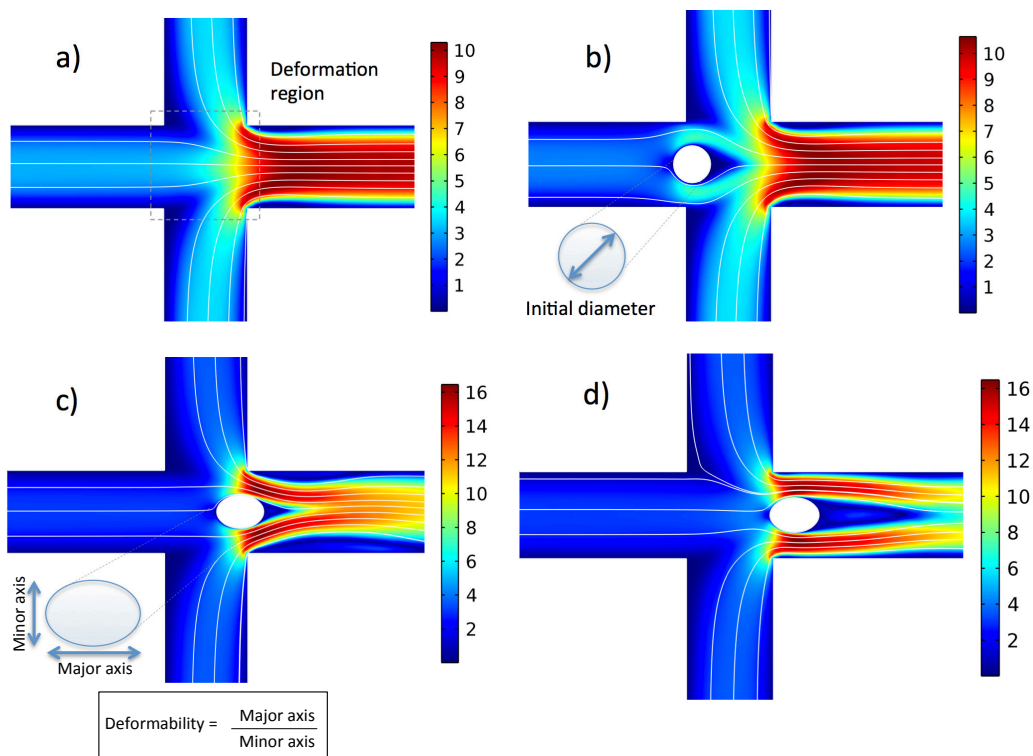


Figure 4.17: Velocity profile and stream lines were evaluated, using Comsol, in the absence of the cell (a), in the presence of a spherical cell at initial position of the deformation region (b), where the cell is not yet exposed to the pinching flow, in the presence of a stretched cell at the position of the maximum deformation (c) and in the case of a stretched cell at the output of the deformation region (d).

4.4. RESULTS

acting on a cell is complex and requires to take into account the fact that the cell deformation and the velocity profile influence each other, as can be seen in Fig. 4.17. On the other hand, to extrapolate the order of magnitude of the stress applied onto each cell one can use a simplified calculation as suggested by Dudani et al. (2013): using the equations 4.31 and 4.33, as well as the data from the numerical simulation, a drag force of about $1.3\mu\text{N}$ was estimated to act on a cell from each sides, for a flow rate $Q_{\text{in}} = 800 \mu\text{L}/\text{min}$. Whereas, the value of the viscous force at the position where cells exhibit maximum deformation is about $0.13 \mu\text{N}$ (as indicated in Table 4.5). The drag force is in the same range of that calculated by Dudani for similar geometries and flow rate (Dudani et al., 2013). Here, for the estimation of the viscous force I am also considering the hydrodynamic shadow downstream of the cell, visible in Fig. 4.17.

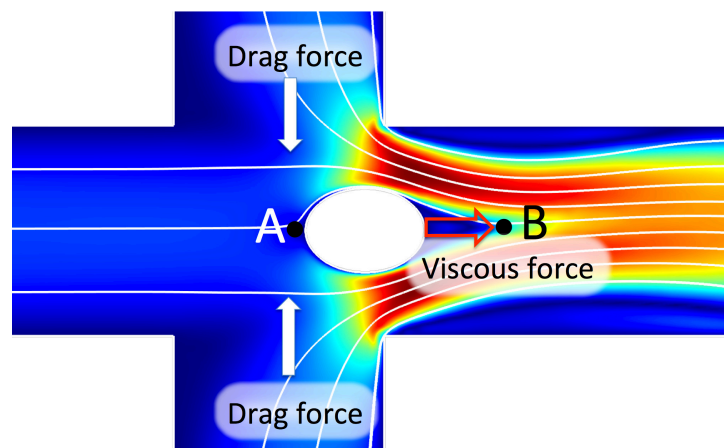


Figure 4.18: Hydrodynamic forces acting on a cell. The drag force acts on the cell from each side, perpendicularly to the direction of the main flow. It is proportional to the square of the mean velocity of the side fluxes. The viscous force is proportional to the difference in fluid speed between *B* and *A* and acts on the cell along the direction of the main flow.

For each cell, two parameters were measured: the initial diameter before being perturbed by the pinched flow and its aspect ratio, also defined as *deformability*, at the position of the maximum deformation, as sketched in Fig. 4.17(b-c).

Parameter	Value	Unit	Description
C_d	1.03		<i>Drag coefficient</i>
D	20	μm	Diameter of the cell
A	314	μm^2	<i>Cross section of the cell</i>
v_{mean}	2.84	m/s	<i>Flow speed</i>
S	1256	μm^2	<i>Surface of the cell</i>
$v_{\text{mean}}(y = a)$	3	m/s	<i>Mean speed at $y = a$</i>
$v_{\text{mean}}(y = b)$	8.5	m/s	<i>Mean speed at $y = b$</i>
Δv	5.5	m/s	$v(b)-v(a)$
Δy	55	μm	Y_b-Y_a
F_d	1.3×10^{-6}	N	<i>Drag force</i>
F_v	1.3×10^{-7}	N	<i>Viscous force</i>

Table 4.5: Parameters used in the calculation of the drag and viscous forces. The value C_d is calculated using the the Eq. 4.32, whereas all the other parameters result from the Comsol simulation.

4.4.2.2 Hydrodynamic stretching of prostate and bladder cancer cells

After having developed and characterised the device, I performed cellular mechanical phenotyping experiments of different cell types. An example of an actual experiment is shown in Fig. 4.19 where a prostate cancer cell DU145 is stretched.

First, I wanted to test the method comparing cells before and after Latrunculin A treatment. This drug is known to prevent actin filaments from polymerising, inducing a global softening of the cell due to the disruption of the actin cytoskeleton (Lyubimova et al., 1999; de Oliveira and Mantovani, 1988). I measured the deformability of a sample of 400 prostate cancer cells (DU145) and a sample of 260 DU145 cells treated with Latrunculin A. I also performed the same measurement on a sample of 230 prostate bladder cells (5637) and a sample of 260 cells after the drug treatment. The results of the analysis are shown in Fig. 4.21.

The histogram in Fig. 4.20 shows the expected increase in deformability after Latrun-

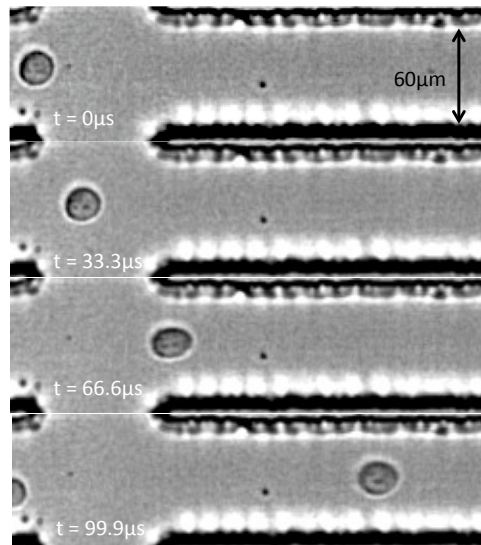


Figure 4.19: Example of a hydrodynamically stretched prostate cancer cell DU145. At the initial frame, the cell enters the deformation region. The cell is unperturbed and hence its shape is spherical. In the second frame the cell starts to experience the effect of the pinched flow and it is slightly deformed. The deformation is around its maximum in the third frame, when the cell is about to leave the deformation region. In the last frame the cell appears less deformed and slightly blurred due to the fact that the flow speed is higher in this region of the device.

culin A treatment for both cell types. Interestingly, a significant difference between prostate and bladder cancer cells before the drug treatment can also be detected. Such a difference is no longer statistically significant after the drug treatment where bladder cancer cells 5637 exhibit a more pronounced softening effect.

4.4.2.3 Hydrodynamic stretching of healthy and cancerous prostate cells

The mechanical phenotyping was also performed on a sample of 2199 healthy prostate cells (PNT2) and on a sample of 2852 prostate cancer cells (DU145), both collected in 13 independent measurements, over three consecutive days. In this case the cellular deformation was achieved using a flow rate of 600 $\mu\text{L}/\text{min}$, that corresponds to a drag force of 0.81 μN and a viscous force of 0.13 μN . Here, in addition to the deformability, I also computed the strain $\delta = (D_{\text{max}} - D_{\text{in}})/D_{\text{in}}$, where D_{max} is the major axis at its maximum deformation and D_{in} is the initial diameter of the cell. Furthermore,

to show the deformability signature of the two different cell types I generated the density scatterplots by plotting the values of the deformability of each cell against the values of their initial diameter. The result of the analysis is shown in Fig. 4.21. Both deformability and strain were statistically different between the two groups. This suggests that the mechanical response of these cells to the external load is a valuable way to discriminate between healthy and cancer cells. Moreover, the density scatterplots exhibited two characteristic profiles.

Intriguingly, a statistically significant difference also emerges between the deformability of PNT2 and DU145 once estimated about 180 μm downstream of the position of maximum deformation. This indicates, not only that the healthy cells PNT2 elongate

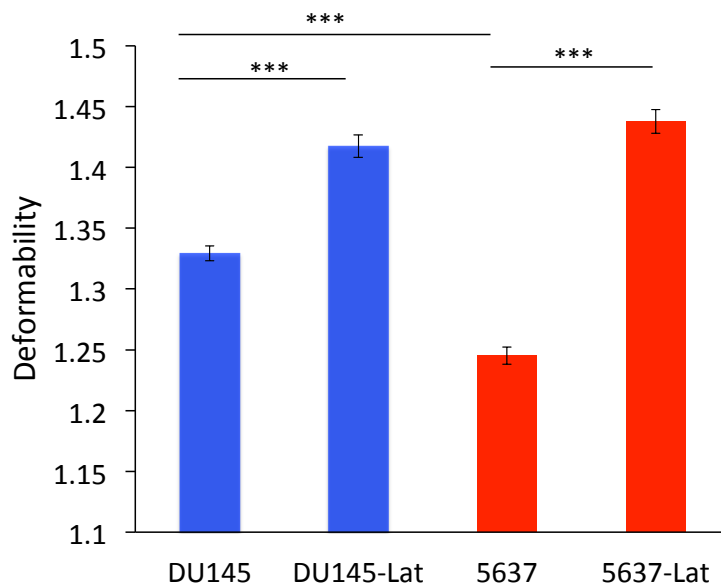


Figure 4.20: Difference in the median deformability between prostate (DU145) and bladder cancer (5637) cells before and after Latrunculin A treatment. Four samples were compared: DU145 cells ($n=400$), DU145 cells treated with Latrunculin A ($n=260$), 5637 ($n=230$) and 5637 treated with Latrunculin A ($n=260$). Error bars represent the standard error. The histogram shows the expected increase in deformability upon Latrunculin A treatment for both cell types ($p < 0.0001$). Moreover, a difference between prostate and bladder cancer cells can be observed as well. One single independent experiment was conducted for each sample.

4.4. RESULTS

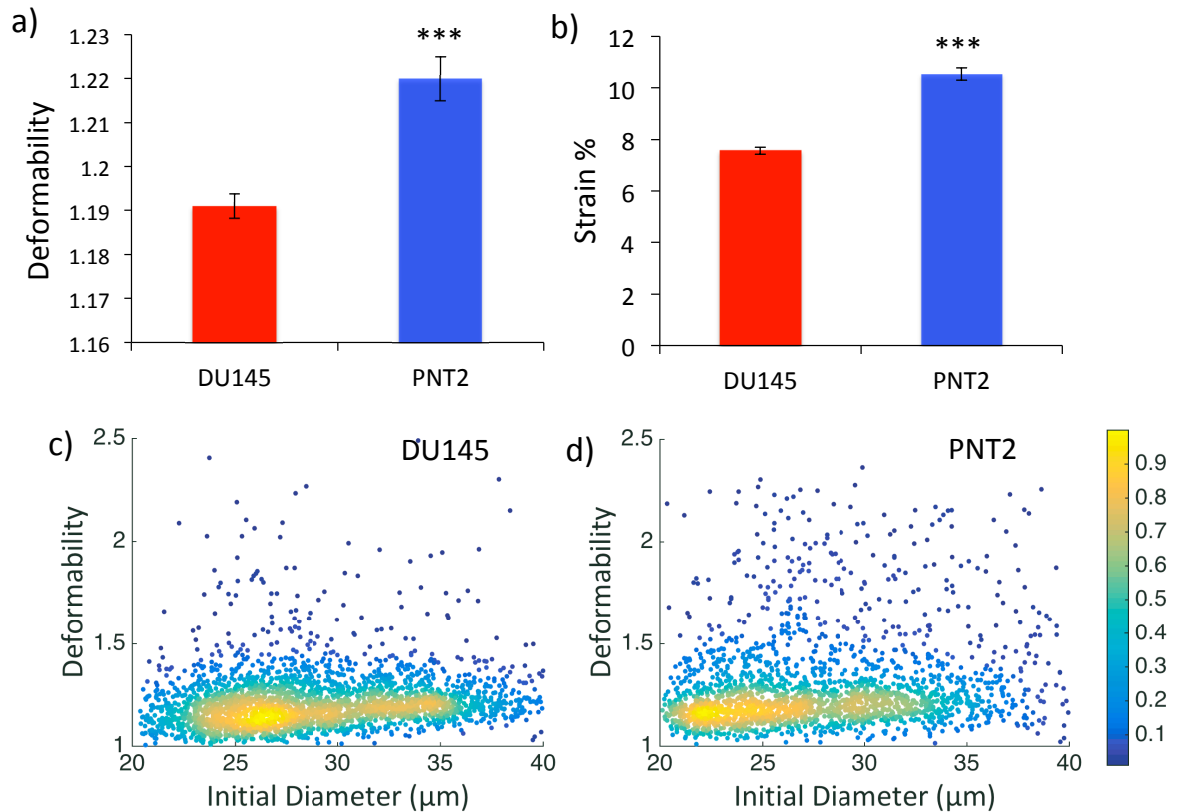


Figure 4.21: Difference in mechanical properties between PNT2 (n=2199) and DU145 (n=2852) cells. For each group data were collected in 13 independent experiments, over three consecutive days. (a) Median deformability of PNT2 cells and DU145 cells. (b) Median strain of PNT2 cells and DU145 cells. Error bars represent standard error. The histograms show that PNT2 cells have a higher deformability and strain compared to the DU145 cells ($p < 0.0001$). (c-d) Density scatterplots of DU145 and PNT2 cells, respectively.

more during the application of the hydrodynamic stress, but also that their recovery is slower than DU145 cells, that conversely exhibit a lower residual deformation.

To test the reproducibility of my measurements I carried out a Wilcoxon rank sum test with deformability as dependent variable and the two independent variables: 'experiment' and 'day'. None of these independent variables affected the deformability ($p > 0.05$). This suggests that no significant effect was observed among different experiments and days.

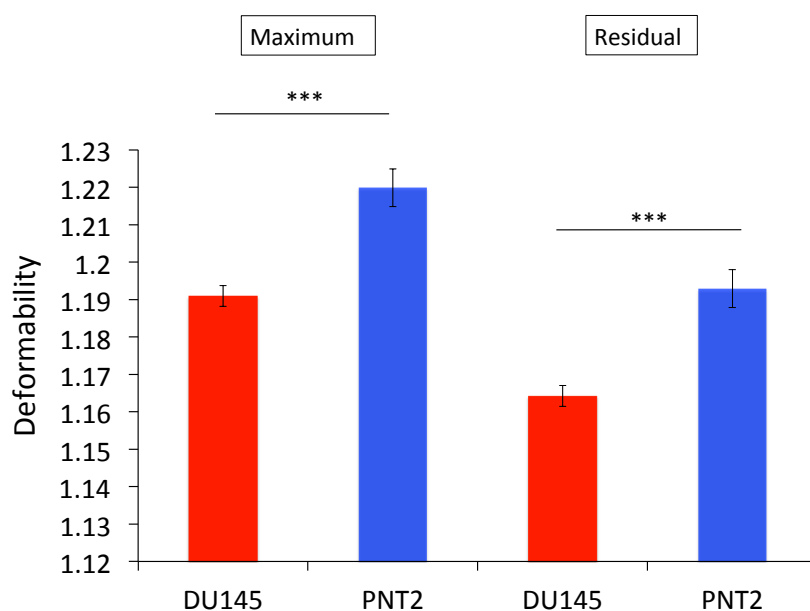


Figure 4.22: The histogram compares the median deformability of PNT2 cells ($n=2199$) and DU145 cells ($n=2852$) at the position of maximum deformation (shown in Fig. 4.21) with the median deformability of the same cells measured $180\ \mu\text{m}$ downstream of such a position, where cells exhibit a residual deformation ($p < 0.0001$). Error bars represent the standard error.

4.5 Discussions

In this chapter I described the two experimental set-ups that I developed to perform cell mechanical phenotyping: the optical stretcher (OS) and the hydrodynamic stretcher (HS). Although the OS allows for the application of a precise step-stress to a cell and to accurately investigate its mechanical response over time, this technique presents few limitations:

- Laser-induced heating was recently observed to strongly affect the cellular mechanical properties, determining a global softening (Yang et al., 2015).
- Its throughput is in the order of 100 cells/h.

Moreover, it proved difficult to obtain a robust device, mainly due to the alignment

4.5. DISCUSSIONS

between the glass capillary and the optical fibres, both vertically and laterally. In fact, the two beams need to have a Gaussian profile and the optical trap has to form at the cells' floating level. In addition, the beam profile, and hence the force profile, at the centre of the trap depends on the distance between the optical fibres and the glass capillary. The fibres-capillary arrangement and their vertical position is dictated by the micropatterned trenches on the PDMS holder (as shown in Fig. 4.11). On the other hand, the distance between the fibres and the capillary has to be manually controlled by carefully sliding the fibres at the desired location. Glass capillaries are fragile, difficult to handle and their dimensions vary within a batch. Thus, as they needed to be replaced often, both vertical and horizontal alignment were easily compromised. In addition, also the fibres are very brittle and small damages of their bare end resulted in a drastic change in the beam quality. Therefore, they required to be continuously inspected, removed from the holder and re-cleaved. In conclusion, this kind of set-up is not ideal as these small adjustments were time-consuming and rendered the measurements non reproducible. A technical improvement of such a system would require an monolithic device, where the fluidic and the optical components were integrated and pre-aligned, for instance through the use of waveguides, as in the work by Bellini et al. (2010, 2012).

As such an improvement was not possible within the time-scale of my PhD and thanks to the acquisition of a high-speed camera, I decided to focus on the development of a purely fluidic device based on the work by Dudani et al. (2013). This approach enabled me to overcome the limitations of the optical stretcher, and reach a throughput in the range of 10^4 cells/s, which accounts for the inherent heterogeneity

of biological samples and makes it a potential candidate for translation into biomedical and clinical settings. Using this technique I demonstrated the possibility to perform label-free detection of different cell types, using the cellular mechanical response as a biomarker. Specifically I found that:

1. The HS was capable of detecting structural softening induced by Latrunculin A (Lautenschläger et al., 2009; Maloney and Van Vliet, 2014) in both prostate and bladder cancer cells (DU145, 5637).
2. Prostate (DU145) and bladder (5637) cancer cells could be discriminated based on their deformability.
3. Healthy (PNT2) and cancer (DU145) prostate cells had a statistically significant different mechanical response to the same hydrodynamic load.

It is important to mention that the experiments were conducted at constant temperature. In fact, cell solutions were kept on ice until the syringe was rapidly moved onto the syringe pump and the experiment was started. The total duration of an experiment is usually less than 2 s. It is also relevant to bare in mind that other factors may influence the cell mechanics, for instance the stiffness of the culturing substrate and the passage number (Huber et al., 2013). In the experiments presented in this chapter all these parameters were controlled. The only influencing factor that cannot be accounted for is the stage within the cell-cycle. The only way to face the cell-to-cell variability is to analyse big samples and therefore the throughput has to be high. Using the HS an inverse relationship between size and deformability was reported by Dudani et al. (2013). Bigger cells would be subjected to lower deformability as their edges are closer to the channel's walls, and therefore the interaction with the

4.5. DISCUSSIONS

parabolic flow would imply smaller forces acting on their surface. Moreover, the same axial elongation corresponds to smaller aspect ratio in a big cell compared to a smaller one (Dudani et al., 2013). Again, the high throughput accounts for this variability unless one wanted to compare two cell types with different mean size. This is the reason why, when comparing two different samples, the use of the strain as a mechanical biomarker would be more accurate. In fact, the strain is a relative deformation with respect to initial size of the cell.

The main limitation of the HS is connected with its tendency to become clogged at the 'cell-fluid separation' region and at the second inertial focuser. In fact, the combination of high flow rates with the effect of the inertial focussing induces a big number of cells to flow on the same equilibrium streamline in a very short time. This eventually results in cell clustering at these two regions of the chip. Partial obstructions would determine slight changes in the stress profile and have a detrimental effect on the measurement reproducibility. A way to reduce this effect would be to flush the channels with a solution of the non-ionic copolymer surfactant Pluronic F-127 (10% w/w in phosphate buffered saline (PBS)), which has been reported to help minimising cell adhesion to the PDMS walls (Hoelzle et al., 2014). Alternatively, an additional inlet could be added to the chip to decouple the flow carrying the cell suspension from the pinching flows. This would remove the requirement for a 'cell-fluid separation' region and introduce the possibility to independently control the flow rate of these different fluxes.

CONCLUSIONS

In this thesis I showed how cell migration in microchannels is influenced by both the dimensionality and the topology of the cellular microenvironment. These physical properties determined the speed at which cells migrate and also the migration strategy adopted by each cell.

Although cells exploited the same biochemical machinery that has been studied for decades in the absence of spatial confinement, they appeared to be able to alter the arrangement of the cytoskeletal components, to adapt to their surrounding environment. For instance, the distribution of actin and myoII appeared different when cells were confined in $2\ \mu\text{m}$ by $2\ \mu\text{m}$ channels, whereas in the case of bigger channels such a distribution was similar to that exhibited by cells migrating on a substrate or in 2D environments. This altered arrangement of the actomyosin cytoskeleton, observed in extremely high constrictions, might play a role in the establishment of the blebbing mode, which occurred with higher percentage in the case of such a small cross sectional areas.

One of the key findings of Chapter 2 was that few processes exhibited a certain degree of periodicity upon spatial confinement, namely: protrusions at the leading edge,

contractile vacuoles' cycles and actin foci activation. This suggests that forcing cells to migrate in a simplified environment induced a reduction in the randomness of these cellular processes. Specifically, the reason behind the correlation between the rate of actin foci and the rate of contractile vacuoles is unknown and will require further investigation. This would suggest the existence of internal clock that regulates different processes inside each individual cell. On the other hand, given the complexity and the dynamic nature of a migrating cell this hypothesis remains extremely challenging to test. Interestingly, using live imaging and the simultaneous labelling of both actin cytoskeleton and microtubules I was able to observe the colocalisation of these two structures. At present, the lack of quantitative techniques impeded me to perform an accurate quantitative analysis of such a dynamic interaction. The development of more sophisticated image analysis tools or customised algorithms will make similar measurements possible.

Another important observation emerged from this study is that instead of a random-like migratory pattern, which characterises the migration in the absence of spatial constriction, once confined cells tended to migrate with constant average speed. Moreover, cells exhibited a wide cell-to-cell variability in their average migratory velocity. I discussed how such a variability could be explained as the result of the interplay among different cellular parameters: the protrusion rate, the mode of migration adopted by the cell, the amount of actin at the leading edge and the number of actin and FRY foci. Moreover, as the spatial confinement was increased, the cell speed tended to decrease. This is allegedly due to the size and mechanical properties of the nucleus. MyoII also turned out to be involved in squeezing the nucleus. In fact, upon dele-

tion of myoII, cells were not able to migrate in channels with 2 μm high ceiling. This result is consistent with previous studies on Dictyostelium cells moving in 2D environments (Jay et al., 1995; Uchida, 2003). In addition, it has been reported that high levels of lamin A expression would hinder the nucleus deformation through narrow constrictions (Rowat et al., 2013). The use of microfluidic devices enabled me to investigate the unknown role of the FRY protein in Dictyostelium, in both adhesions and cytoskeleton integrity. These results were only preliminary, and this will require additional quantitative investigations. Moreover, the role of microtubules was also investigated. More specifically, the number of microtubules appeared to decrease by reducing the cross section of the channels, while the centrosome tended to localise between the nucleus and the leading edge in the majority of the cases. Such a spatial bias in the distribution of MTs suggests that they might play a role in the polarity of confined cells. On the other hand, it remains to be understood how cells with inverted *Nuclear-Centrosomal* orientation (centrosome localised between the nucleus and the trailing edge) are able to migrate directionally. Another aspect to be further investigated is whether microtubules inhibition or stabilisation would induce instability in directional migration in 3D migration, as demonstrated in epithelial cells and fibroblasts migrating on micropatterned strips (Zhang et al., 2014). More specifically, Nocodazole and Taxol treatments would help me understanding whether microtubules are required in defining polarity and preserving directionality in Dictyostelium cells migrating in confined microchannels.

Blebs have only recently been identified as an alternative mode of migration and therefore novel properties are yet to be investigated. In this thesis I found that multiple pro-

teins translocate into blebs at the early stage of their generation, namely myoVII, VatM and PaxB. All of them exhibited a different lifetime and this could presumably suggest a distinct role of these proteins at different stages of the bleb growth. Potential interactions among these proteins could also be possible. On the other hand, it remains to be verified whether they have an active role or are passively pushed into the blebs by the intracellular flow responsible for the initiation stage of the bleb generation. For instance, the comparison between the spatio-temporal distribution of these proteins with that of a fluorescent diffusible cytosolic marker should give more insights into the role of these proteins in blebbing.

The development of microchannels harbouring asymmetric bifurcations allowed me to investigate the hydrodynamic interaction between each migrating cell and its microenvironment. Specifically, if a cell encountered an asymmetric bifurcating path, it exhibited a directional 'decision'. This phenomenon has been recently observed in human neutrophils (Prentice-Mott et al., 2013) and interpreted as a tendency to follow the fluidic path of least hydraulic resistance. In the first instance, my results appeared to be consistent with those presented by Prentice-Mott et al. (2013). In fact, in Chapter 3 I showed how such a tendency appeared to be proportional to the hydraulic resistance ratio between the two branches, regardless of the wide range of chemoattractant concentrations used. On the other hand, a further investigation showed that many cells were able to invade dead-end channels, in spite of their infinite hydraulic resistance. Cells can rapidly change their shape due to actin polymerisation, and active protrusions are constantly generated at the leading edge. If the protrusion is thinner than the cross section of the channel, it could induce a quick displacement of the fluid

around the advancing leading edge. Such a dynamic shape adaptation would prevent cells from generating pressure against the liquid column downstream of them. Hence, the effect of the hydraulic resistance would become negligible compared to the presence of a chemical gradient. To test the separate role of these two competing signals, *i.e.* the chemical gradient and the hydraulic resistance, I developed a novel design capable of decoupling them. Such a topology disproved the role of hydraulic resistance in the 'decision making' process exhibited by Dictyostelium cells. On the other hand, chemotaxis towards increasing concentration of cAMP also fails to fully explain this behaviour as the directional bias did not appear to depend on the concentration and type of chemoattractant used. Interestingly, my results suggested that the directional 'choice' correlated with the local difference in chemical concentration between two asymmetric bifurcating channels. The type of chemical signal cells respond to remains to be determined. A fascinating hypothesis is that cells might undergo *autologous chemotaxis*, as previously observed in cancer cells and neutrophils (Shields et al., 2007; Swartz and Lund, 2012). Within this framework cells would secrete local gradients of chemokines at the leading edge and then respond to them. In the future I will focus on investigating this hypothesis and finding the specific chemokines involved in this process. Another aspect to bear in mind is the *biological redundancy* that underlies cell migration. Recent studies showed how multiple mechanisms could be spatio-temporally coordinated in order to compensate for missing functionalities and ensure a robust cellular locomotion (Ridley et al., 2003; Pollard and Borisy, 2003; Rafelski and Theriot, 2004). Therefore, the complete understanding of the directional 'decision making' would require further investigation.

Additionally, microtubules did not seem to play any role in the directional bias, at least at the concentration of Nocodazole tested. It is yet to be demonstrated whether higher concentration of Nocodazole might have an effect.

The magnitude of the velocity of a confined cell is also associated with its mechanical properties (Sieminski et al., 2006). The ability to change shape according to the local topology has a pivotal importance in cell motility in tissues, where cells are closely packed (Guck et al., 2010). It is currently accepted that the main contribution to cellular elasticity is given by the actin cytoskeleton (Fletcher and Mullins, 2010). For instance, the ability exhibited by neutrophils to squeeze through narrow constrictions *in vitro* was shown to be linked to rapid depolymerisation, followed by reconstitution of the F-actin meshwork (Yap and Kamm, 2005). Neutrophils isolated from the bone marrow were reported to be stiffer than circulating neutrophils, and such an increased stiffness was associated with higher levels of F-actin in the cell cortex (Saito, 2002). Furthermore, drug-induced depolymerisation of actin filaments induces cell softening (Lyubimova et al., 1999; de Oliveira and Mantovani, 1988). This effect is a consequence not only of the reduced number of filaments, but also of the lower degree of cross-linking among them (Gardel et al., 2004). Cell compliance has been demonstrated to allow differentiating between healthy and cancer cells and diminished stiffness has been recognised as a hallmark of the metastatic potential of cancer cells (Guck et al., 2005; Faria et al., 2008). These observations prompted the development of the microfluidic device discussed in Chapter 4. Such a device enabled me to detect differences between prostate and bladder cancer cells, as well as, between healthy and cancerous prostate cells, based on the median single-cell deformability

estimated from large samples of cells.

A further improvement of this technique will be to develop an automated tracking algorithm to detect the cell's deformation over time. This will considerably reduce the user's unconscious bias and time commitment, as well as providing time-dependent measurements of the cellular mechanical response. The edge of each cell will be tracked frame by frame, enabling to investigate also the time-dependent deformability, which could potentially provide additional information on the mechanical response, as I have already shown by analysing the deformability at different position across the flow (Fig. 4.22). Currently, my collaborator Mr Tianjun Huang, who works in Professor Stephen McKenna's group (School of Computing, University of Dundee) is working on the adaptation of his method (Huang et al., 2014). In this algorithm cells are detected based on their approximate radial symmetry and then segmented using a radial active contour model. It is important to note that the analysis of bladder and prostate cells was both motivated and made possible by the collaboration with Professor Ghulam Nabi, leader of the division of surgical uro-oncology at Ninewells Hospital (School of Medicine - University of Dundee). Additionally, I am collaborating with Ms Serenella Tolomeo, who works in Professor Douglas Steele's lab (Ninewells Hospital and Medical School (Neuroscience), Medical Research Institute, University of Dundee). Our aim will be to explore the use of statistical predictive methods and machine learning to classify single cells based on their mechanical properties. Future work will focus on testing this technique on primary cells and clinical samples of known malignancy. An aspect that will be explored is the addition of prognostic capabilities to the technique presented in Chapter 4. Being able, not only to recognise if a cell or

a small subgroup of cells is cancerous, but also to detect its type and aggressiveness would be an ideal aim to pursue. This will require clinical trials to characterise the mechanical properties of many different types of cancer cells from the urinary tract and to compare this information with that provided by standard screening techniques. Additional measurements of different single-cell properties (e.g. biochemical and optical) could also be performed in parallel to the mechanical phenotyping, to increase the sensitivity and specificity of the single-cell classification. If this were successful it would help clinicians making personalised decisions, avoid unnecessary treatments and surgeries, accounting for the *lead time bias*¹ and therefore improving the existing clinical setting.

A more detailed estimation of the force profile acting on every single cell will be carried out in the future, to better describe the cellular mechanical response. The development of alternative topologies will also be explored, aiming to further elucidate the cell-flow interactions, simplify the existing setup and allowing to extract time-dependent information. The estimation of the temporal response represents an important advance as it would be a key adding value to microfluidic devices, which currently lack such a capability, as discussed in section 4.1.4.

Interestingly, Otto et al. (2015) introduced an on-the-fly analysis of deformed cells. This method enables analysis rates of only 100 cells/s but in a continuous fashion, so that of an unlimited number of cells can be probed. This feature would be an advantage over the method presented in this thesis, where the data analysis is performed off-line and the number of cells that can be analysed is restricted by total amount

¹Time between cancer detection through early-stage screening and cancer detection from symptoms.

of cells recorded within one video. Furthermore, the flow rates required to induce a measurable strain (between $0.02 \mu\text{L/s}$ and $0.2 \mu\text{L/s}$) would be much lower than those required in my experimental setup. Therefore, lower-specification and cheaper high speed cameras could be adopted. On the other hand, the technique proposed by Otto et al. (2015) does not allow for a time-resolved estimation of the cell shape but only a static measurement of it. Additionally, the absence of an inertial focuser that guarantees cell-to-cell spacing, together with the use of a constriction with fixed width, might render the system described by Otto et al. (2015) prone to clogging.

The microfluidic device discussed in Chapter 4, coupled with an optimised automatic image analysis toolbox and advanced statistical methods might enable me to perform mechanical phenotyping of a variety of cell types. This would open up the possibility to tackle different biomedical issues, as well as to investigate open questions in developmental biology. For instance looking at *Dictyostelium* cells carrying mutations or treated with specific drugs, might help elucidating the role of new proteins and pathways associated with cell mechanics. Moreover, the combination of the two microfluidic techniques developed in this thesis could also be used in parallel, to study potential relationships between the mechanical properties of a cell and its migratory characteristics.

In conclusion the work presented in this thesis highlights the interdisciplinarity required to investigate complex biological problems. The use of quantitative approaches that span from microtechnology, live imaging, computer vision and computational modelling enabled me to link processes at the molecular and cytoskeletal level with global cellular behaviours. The ability to engineer the cellular microenvironment made

it possible to fine control the physical and chemical landscapes each cell experiences and to investigate the complex and dynamic cellular response. Finally, I showed how this multidisciplinary approach and the methods developed during my doctoral training could also be translated into biomedical applications, where novel label-free, high-throughput methods are needed to improve diagnostic and prognostic standards, and could give an important contribution to the future healthcare.

BIBLIOGRAPHY

- Abhyankar, V. V., Lokuta, M. a., Huttenlocher, A., and Beebe, D. J. (2006). Characterization of a membrane-based gradient generator for use in cell-signaling studies. *Lab on a Chip*, 6(3):389–393.
- Abkarian, M., Faivre, M., and Stone, H. a. (2006). High-speed microfluidic differential manometer for cellular-scale hydrodynamics. *Proceedings of the National Academy of Sciences of the United States of America*, 103(3):538–542.
- Adessi, C., Chapel, A., Vinçon, M., Rabilloud, T., Klein, G., Satre, M., and Garin, J. (1995). Identification of major proteins associated with Dictyostelium discoideum endocytic vesicles. *Journal of Cell Science*, 108(10):3331–3337.
- Ahmed, T., Shimizu, T. S., and Stocker, R. (2010). Microfluidics for bacterial chemotaxis. *Integrative Biology: Quantitative Biosciences from Nano to Macro*, 2(11-12):604–629.
- Alberts, B., Johnson, A., Lewis, J., Raff, M., Roberts, K., and Walter, P. (2007). *Molecular Biology of the Cell*, volume 16. Garland Science.
- Alexander, S., Koehl, G. E., Hirschberg, M., Geissler, E. K., and Friedl, P. (2008). Dynamic imaging of cancer growth and invasion: a modified skin-fold chamber model. *Histochemistry and Cell Biology*, 130(6):1147–1154.
- Allen, G. M., Mogilner, A., and Theriot, J. a. (2013). Electrophoresis of cellular membrane components creates the directional cue guiding keratocyte galvanotaxis. *Current Biology*, 23(7):560–568.
- Allsbrook, W. C., Mangold, K. a., Johnson, M. H., Lane, R. B., Lane, C. G., Amin, M. B., Bostwick, D. G., Humphrey, P. a., Jones, E. C., Reuter, V. E., Sakr, W., Sesterhenn, I. a., Troncoso, P., Wheeler, T. M., and Epstein, J. I. (2001). Interobserver reproducibility of Gleason grading of prostatic carcinoma: Urologic pathologists. *Human Pathology*, 32(1):74–80.
- Amann, K. J. and Pollard, T. D. (2001). The Arp2/3 complex nucleates actin filament branches from the sides of pre-existing filaments. *Nature Cell Biology*, 3(3):306–310.
- Ambravaneswaran, V., Wong, I. Y., Aranyosi, A. J., Toner, M., and Irimia, D. (2010). Directional decisions during neutrophil chemotaxis inside bifurcating channels. *Integrative Biology : quantitative biosciences from nano to macro*, 2(11-12):639–647.
- Ananthakrishnan, R. and Ehrlicher, A. (2007). The forces behind cell movement. *International Journal of Biological Sciences*, 3(5):303–317.

- Andrew, N. and Insall, R. H. (2007). Chemotaxis in shallow gradients is mediated independently of PtdIns 3-kinase by biased choices between random protrusions. *Nature Cell Biology*, 9(2):193–200.
- Ashworth, J. M. and Watts, D. J. (1970). Metabolism of the cellular slime mould *Dictyostelium discoideum* grown in axenic culture. *The Biochemical Journal*, 119(2):175–182.
- Asmolov, E. S. (1999). The inertial lift on a spherical particle in a plane Poiseuille flow at large channel Reynolds number. *Journal of Fluid Mechanics*, 381:63–87.
- Axelrod, D., Hellen, E., and Fulbright, R. (2002). Total internal reflection fluorescence. In Lakowicz, J. R., editor, *Topics in Fluorescence Spectroscopy*, volume 3 of *Topics in Fluorescence Spectroscopy*, pages pp 289–343. Kluwer Academic Publishers, Boston.
- Bagorda, A., Das, S., Rericha, E. C., Chen, D., Davidson, J., and Parent, C. a. (2009). Real-time measurements of cAMP production in live *Dictyostelium* cells. *Journal of Cell Science*, 122(21):3907–3914.
- Bajno, L. (2000). Focal Exocytosis of VAMP3-containing Vesicles at Sites of Phagosome Formation. *The Journal of Cell Biology*, 149(3):697–706.
- Balzer, E. M., Tong, Z., Paul, C. D., Hung, W. C., Stroka, K. M., Boggs, A. E., Martin, S. S., and Konstantopoulos, K. (2012). Physical confinement alters tumor cell adhesion and migration phenotypes. *FASEB Journal*, 26(10):4045–4056.
- Batchelor, G. K. (2000). *An Introduction to Fluid Dynamics*. Cambridge University Press.
- Bausch, a. R., Möller, W., and Sackmann, E. (1999). Measurement of local viscoelasticity and forces in living cells by magnetic tweezers. *Biophysical Journal*, 76(1):573–579.
- Beckham, Y., Vasquez, R. J., Stricker, J., Sayegh, K., Campillo, C., and Gardel, M. L. (2014). Arp2/3 inhibition induces amoeboid-like protrusions in MCF10A epithelial cells by reduced cytoskeletal-membrane coupling and focal adhesion assembly. *PLoS ONE*, 9(6):p.e100943.
- Bellini, N., Bragheri, F., Cristiani, I., Guck, J., Osellame, R., and Whyte, G. (2012). Validation and perspectives of a femtosecond laser fabricated monolithic optical stretcher. *Biomedical Optics Express*, 3(10):2658–68.
- Bellini, N., Vishnubhatla, K., and Bragheri, F. (2010). Femtosecond laser fabricated monolithic chip for optical trapping and stretching of single cells. *Optics Express*, 18(5):4679–4688.
- Bhushan, B. E. (2010). *Springer Handbook of Nanotechnology*. Springer.
- Blaser, H., Reichman-Fried, M., Castanon, I., Dumstrei, K., Marlow, F. L., Kawakami, K., Solnica-Krezel, L., Heisenberg, C.-P., and Raz, E. (2006). Migration of zebrafish

BIBLIOGRAPHY

- primordial germ cells: a role for myosin contraction and cytoplasmic flow. *Developmental Cell*, 11(5):613–627.
- Bonner, J. T., Har, D., and Suthers, H. B. (1989). Ammonia and thymotaxis: Further evidence for a central role of ammonia in the directed cell mass movements of *Dictyostelium discoideum*. *Proceedings of the National Academy of Sciences of the United States of America*, 86(8):2733–2736.
- Bornens, M. (2008). Organelle positioning and cell polarity. *Nature Reviews. Molecular Cell Biology*, 9(11):874–886.
- Boyden, S. (1962). The Chemotactic Effect Of Mixtures Of Antibody and Antigen on Polymorphonuclear Leucocytes. *The Journal of Experimental Medicine*, 115(3):453–466.
- Brangwynne, C. P. (2006). Microtubules can bear enhanced compressive loads in living cells because of lateral reinforcement. *The Journal of Cell Biology*, 173(5):733–741.
- Bruus, H. (2008). Theoretical microfluidics. *Physics*, 18(33235):363.
- Brzostowski, J. A. and Kimmel, A. R. (2006). Nonadaptive regulation of ERK2 in *Dictyostelium*: implications for mechanisms of cAMP relay. *Molecular Biology of the Cell*, 17(10):4220–4227.
- Buenemann, M., Levine, H., Rappel, W.-J., and Sander, L. M. (2010). The role of cell contraction and adhesion in *dictyostelium* motility. *Biophysical Journal*, 99(1):50–8.
- Bukharova, T., Bukahrova, T., Weijer, G., Bosgraaf, L., Dormann, D., van Haastert, P. J., and Weijer, C. J. (2005). Paxillin is required for cell-substrate adhesion, cell sorting and slug migration during *Dictyostelium* development. *Journal of Cell Science*, 118(Pt 18):4295–310.
- Cai, H. and Devreotes, P. N. (2011). Moving in the right direction: How eukaryotic cells migrate along chemical gradients. *Seminars in Cell & Developmental Biology*, 22(8):834–841.
- Caille, N., Thoumine, O., Tardy, Y., and Meister, J.-J. (2002). Contribution of the nucleus to the mechanical properties of endothelial cells. *Journal of Biomechanics*, 35(2):177–187.
- Carrier, A. M.-f., Laurent, V., Santolini, J., Melki, R., Xia, G.-x., Hong, Y., Chua, N.-h., Pantaloni, D., Laurent, V., Santolini, J., and Didry, D. (2012). Factor (ADF / Cofilin) Enhances the Rate of Actin Depolymerizing Filament Turnover : Motility Implication in Actin-based. *The Journal of Cell Biology*, 136(6):1307–1322.
- Charras, G. and Paluch, E. (2008). Blebs lead the way: how to migrate without lamellipodia. *Nature Reviews. Molecular Cell Biology*, 9(9):730–736.
- Charras, G. T., Coughlin, M., Mitchison, T. J., and Mahadevan, L. (2008). Life and times of a cellular bleb. *Biophysical Journal*, 94(5):1836–1853.

- Charras, G. T., Hu, C.-K., Coughlin, M., and Mitchison, T. J. (2006). Reassembly of contractile actin cortex in cell blebs. *The Journal of Cell Biology*, 175(3):477–490.
- Charras, G. T., Yarrow, J. C., Horton, M. a., Mahadevan, L., and Mitchison, T. J. (2005). Non-equilibration of hydrostatic pressure in blebbing cells. *Nature*, 435(7040):365–369.
- Chiba, S., Ikeda, M., Katsunuma, K., Ohashi, K., and Mizuno, K. (2009). MST2- and Furry-Mediated Activation of NDR1 Kinase Is Critical for Precise Alignment of Mitotic Chromosomes. *Current Biology*, 19(8):675–681.
- Chin, C. D., Laksanasopin, T., Cheung, Y. K., Steinmiller, D., Linder, V., Parsa, H., Wang, J., Moore, H., Rouse, R., Umviligihozo, G., Karita, E., Mwambarangwe, L., Braunstein, S. L., van de Wijgert, J., Sahabo, R., Justman, J. E., El-Sadr, W., and Sia, S. K. (2011). Microfluidics-based diagnostics of infectious diseases in the developing world. *Nature Medicine*, 17(8):1015–1019.
- Christopher R. Jacobs, Hayden Huang, R. Y. K. (2012). *Introduction to Cell Mechanics and Mechanobiology*, volume 16. Garland Science.
- Chung, B. G., Flanagan, L. A., Rhee, S. W., Schwartz, P. H., Lee, A. P., Monuki, E. S., and Jeon, N. L. (2005). Human neural stem cell growth and differentiation in a gradient-generating microfluidic device. *Lab on a Chip*, 5(4):401–406.
- Cicuta, P and Donald, A. M. (2007). Microrheology: a review of the method and applications. *Soft Matter*, 3(12):1449–1455.
- Clarke, M., Köhler, J., Arana, Q., Liu, T., Heuser, J., and Gerisch, G. (2002). Dynamics of the vacuolar H(+)-ATPase in the contractile vacuole complex and the endosomal pathway of Dictyostelium cells. *Journal of Cell Science*, 115(14):2893–2905.
- Clift, R., Grace, J., and Weber, M. (2005). *Bubbles, Drops and Particles*. Courier Corporation.
- Coleman, M. L., Sahai, E. a., Yeo, M., Bosch, M., Dewar, A., and Olson, M. F. (2001). Membrane blebbing during apoptosis results from caspase-mediated activation of ROCK I. *Nature Cell Biology*, 3(4):339–345.
- Cong, J., Geng, W., He, B., and Liu, J. (2001). The furry gene of Drosophila is important for maintaining the integrity of cellular extensions during morphogenesis. *Development*, 128(14):2793–2802.
- Conrad, P a., Giuliano, K. a., Fisher, G., Collins, K., Matsudaira, P T., and Taylor, D. L. (1993). Relative distribution of actin, myosin I, and myosin II during the wound healing response of fibroblasts. *Journal of Cell Biology*, 120(6):1381–1391.
- Cooper, G. M. (2000). *The cell: a molecular approach 2*. Sinauer Associates.
- Cooper, J. (1973). Effects of cytochalasin B on actin filaments. In *Cold Spring Harbor Symposia on Quantitative Biology*, volume 37, pages 585–593. Cold Spring Harbor

Laboratory Press.

- Cornillon, S., Gebbie, L., Benghezal, M., Nair, P., Keller, S., Wehrle-Haller, B., Charette, S. J., Brückert, F., Letourneur, F., and Cosson, P. (2006). An adhesion molecule in free-living Dictyostelium amoebae with integrin beta features. *EMBO Reports*, 7(6):617–621.
- Cross, S. E., Jin, Y.-S., Rao, J., and Gimzewski, J. K. (2007). Nanomechanical analysis of cells from cancer patients. *Nature Nanotechnology*, 2(12):780–783.
- Dahl, K. N., Ribeiro, a. J., and Lammerding, J. (2008). Nuclear Shape, Mechanics, and Mechanotransduction. *Circulation Research*, 102(11):1307–1318.
- Davies, L., Satre, M., Martin, J. B., and Gross, J. D. (1993). The target of ammonia action in dictyostelium. *Cell*, 75(2):321–327.
- de Oliveira, C. A. and Mantovani, B. (1988). Latrunculin A is a potent inhibitor of phagocytosis by macrophages. *Life Sciences*, 43(22):1825–1830.
- Dertinger, S. K. W., Chiu, D. T., Jeon, N. L., and Whitesides, G. M. (2001). Generation of Gradients Having Complex Shapes Using Microfluidic Networks. *Analytical Chemistry*, 73(6):1240–1246.
- Di Carlo, D. (2009). Inertial microfluidics. *Lab on a Chip*, 9(21):3038–3046.
- Di Carlo, D., Irimia, D., Tompkins, R. G., and Toner, M. (2007). Continuous inertial focusing, ordering, and separation of particles in microchannels. *Proceedings of the National Academy of Sciences of the United States of America*, 104(48):18892–18897.
- Discher, D., Mohandas, N., and Evans, E. (1994). Molecular maps of red cell deformation: hidden elasticity and in situ connectivity. *Science*, 266(5187):1032–1035.
- Discher, D. E., Janmey, P., and Wang, Y.-L. (2005). Tissue cells feel and respond to the stiffness of their substrate. *Science*, 310(5751):1139–1143.
- Diz-Muñoz, A., Krieg, M., Bergert, M., Ibarlucea-Benitez, I., Muller, D. J., Paluch, E., and Heisenberg, C. P. (2010). Control of directed cell migration in vivo by membrane-to-cortex attachment. *PLoS Biology*, 8(11):1000544.
- Dogterom, M., Kerssemakers, J. W. J., Romet-Lemonne, G., and Janson, M. E. (2005). Force generation by dynamic microtubules. *Current Opinion in Cell Biology*, 17(1):67–74.
- Dormann, D. and Weijer, C. J. (2001). Propagating chemoattractant waves coordinate periodic cell movement in Dictyostelium slugs. *Development (Cambridge, England)*, 128(22):4535–4543.
- Dormann, D. and Weijer, C. J. (2006). Imaging of cell migration. *The EMBO Journal*, 25(15):3480–3493.
- Doyle, A. D., Wang, F. W., Matsumoto, K., and Yamada, K. M. (2009). One-dimensional

- topography underlies three-dimensional fibrillar cell migration. *The Journal of Cell Biology*, 184(4):481–490.
- Dudani, J. S., Gossett, D. R., Tse, H. T. K., and Di Carlo, D. (2013). Pinched-flow hydrodynamic stretching of single-cells. *Lab on a Chip*, 13(18):3728–3734.
- Duffy, D. C., McDonald, J. C., Schueller, O. J. a., and Whitesides, G. M. (1998). Rapid prototyping of microfluidic systems in poly(dimethylsiloxane). *Analytical Chemistry*, 70(23):4974–4984.
- Dufour, A., Thibeaux, R., Labruyère, E., Guillén, N., and Olivo-Marin, J. C. (2011). 3-D active meshes: Fast discrete deformable models for cell tracking in 3-D time-lapse microscopy. *IEEE Transactions on Image Processing*, 20(7):1925–1937.
- Dworkin, M. and Keller, K. (1977). Solubility and diffusion coefficient of adenosine 3': 5'-monophosphate. *Journal of Biological Chemistry*, 252(3):864–865.
- Eddy, R. J., Pierini, L. M., Matsumura, F., and Maxfield, F. R. (2000). Ca²⁺-dependent myosin II activation is required for uropod retraction during neutrophil migration. *Journal of Cell Science*, 113(7):1287–1298.
- Eichinger, L. and Noegel, A. A. (2003). Crawling into a new era—the Dictyostelium genome project. *The EMBO Journal*, 22(9):1941–1946.
- Emoto, K., He, Y., Ye, B., Grueber, W. B., Adler, P. N., Jan, L. Y., and Jan, Y. N. (2004). Control of dendritic branching and tiling by the tricornered-kinase/furry signaling pathway in Drosophila sensory neurons. *Cell*, 119(2):245–256.
- Esue, O., Carson, A. A., Tseng, Y., and Wirtz, D. (2006). A Direct Interaction between Actin and Vimentin Filaments Mediated by the Tail Domain of Vimentin. *Journal of Biological Chemistry*, 281(41):30393–30399.
- Etienne-Manneville, S. (2010). From signaling pathways to microtubule dynamics: the key players. *Current Opinion in Cell Biology*, 22(1):104–111.
- Etienne-Manneville, S. (2013). Microtubules in cell migration. *Annual Review of Cell and Developmental Biology*, 29:471–99.
- Fabry, B., Maksym, G. N., Butler, J. P., Glogauer, M., Navajas, D., and Fredberg, J. J. (2001). Scaling the Microrheology of Living Cells. *Physical Review Letters*, 87(14):148102.
- Falet, H., Hoffmeister, K. M., Neujahr, R., and Hartwig, J. H. (2002). Normal Arp2/3 complex activation in platelets lacking WASp. *Blood*, 100(6):2113–2122.
- Faria, E. C., Ma, N., Gazi, E., Gardner, P., Brown, M., Clarke, N. W., and Snook, R. D. (2008). Measurement of elastic properties of prostate cancer cells using AFM. *The Analyst*, 133(11):1498–1500.
- Flegel, K. A., Pineda, J. M., Smith, T. S., Laszczyk, A. M., Price, J. M., Karasiewicz, K. M., and Damer, C. K. (2011). Copine A is expressed in prestalk cells and regulates

BIBLIOGRAPHY

- slug phototaxis and thertotaxis in developing Dictyostelium. *Development Growth and Differentiation*, 53(8):948–959.
- Fletcher, D. a. and Mullins, R. D. (2010). Cell mechanics and the cytoskeleton. *Nature*, 463(January):485–492.
- Fok, a. K., Clarke, M., Ma, L., and Allen, R. D. (1993). Vacuolar H(+)-ATPase of Dictyostelium discoideum. A monoclonal antibody study. *Journal of Cell Science*, 106(4):1103–1113.
- Fountain, S. J., Parkinson, K., Young, M. T., Cao, L., Thompson, C. R. L., and North, R. A. (2007). An intracellular P2X receptor required for osmoregulation in Dictyostelium discoideum. *Nature*, 448(7150):200–203.
- Friedl, P. (2004). Prespecification and plasticity: shifting mechanisms of cell migration. *Current Opinion in Cell Biology*, 16(1):14–23.
- Friedl, P. and Alexander, S. (2011). Cancer invasion and the microenvironment: Plasticity and reciprocity. *Cell*, 147(5):992–1009.
- Friedl, P. and Wolf, K. (2003). Tumour-cell invasion and migration: diversity and escape mechanisms. *Nature Reviews. Cancer*, 3(5):362–374.
- Gabriel, D., Hacker, U., Köhler, J., Müller-Taubenberger, A., Schwartz, J. M., Westphal, M., and Gerisch, G. (1999). The contractile vacuole network of Dictyostelium as a distinct organelle: its dynamics visualized by a GFP marker protein. *Journal of Cell Science*, 112 Pt 2:3995–4005.
- Gardel, M. L., Nakamura, F., Hartwig, J., Crocker, J. C., Stossel, T. P., and Weitz, D. a. (2006). Stress-dependent elasticity of composite actin networks as a model for cell behavior. *Physical Review Letters*, 96(8):12–15.
- Gardel, M. L., Schneider, I. C., Aratyn-Schaus, Y., and Waterman, C. M. (2010). Mechanical integration of actin and adhesion dynamics in cell migration. *Annual Review of Cell and Developmental Biology*, 26:315–333.
- Gardel, M. L., Shin, J. H., MacKintosh, F. C., Mahadevan, L., Matsudaira, P., and Weitz, D. a. (2004). Elastic behavior of cross-linked and bundled actin networks. *Science*, 304(5675):1301–1305.
- Gerisch, G., Albrecht, R., Heizer, C., Hodgkinson, S., and Maniak, M. (1995). Chemoattractant-controlled accumulation of coronin at the leading edge of Dictyostelium cells monitored using a green fluorescent protein-coronin fusion protein. *Current Biology*, 5(11):1280–1285.
- Gerisch, G., Bretschneider, T., Müller-Taubenberger, A., Simmeth, E., Ecke, M., Diez, S., and Anderson, K. (2004). Mobile actin clusters and traveling waves in cells recovering from actin depolymerization. *Biophysical Journal*, 87(5):3493–3503.
- Gerisch, G. and Keller, H. U. (1981). Chemotactic reorientation of granulocytes stimu-

- lated with micropipettes containing fMet-Leu-Phe. *Journal of Cell Science*, 52(1):1–10.
- Giannone, G., Dubin-Thaler, B. J., Döbereiner, H.-G., Kieffer, N., Bresnick, A. R., and Sheetz, M. P. (2004). Periodic lamellipodial contractions correlate with rearward actin waves. *Cell*, 116(3):431–443.
- Goode, B. L., Drubin, D. G., and Barnes, G. (2000). Functional cooperation between the microtubule and actin cytoskeletons. *Current Opinion in Cell Biology*, 12(1):63–71.
- Gossett, D. R., Tse, H. T. K., Lee, S. a., Ying, Y., Lindgren, A. G., Yang, O. O., Rao, J., Clark, A. T., and Di Carlo, D. (2012). Hydrodynamic stretching of single cells for large population mechanical phenotyping. *Proceedings of the National Academy of Sciences*, 109(20):7630–7635.
- Goudarzi, M., Banisch, T. U., Mobin, M. B., Maghelli, N., Tarbashevich, K., Strate, I., van den Berg, J., Blaser, H., Bandemer, S., Paluch, E., Bakkers, J., Tolić-Nørrelykke, I. M., and Raz, E. (2012). Identification and Regulation of a Molecular Module for Bleb-Based Cell Motility. *Developmental Cell*, 23(1):210–218.
- Gros-Louis, F., Dupré, N., Dion, P., Fox, M. a., Laurent, S., Verreault, S., Sanes, J. R., Bouchard, J.-P., and Rouleau, G. a. (2007). Mutations in SYNE1 lead to a newly discovered form of autosomal recessive cerebellar ataxia. *Nature Genetics*, 39(1):80–85.
- Gruenberg, J. and van der Goot, F. G. (2006). Mechanisms of pathogen entry through the endosomal compartments. *Nature Reviews Molecular Cell Biology*, 7(7):495–504.
- Guck, J. and Ananthakrishnan, R. (2000). Optical deformability of soft biological dielectrics. *Physical Review Letters*, 84(23):5451–5454.
- Guck, J., Ananthakrishnan, R., Cunningham, C. C., and Käs, J. (2002). Stretching biological cells with light. *Journal of Physics: Condensed Matter*, 14(19):4843–4856.
- Guck, J., Ananthakrishnan, R., and Mahmood, H. (2001). The optical stretcher: a novel laser tool to micromanipulate cells. *Biophysical Journal*, 81(2):767–784.
- Guck, J., Lautenschläger, F., Paschke, S., and Beil, M. (2010). Critical review: cellular mechanobiology and amoeboid migration. *Integrative Biology*, 2(11-12):575–583.
- Guck, J., Schinkinger, S., Lincoln, B., and Wottawah, F. (2005). Optical deformability as an inherent cell marker for testing malignant transformation and metastatic competence. *Biophysical Journal*, 88(5):3689–3698.
- Guilak, F., Tedrow, J. R., and Burgkart, R. (2000). Viscoelastic Properties of the Cell Nucleus. *Biochemical and Biophysical Research Communications*, 269(3):781–786.
- Hasson, T. (1999). Molecular motors: sensing a function for myosin-VIIa. *Current Biology*, 9(22):838–841.

BIBLIOGRAPHY

- Hauser, H. and Wagner, R. (1997). *Mammalian cell biotechnology in protein production*. Walter de Gruyter.
- Hawkins, R. J. and Voituriez, R. (2010). Mechanisms of Cell Motion in Confined Geometries. *Mathematical Modelling of Natural Phenomena*, 5(1):84–105.
- Heuser, J., Zhu, Q., and Clarke, M. (1993). Proton pumps populate the contractile vacuoles of Dictyostelium amoebae. *Journal of Cell Biology*, 121(6):1311–1327.
- Hochmuth, R. M. (2000). Micropipette aspiration of living cells. *Journal of Biomechanics*, 33(1):15–22.
- Hoelzle, D. J., Varghese, B. A., Chan, C. K., and Rowat, A. C. (2014). A microfluidic technique to probe cell deformability. *Journal of visualized experiments : JoVE*, (91):51474–51474.
- Hoffman, B. D. and Crocker, J. C. (2009). Cell Mechanics: Dissecting the Physical Responses of Cells to Force. *Annual Review of Biomedical Engineering*, 11(1):259–288.
- Hoffmann, E. K., Lambert, I. H., and Pedersen, S. F. (2009). Physiology of cell volume regulation in vertebrates. *Physiological Reviews*, 89(1):193–277.
- Hricak, H. and Scardino, P. (2009). *Prostate Cancer*. Macmillan Cancer Support.
- Hu, S., Chen, J., Butler, J. P., and Wang, N. (2005). Prestress mediates force propagation into the nucleus. *Biochemical and Biophysical Research Communications*, 329(2):423–428.
- Huang, T., Hacker, C., Lucocq, J., and McKenna, S. J. (2014). Detecting and Segmenting Nanodiscs in Immuno-Electron Micrographs. *Medical Image Understanding and Analysis (MIUA)*, pages 53–58.
- Huber, F., Schnauß, J., Rönicke, S., Rauch, P., Müller, K., Fütterer, C., and Käs, J. (2013). Emergent complexity of the cytoskeleton: from single filaments to tissue. *Advances in Physics*, 62(1):1–112.
- Humphrey, P. A. (2004). Gleason grading and prognostic factors in carcinoma of the prostate. *Modern Pathology*, 17(3):292–306.
- Hur, S. C., Mach, A. J., and Di Carlo, D. (2011). High-throughput size-based rare cell enrichment using microscale vortices. *Biomicrofluidics*, 5(2):22206.
- Huttenlocher, A. and Horwitz, A. R. (2011). Integrins in cell migration. *Cold Spring Harbor Perspectives in Biology*, 3(9):1–16.
- Hynes, R. O. (2002). Integrins: Bidirectional, allosteric signaling machines. *Cell*, 110(6):673–687.
- Ichetovkin, I., Grant, W., and Condeelis, J. (2002). Cofilin produces newly polymerized actin filaments that are preferred for dendritic nucleation by the Arp2/3 complex.

- Current Biology*, 12(1):79–84.
- Ingber, D. E., Madri, J. a., and Jamieson, J. D. (1981). Role of basal lamina in neoplastic disorganization of tissue architecture. *Proceedings of the National Academy of Sciences of the United States of America*, 78(6):3901–3905.
- Insall, R. (2013). The interaction between pseudopods and extracellular signalling during chemotaxis and directed migration. *Current Opinion in Cell Biology*, 25(5):526–531.
- Iranfar, N., Fuller, D., and Loomis, W. F. (2003). Genome-Wide Expression Analyses of Gene Regulation during Early Development of *Dictyostelium discoideum*. *Eukaryotic Cell*, 2(4):664–670.
- Irimia, D., Charras, G., Agrawal, N., Mitchison, T., and Toner, M. (2007). Polar stimulation and constrained cell migration in microfluidic channels. *Lab on a Chip*, 7(12):1783–1790.
- Isambert, H. and Maggs, a. C. (1996). Dynamics and Rheology of Actin Solutions. *Macromolecules*, 29(3):1036–1040.
- Ito, H. (1987). Flow in curved pipes. *JSME International Journal*, 30(262):543–552.
- Iwadate, Y. and Yumura, S. (2008). Actin-based propulsive forces and myosin-II-based contractile forces in migrating *Dictyostelium* cells. *Journal of Cell Science*, 121(8):1314–1324.
- Janmey, P. a. and McCulloch, C. a. (2007). Cell Mechanics: Integrating Cell Responses to Mechanical Stimuli. *Annual Review of Biomedical Engineering*, 9(1):1–34.
- Janson, M. E. and Dogterom, M. (2004). A bending mode analysis for growing microtubules: evidence for a velocity-dependent rigidity. *Biophysical Journal*, 87(4):2723–2736.
- Jay, P. Y., Pham, P. A., Wong, S. A., and Elson, E. L. (1995). A mechanical function of myosin II in cell motility. *Journal of Cell Science*, 108(1):387–393.
- Joints, S. (2012). Applications of Statics to Biomechanics 5 5.1. pages 61–86.
- Kaverina, I., Rottner, K., and Small, J. V. (1998). Targeting, capture, and stabilization of microtubules at early focal adhesions. *The Journal of Cell Biology*, 142(1):181–190.
- Kay, R. R., Langridge, P., Traynor, D., and Hoeller, O. (2008). Changing directions in the study of chemotaxis. *Nature Reviews. Molecular Cell Biology*, 9(6):455–463.
- Kim, S., Kim, H. J., and Jeon, N. L. (2010). Biological applications of microfluidic gradient devices. *Integrative Biology*, 2(11-12):584–603.
- King, J. S. and Insall, R. H. (2009). Chemotaxis: finding the way forward with *Dictyostelium*. *Trends in Cell Biology*, 19(10):523–530.

BIBLIOGRAPHY

- Klein, P. S., Sun, T. J., Saxe, C. L., Kimmel, a. R., Johnson, R. L., and Devreotes, P. N. (1988). A chemoattractant receptor controls development in *Dictyostelium discoideum*. *Science*, 241(4872):1467–1472.
- Koh, K. S., Chin, J., Chia, J., and Chiang, C. L. (2012). Quantitative studies on PDMS-PDMS interface bonding with piranha solution and its swelling effect. *Micromachines*, 3(2):427–441.
- Kollmar, M. (2006). Thirteen is enough: the myosins of *Dictyostelium discoideum* and their light chains. *BMC Genomics*, 7(1):1–15.
- Konijn, T. and Meene, J. V. D. (1967). The acrasin activity of adenosine-3', 5'-cyclic phosphate. *Proceedings of the National Academy of Sciences of the United States of America*, 58(3):1152–1154.
- Koonce, M. P., Köhler, J., Neujahr, R., Schwartz, J. M., Tikhonenko, I., and Gerisch, G. (1999). Dynein motor regulation stabilizes interphase microtubule arrays and determines centrosome position. *The EMBO Journal*, 18(23):6786–6792.
- Kundu, T., Bereiter-Hahn, J., and Hillmann, K. (1991). Measuring elastic properties of cells by evaluation of scanning acoustic microscopy V(Z) values using simplex algorithm. *Biophysical Journal*, 59(6):1194–1207.
- Ladam, G., Vonna, L., and Sackmann, E. (2005). Protrusion force transmission of amoeboid cells crawling on soft biological tissue. *Acta Biomaterialia*, 1(5):485–497.
- Ladoux, B. and Nicolas, A. (2012). Physically based principles of cell adhesion mechanosensitivity in tissues. *Reports on Progress in Physics. Physical Society*, 75(11):116601.
- Lämmermann, T., Bader, B. L., Monkley, S. J., Worbs, T., Wedlich-Söldner, R., Hirsch, K., Keller, M., Förster, R., Critchley, D. R., Fässler, R., and Sixt, M. (2008). Rapid leukocyte migration by integrin-independent flowing and squeezing. *Nature*, 453(7191):51–55.
- Lämmermann, T. and Sixt, M. (2009). Mechanical modes of 'amoeboid' cell migration. *Current Opinion in Cell Biology*, 21(5):636–644.
- Lang, F. (2007). Mechanisms and significance of cell volume regulation. *Journal of the American College of Nutrition*, 26(5 Suppl):613–623.
- Lang, I., Scholz, M., and Peters, R. (1986). Molecular mobility and nucleocytoplasmic flux in hepatoma cells. *Journal of Cell Biology*, 102(4):1183–1190.
- Lang, F; Busch, G L; Völkl, H. (1998). The Diversity of Volume Regulatory Mechanisms. pages 1–45.
- Lange, J. R., Steinwachs, J., Kolb, T., Lautscham, L. A., Harder, I., Whyte, G., and Fabry, B. (2015). Microconstriction Arrays for High-Throughput Quantitative Measurements of Cell Mechanical Properties. *Biophysical Journal*, 109(1):26–34.

- Langridge, P. D. and Kay, R. R. (2006). Blebbing of Dictyostelium cells in response to chemoattractant. *Experimental Cell Research*, 312(11):2009–2017.
- Laurent, V. M., Hénon, S., Planus, E., Fodil, R., Baland, M., Isabey, D., and Gallet, F. (2002). Assessment of mechanical properties of adherent living cells by bead micromanipulation: comparison of magnetic twisting cytometry vs optical tweezers. *Journal of Biomechanical Engineering*, 124(4):408–421.
- Lautenschlaeger, F. and Guck, J. R. (2009). Microfluidic integration of high power dual-beam laser traps for cell mechanical measurements. *2009 International Symposium on Optomechatronic Technologies*, pages 419–422.
- Lautenschläger, F., Paschke, S., Schinkinger, S., Bruel, A., Beil, M., and Guck, J. (2009). The regulatory role of cell mechanics for migration of differentiating myeloid cells. *Proceedings of the National Academy of Sciences of the United States of America*, 106(37):15696–15701.
- Lee, J. N., Jiang, X., Ryan, D., and Whitesides, G. M. (2004). Compatibility of mammalian cells on surfaces of poly(dimethylsiloxane). *Langmuir*, 20(26):11684–11691.
- Li, J. and Lin, F. (2011). Microfluidic devices for studying chemotaxis and electrotaxis. *Trends in Cell Biology*, 21(8):489–497.
- Li, R. and Gundersen, G. G. (2008). Beyond polymer polarity: how the cytoskeleton builds a polarized cell. *Nature Reviews. Molecular Cell Biology*, 9(11):860–873.
- Li Jeon, N., Baskaran, H., Dertinger, S. K. W., Whitesides, G. M., Van de Water, L., and Toner, M. (2002). Neutrophil chemotaxis in linear and complex gradients of interleukin-8 formed in a microfabricated device. *Nature Biotechnology*, 20(8):826–830.
- Lincoln, B., Schinkinger, S., Travis, K., Wottawah, F., Ebert, S., Sauer, F., and Guck, J. (2007a). Reconfigurable microfluidic integration of a dual-beam laser trap with biomedical applications. *Biomedical Microdevices*, 9(5):703–710.
- Lincoln, B., Wottawah, F., Schinkinger, S., Ebert, S., and Guck, J. (2007b). High-Throughput Rheological Measurements with an Optical Stretcher. *Methods in Cell Biology*, 83:397–423.
- Lo, C.-M., Wang, H.-B., Dembo, M., and Wang, Y.-I. (2000). Cell Movement Is Guided by the Rigidity of the Substrate. *Biophysical Journal*, 79(1):144–152.
- Loitto, V. M., Karlsson, T., and Magnusson, K. E. (2009). Water flux in cell motility: Expanding the mechanisms of membrane protrusion. *Cell Motility and the Cytoskeleton*, 66(5):237–247.
- Loomis, W. F. (2006). The Dictyostelium genome. *Current Issues in Molecular Biology*, 8(2):63–74.

- Luxton, G. W. G. and Gundersen, G. G. (2011). Orientation and function of the nuclear-centrosomal axis during cell migration. *Current Opinion in Cell Biology*, 23(5):579–588.
- Lyubimova, A., Bershadsky, A. D., and Ben-Ze'ev, A. (1999). Autoregulation of actin synthesis requires the 3'-UTR of actin mRNA and protects cells from actin overproduction. *Journal of Cellular Biochemistry*, 76(1):1–12.
- Ma, L., Janetopoulos, C., Yang, L., Devreotes, P. N., and Iglesias, P. a. (2004). Two complementary, local excitation, global inhibition mechanisms acting in parallel can explain the chemoattractant-induced regulation of PI(3,4,5)P3 response in dictyostelium cells. *Biophysical Journal*, 87(6):3764–3774.
- Mahadeo, D. C. and Parent, C. A. (2006). Signal Relay During the Life Cycle of Dictyostelium. *Current Topics in Developmental Biology*, 73:115–140.
- Mahmoudian, J., Hadavi, R., Jeddi-Tehrani, M., Mahmoudi, A. R., Bayat, A. A., Shaban, E., Vafakhah, M., Darzi, M., Tarahomi, M., and Ghods, R. (2011). Comparison of the photobleaching and photostability traits of Alexa fluor 568- and fluorescein isothiocyanate- conjugated antibody. *Cell Journal*, 13(3):169–172.
- Maloney, J. M. and Van Vliet, K. J. (2014). Chemoenvironmental modulators of fluidity in the suspended biological cell. *Soft Matter*, 10(40):8031–8042.
- Manahan, C. L., Iglesias, P. a., Long, Y., and Devreotes, P. N. (2004). Chemoattractant signaling in dictyostelium discoideum. *Annual Review of Cell and Developmental Biology*, 20:223–253.
- Maniak, M. (2001). Cell adhesion: Ushering in a new understanding of myosin VII. *Current Biology*, 11(8):315–317.
- Martinez, A. W., Phillips, S. T., Whitesides, G. M., and Carrilho, E. (2010). Diagnostics for the developing world: microfluidic paper-based analytical devices. *Analytical Chemistry*, 82(1):3–10.
- Martynova, L., Locascio, L. E., Gaitan, M., Kramer, G. W., Christensen, R. G., and MacCrehan, W. a. (1997). Fabrication of plastic microfluid channels by imprinting methods. *Analytical Chemistry*, 69(23):4783–4789.
- Mathias, J. R., Walters, K. B., and Huttenlocher, A. (2009). Neutrophil motility in vivo using zebrafish. *Methods in Molecular Biology*, 571:151–166.
- Mattheyses, A. L., Simon, S. M., and Rappoport, J. Z. (2010). Imaging with total internal reflection fluorescence microscopy for the cell biologist. *Journal of Cell Science*, 123(Pt 21):3621–3628.
- Mattila, P. K. and Lappalainen, P. (2008). Filopodia: molecular architecture and cellular functions. *Nature Reviews Molecular Cell Biology*, 9(6):446–454.
- Maugis, B., Brugués, J., Nassoy, P., Guillen, N., Sens, P., and Amblard, F. (2010). Dy-

- namic instability of the intracellular pressure drives bleb-based motility. *Journal of Cell Science*, 123(Pt 22):3884–3892.
- McCann, C. P., Kriebel, P. W., Parent, C. a., and Losert, W. (2010). Cell speed, persistence and information transmission during signal relay and collective migration. *Journal of cell science*, 123(10):1724–1731.
- McCormick, R. M., Nelson, R. J., Alonso-Amigo, M. G., Benvegnu, D. J., and Hooper, H. H. (1997). Microchannel electrophoretic separations of DNA in injection-molded plastic substrates. *Analytical Chemistry*, 69(14):2626–2630.
- Mcdonald, J. C., Duffy, D. C., Anderson, J. R., and Chiu, D. T. (2000). Fabrication of microfluidic systems in poly (dimethylsiloxane). *Electrophoresis*, 21(1):27–40.
- McDonald, J. C. and Whitesides, G. M. (2002). Poly(dimethylsiloxane) as a material for fabricating microfluidic devices. *Accounts of Chemical Research*, 35(7):491–499.
- Miller-Keane (2003). Miller-Keane Encyclopedia and Dictionary of Medicine, Nursing, and Allied Health, Seventh Edition.
- Minsky, M. (1988). Memoir on Inventing the Confocal Scanning Microscope. *Scanning*, 10(4):128–138.
- Moeendarbary, E. and Harris, A. R. (2014). Cell mechanics: principles, practices, and prospects. *Wiley Interdisciplinary Reviews: Systems Biology and Medicine*, 6(5):371–388.
- Moeendarbary, E., Valon, L., Fritzsche, M., Harris, A. R., Moulding, D. a., Thrasher, A. J., Stride, E., Mahadevan, L., and Charras, G. T. (2013). The cytoplasm of living cells behaves as a poroelastic material. *Nature Materials*, 12(3):253–61.
- Mohandas, N. and Evans, E. (1994). Mechanical properties of the red cell membrane in relation to molecular structure and genetic defects. *Annual Review of Biophysics and Biomolecular Structure*, 23(1):787–818.
- Morote, J., Raventos, C. X., Lorente, J. A., Lopez-Pacios, M. A., Encabo, G., De Torres, I., and Andreu, J. (1997). Comparison of percent free prostate specific antigen and prostate specific antigen density as methods to enhance prostate specific antigen specificity in early prostate cancer detection in men with normal rectal examination and prostate specific antigen b. *Journal of Urology*, 158(2):502–504.
- Müller, D. J. and Dufrêne, Y. F. (2008). Atomic force microscopy as a multifunctional molecular toolbox in nanobiotechnology. *Nature Nanotechnology*, 3(5):261–269.
- Nagai, T. and Mizuno, K. (2014). Multifaceted roles of furry proteins in invertebrates and vertebrates. *Journal of Biochemistry*, 155(3):137–146.
- Nagel, O., Guven, C., Theves, M., Driscoll, M., Losert, W., and Beta, C. (2014). Geometry-Driven Polarity in Motile Amoeboid Cells. *PLoS ONE*, 9(12):113382.
- Neilson, M. P., Veltman, D. M., van Haastert, P. J. M., Webb, S. D., Mackenzie, J. a., and

- Insall, R. H. (2011). Chemotaxis: a feedback-based computational model robustly predicts multiple aspects of real cell behaviour. *PLoS Biology*, 9(5):e1000618.
- Ofer, N., Mogilner, A., and Keren, K. (2011). From the Cover: Actin disassembly clock determines shape and speed of lamellipodial fragments. *Proceedings of the National Academy of Sciences*, 108(51):20394–20399.
- Otto, O., Rosendahl, P., Mietke, A., Golfier, S., Herold, C., Klaue, D., Girardo, S., Pagliara, S., Ekpenyong, A., Jacobi, A., Wobus, M., Töpfner, N., Keyser, U. F., Mansfeld, J., Fischer-Friedrich, E., and Guck, J. (2015). Real-time deformability cytometry: on-the-fly cell mechanical phenotyping. *Nature Methods*, 12(3):199–202.
- P. A. Weiss (1961). *The Molecular Control of Cellular Activity*, volume 34. McGraw-Hill.
- Pajerowski, J. D., Dahl, K. N., Zhong, F. L., Sammak, P. J., and Discher, D. E. (2007). Physical plasticity of the nucleus in stem cell differentiation. *Proceedings of the National Academy of Sciences of the United States of America*, 104(40):15619–15624.
- Paliwal, S., Iglesias, P. a., Campbell, K., Hilioti, Z., Groisman, A., and Levchenko, A. (2007). MAPK-mediated bimodal gene expression and adaptive gradient sensing in yeast. *Nature*, 446(7131):46–51.
- Paluch, E., Piel, M., Prost, J., Bornens, M., and Sykes, C. (2005). Cortical actomyosin breakage triggers shape oscillations in cells and cell fragments. *Biophysical Journal*, 89(1):724–733.
- Paluch, E. K. and Raz, E. (2013). The role and regulation of blebs in cell migration. *Current Opinion in Cell Biology*, 25(5):582–590.
- Pang, K. M., Lee, E., and Knecht, D. a. (1998). Use of a fusion protein between GFP and an actin-binding domain to visualize transient filamentous-actin structures. *Current Biology*, 8(7):405–408.
- Pathak, A. and Kumar, S. (2012). Independent regulation of tumor cell migration by matrix stiffness and confinement. *Proceedings of the National Academy of Sciences of the United States of America*, 109(26):10334–10339.
- Peskin, C. S., Odell, G. M., and Oster, G. F. (1993). Cellular motions and thermal fluctuations: the Brownian ratchet. *Biophysical Journal*, 65(1):316–324.
- Petrie, R. J., Doyle, A. D., and Yamada, K. M. (2009). Random versus directionally persistent cell migration. *Nature Reviews. Molecular Cell Biology*, 10(8):538–549.
- Phillips, R., Kondev, J., Theriot, J., Garcia, H., and Chasan, B. (2010). Physical Biology of the Cell. *American Journal of Physics*, 78(11):1230.
- Piruska, A., Nikcevic, I., Lee, S. H., Ahn, C., Heineman, W. R., Limbach, P. A., and Seliskar, C. J. (2005). The autofluorescence of plastic materials and chips measured under laser irradiation. *Lab on a Chip*, 5(12):1348–1354.
- Pollard, T. D., Blanchoin, L., and Mullins, R. D. (2000). Molecular mechanisms con-

- trolling actin filament dynamics in nonmuscle cells. *Annu. Rev. Biophys. Biomol. Struct.*, 29(1):545–576.
- Pollard, T. D. and Borisy, G. G. (2003). Cellular motility driven by assembly and disassembly of actin filaments. *Cell*, 112(4):453–465.
- Pouthas, F., Girard, P., Lecaudey, V., Ly, T. B. N., Gilmour, D., Boulin, C., Pepperkok, R., and Reynaud, E. G. (2008). In migrating cells, the Golgi complex and the position of the centrosome depend on geometrical constraints of the substratum. *Journal of Cell Science*, 121(14):2406–2414.
- Prasad, V., Semwogerere, D., and Weeks, E. R. (2007). Confocal microscopy of colloids. *Journal of Physics: Condensed Matter*, 19(11):113102.
- Prentice-Mott, H. V., Chang, C.-H., Mahadevan, L., Mitchison, T. J., Irimia, D., and Shah, J. V. (2013). Biased migration of confined neutrophil-like cells in asymmetric hydraulic environments. *Proceedings of the National Academy of Sciences of the United States of America*, 110(52):21006–21011.
- Putnam, a. J., Schultz, K., and Mooney, D. J. (2001). Control of microtubule assembly by extracellular matrix and externally applied strain. *American Journal of Physiology. Cell Physiology*, 280(3):556–564.
- Rachel, R., Meyer, C., Klingl, A., Gürster, S., Heimerl, T., Wasserburger, N., Burghardt, T., Küper, U., Bellack, A., Schopf, S., Wirth, R., Huber, H., and Wanner, G. (2010). *Electron Microscopy of Model Systems*, volume 96. Academic Press.
- Rafelski, S. M. and Theriot, J. a. (2004). Crawling toward a unified model of cell mobility: spatial and temporal regulation of actin dynamics. *Annual Review of Biochemistry*, 73(1):209–39.
- Reinsch, S. and Gönczy, P. (1998). Mechanisms of nuclear positioning. *Journal of Cell Science*, 111 (Pt 1):2283–2295.
- Ren, X. D., Kiosses, W. B., and Schwartz, M. A. (1999). Regulation of the small GTP-binding protein Rho by cell adhesion and the cytoskeleton. *EMBO Journal*, 18(3):578–585.
- Rentsch, P. S. and Keller, H. (2000). Suction pressure can induce uncoupling of the plasma membrane from cortical actin. *European Journal of Cell Biology*, 79(12):975–981.
- Ridley, A. J., Schwartz, M. A., Burridge, K., Firtel, R. A., Ginsberg, M. H., Borisy, G., Parsons, J. T., and Horwitz, A. R. (2003). Cell migration: integrating signals from front to back. *Science*, 302(5651):1704–1709.
- Riedl, J., Crevenna, A. H., Kessenbrock, K., Yu, J. H., Bista, M., Bradke, F., Jenne, D., Holak, T. a., Werb, Z., Sixt, M., Wedlich-soldner, R., Klopferspitz, A., Avenue, P., and Francisco, S. (2010). Lifeact: a versatile marker to visualize F-actin. *Nature Methods*, 5(7):1–8.

BIBLIOGRAPHY

- Roberts, M. a., Rossier, J. S., Bercier, P., and Girault, H. (1997). UV laser machined polymer substrates for the development of microdiagnostic systems. *Analytical Chemistry*, 69(11):2035–2042.
- Rodriguez, O. C., Schaefer, A. W., Mandato, C. a., Forscher, P., Bement, W. M., and Waterman-Storer, C. M. (2003). Conserved microtubule-actin interactions in cell movement and morphogenesis. *Nature Cell Biology*, 5(7):599–609.
- Rolli, C. G., Seufferlein, T., Kemkemer, R., and Spatz, J. P. (2010). Impact of tumor cell cytoskeleton organization on invasiveness and migration: a microchannel-based approach. *PloS One*, 5(1):8726.
- Rosenbluth, M. J., Lam, W. a., and Fletcher, D. a. (2008). Analyzing cell mechanics in hematologic diseases with microfluidic biophysical flow cytometry. *Lab on a Chip*, 8(7):1062–1070.
- Rowat, A. C., Jaalouk, D. E., Zwerger, M., Ung, W. L., Eydelnant, I. A., Olins, D. E., Olins, A. L., Herrmann, H., Weitz, D. A., and Lammerding, J. (2013). Nuclear Envelope Composition Determines the Ability of Neutrophil-type Cells to Passage through Micron-scale Constrictions. *Journal of Biological Chemistry*, 288(12):8610–8618.
- Russom, A., Gupta, A. K., Nagrath, S., Di Carlo, D., Edd, J. F., and Toner, M. (2009). Differential inertial focusing of particles in curved low-aspect-ratio microchannels. *New Journal of Physics*, 11(7):75025.
- Sackmann, E. K., Fulton, A. L., and Beebe, D. J. (2014). The present and future role of microfluidics in biomedical research. *Nature*, 507(7491):181–189.
- Saetzler, K., Sonnenschein, C., and Soto, a. M. (2011). Systems biology beyond networks: Generating order from disorder through self-organization. *Seminars in Cancer Biology*, 21(3):165–174.
- Saito, H. (2002). Mechanical properties of rat bone marrow and circulating neutrophils and their responses to inflammatory mediators. *Blood*, 99(6):2207–2213.
- Sameshima, M., Imai, Y., and Hashimoto, Y. (1988). The position of the microtubule-organizing center relative to the nucleus is independent of the direction of cell migration in *Dictyostelium discoideum*. *Cell Motility and the Cytoskeleton*, 9(2):111–6.
- Scherber, C., Aranyosi, A. J., Kulemann, B., Thayer, S. P., Toner, M., Iliopoulos, O., and Irimia, D. (2012). Epithelial cell guidance by self-generated EGF gradients. *Integrative Biology*, 4(3):259.
- Schindler, J. and Sussman, M. (1979). Inhibition by ammonia of intracellular cAMP accumulation in *Dictyostelium discoideum*: Its significance for the regulation of morphogenesis. *Developmental Genetics*, 1(1):13–20.
- Schliwa, M., Euteneuer, U., Gräf, R., and Ueda, M. (1998). Centrosomes, microtubules and cell migration. In *Biochemical Society Symposium*, volume 65, pages 223–231.

- Schrödinger, E. (1944). *What is life?*
- Schumann, K., Lämmermann, T., Bruckner, M., Legler, D. F., Polleux, J., Spatz, J. P., Schuler, G., Förster, R., Lutz, M. B., Sorokin, L., and Sixt, M. (2010). Immobilized Chemokine Fields and Soluble Chemokine Gradients Cooperatively Shape Migration Patterns of Dendritic Cells. *Immunity*, 32(5):703–713.
- Schütze, K., Maniotis, A., and Schliwa, M. (1991). The position of the microtubule-organizing center in directionally migrating fibroblasts depends on the nature of the substratum. *Proceedings of the National Academy of Sciences of the United States of America*, 88(19):8367–8371.
- Schwab, A. (2001). Function and spatial distribution of ion channels and transporters in cell migration. *American Journal of Physiology. Renal Physiology*, 280(5):739–747.
- Sedzinski, J., Biro, M., Oswald, A., Tinevez, J.-Y., Salbreux, G., and Paluch, E. (2011). Polar actomyosin contractility destabilizes the position of the cytokinetic furrow. *Nature*, 476(7361):462–466.
- Selden, L. A., Kinoshita, H. J., Estes, J. E., and Gershman, L. C. (1999). Impact of profilin on actin-bound nucleotide exchange and actin polymerization dynamics. *Biochemistry*, 38(9):2769–2778.
- Servant, G., Weiner, O. D., Neptune, E. R., Sedat, J. W., and Bourne, H. R. (1999). Dynamics of a chemoattractant receptor in living neutrophils during chemotaxis. *Molecular Biology of the Cell*, 10(4):1163–1178.
- Shelby, J. P. and Chiu, D. T. (2004). Controlled rotation of biological micro- and nanoparticles in microvortices. *Lab on a Chip*, 4(3):168–170.
- Shields, J. D., Fleury, M. E., Yong, C., Tomei, A. A., Randolph, G. J., and Swartz, M. A. (2007). Autologous Chemotaxis as a Mechanism of Tumor Cell Homing to Lymphatics via Interstitial Flow and Autocrine CCR7 Signaling. *Cancer Cell*, 11(6):526–538.
- Siegel, R. L., Miller, K. D., and Jemal, A. (2015). Cancer Statistics, 2015. *CA: A Cancer Journal for Clinicians*, 65(1):5–29.
- Sieminski, A. L., Mackellar, D., Gong, H., Kamm, R. D., Wells, A., Lauffenburger, D. A., Zaman, M. H., Trapani, L. M., Sieminski, A. L., Mackellar, D., Gong, H., Kamm, R. D., Wells, A., Lauffenburger, D. A., and Matsudaira, P. (2006). Migration of tumor cells in 3D matrices is governed by matrix stiffness along with cell-matrix adhesion and proteolysis. *Proceedings of the National Academy of Sciences of the United States of America*, 103(15):15–16.
- Skoge, M., Adler, M., Groisman, A., Levine, H., Loomis, W. F., and Rappel, W.-j. J. (2010). Gradient sensing in defined chemotactic fields. *Integrative Biology*, 2(11-12):659–668.
- SMETS, P. and Bartholomay, i. A. F. (1971). Repetitive Pattern and Biological Periodicity: A Mathematical Interpretation. *Mathematical Biosciences*, 10(3):333–351.

- Smilenov, L. B., Mikhailov, A., Pelham, R. J., Marcantonio, E. E., and Gundersen, G. G. (1999). Focal adhesion motility revealed in stationary fibroblasts. *Science*, 286(5442):1172–1174.
- Sofla, A. Y. N. and Martin, C. (2010). Vapor-assisted bonding of poly (dimethylsiloxane) and silicon-based substrates. *Methods*, 2:442–444.
- Sok Won, K., Yesul, H., and Jaeran, L. (2011). Measurement of Diffusion Coefficients of Fluorescence Beads and Quantum Dots Using Fluorescence Correlation Spectroscopy. *Journal of the Korean Physical Society*, 59(51):3177.
- Song, L., Nadkarni, S. M., Bödeker, H. U., Beta, C., Bae, A., Franck, C., Rappel, W.-J. J., Loomis, W. F., and Bodenschatz, E. (2006). Dictyostelium discoideum chemotaxis: threshold for directed motion. *European Journal of Cell Biology*, 85(9-10):981–989.
- Squires, T. M. and Quake, S. R. (2005). Microfluidics: Fluid physics at the nanoliter scale. *Reviews of Modern Physics*, 77(3):977–1026.
- Sraj, I., Szatmary, A., and Desai, S. (2012). Erythrocyte deformation in high-throughput optical stretchers. *Physical Review E*, 85(4):41923.
- Stachurski, Z. H. (2009). *Mechanical behavior of materials*, volume 12. Cambridge University Press.
- Stevense, M., Chubb, J. R., and Muramoto, T. (2011). Nuclear organization and transcriptional dynamics in Dictyostelium. *Development Growth and Differentiation*, 53(4):576–586.
- Stroka, K. M., Gu, Z., Sun, S. X., and Konstantopoulos, K. (2014a). Bioengineering paradigms for cell migration in confined microenvironments. *Current Opinion in Cell Biology*, 30(1):41–50.
- Stroka, K. M., Jiang, H., Chen, S. H., Tong, Z., Wirtz, D., Sun, S. X., and Konstantopoulos, K. (2014b). Water permeation drives tumor cell migration in confined microenvironments. *Cell*, 157(3):611–623.
- Suozi, K. C., Wu, X., and Fuchs, E. (2012). Spectraplakins: Master orchestrators of cytoskeletal dynamics. *Journal of Cell Biology*, 197(4):465–475.
- Svitkina, T. M., Verkhovsky, A. B., McQuade, K. M., and Borisy, G. G. (1997). Analysis of the actin-myosin II system in fish epidermal keratocytes: Mechanism of cell body translocation. *Journal of Cell Biology*, 139(2):397–415.
- Swaney, K., Huang, C.-H., and Devreotes, P. (2010). Eukaryotic Chemotaxis: A Network of Signaling Pathways Controls Motility, Directional Sensing, and Polarity Kristen. *Annual Review of Biophysics*, 39:265–289.
- Swartz, M. a. and Lund, A. W. (2012). Lymphatic and interstitial flow in the tumour microenvironment: linking mechanobiology with immunity. *Nature Reviews Cancer*, 12(3):210–219.

- Tabeling, P. (2010). *Introduction to Microfluidics*. Oxford University Press.
- Tambe, D. T., Corey Hardin, C., Angelini, T. E., Rajendran, K., Park, C. Y., Serra-Picamal, X., Zhou, E. H., Zaman, M. H., Butler, J. P., Weitz, D. A., Fredberg, J. J., and Trepap, X. (2011). Collective cell guidance by cooperative intercellular forces. *Nature Materials*, 10(6):469–475.
- Tani, T. (2002). Development of Periodic Tension in the Contractile Vacuole Complex Membrane of Paramecium Governs Its Membrane Dynamics. *Cell Biology International*, 26(10):853–860.
- Taylor, A. M., Rhee, S. W., Tu, C. H., Cribbs, D. H., Cotman, C. W., and Jeon, N. L. (2003). Microfluidic Multicompartment Device for Neuroscience Research. *Langmuir : the ACS Journal of Surfaces and Colloids*, 19(5):1551–1556.
- Terry, S. C., Jerman, J. H., and Angell, J. B. (1979). A gas chromatographic air analyzer fabricated on a silicon wafer. *IEEE Transactions on Electron Devices*, 26(12):1880–1886.
- Théry, M. and Bornens, M. (2008). Get round and stiff for mitosis. *HFSP Journal*, 2(2):65–71.
- Tikhonenko, I., Nag, D. K., Robinson, D. N., and Koonce, M. P. (2009). Microtubule-nucleus interactions in dictyostelium discoideum mediated by central motor kinases. *Eukaryotic Cell*, 8(5):723–731.
- Toepke, M. W. and Beebe, D. J. (2006). PDMS absorption of small molecules and consequences in microfluidic applications. *Lab on a Chip*, 6(12):1484–1486.
- Tomchik, K. J. and Devreotes, P. N. (1981). Adenosine 3',5'-monophosphate waves in Dictyostelium discoideum: a demonstration by isotope dilution-fluorography. *Science*, 212(4493):443–446.
- Tominaga, D. (2010). Periodicity detection method for small-sample time series datasets. *Bioinformatics and Biology Insights*, 4:127–136.
- Traynor, D. and Kay, R. R. (2007). Possible roles of the endocytic cycle in cell motility. *Journal of Cell Science*, 120(14):2318–27.
- Trepap, X., Deng, L., An, S. S., Navajas, D., Tschumperlin, D. J., Gerthoffer, W. T., Butler, J. P., and Fredberg, J. J. (2007). Universal physical responses to stretch in the living cell. *Nature*, 447(7144):592–595.
- Tuxworth, R. I., Weber, I., Wessels, D., Addicks, G. C., Soll, D. R., Gerisch, G., and Titus, M. a. (2001). A role for myosin VII in dynamic cell adhesion. *Current Biology*, 11(5):318–329.
- Tyson, R. a., Zatulovskiy, E., Kay, R. R., and Bretschneider, T. (2014). How blebs and pseudopods cooperate during chemotaxis. *Proceedings of the National Academy of Sciences*, 111(32):11703–11708.

BIBLIOGRAPHY

- Uchida, K. and Yumura, S. (2004). Dynamics of novel feet of Dictyostelium cells during migration. *Journal of Cell Science*, 117(8):1443–1455.
- Uchida, K. S. K. (2003). Myosin II contributes to the posterior contraction and the anterior extension during the retraction phase in migrating Dictyostelium cells. *Journal of Cell Science*, 116(1):51–60.
- Ueda, M., Gräf, R., MacWilliams, H. K., Schliwa, M., and Euteneuer, U. (1997). Centrosome positioning and directionality of cell movements. *Proceedings of the National Academy of Sciences of the United States of America*, 94(18):9674–9678.
- Ueda, M. and Ogihara, S. (1994). Microtubules are required in amoeba chemotaxis for preferential stabilization of appropriate pseudopods. *Journal of Cell Science*, 107, (Pt 8):2071–2079.
- Van Haastert, P. J. M. and Devreotes, P. N. (2004). Chemotaxis: signalling the way forward. *Nature Reviews. Molecular Cell Biology*, 5(8):626–634.
- Velve-Casquillas, G., Le Berre, M., Piel, M., and Tran, P. T. (2010). Microfluidic tools for cell biological research. *Nano Today*, 5(1):28–47.
- Vicker, M. G. and Grutsch, J. F. (2008). Dual chemotaxis signalling regulates Dictyostelium development: intercellular cyclic AMP pulses and intracellular F-actin disassembly waves induce each other. *European journal of cell biology*, 87(10):845–861.
- Vinogradova, T., Miller, P. M., and Kaverina, I. (2009). Microtubule network asymmetry in motile cells: Role of Golgi-derived array. *Cell Cycle*, 8(14):2168–2174.
- Vogel, V. and Sheetz, M. (2006). Local force and geometry sensing regulate cell functions. *Nature Reviews Molecular Cell Biology*, 7(4):265–275.
- Walker, G. (2004). Cell infection within a microfluidic device using virus gradients. *Sensors and Actuators B: Chemical*, 98(2-3):347–355.
- Warrick, E. L., Hunter, J., and Barr, a. J. (1952). Polymer Chemistry of the Linear Siloxanes. *Industrial and Engineering Chemistry*, 44(9):2196–2202.
- Waterman-Storer, C. M. and Salmon, E. (1999). Positive feedback interactions between microtubule and actin dynamics during cell motility. *Current Opinion in Cell Biology*, 11(1):61–67.
- Waterman-Storer, C. M., Worthylake, R. a., Liu, B. P., Burridge, K., and Salmon, E. D. (1999). Microtubule growth activates Rac1 to promote lamellipodial protrusion in fibroblasts. *Nature Cell Biology*, 1(1):45–50.
- Webb, D. J., Donais, K., Whitmore, L. a., Thomas, S. M., Turner, C. E., Parsons, J. T., and Horwitz, A. F. (2004). FAK-Src signalling through paxillin, ERK and MLCK regulates adhesion disassembly. *Nature Cell Biology*, 6(2):154–161.
- Weijer, C. J. (1999). Morphogenetic cell movement in Dictyostelium. *Seminars in Cell*

- & *Developmental Biology*, 10(6):609–619.
- Weijer, C. J. (2009). Collective cell migration in development. *Journal of Cell Science*, 122(Pt 18):3215–3223.
- Weijer, C. J. and Williams, J. G. (2009). Dictyostelium: Cell Sorting and Patterning. *eLS*, pages 1–12.
- Weiner, O. D., Marganski, W. a., Wu, L. F., Altschuler, S. J., and Kirschner, M. W. (2007). An actin-based wave generator organizes cell motility. *PLoS Biology*, 5(9):221.
- Whitesides, G. M. (2006). The origins and the future of microfluidics. *Nature*, 442(7101):368–373.
- Williams, G. B., Elder, E. M., and Sussman, M. (1984). Modulation of the cAMP relay in Dictyostelium discoideum by ammonia and other metabolites: Possible morphogenetic consequences. *Developmental Biology*, 105(2):377–388.
- Wilson, C., Tsuchida, M., and Allen, G. (2010). Myosin II contributes to cell-scale actin network treadmill through network disassembly. *Nature*, 465(7296):373–377.
- Wirtz, D., Konstantopoulos, K., and Searson, P. C. (2011). The physics of cancer: the role of physical interactions and mechanical forces in metastasis. *Nature Reviews. Cancer*, 11(7):512–522.
- Wottawah, F., Schinkinger, S., and Lincoln, B. (2005). Characterizing single suspended cells by optorheology. *Acta Biomaterialia*, 1(3):263–271.
- Yang, T., Nava, G., Minzioni, P., Vegliione, M., Bragheri, F., Lelii, F. D., Vazquez, R. M., Osellame, R., and Cristiani, I. (2015). Investigation of temperature effect on cell mechanics by optofluidic microchips. *Biomedical Optics Express*, 6(8):2991.
- Yap, B. and Kamm, R. D. (2005). Cytoskeletal remodeling and cellular activation during deformation of neutrophils into narrow channels. *Journal of Applied Physiology*, 99(6):2323–2330.
- Yoshida, K. and Soldati, T. (2006). Dissection of amoeboid movement into two mechanically distinct modes. *Journal of Cell Science*, 119(18):3833–3844.
- Yoshimura, T., Matsushima, K., Tanaka, S., Robinson, E. A., Appella, E., Oppenheim, J. J., and Leonard, E. J. (1987). Purification of a human monocyte-derived neutrophil chemotactic factor that has peptide sequence similarity to other host defense cytokines. *Proceedings of the National Academy of Sciences of the United States of America*, 84(24):9233–9237.
- Yumura, S. and Kitanishi-Yumura, T. (1990). Fluorescence-mediated visualization of actin and myosin filaments in the contractile membrane-cytoskeleton complex of Dictyostelium discoideum. *Cell Structure and Function*, 15(6):355–364.
- Zatulovskiy, E., Tyson, R., Bretschneider, T., and Kay, R. R. (2014). Bleb-driven chemotaxis of Dictyostelium cells. *Journal of Cell Biology*, 204(6):1027–1044.

BIBLIOGRAPHY

- Zeman, K., Engelhard, H., and Sackmann, E. (1990). Bending undulations and elasticity of the erythrocyte membrane: effects of cell shape and membrane organization. *European Biophysics Journal*, 18(4):203–219.
- Zemel, a., Rehfeldt, F., Brown, a. E. X., Discher, D. E., and Safran, S. a. (2010). Optimal matrix rigidity for stress fiber polarization in stem cells. *Nature Physics*, 6(6):468–473.
- Zhang, J., Guo, W.-H., and Wang, Y.-L. (2014). Microtubules stabilize cell polarity by localizing rear signals. *Proceedings of the National Academy of Sciences*, 111(46):16383–16388.
- Zhang, Q., Bethmann, C., Worth, N. F., Davies, J. D., Wasner, C., Feuer, A., Ragnauth, C. D., Yi, Q., Mellad, J. a., Warren, D. T., Wheeler, M. a., Ellis, J. a., Skepper, J. N., Vorgerd, M., Schlotter-Weigel, B., Weissberg, P. L., Roberts, R. G., Wehnert, M., and Shanahan, C. M. (2007). Nesprin-1 and -2 are involved in the pathogenesis of Emery - Dreifuss muscular dystrophy and are critical for nuclear envelope integrity. *Human Molecular Genetics*, 16(23):2816–2833.
- Zicha, D., Dunn, G. A., and Brown, A. F. (1991). A new direct-viewing chemotaxis chamber. *Journal of Cell Science*, 99(4):769–775.
- Zigmond, S. H. (1977). Ability of polymorphonuclear leukocytes to orient in gradients of chemotactic factors. *Journal of Cell Biology*, 75(2):606–616.